

Instigating and monitoring transdermal drug delivery using ultrasound-mediated cavitation

Anne Charlotte van Blokland
Magdalen College
University of Oxford

Supervisors
Professor Constantin C. Coussios
Professor Robert C. Carlisle

Trinity 2018

A thesis submitted for the degree of Doctor of Philosophy

Abstract

Injections are a commonly used and widely accepted method of drug administration to prevent and treat diseases. Although using a needle and syringe provides a rapid, low-cost, and direct way of administering almost any kind of therapeutic agent into the body, it is a painful and invasive method leading to issues of patient compliance and needle–phobia. The delivery of drugs through the skin (transdermal delivery) is an attractive alternative approach because it is non-invasive and has low associated risks. However, the penetration of molecules into/through the skin is severely restricted by the outermost layer of the skin (stratum corneum). Initial studies of ultrasound-mediated, cavitation-enhanced transdermal drug delivery have shown great promise by utilising a gel formulation containing polymeric cavitation nuclei to help deliver a model immunogen (Ovalbumin) into the skin. However, enhanced adoption of this technology to permit delivery of several classes of therapeutic agents requires further validation and optimisation and is currently stymied by the lack of real-time monitoring when used across a broad range of therapeutic classes and environmental conditions. Such monitoring is especially important in situations where the dose of the delivered therapeutic agent needs to be precisely defined. Therefore, the focus of this thesis is to achieve transdermal delivery using cavitation-enhanced transport and develop methodologies to monitor or at least confirm successful delivery in real-time.

Work reported in this thesis focusses on replicating and further optimising the current methodology for cavitation-enhanced delivery, with the intent of extending its application to a wide range of therapeutic agents of different molecular size ranges: a small molecule (Sumatriptan, 413 Da); an antibody (IgG, 150 kDa); and a DNA vaccine (2.6 kDa, Touchlight Genetics Ltd.). Since the predominant mechanism of ultrasound-enhanced skin permeability and transport was found to be inertial cavitation, polymeric nanocups (NCs) capable of lowering the acoustic pressure required for cavitation inception, were used to generate sustained inertial cavitation in the applied formulation. This was achieved at an ultrasound frequency of 265 kHz, 10% duty cycle, 10 ms pulse length, 10 Hz pulse repetition frequency, and peak rarefactional pressures of $\geq$ 1.0 MPa.

The first set of studies (Chapter 2) aimed to investigate the utility of pig skin *ex vivo* as a model for testing cavitation-mediated transdermal transport of a large protein-based

therapeutic agent (i.e. IgG antibody) and identified important parameters which may enable such transport.

Studies reported in Chapter 3 focus on cavitation-mediated delivery of low-molecular-weight drugs. The focus of the ultrasound setup was optimised and a vascularised skin model with reproducible skin thickness was chosen for *in vivo* studies. In addition, a small therapeutic agent for the treatment of migraine (i.e. Sumatriptan) was chosen to improve the selective separation of delivered drug from other skin homogenate contents and therefore allow easier detection of the drug using a validated and standardised technique (HPLC). The results showed that, in the presence of 10-minutes sustained inertial cavitation (> 15 μJ, 1.6-1.8 MPa acoustic pressure), a total delivery of up to 800 μg Sumatriptan (corresponding to ~8% of the 10.4 mg applied dose) was detected in the skin and bloodstream 20 minutes after the start of the treatment. The blood plasma concentrations (up to 568 μg/mL Sumatriptan) were around 1000-fold higher than the therapeutic Sumatriptan concentration (0.23-0.75 μg/mL) required in mice. In contrast, only 0.02% of the applied dose was found in the murine skin after insonation at less than 1.0 MPa with no Sumatriptan detected in the bloodstream.

In Chapter 4, the feasibility of inducing an *in vivo* immune response to a therapeutic DNA vaccine as a result of cavitation-enhanced delivery was studied. A luciferase reporter vector (i.e. dbDNA™/Luc) was used to assess whether cavitation-enhanced transport can enable the transfection of cells and provide raised transgene expression levels. When performing the experiments with a therapeutic DNA vaccine against influenza A virus (i.e. dbDNA™/Cal09), an immune response was induced after treating the mice with sustained inertial cavitation during the 'Prime' (on day 0) and the 'Boost' (on day 20) treatment. Quantification of delivery using real-time PCR demonstrated that during a single cavitation treatment ~ 0.01% of the 50 μg applied dbDNA™ dose was delivered into the skin. Remarkably, however, cavitation-mediated delivery achieved a 34.2% transfection efficiency compared to 0.1% for the conventional needle-and-syringe approach. Consequently, the delivered dbDNA™ copies were sufficient to generate specific antibodies against the HA1 peptide. These antibodies were first detected 21 days after the 'Boost' treatment and increased to day 50. However, at all time points the cavitation-induced immune response was still 37-fold lower than the level achieved after needle-and-syringe injection.

The work reported here therefore helps to develop and validate an experimental setup and has demonstrated the clinical potential of using cavitation-mediated transport as a promising novel needle-free transdermal technology to deliver therapeutic levels of a small molecule drug into the bloodstream. Furthermore, with the potential of inducing 34.2% transfection efficiency by ultrasound-mediated cavitation, it is believed that this non-invasive delivery technology has further potential when used as a needle-free gene delivery system.

Statement of Originality

I hereby declare that this submission is my own work and, to the best of my knowledge, it contains no materials previously published or written by another person, or substantial proportions of material which have been accepted for the award of any other degree or diploma at the University of Oxford or any other educational institution, except where due acknowledgement is made in the thesis.

Any contribution made to the research by others, with whom I have worked at the University of Oxford or elsewhere, is explicitly acknowledged in the thesis.

I also declare that the intellectual content of this thesis is the product of my own work, except to the extent that assistance from others in the project's design and conception or in style, presentation and linguistic expression is acknowledged.



Anne Charlotte van Blokland

August 2018

Acknowledgements

This thesis would not have been possible without the tremendous support of so many people. I would like to express my very great appreciation to Prof. Constantin Coussios and Prof. Robert Carlisle for entrusting me with this research, for supporting me through the peaks and troughs of my DPhil journey, and for sharing their valuable expertise and inspirational passion for biomedical research. I am thankful to Owen Mumford for sponsoring my doctoral research work and in particular Andy Vardé and Toby Cowe for their collaboration with the project. My special thanks also extend to the collaborators at Touchlight Genetics for enabling the advancement of my research into Chapter 4. My heartfelt gratitude goes to the BUBBL family, for their assistance, support, and their endless resources of finding solutions to any brainteaser. Appreciation is also due to the workshop technicians Jim Fisk and David Salisbury for bringing to reality my hand-drawn designs, and for their friendly advice. I would like to thank Jane Clark, my dyslexia support tutor, for teaching me how to read and write all over again. Finally, I owe more than words can express to my dear family for their immense support, patience, and restoring my sense of perspective time after time. Last, but not least, I am particularly grateful for all the mice that have contributed to this thesis.

Statement of Contribution

I gratefully acknowledge the following who contributed to this doctoral research.

Chapter 2

- **Dr. Sunali Bhatnagar**: Offered training to fabricate NC batches, and collaborated in performing 'IgG-FITC Study'.
- **James Fisk:** Fabricating formulation holder.
- **Richard Stillion:** Histology slicing and H&E staining porcine skin.

Chapter 3

- **Prof. Robert Carlisle:** Performing mouse handling procedures.
- **Dr. Luca Bau:** Supported establishing and optimising HPLC method.
- **James Fisk:** Fabricating formulation holder II in Perspex.
- **Fabio Bianchi:** Converting coupling cone II design to 3D print product.
- **Ida Parisi:** Histology slicing and Masson's trichrome staining murine skin.

Chapter 4

- **Prof. Robert Carlisle:** Performing mouse handling procedures.
- **Dr. Lisa Caproni & Sarah Milson:** provision of dbDNA™/Luc and dbDNA™/Cal09.

Dissemination

Peer-Reviewed Journal Publications

van Blokland, A.C., Bau, L., Cowe, T., Varde, A., Coussios, C.C. & Carlisle, R. (2018). *'Controlling cavitation activity for ultrasound-enhanced transdermal delivery of small molecule therapeutics into the bloodstream'* (in preparation).

Owen, J., Menon, J., Gray, M., Gill, M., Miller, R.L., **van Blokland, A.C.**, Vallis, K., & Carlisle, R., '*A Clinically applicable technique for actively loading liposomes with EGF-DTPA-In^{111} for targeted therapeutic delivery via ultrasound induced cavitation'* (in preparation).

Conference Presentations

Van Blokland, A.C., Bhatnagar, S., Feddern, L., Carlisle, R. & Coussios, C.C., '*Instigation and monitoring transdermal drug delivery using cavitation-enhanced ultrasound'*, MeiBioEng16, United Kingdom, Oxford, 5-6 September 2016.

Van Blokland, A.C., Bhatnagar, S., Carlisle, R., Coussios, C.C., '*Mediating and monitoring transdermal drug delivery using cavitation-enhanced ultrasound'*, BioEngenuity: Improving Human Health Keynotes, Oxford, United Kingdom, 10 November 2016.

Van Blokland, A.C., Cowe, T., Varde, A., Coussios, C.C., Carlisle, R., '*In vivo mediating and monitoring transdermal delivery using cavitation-enhanced ultrasound',* Controlled Release Society, Annual meeting 2017, Boston, USA, 15-19 July 2017.

Table of Contents

List of Figures x
Acronyms and abbreviations xiii

Chapter 1: Literature Review and Research Objectives 1

1.1 Transdermal drug delivery 1
1.2 The skin 3
1.2.1 The structure and function of the skin 3
1.2.2 The skin as an immune site 6
1.3 Crossing the skin barrier 9
1.3.1 Passive enhancement techniques 9
1.3.2 Active enhancement techniques 10
1.4 Acoustic principles in cavitation-enhanced transdermal delivery 18
1.4.1 Acoustic waves 18
1.4.2 Attenuation, Scattering and Absorption 18
1.4.3 Acoustic impedance 20
1.4.4 Mechanisms of sonophoresis 20
1.4.5 Localised transport regions 24
1.4.6 Acoustic cavitation detection 25
1.4.7 Ultrasound-mediated transdermal delivery 26
1.5 Current limitations to transdermal drug delivery systems 31

Chapter 2: *Ex vivo* delivery study of therapeutic agents into pig skin 33

2.1 Introduction 33
2.2 Materials and Methods 37
2.2.1 Therapeutic Ultrasound Setup 37
2.2.2 Calibration of the transducer pressure field 40
2.2.3 Cavitation nuclei 42
2.2.4 Passive cavitation monitoring 44
2.2.5 Gel formulation 46
2.2.6 Ex vivo delivery study 52
2.2.7 Histology on porcine skin 61
2.2.8 Statistical analysis 62
2.3 Results 63
2.3.1 IgG-FITC Study 63
2.3.2 IgG Repeat Studies 71
2.4 Conclusions and Discussion 80
2.4.1 Cavitation activity 81
2.4.2 Method of detection 82
2.4.3 Ex vivo skin model 84
2.5 Summary 85

Chapter 3: *In vivo* cavitation-enhanced transdermal delivery of Sumatriptan ... 86

3.1 Introduction 86
3.1.1 Migraine 87
3.1.2 Sumatriptan administration routes 88
3.1.3 Ultrasound-enhanced transdermal delivery 91

3.2 Materials and Methods 94
3.2.1 Therapeutic ultrasound setup 95
3.2.2 Passive cavitation monitoring 99
3.2.3 Experimental groups 100
3.2.4 Formulation preparation 105
3.2.5 Animal model 105
3.2.6 General experimental protocol 106
3.2.7 Histology on BALB/c skin 107
3.2.8 Detection Sumatriptan by HPLC 107
3.2.9 Sample preparation 109
3.2.10 HPLC method 112
3.2.11 Data analysis of chromatograms 117
3.3 Results 122
3.3.1 In vivo Sumatriptan delivery – Safety Study 122
3.3.2 In vivo Sumatriptan Repeat Study 1 132
3.3.3 In vivo Sumatriptan Repeat Study 2 144
3.4 Summary 163

Chapter 4: *In vivo* cavitation-enhanced epidermal vaccine delivery 166

4.1 Introduction 166
4.1.1 Vaccination 166
4.1.2 Type of vaccines 167
4.1.3 Influenza virus 168
4.1.4 Production of influenza vaccines 170
4.1.5 Working mechanism of DNA vaccine 174
4.1.6 DNA vaccine delivery methods 175
4.1.7 Validating successful immunity induced by DNA vaccine 179
4.2 Materials and Methods 182
4.2.1 Luciferase Studies 182
4.2.2 Luciferase Study 2 185
4.2.3 Dose Delivery Efficiency 191
4.2.4 Influenza Vaccination 194
4.3 Results 197
4.3.1 Luciferase Study 1 197
4.3.2 Luciferase Study 2 201
4.3.3 Influenza Vaccination 215
4.4 Summary 221

Chapter 5: Conclusions and Future Work 223

5.1 Research overview 223
5.2 Research limitations and future directions 230
5.2.1 Research skills 230
5.2.2 Skin model 232
5.2.3 Ultrasound parameters 234
5.2.4 Formulation 235
5.2.5 Cavitation optimisation 236
5.2.6 Therapeutic agent 237
5.2.7 Clinical relevance and development 238
References 240

List of Figures

Figure 1.1	Major skin structures illustration.	4
Figure 1.2	Illustration of skin structure and immunological network.	7
Figure 1.3	3D Visualisation of particle penetration in porcine skin.	29
Figure 2.1	Schematic representation of the therapeutic ultrasound setup.	37
Figure 2.2	Characterisation of ultrasound field of therapeutic setup.	41
Figure 2.3	Nanocup characterisation.	43
Figure 2.4	Example of PCD voltage trace and time-frequency diagram.	44
Figure 2.5	Ready-to-use Anagel® versus degassed Carpobol®.	48
Figure 2.6	Acoustic emission spectrograms of different NC concentrations.	51
Figure 2.7	Acoustic emission spectrograms of IgG-FITC study.	64
Figure 2.8	IgG-FITC delivery into the skin.	65
Figure 2.9	Excitation and emission spectra of two fluorescent dyes.	67
Figure 2.10	Co-registered histological sections of pig skin.	69
Figure 2.11	Combined acoustic emission spectrograms.	72
Figure 2.12	Acoustic emission spectrograms – IgG Repeat Studies.	74
Figure 2.13	IgG delivery into the skin – IgG Repeat Studies.	76
Figure 2.14	Correlation between acoustic emissions and dermal delivery.	81
Figure 3.1	Sumatriptan plasma concentration over time in humans.	89
Figure 3.2	Schematic timeframe of sample collection.	95
Figure 3.3	Characterisation pressure profile of therapeutic setup.	96
Figure 3.4	Re-design and characterisation of coupling cone II.	97
Figure 3.5	Schematic representation of the therapeutic ultrasound setup.	98
Figure 3.6	Example PCD voltage trace and windowing signal.	100
Figure 3.7	Plot defining the ‘Sub cavitation’ and ‘Cavitation’ regime.	102
Figure 3.8	Buffer and pump gradient chart for HPLC method.	112
Figure 3.9	Representative chromatograms of blank run and skin sample.	113
Figure 3.10	Retention time drift of chromatograms.	115
Figure 3.11	Re-alignment of chromatogram to correct for the retention drift.	117
Figure 3.12	Calibration samples Sumatriptan in skin.	119
Figure 3.13	Calibration samples Sumatriptan in blood.	120
Figure 3.14	Inspection pre-focal acoustic activity.	122
Figure 3.15	Acoustic emissions from NCs with Sumatriptan.	124
Figure 3.16	Assessment of skin damage after treatment.	125

Figure 3.17	Sumatriptan delivery into the skin.	127
Figure 3.18	Sumatriptan delivery into the blood.	129
Figure 3.19	Characterisation of pre-focal cavitation.	133
Figure 3.20	Acoustic emissions from NCs with Sumatriptan.	135
Figure 3.21	Assessment of skin damage after treatment.	137
Figure 3.22	Sumatriptan delivery into the skin.	138
Figure 3.23	Sumatriptan delivery into the blood.	140
Figure 3.24	Correlation between acoustic emissions and total delivery.	141
Figure 3.25	Comparison acoustic emissions detected.	143
Figure 3.26	Acoustic emissions from NCs with Sumatriptan.	145
Figure 3.27	Assessment of skin damage after treatment.	146
Figure 3.28	Histology cross-section of non-treated BALB/c mouse skin.	148
Figure 3.29	Assessment of skin damage on macroscopic and microscopic level.	149
Figure 3.30	Sumatriptan delivery into the skin.	151
Figure 3.31	Sumatriptan delivery into the blood.	153
Figure 3.32	Correlation between acoustic emissions and total delivery.	154
Figure 3.33	Comparison acoustic emissions detected.	155
Figure 3.34	Influence mice strain on Sumtriptan delivery.	157
Figure 4.1	Illustration routes inducing DNA immunisation.	174
Figure 4.2	Illustration important steps in immunisation by DNA vaccine.	179
Figure 4.3	Treatment locations of cavitation-enhanced gene delivery.	183
Figure 4.4	Calibration samples of dbDNA™ /Luc in skin.	190
Figure 4.5	Calibration samples of dbDNA™ /Cal09 in skin.	194
Figure 4.6	Timeline of Influenza vaccination.	195
Figure 4.7	Acoustic emissions from NCs with dbDNA™/ Luc.	197
Figure 4.8	Luciferase activity 18 hours post-treatment.	198
Figure 4.9	Correlation between acoustic emissions and the bioluminescence.	200
Figure 4.10	Acoustic emissions from NCs with dbDNA™/ Luc.	202
Figure 4.11	Luciferase activity 24 hours post-treatment.	204
Figure 4.12	Transfection and delivery efficiency dbDNA™.	207
Figure 4.13	Correlation between acoustic emissions and the bioluminescence.	211
Figure 4.14	Bioluminescence versus dbDNA™ copies.	213
Figure 4.15	Acoustic emissions from NCs with dbDNA™/ Cal09.	216
Figure 4.16	Titre levels of antibodies against dbDNA™/ Cal09 in the blood.	218

List of Tables

Table 2.1	Thickness of human and animal skin.	34
Table 2.2	Ultrasound parameters *ex vivo* experiment.	39
Table 2.3	Experimental groups for *ex vivo* experiment.	54
Table 3.1	Ultrasound parameters *in vivo* experiments.	99
Table 3.2	Experimental groups in 'Safety Study'.	101
Table 3.3	Experimental groups in 'Sumatriptan Repeat Studies'.	104
Table 3.4	Pharmacokinetic parameters of Sumatriptan.	159
Table 3.5	Overview Sumatriptan delivery in the three *in vivo* studies.	163
Table 4.1	Overview experimental groups 'Influenza Vaccine Study'.	186
Table 4.2	qPCR primers and probe dbDNA™/ Luc.	189
Table 4.3	Experimental groups 'Dose Delivery Efficiency'.	192
Table 4.4	qPCR primers and probe dbDNA™/ Cal09.	193
Table 5.1	Overview of drug delivery results.	231

Acronyms and abbreviations

ANOVA	Analysis Of Variance
APC	Antigen Presenting Cell
ATP	Adenosine triphosphate
BALB/c	Albino laboratory mouse
bp	base pair
CO_2	carbon dioxide
C_T	threshold cycle
DAQ	Data acquisition
DC	Duty Cycle
dbDNA	doggy bone DNA
DI	Deionised (e.g. DI water)
DLS	Dynamic Light Scattering
DNA	deoxyribonucleic acid
ELISA	Enzym Linked Immunosorbant Assay
e.g.	for example
Ep	Epidermis
Er:YSGG	Erbium: yttrium-aluminium-garnet
FDA	Food and Drug Administration of the USA
FITC	fluorescein isothiocyanate
H&E	hematoxylin and eosin
GMP	Good Manufacturing Practice
Hd	Hypodermis
HIFU	High Intensity Focused Ultrasound
HRP	Horseradish Peroxidase
HPLC	High Performance Liquid Chromatography
HSE	0.1 M sodium phosphate buffer with 0.1 M sodium chloride
ID	intradermal
i.e.	that is
IgG	Immunoglobulin G
IVIS	*In Vivo* Imaging System
J	Joules

kDa	kilo Daltons
LTR	Localised transport region
mg	milligram
mL	millilitre
mT	millitesla
MPa	megapascal
MHC	Major Histocompatibility Complex
MW	molecular weight
OVA	Ovalbumin
N_2	Nitrogen
NC	NanoCup
ng	nanogram
PBS	Phosphate-Buffered Saline,
PBS-T	PBS with 0.05% Tween
PCD	Passive Cavitation Detection
PRF	Pulse Repetition Frequency
PRFP	Peak Rarefactional Focal Pressure
qPCR	quantitative Polymerase Chain Reaction
RF	Radio Frequency
RMS	root mean square
SbG	Sebaceous glands
s.c.	subcutaneous
SC	stratum corneum
SD	standard deviation
SG	Sweat glands
SDS	Sodium Dodecyl Sulphate
TASE	Total Acoustic Sensor Energy
TEM	Transmission Electron Microscopy
USP	United States Pharmacopeia
Vpp	voltage peak-to-peak
WHO	Wold Health Organization
wt.%	weight percentage by mass
w/v	weight by volume

Chapter 1: Literature Review and Research Objectives

1.1 Transdermal drug delivery

Injections are a commonly used and widely accepted method of drug administration to prevent and treat diseases. Although using a needle and syringe provides a rapid, low-cost, and direct way of administering almost any kind of therapeutic agent into the body, it is a painful and invasive method leading to issues with patient compliance and needle–phobia, especially for children. It has been calculated that by the age of 10 a child in the United Kingdom will have received 17 separate needle-based vaccinations [1]. Furthermore, transmission of diseases such as HIV, Hepatitis B and C, is a significant risk through unintentional injury and the re-use of needles and syringes in the absence of sterilisation processes, especially in developing countries [2]. Therefore, strict guidelines and protocols are in place for which trained personnel are required. This reduces the ease and patient compliance of self-administration injectables intended for the in-home setting. As the drive towards in-home care increases, this will become an increasingly important issue.

Achieving a drug delivery system that does not rely on the use of needles and syringes could help to mitigate some of these issues. Although oral drug delivery has been the mainstay for treating many diseases, the physicochemical property of the drug, its ability to achieve absorption from the gastrointestinal tract and its susceptibility to first pass metabolism all impact on bioavailability and therapeutic efficacy [3].

Inhalation drug delivery systems help to circumnavigate these issues. However, this route of drug delivery is complex, provides little means of dose delivery validation and is subject to high variability in the level and site of drug deposition in the lungs [4].

The delivery of drugs through the skin (*transdermal delivery*) is an attractive alternative route, because of its non-invasiveness and low associated risks. The application of medication to the skin to achieve topical effects has a longstanding history, including poultices, gels, ointments, creams and pastes that contain drugs and rubefacient chemicals to treat local inflammation and pain. However, the use of adhesive skin patches to deliver drugs for non-skin related diseases through the skin is relatively new. The first transdermal delivery patch, a three-day patch of scopolamine to treat motion sickness [2], was approved by the Food and Drug Administration (FDA) in 1979. In 1981, nitroglycerin patches were approved and active development of transdermal patches has continued since [5].

Currently, there exists a number of patches containing a single drug (e.g. clonidine, nicotine and fentanyl), and combination patches with multiple drugs (e.g. contraception and hormone replacements). The drugs in these patches are delivered to and through the skin by passive diffusion [6]. However, the anatomy of the skin limits the range and dose of drugs, which can passively diffuse through the skin without the application of additional stimuli [7-9].

To date, multiple chemical and physical interventions have been developed to increase the efficacy of drug transfer across intact skin. However, achieving a sufficiently high and consistent delivered drug dose without causing excessive skin damage is a

challenge. Although there have been some notable successes, limitations in sensitive and accurate drug monitoring systems increase the difficulty in achieving FDA approval of transdermal delivery systems.

Monitoring of the dose delivered is a high priority for drugs with a narrow therapeutic window where a slight variation in the administered range can result in low clinical effect or significant side effects and toxicity. The most common method to control the drug concentration relies on the invasive sampling of the blood from the vein or fingertip. This is not only painful, thereby decreasing patient compliance (especially when the frequency of the blood sampling is high), but also creates a temporal disconnect between when the drug is delivered and the time of measurement. Non-invasive monitoring methods are therefore an essential component of moving transdermal drug delivery technologies into more widespread clinical practice.

In this chapter, the current challenges and proposed solutions for enhancing drug delivery into the skin will be discussed. Conclusions will be drawn about the important barriers to successful transdermal delivery and the pathways to enhanced delivery that appear most promising.

1.2 The skin

1.2.1 The structure and function of the skin

The skin is the largest organ of the body with a surface area of 1.2 to 2.2 square meters and a weight of between 4 and 5 kilograms [10]. The skin is a metabolically active organ with a variety of vital functions in the protection and regulation of the body. Its primary function is to act as a barrier against mechanical impact and pressure, variation in temperature, and exposure to pathogens, chemicals, and biological agents.

The skin also serves as a sensory organ that can detect and relay changes in the environment and it has an essential role in the production of vitamin D.

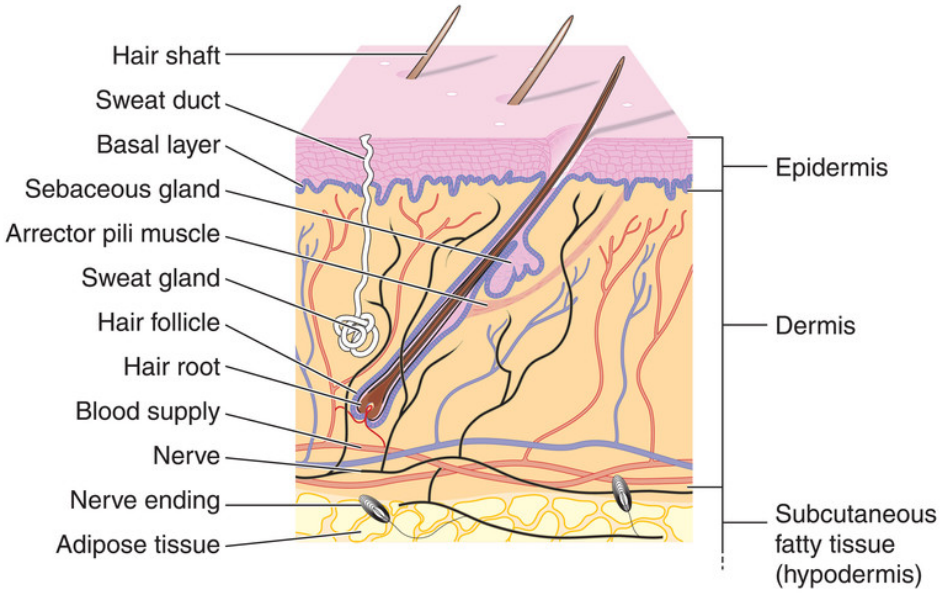

Figure 1.1: Schematic representation of the different skin layers and the features of the skin [11].

The skin is anatomically comprised of three distinct regions (Figure 1.1): the outermost epidermis, the dermis and the underlying hypodermis (also known as subcutaneous (s.c.) adipose tissue) [10]. The thickness of these layers varies between and within species and is dependent on age, gender, location, and ethical origin [12, 13]. The epidermis and dermis are of particular interest in transdermal delivery due to the presence of immune cells in the epidermis and the blood vessels in the dermis.

The epidermis is multi-layered, varying in thickness from 0.05 mm on the eyelids to 1.55 mm on the palms and soles [14]. There are no blood vessels in the epidermis and consequently, the nutrients reach the epidermis from the blood vessels in the underlying dermis by diffusion through the interstitial fluid. The epidermis is further divisible into four distinct layers: the *stratum basale, stratum spinosum, stratum granulosum,* and *stratum corneum* (SC).

In the epidermis, keratinocytes constitute around 90% of the total epidermal cell population [15]. At the lowest region of the epidermis (*stratum basale*), the immature keratinocytes rapidly divide and some of the dividing cells move up to the next layer *stratum spinosum*. In this layer, the cells are anchored to each other by desmosomes and contain thick bundles of intermediate filaments (keratin) [16]. As the keratinocytes further mature and move up into the *stratum granulosum*, the cells start to secrete lamellar bodies to the extracellular domains, which results in the formation of a cross-linked organised lipid envelope that serves as water barrier [17]. In addition, the cells lose their nuclei and cytoplasmic organelles, and the filaggrin protein aggregates the keratin filaments in the cells into tight bundles (i.e. microfibrils) that promote the collapse of the cells to eventually reach the SC as terminally differentiated and flattened keratinocyte (i.e. corneocyte) [16, 18]. Furthermore, the phospholipid cell membrane is replaced by a cell envelope to survive exposure to air in a dry environment. The extremely insoluble cell envelope is a result of macromolecular polymerisation of various keratinocyte proteins (e.g. involucrin, loricrin, cystatin A, and elafin) by both disulphide and isopeptide bond formations [19].

As the outermost layer of the skin, the SC is the limiting barrier to skin absorption in transdermal delivery and provides protection to the more delicate layers underneath. The SC is composed of desmosome-interconnected corneocytes that are highly organised in a lamellar structure, and often described as ‘brick and mortar’ [10, 16]. The corneocytes (i.e. the bricks) form the mechanical and chemical protection of the skin and are embedded in a highly cross-linked, dense hydrophobic matrix (containing mainly long hydrocarbon chains (20-36C), cholesterol and ceramides [20]) (i.e. the mortar). In a healthy skin this barrier becomes highly water-impermeable and restrict

the passage of molecules that are larger than 500 Da or are strongly hydrophilic across the SC [7-9]. In human skin, the SC has a thickness of about 15-20 μm and the entire SC is renewed every two to four weeks [21].

Other specialised cell types in the epidermis are melanocytes that produce the pigment protein melanin that determines the pigment intensity of the skin [14]. In addition, Merkel cells pay a role in sensation. Immunologically active cells such as Langerhans cells, lymphocytes, and macrophages are also found in the epidermis.

The skin layer between the epidermis and the hypodermis is called the dermis. With a thickness varying between 0.3 mm on the eyelid to 3.0 mm on the back, the dermis is thicker than the epidermis [14]. The dermis is a highly vascularised and contains elastic connective tissue that is comprised of collagen, elastic and reticular fibres, which are produced by the dermal fibroblasts [22]. Furthermore, nerve endings, lymphatic vessels, as well as hair follicles and sweat glands can also be found in this layer [10]. Like the epidermis, immunologically active cells are also found in the dermis and they play a critical role in skin-mediated immune responses, which will be described in more detail in the next section.

1.2.2 The skin as an immune site

The epidermis and the dermis contain a wide range of immunologically active cells which form a defence against invading pathogens [15]. Depending on the type of pathogen, the immune system can generate an innate or adaptive response [23]. Innate immunity provides a mechanism for an immediate and short-lasting defence of the body against the invading pathogens, whereas the adaptive immunity stimulates a memory response by the production of antigen-specific humoral (antibodies) and cellular

immunity. An illustration of the immunological networks in the skin is shown in Figure 1.2.

The keratinocytes present in the epidermis play an essential role in the immunity of the skin by producing antimicrobial peptides to fight the invading pathogens and also excrete signalling molecules to recruit immune cells [24]. Furthermore, the antigen-presenting cells (APC) in the skin, such as Langerhans cells and dendritic cells, play a crucial role in sampling the local microenvironment and taking up foreign material (antigen) [23].

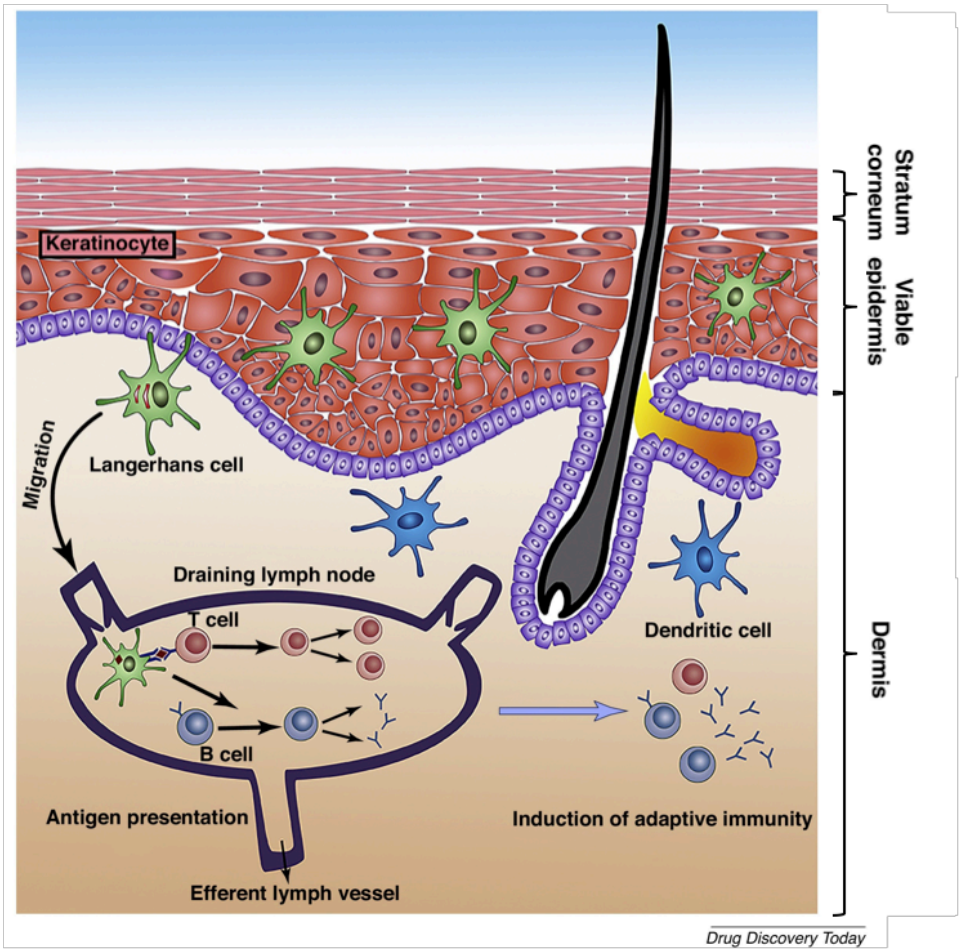

Figure 1.2: Illustration of the skin structure and immunological network [15].

Once an APC cell has taken up foreign material, the antigen-loaded APC matures and migrates to the skin-draining lymph nodes where the antigens are presented to antigen-specific naïve T-cells [25] (Figure 1.2). Under the influence of co-stimulatory molecules, the proliferation of T- and B-cells is initiated for activation of the adaptive immune system. The T-cells further differentiate into either CD4+ (helper) or CD8+ (cytotoxic) T-cells that can recognise and bind to the antigen when it is presented on the cell membrane on the infected cell or pathogen [26]. Via up-regulation of co-stimulatory molecules, phagocytic cells like macrophages are activated to clean up the recognised pathogens [25].

When B-cells interact with the antigen presented by the APCs via the B-cell receptor, the morphology of the B-cells changes so that they become plasma cells [15]. These cells cause the humoral response through the production and secretion of highly antigen-specific antibodies. The antibodies bind to the recognised antigen on the pathogen and the complex becomes an easy target for the phagocytes and the complement system to clear and deactivate the pathogen [27].

After the elimination of the pathogen, a small number of T- and B-cells are transformed into memory cells [23]. In case of re-exposure, the memory cells can recognise the antigens and reactivate the immune system resulting in a fast and strong immune response to neutralise the pathogen before it causes substantial ill effects [15].

1.3 Crossing the skin barrier

In addition to the protective function of the skin, both physical and biological, the skin also regulates the transport of water molecules and other small molecules into and out of the body to maintain homeostasis [9]. These molecules are typically fairly lipophilic (partition coefficient, log P > 1.5) and have molecular weights of less than 500 Da.

Due to the physical structure and chemical properties of the SC, the outer layer of the skin is at least three to five orders of magnitude less permeable to most substances than the epidermis or the dermis [28-31]. As a result, the SC functions as a dominant resistor, preventing passive penetration of most therapeutic molecules, especially proteins and peptide based medicines. Disruption or perturbation of the SC layer can help to improve drug delivery into the skin and even permit entry into the blood circulation [32]. The biggest challenge is to safely and reversibly open the SC barrier and to deliver a reproducible amount of the therapeutic agents across the SC. This can be achieved through passive and active methods, with the latter method requiring an external energy source to permeabilise the skin.

1.3.1 Passive enhancement techniques

Chemical penetration enhancers can disrupt the SC barrier to promote the transport of therapeutic agents across the skin by passive diffusion [33]. There are over 350 different chemicals known to achieve this disruption and extensive literature is available on their classes and their mechanism of action [21]. The most widely studied chemical penetration enhancers are sulphoxides (e.g. dimethyl sulphoxide), pyrrolidones, azone, urea, fatty acids, alcohols (e.g. ethanol), polyols (e.g. glycerol), surfactants (e.g. sodium dodecyl sulphate (SDS)), and chelating agents [34, 35].

However, most chemical penetration enhancers do not achieve a suitable balance between increased drug delivery across the SC and avoiding damage to the deeper tissue, thereby causing skin irritation, skin damage and pain [35]. Consequently, lower doses of chemical penetration enhancers are often used in combination with other physical permeation methods to enhance the permeability of the SC [36]. In addition, the use of chemical penetration enhancers gives rise to long lag times, as the process is still reliant on diffusion. These lag-times can in some cases last hours in duration. Therefore, this method cannot be used when rapid drug administration is required.

1.3.2 Active enhancement techniques

Active methods increase the transdermal drug transport by physically disrupting the SC or by using an external driving force to enhance drug transport. Increasing interest from academic and industrial researchers has led to the clinical and commercial development of a number of technologies designed to increase the drug delivery efficiency of hydrophilic and macromolecular drugs across intact skin. Furthermore, active methods provide better control over the onset and delivery profile of the therapeutic agents into the skin and blood circulation in comparison to passive diffusion dependent methods.

Depending on the type of drug, different physical enhancement techniques are being developed to reach therapeutic concentrations in the blood circulation (transdermal delivery) and/or to target the delivery to the skin itself (epidermal delivery) (e.g. vaccination). A brief overview of current active skin permeation technologies is provided in the subsequent sections.

1.3.2.1 Iontophoresis

Low amplitude electric current can be applied to facilitate the movement of ions across the SC, a phenomenon referred to as iontophoresis [37].

An iontophoretic transdermal device is worn on the skin with an anode in the reservoir containing a positively charged drug, and the cathode in a reservoir containing a negatively charged solution. By applying a low-intensity electric current (usually 0.5 mA/cm^2) [2], the positively charged drug molecules are carried from the patch across the SC into the skin, where they are absorbed and systemically distributed. Charged drugs are moved by electromigration, while uncharged drug molecules can be moved by a flow of solvent from the anode to cathode called electro-osmosis [37].

Iontophoresis is used for a broad range of therapeutics; from small molecules such as local anaesthesia (e.g. E-TRANS® and Ionsys® by ALZA Corporation, USA [38]), and analgesics such as Sumatriptan (Zecuity®, Teva Pharmaceuticals Industry, Israel), to large peptide molecules (e.g. gonadotropin-releasing hormone [39] and insulin [40]).

Notably, high-molecular-weight molecules like oligonucleotides have been found to be ineffectively delivered across the skin using iontophoresis, even in combination with chemical penetration enhancers [41]. Other limitations of this technology include its applicability to a narrow range of drug sizes and the fact that the maximum delivery rate (correlated with applied current) is limited by skin irritation and pain at the site of application [42].

1.3.2.2 Electroporation

Another technique to increase transdermal transport using electric fields is electroporation. Under the influence of high voltage electric pulses, lasting for 10 μs – 10 ms, aqueous pores are formed in the lipid bilayers of the SC and the cellular membrane [43]. This action allows macromolecules (e.g. DNA, proteins, and antibodies) to enter the cell [44]. Electrochemotherapy involves the use of

electroporation and chemotherapeutic drugs into cutaneous and subcutaneous metastases [45]. This treatment consists of local or systematic administration of the chemotherapeutic drugs followed by the application of electric pulses at the tumour site.

Electroporation has been shown to be efficient in gene delivery and DNA vaccination, compared to direct intramuscular injection. In pre-clinical animal models and human clinical trials, it has been shown that applying electroporation immediately after intramuscular or intradermal injection of a DNA vaccine gave an increased response relative to injection of DNA vaccine alone [46-48]. CELLECTRA® (Inovio Biomedical Corporation, San Diego, USA) is a commercial electroporation-based device currently on the market. This device is designed for transdermal delivery of DNA and is being tested in a number of different clinical studies [49-51]. This device has a five-needle electrode array that is applied into the muscle or dermis to enhance DNA plasmid uptake.

The main draw-backs of electroporation are the intense pain imparted and the low reproducibility of the drug delivery achieved, as well as the need for the use of penetrating needle electrodes such as those used in CELLECTRA®. There are also non-penetrating electrodes commercially available, but they have been found to be less efficient than the needle electrodes [52]. There are also concerns regarding the use of high voltage pulses that cause skin irritation, damage and muscle contraction [53, 54].

1.3.2.3 Magnetophoresis

The phenomenon of magnetophoresis is the migration of magnetical materials under the influence of an external magnetic field (5 to 300 mT) [55]. The application of this technology as a physical enhancement strategy for transdermal delivery is a novel

approach. Work by Murthy and co-workers has shown the potential of magnetophoresis to enhance delivery *in vitro* [56] and *in vivo* [57] of diamagnetic drugs such as benzoic acid and lidocaine. They found that increasing the strength of the magnetic field increased the diffusion flux [56]. In comparison to other physical enhancement methods, magnetophoresis is a phenomenon that only occurs in the presence of the magnetic field. Therefore, this technique could potentially be incorporated into a transdermal patch system designed for prolonged application, and *in vivo* studies have reported the potential for further development [57, 58].

1.3.2.4 High-pressure devices

In these technologies, jet injectors use a high-speed liquid jet to puncture the skin and deliver the drugs without using needles. The basic design contains compressed gas or a spring system, which pushes a piston when triggered [59]. The piston impacts the drug-loaded compartment, and this causes a rapid increase in pressure. As a result, the drug-loaded particles are released through the nozzle as a jet, reaching a high velocity between 100 and 200 m/s [60]. Upon impinging on the skin surface, the high-velocity jet punctures it and delivers the drug-loaded particles into the skin, or even deeper into fat and muscles, depending on the characteristics of the jet [61]. The jet can be liquid or gaseous, with the drug-loaded particles in the form of a solution or a dry powder, respectively.

Liquid jet injectors have been shown to be successful in the transdermal delivery of a range of drug molecules. Some examples of the liquid jet injectors that are available on the market are Biojector® 2000 (for vaccine delivery, Bioject Medical Technologies Inc., USA), Serojet® (for human growth hormone, Bioject Medical Technologies Inc., USA), and MediJector® (insulin, Antares Pharma Inc., USA) [62].

Other commonly used terms to describe powder jet injectors are biolistic injectors and gene guns, with the latter term exclusively used for DNA delivery. For the transdermal delivery of powder formulations, the particles are formulated in fine powder (20-100 μm diameter particles) and these formulations are in general more stable to store and transport than liquid formulations [63].

Immunization by powder injectors has been shown to induce similar immune responses in comparison to intramuscular injection in animal [64-66] and human studies [67, 68]. In a variation of this technology, DNA vaccines can be coated on gold microparticles and delivered into the skin by the powder injector (e.g. PowderJect® XR-1, PowderMed Ltd., United Kingdom). However, clinical studies have reported less immunogenic response in comparison to the standard vaccine delivery methods using a needle and syringe [69].

Although the technology behind the jet injectors has been improved over the years, different studies have shown occasional pain and bleeding at the site of impact after treatment, leading to a mixed acceptance among patients [70-72].

1.3.2.5 Thermal ablation

Thermal ablation alters target tissue by the generation of high temperatures induced by various energy sources (e.g. laser and electrical energy) which generate micropores in the skin. In laser ablation, the optimal wavelength can be achieved by using Erbium: yttrium-aluminium-garnet (Er:YSGG) or carbon dioxide (CO_2) lasers that match the main absorbance wavelength of water (2970 nm) in tissue. As a result, the water rapidly evaporates in the tissue and causes the disruption of the cellular structure, resulting in the formation of micropores [73]. The commercial device P.L.E.A.S.E.® (Painless Laser

Epidermal System) (Pantec Biosolutions, Liechtenstein) is available on the market to deliver several macromolecular drugs [74, 75] and vaccines [76].

Radiofrequency (RF) ablation uses a high-frequency electrical current (100-500 kHz) to locally heat the skin and destroy the SC in a somewhat similar way as to laser ablation [77]. Devices are composed of micro-electrodes arrays, and local heating is induced by passing the current through the SC, which results in liquid evaporation and the formation of micropores. A combination technology ViaDor® (also known as Viaderm®) was developed by Transpharma Medical (now taken over by Syneron Medical). Pre-treating the skin with RF ablation followed by an iontophoretic patch has shown enhanced transdermal delivery of a range of therapeutics such as insulin [78], human growth hormone [79], and teriparatide (ViaDerm®-hPTH).

The main factors limiting the use of thermal ablation are the long-term effects, the healing time after the treatment, and the absence of a feedback system to regulate and control the depth of the micropores or the amount of dose delivered.

1.3.2.6 Microneedles

Microneedles are arrays of downsized needles (25 μm - 2 mm in length) that pierce the SC to generate microscopic holes [80, 81]. Due to the reduced needle length, the microneedles do not penetrate deep enough into the skin to stimulate the pain nerves, theoretically making this technology painless [80]. In general, there are four different types of microneedles: (i) solid microneedles used to pierce the skin followed by the application of a drug patch, (ii) solid microneedles which are coated with dry powered drug or vaccines, (iii) dissolving microneedles which contain the encapsulated drug in biodegradable and/or polymeric microneedles, and (iv) hollow microneedles for

infusion of larger quantities of drug into the skin [81, 82]. A detailed review covering microneedle materials and manufacturing techniques can be found in [83].

In recent years, the research and development of microneedles have been fast growing, with a wide variety of completed clinical trials reported. The recently completed or ongoing clinical trials involving microneedle technology have used a range of drugs, such as influenza vaccine, insulin, parathyroid hormone, anaesthetics and hyaluronic acid (cosmetic application to reduce wrinkles) [83].

Microneedles have the advantage of being easily applied and potentially allowing self-administration by minimally trained patients. Also, the small package size of the microneedle patches, as well as their thermostability, improves logistics and storage [84]. When using dissolving microneedles, no sharp objects remain on the patch after application, therefore reducing levels of waste which is hazardous and costly to dispose of. However, fabricating large-scale microneedles batches with reproducible drug content and tip sharpness has been found to be challenging [83].

Microneedle technology has been extensively studied in animals, and multiple clinical trials have been performed or are under investigation [84]. For example, Zosano Pharmaceuticals has performed several clinical trials with the ZP Patch Technology® (previously known as Macroflux®). The patch contains an array of metallic microneedles dry-coated with the drug or compound. Several phase II clinical trails have been performed with parathyroid hormone (ZP-PTH) [85], and glucagon (ZP-Glucagon) [86]. Furthermore, the use of a ZP patch containing Zolmitriptan for migraine therapy (ZP-Triptan) is currently undergoing a phase III clinical trial [87].

There is also a growing interest in using microneedles for vaccination to deliver the antigenic material directly to the immune cells in the skin. Administration of the vaccines via the microneedles has been reported to elicit immune response comparable to intramuscular injection with similar or lower dosages [88]. Recently, two human phase I clinical trials were reported using a dissolving microneedle patch and inactivated influenza vaccine [89, 90]. More information about on-going and completed clinical studies with the microneedle technology can be found in references [83] and [84].

The current limitation of microneedles relates to their inability to deliver high concentrations of the therapeutic agent to consistent penetration depths. In addition, the thickness of the s.c fat layer in humans can significantly affect the penetration depth of the microneedles after application, which may lead to variation in delivered dosage in the skin, as well as pain by reaching the nerves in the lower part of the dermis [91].

1.3.2.7 Sonophoresis or ultrasound-mediated transdermal delivery

Ultrasound can enhance transdermal delivery through both mechanical and thermal effects. A brief literature review of the key physical principles is presented in the next section to gain understanding of the main effects of cavitation-enhanced delivery in transdermal delivery.

1.4 Acoustic principles in cavitation-enhanced transdermal delivery

1.4.1 Acoustic waves

As an acoustic wave passes through a medium, particles are displaced locally, generating regions of compression (high density/pressure) and rarefaction (low density/pressure). Ultrasound waves are longitudinal in nature (i.e. particles in the medium are displaced parallel to the direction of the propagating wave). These pressure perturbations are generated at a frequency (*f*) and propagate through a medium at the speed of sound (c).

1.4.2 Attenuation, Scattering and Absorption

During the propagation of the acoustic wave through a medium, acoustic energy can be lost (attenuation) due to scattering and absorption. The loss in acoustic energy in a medium is characterised by its attenuation coefficient (α), which is the sum of the absorption (μ_a) and the scattering (μ_s) coefficient. The acoustic intensity (I) of the travelling wave at a distance (x) to the medium is given by:

$$I(x) = I_0 e^{-\alpha x} \tag{1.1}$$

where I_0 is the initial intensity of the ultrasound beam, and the acoustic intensity (I) the amount of acoustic power generated per unit area given by:

$$I = \frac{P^2}{2\rho c} \tag{1.2}$$

where P is the acoustic pressure, ρ density of the medium, and c the speed of sound through the medium.

Scattering is the reflection of the acoustic wave from inhomogeneities in the medium in other directions than the direction of the propagating wave. Absorption converts acoustic energy into heat as a result of viscous dissipation in the medium and molecular

relaxation processes [92]. The attenuation coefficient (α) is known to be related to the ultrasound frequency via a power law given by:

$$\alpha = af^b \tag{1.3}$$

where a and b are material-specific constants. For a variety of biological tissues, b is commonly found to be around 1.1 [93].

The variation of the acoustic attenuation with frequency is important when considering the appropriate ultrasound frequency for transdermal delivery. Increasing ultrasound frequency results in higher attenuation and heating, and as a result limits the penetration depth of the ultrasound waves into the tissue. Shorter wavelength will also result in a tighter ultrasound focus and therefore a small treatment area.

The frequency dependence of attenuation induces an extra complexity during non-linear wave propagation through biological tissue. At high acoustic intensities, local fluctuations in pressure and density become more significant [94]. As a plane wave travels through tissue, the compressive regions (where the local velocity is positive) tend to move faster than the rarefactive regions (where the local velocity is negative). Also, when a fluid is compressed, the bulk modulus and stiffness increases, which leads to an increase in its sound speed. Altogether, this leads to the gradual steepening of the initially sinusoidal waveforms and after a sufficient propagation distance the formation of a shockwave [95]. Such distortion of an initially sinusoidal waveform appears in a frequency spectrum as harmonics of the driving frequency. Consequently, higher frequencies are more attenuated, and therefore the acoustic energy in the ultrasound focus will be lower in a non-linear medium than in a linear case.

1.4.3 Acoustic impedance

The characteristic acoustic impedance (Z) of a medium describes the ratio of acoustic pressure to particle velocity. For a plane wave travelling through this medium, where particles exhibit harmonic motion, the characteristic acoustic impedance can also be described by the density of the medium (ρ) and the speed of sound (c).

$$Z = \rho\, c \tag{1.4}$$

The characteristic impedances for skin, bone and air are 1.6 x 10^6, 6.3 x 10^6, and 400.0 kg/(m^2s), respectively [96].

The ability of an ultrasound wave to transfer the acoustic energy from one medium to another depends on the difference in impedance between the two media. Optimal transmission occurs when the two media have similar acoustic impedances. With the exception of fat, air and bone, most tissues have similar acoustic properties, corresponding to that of water. Therefore, at the tissue interfaces there is little difference in acoustic impedances and the reflections are generally weak when propagating ultrasound through tissue. Furthermore, it is therefore optimal to use aqueous media to enhance the acoustic coupling between the transducer and the skin.

1.4.4 Mechanisms of sonophoresis

Although sonophoresis is known to increase the permeability of the skin, the fundamental mechanism is still not clearly understood. A number of effects are observed when ultrasound interacts with a biological tissue, and these are described in this section.

1.4.4.1 Thermal effects

Absorption of ultrasound waves can locally increase the temperature in the tissue. The amount of heating is dependent on the ultrasound frequency, intensity, exposure time and the absorption coefficient of the medium, and on the rate of heat removal from the tissue by blood flow or conduction in the tissue [97, 98].

The temperature rise in the skin can increase skin permeability and transport by increasing the kinetic energy of the drug molecules and therefore the diffusion rate. In a study by Merino et al., the skin temperature was increased by 20 °C with low-frequency ultrasound (20 kHz), leading to the delivery of mannitol increasing 35-fold [97]. However, it is notable that the delivery of mannitol was only 25% of this value when the same temperature increase was achieved without ultrasound exposure. This shows that thermal effects may have a positive influence on drug delivery, but that they play a minimal role in ultrasound-enhanced drug delivery. Furthermore, no significant influence of thermal effects on drug delivery was found with short exposure times [97, 99, 100], although prolonged and excessive exposure of the skin to ultrasound can cause unwanted skin damage.

1.4.4.2 Acoustic radiation force and acoustic streaming

As an acoustic wave travels through a medium, the wave is attenuated. As an effect of the pressure gradient, a net force is induced in the direction of wave propagation, known as the acoustic radiation force. The radiation force (F) is known to be related to the attenuation coefficient (α), the acoustic intensity (I), and the speed of sound in the medium (c) [101] and defined by:

$$[F] = \frac{2\alpha I}{c} \tag{1.5}$$

In an inhomogeneous medium such as a biological tissue, the primary cause of attenuation is absorption, with a relatively small contribution of acoustic scattering such that in many cases the scattering can be ignored.

When a particle is placed in the path of a propagating wave, the acoustic radiation force can act on the particle resulting in particle movement. The force is proportional to the particle density and volume, as well as the compressibility contrast between the particle and the surrounding medium. For non-absorbing interfaces and particles much smaller than the acoustic wavelength, the direction and amplitude of the acoustic radiation force depend on the elastic properties of the medium. In the presence of a standing wave, this can lead to particles collecting at pressure nodes or antinodes depending on the properties of the particles and fluid [102].

When a fluid is insonated, energy from the acoustic field is absorbed and causes a transfer of momentum to generate a liquid flow in the direction of the propagating wave with recirculation vortices to bring back the fluid to the transducer face [103]. This phenomenon is called *acoustic streaming*.

1.4.4.3 Cavitation

Cavitation describes the formation of gaseous cavities as well as the expansion, contraction, and collapse of pre-existing cavities in a medium upon ultrasound exposure [104]. Acoustic cavitation can be categorised into two types: *stable* and *inertial cavitation* [105]. Stable cavitation typically describes the repetitive (i.e. stable), linear or non-linear oscillation of a bubble without collapse under acoustic excitation, which is controlled by the balance between the pressure inside the bubble and the inertia of the

surrounding liquid [106]. The radiated sound field of a stable cavitating bubble will contain discrete harmonic components in the frequency spectrum [107].

Bubbles undergoing stable oscillations can cause a unidirectional fluid flow in response to the bubble dynamics in an acoustic field, a phenomenon called *microstreaming*. These circulating eddies around the oscillating bubble impose high-velocity gradients and hydrodynamic shear stresses on nearby surfaces, such as cell membrane [108, 109]. These convective process can play a role in enhanced drug uptake in cells [110] and skin [111].

If the peak negative pressure in the acoustic field is increased, the phenomenon of *inertial cavitation* occurs, whereby the bubble grows rapidly and uncontrollably during the peak-negative pressure cycle, followed by violent collapse due to the inertia of the surrounding medium [112]. This is a very violent process and the radiated sound field contains a range of frequencies (i.e. broadband noise) rather than discrete harmonic components [107].

During inertial cavitation at lower driving frequencies, the bubble has more time to grow in the peak negative pressure cycle and consequently produces a more violent collapse during the compression cycle. The collapsing bubble can generate (besides microstreaming) a shock wave or, when near a boundary, a microjet due to asymmetric collapse [113]. Depending on the properties of the interface, the collapsing bubble can generate a jet towards or away from the interface, or collapse in an alternate shape [114]. It has been suggested that a bubble generating a high-velocity microjet towards the skin can cause perturbations in the SC lipid bilayers [115].

To investigate which cavitation phenomenon plays a more prominent role in skin permeability enhancement, two independent studies have been performed that correlated enhancements in skin permeability with both types of acoustic emissions [99, 100]. Both studies found that there was a strong correlation between broadband noise and increased skin permeability, concluding that inertial cavitation is the dominant mechanism underpinning low-frequency sonophoresis.

1.4.5 Localised transport regions

Enhanced skin permeability in low-frequency ultrasound treatment has been found to occur heterogeneously over the treatment area. Studies by Tang et al. [116] and Tezel et al. [117] have observed highly-stained regions on the skin after insonating a coupling medium containing coloured permeant with 20 kHz. The localised regions of high permeability are described as *localised transport regions* (LTRs). Further studies combining low-frequency ultrasound (20-60 kHz) with a surfactant sodium lauryl sulfate (SLS) showed LTRs across the skin surface covering 5-25% of the surface area in a stochastic pattern [116-120]. In addition, Polat et al. have shown a strong correlation between skin pore radius within LTRs and ultrasound frequency when conducting experiments at multiple frequencies (20 - 60 kHz) [118]. Also, Tezel et al. found increasing number of transport regions with increasing frequencies [117]. However, identification of the LTRs at 76.6 and 93.4 kHz was found to be difficult due to their small size.

For each acoustic frequency, there is a minimum acoustic pressure required to initiate inertial cavitation [121], called *inertial cavitation threshold.* This threshold is dependent on the dissolved gas concentration and the viscoelastic properties of the medium, the number and size distribution of pre-existing gas or vapour nuclei, the ultrasound

frequency and the local temperature. For a given nuclei population in a given medium, cavitation occurs more readily at lower ultrasound frequencies than at higher acoustic frequencies.

Very few cavitation nuclei exist normally in tissue or blood. However, introducing nano- or micron-sized bubbles can substantially increase the number of cavitation nuclei and thereby reduce the cavitation threshold. Bubble growth and collapse are hard to achieve within densely packed tissue like skin, therefore cavitation occurs preferentially within the coupling medium between the skin and the ultrasound transducer.

1.4.6 Acoustic cavitation detection

Drug delivery monitoring is crucial to ensure not only that the device is working, but also to achieve reproducible therapeutic safe concentrations of the delivered drug. Since inertial cavitation plays a crucial role in skin permeability, monitoring the cavitation activity in real-time in the treatment area is important in controlling and enhancing the transdermal delivery.

A method known as *passive cavitation detection* (PCD) can be used to characterise bubble activity by detecting the acoustic emissions of cavitating bubbles [122]. PCD uses a 'detection' ultrasound transducer with a centre frequency greater than the driving frequency of the 'therapeutic transducer' to record the acoustic emission from the cavitation activity generated by the 'therapeutic transducer'. In this way, the lower frequency transducer can be used to induce sonophoresis and the second transducer of higher frequency can detect in real-time the generated acoustic emissions from the treatment area. Notably, the higher frequency PCD transducer has a better spatial resolution and frequency separation in comparison to the therapeutic transducer.

PCD can be used to characterise the nature of cavitation activity occurring within the focal region of the transducer, especially when analysing the frequency components of the acoustic emissions [107, 123]. Stable cavitation tends to be characterised by the presence of harmonics, sub- and ultra- harmonics of the driving frequency. In contrast, the frequency spectrum of inertial cavitating bubbles generates broadband emissions [107]. Passive imaging techniques using ultrasound have been applied to non-invasively classify and localise cavitation activity in different therapeutic applications [124, 125].

1.4.7 Ultrasound-mediated transdermal delivery

Sonophoresis (or phonophoresis) describes the effect of ultrasound on the movement of drug molecules across the SC barrier into or through the skin. Ultrasound is defined as the transmission of sound pressure waves with a frequency higher than 20 kHz, which lies at the upper-frequency limit of human hearing. Ultrasound can be categorised into three frequency ranges: low frequency (20-100 kHz), therapeutic (0.7-3.0 MHz), and high frequency (>3 MHz – 10.0 MHz).

In the early-mid 1990s, the use of low-frequency ultrasound was found to be more effective for transdermal drug delivery than high-frequency ultrasound (1-3 MHz). This was found to be the case both for low-molecular-weight drugs (like salicylic acid and corticosterone) as well as high-molecular-weight drugs, including proteins and nucleotides [126, 127].

The mechanism of sonophoresis is believed to rely on factors including instigation of cavitation, namely the linear or non-linear oscillation of gas- and/or vapour-containing cavities under the effect of an applied ultrasound field. The interaction between the ultrasound waves and the gas content in the coupling medium or in the skin induces

nano-scale disruption of the lipid bilayer of the SC, increasing the skin permeability [128].

Low-frequency sonophoresis of the SC can be used as a pre-treatment prior to the application of the drug, or simultaneously with the application of the drug to the skin. The use of a short application of ultrasound prior to the treatment has been used to permeabilise the skin surface, which then remains highly permeable for several hours, allowing drug molecules to passively diffuse into the skin [129]. In studies performed by Tang et al. simultaneous sonophoresis showed more effective transdermal transport than ultrasound pre-treatment [116, 130].

Furthermore, sonophoresis has also been used to extract analytes from the skin for diagnostic measurement after ultrasound irradiation [131]. The enhanced skin permeability after insonation has allowed the extraction of various solutes, including glucose, albumin, calcium, urea and lactate [131, 132]. This opens up the potential of using ultrasound to achieve delivery and simultaneously monitoring of analytes.

Several transdermal ultrasound devices have been on the market for many years. Most commonly these devices are used to enhance the delivery of steroids and other anti-inflammatory drugs into the skin in the clinical environment of physiotherapy [133]. Typically, these ultrasound devices operate at 1-3 MHz.

Another example is the SonoPrep® (Sontra Medical, USA) which was approved by the FDA in 2004 and uses a frequency range of 53-56 kHz on an ultrasonic coupling medium [134]. The application of SonoPrep® followed by five minutes application of

local anaesthetics cream showed significant benefit in pain reduction in paediatric patients when used prior to intravenous cannulation [135]. Also, Transdermal Specialties Inc. (USA) (former Dermisonics) has developed multiple portable ultrasonic transdermal devices [136]. The U-Strip™ was developed to deliver high-molecular weight molecules such as insulin into the blood circulation, and the U-Wand™ is an ultrasonic skin care device to enhance the delivery of skincare products like hyaluronic acid and vitamins [137].

Low-frequency sonophoresis has also been tested in combination with chemical penetration enhancers. The chemical breaks down the lipid structure of the SC, thereby increasing skin permeability. In *in vitro* studies using pig skin, a 200-fold increase in mannitol delivery was observed when the chemical penetration enhancer was included in the formulation gel, compared to an eight-fold increase with ultrasound alone [138]. However, not all therapeutic agents are stable in solution with chemical penetration enhancers, and this approach can also cause skin irritation.

Ultrasound used in combination with other physical penetration technologies like microneedles [139-141], electroporation [142, 143], and iontophoresis [144-148] has been shown to provide a synergistic enhancement of skin permeabilisation and transdermal drug delivery.

Work carried out by Bhatnagar et al. investigated a new approach, which sought to create a gel formulation embedding cavitation nuclei and the drug [149]. The advantage of this approach is that it seeks to simultaneously achieve cavitation-mediated skin

permeabilisation *and* enhanced drug transport from a viscous gel into the permeabilised skin by cavitational microstreaming.

This approach was first investigated using non-biocompatible cavitation nuclei to demonstrate enhance delivery of insulin in excised skin [150]. In a series of subsequent *ex vivo* studies [151], a novel type of fluorescently labelled nano-sized cavitation nuclei (i.e. Nanocup, NC) [152] was used to lower the inertial cavitation threshold in the gel. This enabled sustained inertial cavitation at the focus of the ultrasound field and enhanced the delivery of the model vaccine Ovalbumin (45 kDa) into the porcine skin at 256 kHz at 10% DC and 10 Hz pulse repetition frequency. Furthermore, Myers et al. showed that these NCs were also successfully used to achieve a 10,000-fold increase in intravenously delivered vaccinia virus activity within target tumours when compared to the application of ultrasound without the NCs [153]. This study also showed that NC mediated cavitation enhanced the virus delivery by six-fold compared to microbubbles.

The results from these experiments (see Figure 1.3) demonstrated that Ovalbumin (green) and the cavitation nuclei (NC, blue) penetrated the porcine skin to depths up to 500 μm and 700 μm, respectively, after 90 seconds insonation. In contrast, without the presence of the NCs, Ovalbumin penetrated the skin to depths of only 100 μm. This exciting result demonstrated for the first time the feasibility and potential of simultaneous skin permeabilisation and transport across the skin using NCs embedded within a viscous gel dosage form.

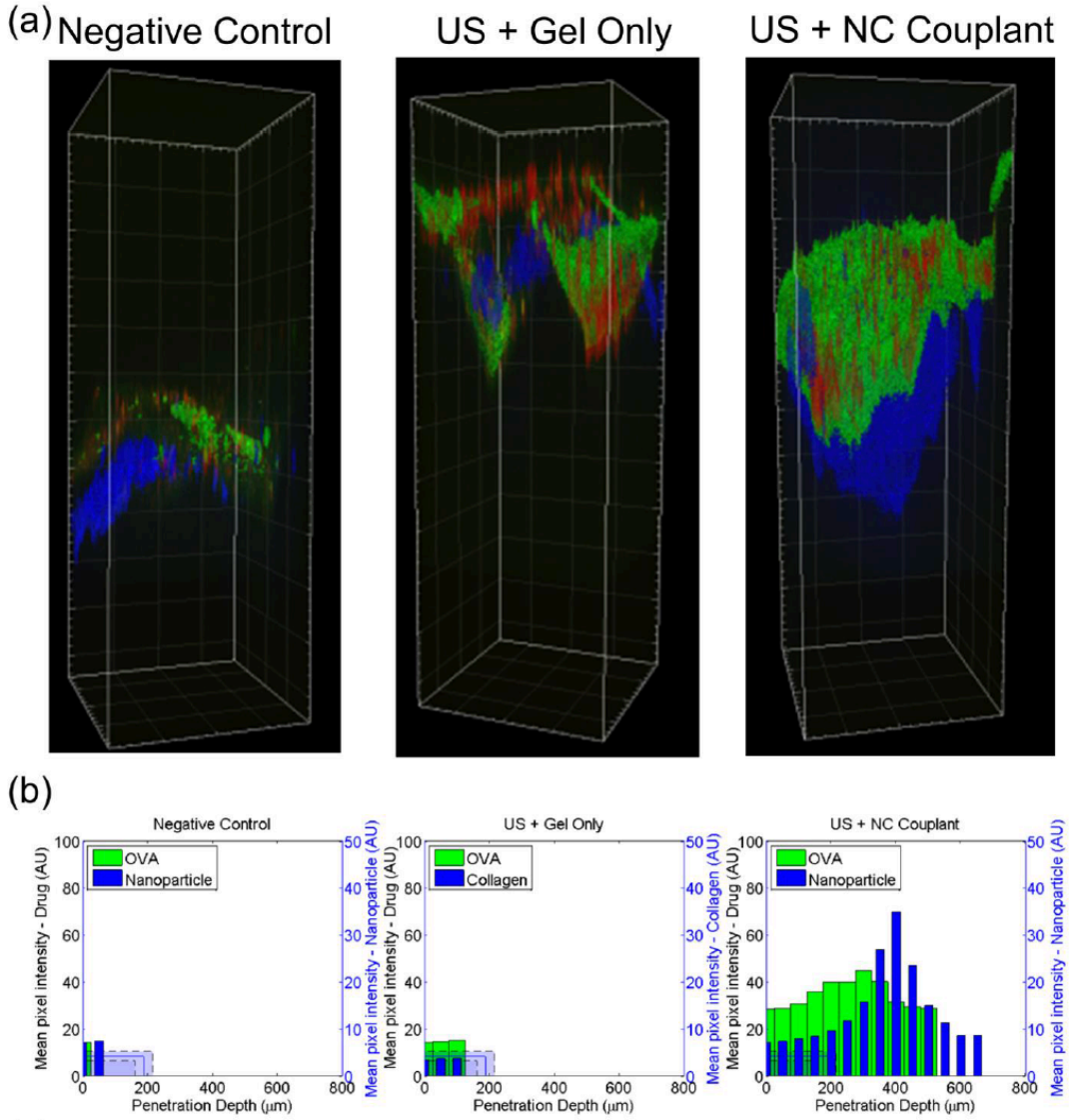

Figure 1.3: a) Three-dimensional visualisation of the penetration of Ovalbumin (OVA, green) and nano-sized cavitation nuclei (NC, blue) in the porcine skin shown for a single representative sample of each of the three experimental conditions. The ultrasound exposure direction is downwards and each square on the grid is 100 μm x 100 μm. The red colour corresponds with the surface of the skin. b) Quantitative OVA and NC distribution profiles for a single representative sample of each of the three experimental conditions. The blue shaded regions in the graphs represent the mean ± 1SD of the signal that may have originated from the collagen present in the skin rather than the NCs [151].

A subsequent *in vivo* study in mice showed significantly ($p<0.05$) higher dose delivery (up to 1 μg Ovalbumin/treatment, 0.04% of the applied dose) after treatment with cavitation-enhanced ultrasound than after treatment with a chemical penetration enhancer (up to 400 ng/treatment) [16]. In addition, it was found that the depth and amount of delivered dose was sufficient to trigger an antigen-specific immune response. The structure of the therapeutic molecule remained unchanged following exposure to

cavitation, in accordance with other studies [154]. Furthermore, the surface of the skin showed only minimal perturbation of the SC, whilst chemical treatment caused severe damage.

In the presence of the NCs, cavitation-enhanced sonophoresis therefore pushes the drug molecule further into the skin without damaging the skin surface or the therapeutic agent. The study was performed with only one drug class, the model vaccine Ovalbumin, and although an immune response was observed in *in vivo* experiments, the dose delivered would not be sufficient clinically. This therefore emphasizes the need to build on this work to extend this enhanced drug delivery technique to a broader range of therapeutic agents. Clinical adoption will require real-time monitoring of drug delivery, especially for drug molecules with a small therapeutic window such as insulin.

1.5 Current limitations to transdermal drug delivery systems

This review demonstrates that there is considerable need for needle-free technologies for drug delivery. Transdermal drug delivery is an attractive approach because of the prevalence and ease of access of the skin, but the penetration of drugs into the skin is highly limited by the SC barrier. Multiple delivery methods have been explored, but most of them struggle with the balance between high dose delivery achieved and the resulting skin damage. Therefore, there is a strong need and rationale for the development of a novel transdermal delivery system.

Cavitation-enhanced drug delivery using ultrasound and a gel formulation seeded with cavitation nuclei to deliver a model vaccine into the skin has shown great early promise. However, to enhance the adoption of this technology to be of clinical use, it requires further validation and optimisation of the technology.

Furthermore, the skin is a heterogeneous tissue and varies with body location, age, hydration level, gender, and ethnic origin. This increases the uncertainty regarding how a particular class of drug may cross the skin under the influence of cavitation. A feedback system is required that monitors and quantifies the dose delivered into the skin for several classes of therapeutic agent whilst adapting exposure to account for variation in skin thickness and hydration.

The research in this thesis was approached from a Biomedical Engineering perspective. This means that concepts from Biology, Medicine and Engineering were integrated into cross-disciplinary activities with the ultimate intention of answering the research aims on this chapter.

In summary, the aims of this thesis are:

1) To demonstrate the feasibility and reproducibility of transdermal delivery of different therapeutic agents by cavitation-enhanced transport.
2) To establish the utility of *ex vivo* pig skin and *in vivo* mouse skin as a model system for testing transdermal delivery.
3) To investigate the potential to quantify the amount delivered into the skin through passive monitoring of the acoustic emissions.
4) To study the potential of using cavitation-enhanced transport as an immunisation system for epidermal delivery of a DNA vaccine *in vivo*.

Chapter 2: *Ex vivo* delivery study of therapeutic agents into pig skin

2.1 Introduction

Before *in vivo* studies can be performed, the transdermal technology must be evaluated and optimised in systems that mimic the *in vivo* situation as closely as possible. The studies described in this chapter aimed to establish whether excised pig skin could serve as a reliable mimic for live murine, and in turn human, skin. They also provided a means to optimise the applied drug formulation composition as well as to identify and standardise the ultrasound exposure parameters and the NC concentrations.

The most relevant model of transdermal delivery to treat human disease would be *in vivo* using human skin. However, such studies are unfeasible to undertake during the initial stage of a transdermal delivery technology development project such as this. Furthermore, although excised human skin is regarded as the gold standard to perform *ex vivo* transdermal delivery experiments, ethical considerations, regulations, and availability has initiated the search to find other skin models that can predict the percutaneous delivery in humans. A wide range of animal models have been reported to be a suitable replacement for human skin, including primates, pigs, mice, rats, and guinea pigs [155, 156]. For the study of skin toxicology and irritancy, *in vitro* skin models have been shown to be acceptable [157]. Since the focus of this thesis is to investigate the ultrasound-mediated delivery on a macroscopic scale, suitable *ex vivo* and *in vivo* animal models needed to be found.

Since the use of primates in research is highly restricted in the United Kingdom, pig skin is found to be the most relevant *ex vivo* animal model for human skin due to its availability from abattoirs, low cost, and its similarities to human skin in terms of its histology, cellular composition, thickness and speed of sound (1720 m/s) [158].

For *in vivo* delivery studies, rodents (mice, rats and guinea pigs) are the most commonly used skin model due to their availability, small size, ease of handling, and relatively low cost [155]. Rodent skin (except for rats) is generally more permeable than human skin, but the permeation kinetics are frequently comparable to human skin [159, 160]. Furthermore, rodents have less variability between each other due to the use of inbred animal strains. In Table 2.1 an overview is given of the thickness of the skin layers of different animal models in comparison to human skin.

Table 2.1: Thickness of human and animal skin [160]. SC: stratum corneum, VE: viable epidermis. Whole skin includes epidermis with dermis.

Species	Location	SC (µm)	VE (µm)	Whole skin (mm)
Human	Abdomen	16.8 ± 0.7	46.9 ± 2.3	2.97 ± 0.28
Pig	Back	26.4 ± 0.4	65.8 ± 1.8	3.43 ± 0.05
Rat	Back	18.4 ± 0.5	32.1 ± 1.3	2.09 ± 0.07
Mouse	Back	5.8 ±0.3	12.6 ± 0.8	0.84 ± 0.02
Hairless mouse	Back	8.9 ± 0.4	28.6 ± 0.9	0.70 ± 0.02

As described in Chapter 1, section 1.4.7, previous transdermal work by Bhatnagar investigated a new transdermal delivery approach which sought to create a gel formulation containing cavitation nuclei and the drug [149]. The advantage of this approach was to simultaneously achieve cavitation-mediated skin permeabilisation *and* simultaneous enhanced drug transport from a viscous gel into the permeabilised skin by cavitational microstreaming [149].

Even at a relatively low-ultrasound frequency of 256 kHz, acoustic gels exhibit significant variability both in threshold and the amount of cavitation that they yield due to their gas content. Therefore, in order to produce robust thresholds and a reproducible amount of cavitation activity, it is important to seed the process with pre-existing cavitation nuclei. All known existing micron-sized cavitation nuclei, such as ultrasound contrast agent microbubbles, are destroyed during the process of cavitation. However, a new generation of nano-sized cavitation nuclei was identified that is capable of lowering the inertial cavitation threshold in the medium (to 1.0 MPa at 256 kHz) and generating sustained cavitation activity [161]. Also, these biocompatible cup-shaped polymeric nanoparticles, referred to as nanocups (NCs), were found to enhance the transdermal permeability and transport of drug molecules [151]. The NCs are designed to entrap a surface nanobubble, which upon exposure to ultrasound can act as a nucleus for the initiation of cavitation.

The *ex vivo* experiments of Bhatnagar et al. in pig skin demonstrated that in the presence of inertial cavitation the Ovalbumin and NCs penetrated the skin to depths up to 500 μm and 700 μm, respectively, after 90 seconds insonation at 256 kHz (see Figure 1.3) [151]. In contrast, in the absence of NCs, Ovalbumin penetrated the skin to depths not exceeding 100 μm. This paper demonstrated for the first time the feasibility and potential of simultaneous skin permeabilisation and transport across the skin using NCs embedded within a viscous gel dosage form.

Notably, the study was performed with only one drug class, the model vaccine Ovalbumin. Although an immune response against Ovalbumin was observed in *in vivo* experiments, the dose delivered after treatment with ultrasound-mediated cavitation

(up to 1 μg Ovalbumin/treatment, 0.04% of the applied dose) would not ultimately be sufficient to produce a clinically useful level of antibodies. This therefore emphasizes the need to build on this work to further validate and optimise this enhanced drug delivery technique. In addition, the presence of inertial cavitation is believed to be the mechanism for both skin permeabilisation and assisted molecular transport. Therefore, the potential of using passive cavitation detection as a feedback system for delivery are also worthy of investigation.

In summary, the aims of this chapter are:

1) To establish the utility of excised pig skin as a model system for testing transdermal delivery.
2) To investigate the feasibility and reproducibility of delivering a large therapeutic molecule (e.g. an antibody) *ex vivo* by cavitation-enhanced transport.
3) To investigate the potential to ascertain successful delivery of adequate dose of the therapeutic agent into the skin using passive monitoring of acoustic emissions.

2.2 Materials and Methods

2.2.1 Therapeutic Ultrasound Setup

An ultrasound setup similar to that described by Bhatnagar (2014) was used [151]. This ultrasonic delivery system utilises ultrasound-initiated cavitation to transport drug molecules from an ultrasound coupling gel into the skin. An overview of the therapeutic ultrasound setup is presented in Figure 2.1. A High Intensity Focussed Ultrasound (HIFU) transducer was used to insonate a formulation holder filled with coupling gel seeded with drugs and cavitation nuclei. For the characterisation studies, an acoustic absorber plate was used as the acceptor layer (Figure 2.1(a)) and for the *ex vivo* studies, the skin was clamped in a Franz diffusion cell (Figure 2.1(b)).

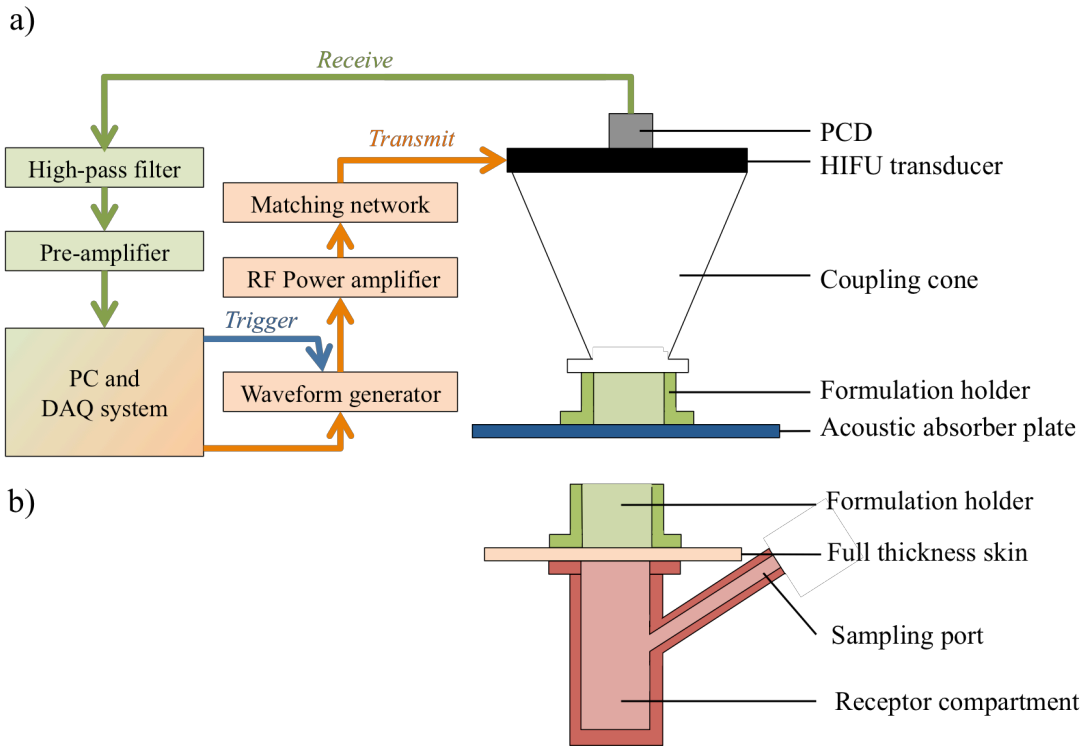

Figure 2.1: Schematic representation of the therapeutic ultrasound setup. a) The sonication loop (left) includes the transmit, receive, trigger, and monitoring pathways. On the right side the ultrasonic delivery system with coupling cone, formulation holder and the acoustic absorber plate. b) Schematic representation of the Franz diffusion cell. The full thickness skin is clamped between the formulation holder (top) and receptor compartment (bottom). The formulation holder is connected to the ultrasound system as shown in a).

The ultrasound setup consists of a 256 kHz HIFU transducer (117D-01, Sonic Concepts, USA), driven by a high-power radiofrequency (RF) amplifier (Model A300, Electronics and Innovation, USA) with an input signal from a computer-controlled waveform generator (33250A, Agilent, United Kingdom). The amplifier output impedance was matched to the HIFU source via a matching network (H-117 SIN-001, Sonic Concepts, USA). The broadband emissions associated with inertial cavitation of the cavitation nuclei in the sample upon exposure to HIFU were detected using a coaxially located passive cavitation detector (PCD) transducer fitted in the central opening of the HIFU transducer with centre frequency of 5 MHz (V309-SU, Panametrics-NDT™, Olympus NDT, USA). Since the centre frequency of the single-element focused piezo-electric receiver was much greater than the 256 kHz driving frequency, the PCD was particularly sensitive to broadband emissions associated with inertial cavitation rather than the harmonics of the fundamental driving frequency of the HIFU transducer.

To provide further isolation of the fundamental HIFU frequency and its harmonics, the received signal was filtered by a 2.0 MHz high-pass filter before being amplified. The amplification of the pre-amplifier (SR445A, Stanford Research Systems, USA) was set on 25 times, or 28 dB, and the signal was digitised using a 14-bit data acquisition (DAQ) card operating at a sampling frequency of 100 MHz.

A hollow Perspex coupling cone was designed by Bhatnagar to form a watertight fit onto the ultrasound transducer [151]. The conical shape of the cone was matched with the outer envelope of the spherically-focused ultrasound field and the focus of the ultrasound field was positioned within the formulation holder of the Franz diffusion cell.

The Franz diffusion cell is the most commonly used and standardised setup for *ex vivo* skin permeation studies. The glass Franz diffusion cell was purchased from PermeGear, Inc. (USA) and consisted of a formulation holder and receptor compartment with a membrane/*ex vivo* skin clamped between the two compartments as shown in Figure 2.1(b).

Acoustically transparent Mylar plastic covered the opening of the coupling cone. Before use, the coupling cone was filled with degassed deionised (DI) water to facilitate the transmission of ultrasound waves from the surface of the transducer to the formulation holder. With this adjustment, the therapeutic ultrasound setup became portable and the setup could be used on the bench top instead of using a large water tank.

Skin permeability and transdermal drug transport was demonstrated in previous *ex vivo* and *in vivo* studies [151] by using the ultrasound settings as presented in Table 2.2. These settings are referred to as the 'standard ultrasound settings' in the rest of this chapter.

Table 2.2: Table of the standard ultrasound settings.

Ultrasound parameters	Settings
Driving frequency	256 kHz
Duty Cycle (DC)	10%
Pulse Repetition Frequency (PRF)	10 Hz
Pulse length	10 ms
Peak Rarefactional Focal Pressure (PRFP)	1.0 MPa

2.2.2 Calibration of the transducer pressure field

The supplied formulation holder of the Franz diffusion cell had a volume of 4 mL (19.6 mm height). To reduce the cost and possible wastage of drug left in the holder after treatment, a new Perspex formulation holder (9.5 mm height, 1.5 mL volume) was fabricated by the IBME workshop. Lowering the height of the formulation holder reduced the distance between the skin and the transducer, and re-calibration of the ultrasound field was required.

As indicated in Figure 2.2(a), the therapeutic ultrasound setup was placed above a degassed water tank (which is similar to the conditions when used on the bench top), with the formulation holder submerged in the water tank. The pressure profile within and beyond the formulation holder was re-characterised by point-by-point scanning with a hydrophone (Onda HNA-0400, Onda Corporation, USA). The Mylar sheet was sealed at the end of the coupling cone (57.26 mm from the transducer) in order to fill the coupling cone with degassed DI water. Furthermore, the formulation holder was fixed to the end of the coupling cone with a silicone seal, and a safety margin of 3.6 mm was used to prevent the hydrophone from touching the Mylar sheet when performing the pressure scans within and beyond the formulation holder. Transverse and longitudinal pressure scans were performed and the normalised pressure profiles are presented in Figure 2.2(b) and (c).

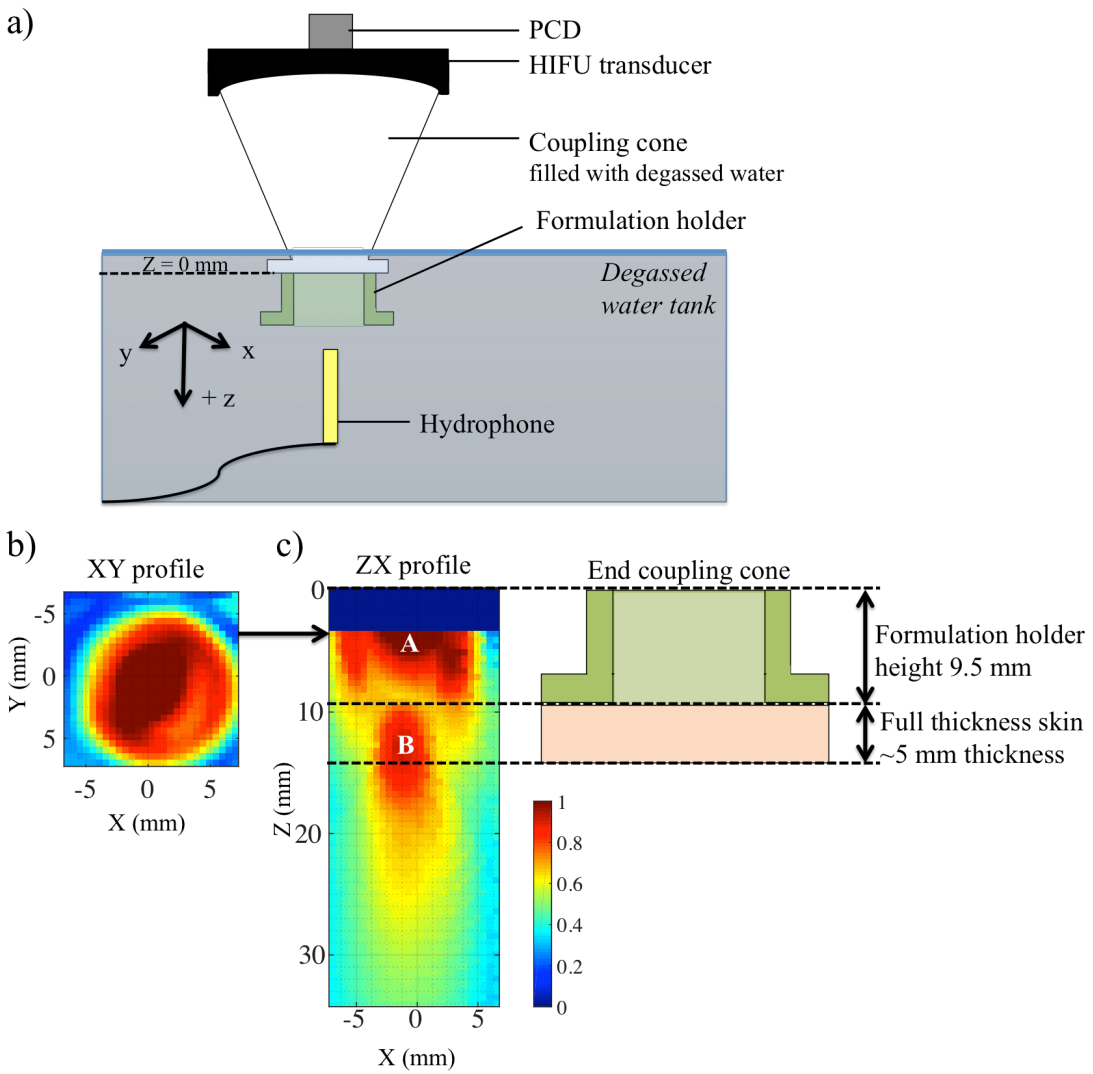

Figure 2.2: Characterisation of the ultrasound field with 9.5 mm height formulation holder. a) Schematic representation of the experimental setup with the therapeutic transducer placed above the degassed water tank. The acoustic field inside and underneath the formulation holder was measured with the hydrophone. b) Normalised transverse pressure profile of the HIFU transducer taken 3.6 mm underneath the end of the coupling cone. c) Normalised longitudinal pressure profile with the representative positions of the formulation holder and full-thickness skin illustrated on the right-hand side. Two ultrasound foci are indicated by 'A' and 'B'. Due to the safety margin of 3.6 mm, no acoustic information was measured between z=0:3.6 mm (dark blue band).

The transverse pressure profile in Figure 2.2(b) shows that the ultrasound field is circular with a -3dB beam diameter of 12.5 mm at 3.6 mm underneath the coupling cone. When looking at the longitudinal pressure profile (Figure 2.2(c)), two ultrasound foci can be observed as highlighted; one focus was located within the formulation holder (indicated as 'A' in Figure 2.2(c)) and a second smaller focus (-3dB beam width: 6.23 mm) was found located beyond the 9.5 mm height formulation holder (indicated as

'B' in Figure 2.2(c)). The location of the smaller focus would be within the *ex vivo* skin when using the Franz diffusion cell (Figure 2.2(c)). With the standard ultrasound settings from Table 2.2, the pressure of the first ultrasound focus ('A') was measured to be 1.2 MPa PRFP and 1.0 MPa PRFP in the smaller second focus ('B').

However, caution has to be taken when interpreting these pressure profiles because Figure 2.2(b) and (c) present the pressure profile without any attenuation, reflections, or standing waves induced by the absorber plate/*ex vivo* skin or by the receiver compartment that may alter the linear pressure profile. Due to the experimental limitations of performing a pressure profile, it is challenging to determine the exact acoustic pressure within the setup when performing an experiment.

From here onwards, the acoustic pressure is presented as the peak negative acoustic pressure calculated in the smaller focus ('B') based on Figure 2.2(c).

2.2.3 Cavitation nuclei

Nanocups (NCs) are nano-sized cavitation nuclei composed of a copolymer of methyl methacrylate and 2-hydroxyethylmethyl methacrylate and formed around and linked to a poly(styrene-co-divinylbenzene) copolymer core as described by Kwan et al. [161]. After drying, the cup-shaped structure is able to stabilise a gas pocket within the rough hydrophobic crevice. Upon insonation, the NC facilitates unconstrained growth of the bubble during the peak rarefactional half-cycle [161]. The characterisation of the cup-shape of the NCs was performed using the transmission electron microscopy (TEM) (Hitachi H-7650, United Kingdom) operating at 120 kV (Figure 2.3(a)). A droplet of NCs sample was air-dried overnight onto a 3.06 mm copper grid supported with Formvar/Carbon 200 meshed grid (Electron Microscopy Sciences, USA).

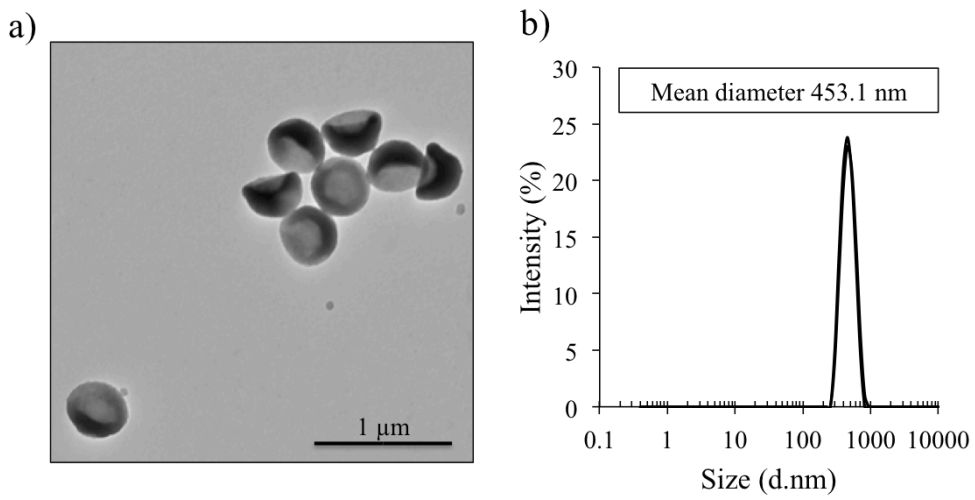

Figure 2.3: Nanocups (NCs) characterisation. a) TEM images of nano-size cavitation nuclei to verify shape. b) The size distribution measured by DLS with a mean diameter of 453.1 nm.

The hydrodynamic diameter of the nanoparticles was characterised by dynamic light scattering (DLS) using a Malvern ZetaSizer Nano ZS (Malvern Instruments Ltd., United Kingdom) (Figure 2.3(b)). Each sample was diluted 1:1000 in DI water and then tested in triplicate with 11 runs each. The Malvern Dispersion Software was used to analyse the acquired correlation function and to obtain the diffusion coefficient (D_m). The obtained D_m was set in the following Strokes-Einstein equation for the calculation of the hydrodynamic diameter (d_H) of the particles in the suspension with the following formula:

$$d_H = \frac{k_B T}{6 \pi \eta D_m} \tag{2.1}$$

where k_B Boltzmann's constant, T absolute temperature, η viscosity. The mean particle size (Z-average) was found to be 450 nm with a polydispersity <0.1.

After characterisation, the NCs were air-dried overnight to allow gas to be entrapped on the surface of the NCs. The powder was suspended in DI water to the required concentration and vigorously mixed for four hours. The entrapped gas pockets then provide the nuclei to instigate inertial cavitation when placed in an ultrasound field.

The final concentration of the NCs suspension was measured via desiccation of 20 µL of sample in an aluminium foil discs. The resulting mass was determined by weighing the foil discs with the Mettler Microbalance (MT5, Mettler-Toledo Ltd., Leicester, United Kingdom). A final DLS measurement was again performed to confirm the creation of a homogenous NCs suspension.

2.2.4 Passive cavitation monitoring

For every ultrasound experiment, the acoustic emissions from the ultrasound focus were recorded by the PCD. Due to the memory restriction of the DAQ card, only the first 200 µs segments of each 10 ms pulse were saved. The harmonics and the sub-harmonics were filtered out the receiving signal with a 2.0 MHz high-pass filter. For every trace, the signal was corrected for the 28 dB pre-amplification. As can be seen in Figure 2.4(a), a 22 µs timeframe was windowed to look at the acoustic emissions originating from the formulation holder and the *ex vivo* skin beneath. Since the NCs have the unique ability to nucleate and sustain cavitation over at least 10-minutes exposure [162], the 25.0 µs time window (96.1 - 121.1 µs) was taken to be representative of the total 10 ms burst.

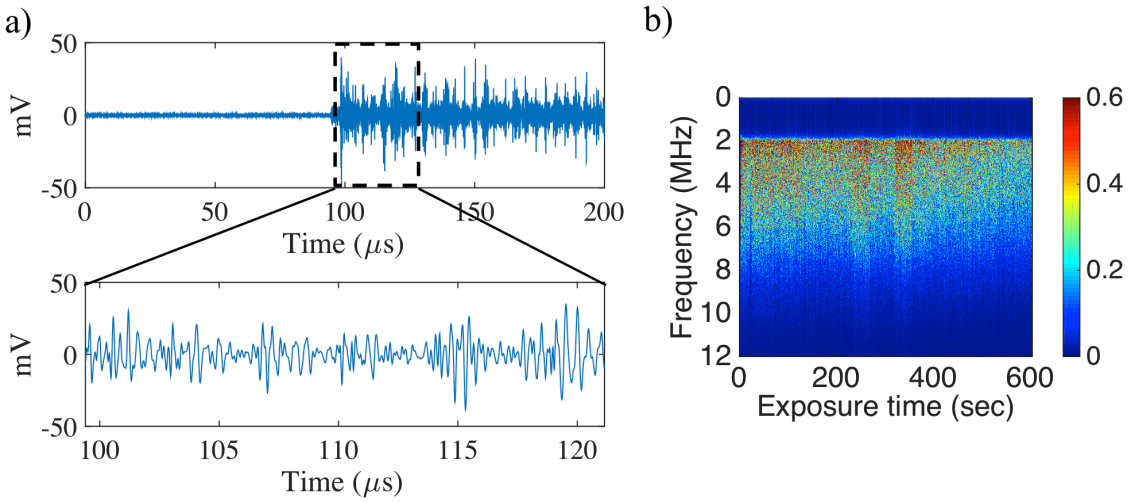

Figure 2.4: Example of recorded raw PCD voltage trace (a) and time-frequency diagram (b). a) The windowed signal contains acoustic emissions originating from the formulation holder and *ex vivo* skin. b) The colour bar on the right axis represents the power spectral density (mV^2/Hz).

The windowed signal was Fourier-transformed and the power spectral density was plotted as a time-frequency diagram. An example given of such an acoustic emission spectrogram from recorded cavitation activity from NCs is shown in Figure 2.4(b). In the therapeutic ultrasound setup, the fundamental frequency and its harmonics are removed from the PCD trace using a 2.0 MHz high-pass filter. As a result, no frequencies are detected in the low-frequency range from 0-2.0 MHz in the acoustic emission spectrogram (hence the 0-2.0 MHz region remains dark blue in colour). In case of broadband acoustic emissions (associated with inertial cavitation), the PCD trace contains a broad range of frequencies that can be identified as a vertical band of coloured pixels from 2.0 MHz to higher frequencies with red presenting the highest power spectral density. The acoustic emission spectrograms were used to identify inertial cavitation happening in the formulation holder and *ex vivo* skin during treatment.

The energy received by the PCD per burst was determined and summed; this is proportional to the total energy of acoustic emissions and will be referred to as the total acoustic sensor energy (TASE) (μJ). This was achieved using the following formula:

$$TASE = \sum_{i=1}^{n} \frac{(V_{RMS}(i))^2}{R} \cdot T_{pulse} \qquad (2.2)$$

Firstly, the first 200 μs of each pulse train was recorded (due to data storage limitations) and the root mean square (RMS) was calculated of the 25.0 μs windowed signal (V_{RMS}) (see Figure 2.4(a)). Secondly, it was assumed that the acoustic emission energy was sustained throughout the 10 ms pulse duration, and therefore the RMS was squared and multiplied by the 10 ms pulse length (T_{pulse}) and divided by the electrical impedance (R) of 50 Ohm to calculate the energy. Finally, the TASE value was calculated throughout the exposure time by taking the sum of the energies for all bursts (n).

2.2.5 Gel formulation

In ultrasonic imaging, clinically-approved ultrasound gel is used to enable good acoustic coupling between the skin and the transducer. Furthermore, a semisolid formulation has the clinical advantages of being easy to apply onto the skin and to prevent drug leakage away from the treatment area. Therefore, in the previous transdermal delivery study [151], the therapeutic application mixture was composed of 50 wt.% ultrasound gel (i.e. polyacrylamide hydrogel, Carbopol®), 25 wt.% NCs suspension in water, and 25 wt.% drug solution. Preparing the homemade Carbopol® is a time-consuming process. Briefly, dried powder (0.5% w/v, Ultrez 21 Carbopol®, Lubrizol Corporation, USA) was re-suspended in polypropylene glycol (20% w/v), and cross-linked by adding 0.5% w/v of Trizma base overnight.

In previous work [151] it was found that during fabrication of the gel the amount of entrapped gas was variable and affected the acoustic properties of the gel. To enhance the reproducibility of the acoustic properties of the gel within a batch as well as between different batches, the hydrogel was degassed for eight hours to remove native gas in the gel content. Furthermore, it was found in previous work that the gas content in the degassed Carbopol® increased over time when stored at room temperature in a sealed airtight centrifuge tube [151]. Consequently, the acoustic properties of the gel had a shelf life of no longer than eight weeks. As a result, Carbopol® was freshly prepared for each experiment.

The addition of the NCs to the Carbopol® formulation enhanced the ability to induce sustained inertial cavitation activity in the gel for up to 90 seconds at an acoustic pressure as low as 1.0 MPa peak negative pressure [151].

The ability to instigate cavitation at these low acoustic pressures decreases concerns about heating, as well as validating the potential of the use of inertial cavitation-mediated mechanisms to increase skin permeability and transdermal drug transport.

To enhance the reproducibility of the hydrogel and reduce the fabrication time, a commercially available, clinically approved, and ready-to-use ultrasound gel (i.e. Anagel®) was considered as an alternative. The key ingredients of Anagel® (Ana Wiz Ltd, United Kingdom) are water and vinyl polymer, along with isothiazolinoes (5-chloro-2-methyl-4-isothiazolin-3-one, 2-methyl-4-isothiazolin-3-one, isothiazolin-3-on), benzylalcohol, and preservation molecules [163]. Thriethanolamine is used to buffer the pH to 7.2 and monoproplene glycol to provide hygroscopic properties to the gel. This ultrasound gel is widely used for medical diagnosis and therapy and is commercially available in ready-to-use tubes.

Anagel® can only be a suitable alternative to Carbopol® provided that (1) the native gas content in the Anagel® is consistent, and (2) it enables the same or higher inertial cavitation response in the presence of NCs when insonating at acoustic pressures above the NCs cavitation threshold (1.0 MPa peak negative pressure [161]).

2.2.5.1 Ready-to-use Anagel® characterisation

To investigate the first of these requirements, the acoustic behaviour of the ready-to-use Anagel® was compared to the degassed Carbopol® without the presence of NCs. Two types of gel formulations were prepared contained 50 wt.% DI water with 50 wt.% Anagel®, or 50 wt.% Carbopol®. To investigate the second requirement, the gel formulations were seeded with 25 wt.% NCs (8.7 mg/mL) and 25 wt.% DI water. The ultrasound setup presented in Figure 2.1(a) was used with the acoustic absorber plate

underneath the holder and the standard ultrasound settings were used (Table 2.2) with a total exposure time of 90 seconds. The cavitation response was recorded with the PCD. In Figure 2.5(a) and (b) representative acoustic emission spectrograms are presented for the gel formulation containing degassed Carbopol® (Figure 2.5(a)) or ready-to-use Anagel® (Figure 2.5(b)) in the absence or presence of NCs.

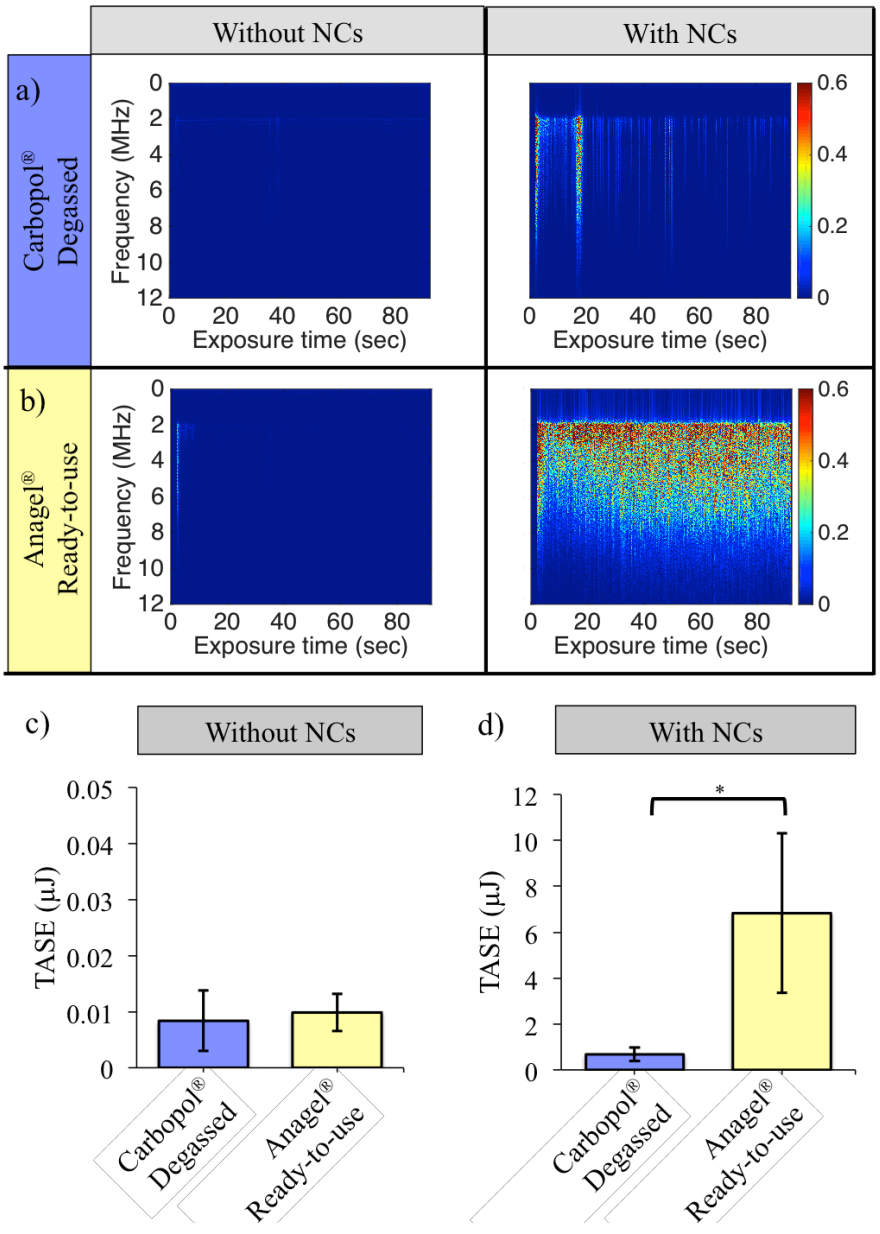

Figure 2.5: Representative acoustic emission spectrograms from gel formulation containing (a) degassed Carbopol®, (b) non-degassed Anagel® with or without NCs insonated at 1.0 MPa PRFP. The colour bar on the right axis represents the power spectral density (mV^2/Hz). c) and d) Bar charts showing the mean total acoustic sensor energy (TASE) detected for different gel formulations (c) without NCs, or (d) with NCs. The error bars represent the standard deviation for n=4 samples. The significant difference was determined by t-test and * corresponds to $p<0.05$.

It can be observed in Figure 2.5(a) and (b) that in the absence of NCs, low acoustic emissions were recorded when using either of the ultrasound gels. This indicates that the gas composition of the ready-to-use Anagel® is acoustically consistent and similar to the eight-hours degassed Carbopol®. Furthermore, broadband emissions were only recorded in the presence of NCs, indicating the ability of the NCs to induce inertial cavitation at these relatively low acoustic pressures. Notably, by using ready-to-use Anagel® enabled significantly ($p<0.05$) higher inertial cavitation response in the presence of NCs when insonating at acoustic pressures of 1.0 MPa peak negative pressure than to eight-hours degassed Carbopol®. Therefore, ready-to-use Anagel® is a suitable alternative to Carbopol® and will be used in all further studies.

2.2.5.2 Optimisation of NC concentration in the formulation

Sustained inertial cavitation throughout the ultrasound exposure would be optimal for drug delivery. To investigate whether increasing the NC concentration has a positive effect on the duration of cavitation response, three different NC concentrations were evaluated. Different NC batches were fabricated and the highest possible NC concentration (without aggregation) was found to be 30 mg/mL. Therefore, the gel formulations were prepared with 50 wt.% Anagel®, 25 wt.% NCs (final concentrations of 0, 2.5, 5.0 and 7.5 mg/mL), and 25 wt.% 0.01 M phosphate buffer (pH 7.22). A phosphate buffer was chosen to mimic the presence of therapeutic agents in buffered solution, which are typically stored in (low salt) physiologic pH buffer.

The holder was placed on top of an acoustic absorber (Figure 2.1(a)) and filled with the prepared gel formulation. The gel formulation was insonated for five minutes instead of 90 seconds used in the previous study [151], to investigate the acoustic activity of the NCs over elongated exposure time. The standard ultrasound settings (Table 2.2) were

used and the gel was discarded afterwards. For every gel condition, three samples were insonated and the acoustic emissions were recorded with the PCD. The total acoustic sensor energies were calculated as described in section 2.2.4 and the data is presented in Figure 2.6.

In Figure 2.6(a) it can be observed that insonating the gel formulation without any NCs (0 mg/mL) caused only some sporadic low energy acoustic emissions (detected as light blue bands) due to the gas entrapped in the formulation. Increasing the NC concentration to 2.5 mg/mL (Figure 2.6(b)) showed stronger broadband acoustic emissions (red bands) alternating with lower broadband emissions visible as green/blue bands. Increasing the NC concentration further to 5.0 mg/mL (Figure 2.6(c)), or 7.5 mg/mL (Figure 2.6(d)) resulted in light blue/green bands throughout the five minutes exposure with longer periods of strong broadband acoustic emissions (red bands). In a single case in Figure 2.6(d), sustained inertial cavitation was observed almost throughout the five minutes exposure. This shows the potential of elongating the ultrasound exposure time to five minutes instead of 90 seconds.

In Figure 2.6(e) it can be observed that the TASE value increased with increasing NC concentration. In the presence of 2.5 mg/mL NCs, TASE value was found to be 4.53 ± 3.09 μJ. Significantly ($p<0.05$) higher energies (two-fold) were found with 5.0 mg/mL NCs in the formulation (9.76 ± 4.39 μJ). Increasing the NC concentration in the gel formulation further to 7.5 mg/mL did increase the TASE value, but this effect was not significantly higher ($p>0.05$) than with 5.0 mg/mL NC concentration in the formulation, due to the large variation within the group (21.63 ± 19.20 μJ).

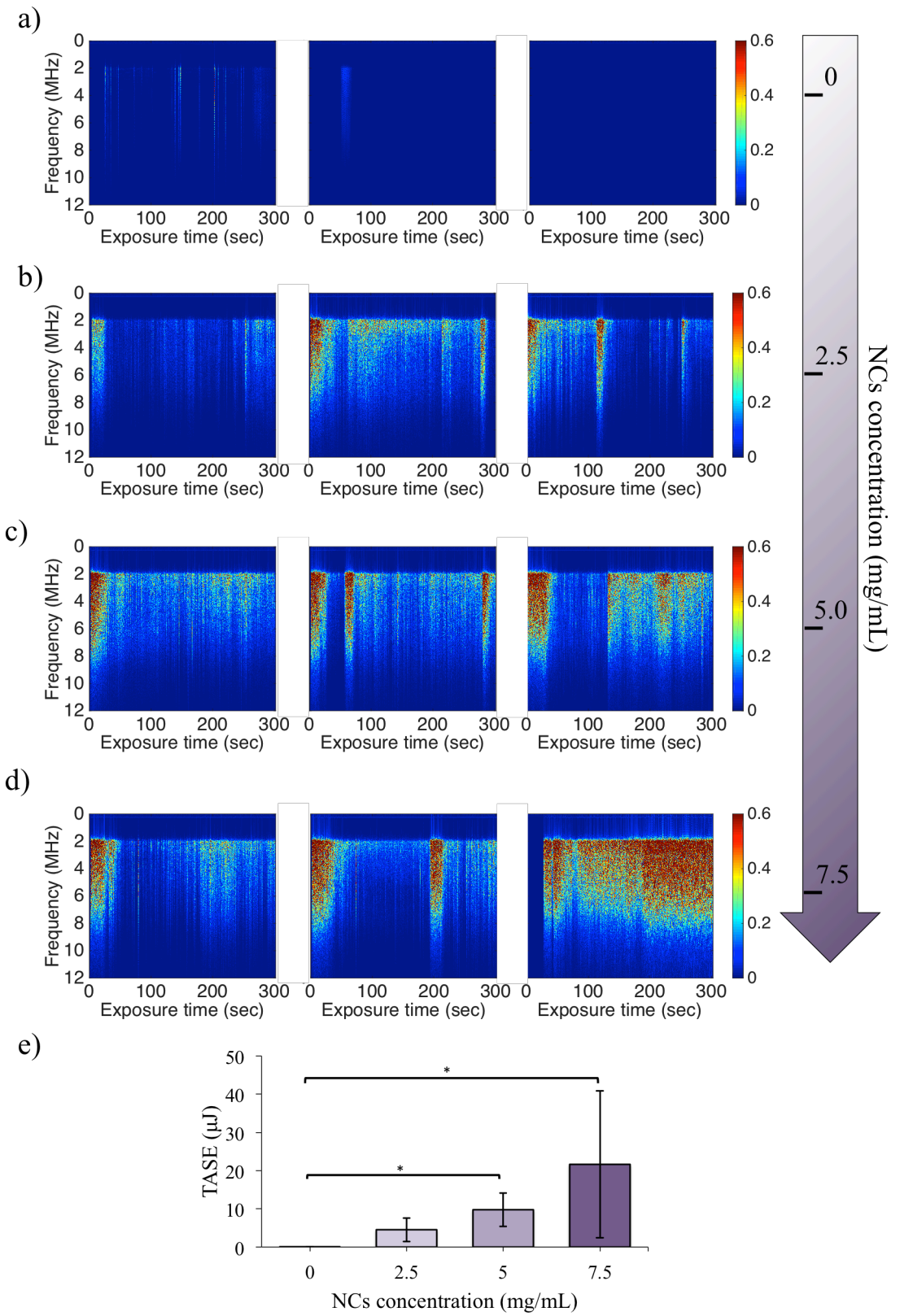

Figure 2.6: Acoustic emission spectrograms from gel formulation containing different NC concentration in Anagel® at 1.0 MPa PRFP. a-d) Three acoustic emission spectrograms per NC concentration making up a final concentration of (a) 0 mg/mL, (b) 2.5 mg/mL, (c) 5 mg/mL, and (d) 7.5 mg/mL NCs in the formulation. The colour bar on the right axis represents the power spectral density (mV^2/Hz). e) The bar chart showing the mean total acoustic sensor energy (TASE) detected per condition. The error bars represent the standard deviation for n=3 samples. The significant difference was determined by one-way ANOVA Bonferroni multiple comparison tests and * corresponds to $p<0.05$.

During the NC fabrication, the particles are air-dried and then re-suspended in water to the required concentration. In this study, a NC concentration of 30 mg/mL was required to prepare the gel formulation containing a final concentration of 7.5 mg/mL NCs. Preparation of a homogeneous NC suspension of this concentration was found to be difficult, even after vigorous mixing of the suspension for eight hours. This was not the case when preparing lower NC concentration for the 5 mg/mL and 2.5 mg/mL NCs in the gel formulation.

Taking into account that higher NC concentration (7.5 mg/mL in the gel formulation) did not significantly increase the average TASE value over 5.0 mg/mL in the gel formulation, and the difficulties associated with the preparation of higher NC concentrations, the optimal NC concentration in the gel formulation was chosen to be 5.0 mg/mL for further experiments. Furthermore, the results in Figure 2.6 showed that the acoustic activity of the NCs continued during the five minutes of ultrasound exposure. To enhance the skin permeability by inertial cavitation, the *ex vivo* experiments were therefore performed with ultrasound exposure of at least five minutes.

2.2.6 Ex vivo delivery study

After changing the size of the formulation holder, validating the use of a ready-to-use Anagel® and optimising the NC concentration in the formulation, the feasibility of delivering a large therapeutic agent by cavitation-enhanced transport was investigated *ex vivo*. For this experiment Immunoglobulin G (IgG, 150 kDa) antibody was chosen as a model for antibody-based therapeutic agents [164]. In total four *ex vivo* studies were undertaken, one IgG study with fluorescently labelled IgG and NCs (called 'IgG-FITC Study') and three repeat experiments (called 'IgG Repeat Studies 1-3'),

which were performed without fluorescent dyes to investigate the reproducibility of the results found in the 'IgG-FITC Study'.

All four *ex vivo* experiments utilised the Franz diffusion cell (as shown in Figure 2.1(b)), where freshly collected porcine skin was clamped between the formulation holder and the receiver compartment (filled with degassed phosphate-buffered saline (PBS)). The skin was insonated for five minutes at the standard ultrasound settings (Table 2.2). The cavitation activity was monitored by PCD. After the treatment, the exposed area of skin was washed, resected and homogenised. An Enzyme-Linked Immune-Sorbent Assay (ELISA) was developed and used to quantify the IgG dose delivered into the skin.

Since the experimental procedures and the rationale behind the used materials and methods are similar for the four *ex vivo* experiments, in the next sections the general experimental procedure will be explained in more detail and special reference will be made to differences between the *ex vivo* experiments. The results from the 'IgG-FITC Study' have been presented in a poster [165, 166] and oral presentation [166].

2.2.6.1 Experimental groups

Six experimental groups were tested in triplicate and a description of the groups is given in Table 2.3. The treatment group contained the formulation 'Anagel® + IgG + NCs' and was insonated at the standard ultrasound settings (Table 2.2) required to generate inertial cavitation and ultimately transdermal delivery. The other five groups were controls designed to isolate NC mediated inertial cavitation as the causative factor in delivery, and also to provide a comparison to the delivery achieved using an alternative benchmark approach (i.e. chemical penetration enhancer).

Table 2.3: Experimental groups for *ex vivo* experiment on porcine skin

Experimental group	Treatment description
Anagel® + NCs (Negative control)	Without the presence of IgG and exposure to ultrasound.
No Ultrasound	Gel formulation containing IgG + NCs. No exposure to ultrasound.
Anagel® + IgG	Exposure to ultrasound but without the generation of inertial cavitation.
Water + IgG + NCs	Liquid formulation containing IgG + NCs and exposure to ultrasound.
Anagel® + IgG + NCs	Gel formulation containing IgG + NCs and exposure to ultrasound.
SDS pre-treatment (Positive control)	Chemical penetration enhancer pre-treatment with 1% w/v sodium dodecyl sulphate (SDS) for five minutes. After washing, IgG in DI water was left on the skin to diffuse for five minutes (no exposure to ultrasound).

Hence, the 'Anagel® + NCs' group that involved placing the IgG negative gel formulation on the skin surface for five minutes, helped to establish the background detection in the ELISA. The 'No Ultrasound' group that involved the use of Anagel® with all the components (IgG and NCs) but no ultrasound exposure, controlled for any potential effect of NCs on the passive diffusion of IgG. The 'Anagel® + IgG' group controlled for the possibility of ultrasound alone without NCs providing a sufficient stimulus for IgG transport. The 'Water + IgG + NCs' group involved a liquid solution and helped to characterise the impact of the viscosity of the Anagel® on any delivery achieved. The 'SDS pre-treatment' involved exposure to a chemical penetration enhancer, the surfactant sodium dodecyl sulphate (SDS), for five minutes to permeabilise the SC, followed by five minutes of IgG solution addition. It therefore provided a positive control and alternative technology to compare against.

SDS is a commonly used chemical penetration enhancer, which temporarily alters the lipid structure of the SC and enhances cutaneous delivery [167-169].

2.2.6.2 Skin model

The e*x vivo* experiments were performed on full-thickness pig skin harvested from the abdomen immediately after abattoir sacrifice. The s.c. fat tissue was removed and the skin resected into 18 pieces of 40x40 mm and stored in PBS at 4°C for a maximum of two days before use.

2.2.6.3 Formulation preparation

In all four *ex vivo* experiments, the gel formulation was prepared with Anagel®, NCs and IgG in the composition 50:25:25 wt.%, respectively. IgG antibodies play a crucial role in the immune system and they are the main isotype of antibody found in the blood circulation. To distinguish the delivered IgG antibody from the IgG antibodies present in the pig skin, it was essential to use an IgG molecule from a host other than pig.

In the 'IgG-FITC Study', NCs were fluorescently labelled with Nile Red and IgG from human serum was conjugated to Fluorescein Isothiocyanate (FITC), purchased from Sigma-Aldrich (F9636, United Kingdom). This allowed microscope based visualisation of the delivery of the NCs and antibody into the skin, as well as detection and potentially quantification of the antibody by ELISA.

In the three repeat experiments ('IgG Repeat Studies 1-3'), the NCs and the IgG were not fluorescently labelled and anti-mouse IgG (M7023, Sigma-Aldrich, United Kingdom) produced in rabbit was used and detected by ELISA. In all four *ex vivo* experiments, the IgG was diluted in stabilising 0.01 M phosphate buffer (pH 7.25) to the

required concentration and added to the Anagel® and NCs to reach a final concentration of 0.6 mg/mL. For all the experimental groups containing no Anagel® and/or no NCs, their percentage by weight was replaced with DI water (since Anagel® and NCs have water as their main component). In the absence of IgG, the liquid volume was replaced with 0.01 M phosphate buffer. The formulations were made on the day of the *ex vivo* experiments and stored at room temperature before use. Different NC batches were fabricated in the laboratory and used to prepare the drug formulations for the *ex vivo* experiments. While preparing the drug formulations with Anagel®, it was observed that the viscosity of the gel formulation reduced when adding the IgG solution, so that the solution became more readily pipettable.

2.2.6.4 General experimental protocol

Prior to performing the *ex vivo* experiment, the porcine skin samples were acclimatised to room temperature for 30 minutes before being mounted in the Franz diffusion cell (Figure 2.1(b)). The receptor compartment was filled with degassed PBS to reduce cavitation activity in the buffer during the ultrasound exposure. The skin was kept hydrated with PBS until the start of the experiment. The PBS in the formulation holder was removed prior to the experiment and filled with the prepared drug formulation (composition depending on the experimental group as listed in Table 2.3).

The skin samples in the treatment groups that required ultrasound exposure were insonated for five minutes at the standard ultrasound settings as indicated in Table 2.2. The cavitation activity was monitored by PCD (as described in section 2.2.4). For the experimental groups not requiring ultrasound, the formulation was placed on the skin surface and left for five minutes to diffuse into the skin. The skin samples in the SDS pre-treatment group received a five-minute pre-treatment with 1% SDS solution to

enhance the cutaneous delivery without inducing too extreme toxicity to the skin [170]. The SDS solution was thoroughly washed off the skin surface before the IgG formulation was placed on the skin for five minutes.

After the intervention, the drug formulation was removed from the holder and the skin was washed three times with PBS and blotted dry. The exposed skin area was then resected and stored at -20°C until homogenisation.

Protocol specification: In 'IgG-FITC Study' one of the three resected skin samples per treatment group was split into two halves; one skin half was used to determine the dermal delivery by ELISA, and the other skin half was used to visualise the delivery of fluorescent NCs and IgG into the skin by histology.

2.2.6.5 Skin homogenisation

To investigate the amount of IgG delivered in the skin after treatment, the exposed skin was homogenised before being analysed by ELISA. At first, the thawed skin samples were weighed and cut into smaller pieces. To enhance the homogenisation process, the skin samples were enzymatically digested by first adding 1000U collagenase type I (Worthington Biochemical, USA) during overnight incubation at room temperature. Secondly, 1000U of hyaluronidase (Worthington Biochemical, USA) in HSE buffer (0.1 M sodium phosphate buffer, pH 5.3 with 0.1 M sodium chloride) was added to every skin sample and left to incubate for three hours at room temperature. Next, PBS was added to the skin samples to achieve a final volume of 1 mL solution/100 mg skin and homogenised on ice using an Ultra-Turrax homogenizer (T25, Ika Works Inc., USA). The homogenates were sonicated on ice using an ultrasonic cell disruptor (Microson Ultrasonic cell disruptor, Misonix, USA) four times for 10 seconds at level six with 10

seconds rest time in between. Samples were then centrifuged for seven minutes at 7000x g (Sorvall Legend X1R, Thermo Scientific, Germany). The supernatant was transferred to eppendorf tubes and centrifuged again in a micro-centrifuge (MSE model Micro-centaur Plus, Sanyo Ltd., United Kingdom) at 14,000x g for seven minutes to remove large skin residues that may block the light path on the ELISA plate. The supernatants were stored at 4°C until further analysis. Besides the experimental skin samples, blank skin samples were prepared using untreated skin.

Protocol specification: In 'IgG Repeat Studies 2' and '3', extra positive control samples were prepared by using non-treated skin spiked with known amounts of IgG. These extra skin samples were homogenised in the same way as the experimental samples.

2.2.6.6 Detection dermal delivery of IgG

IgG is comprised of protein and is therefore amenable to be detected using ELISA. The homogenised and enzyme-treated skin samples were placed at room temperature before adding to a 96 well-Nunc ImmunoPlate MaxiSorp (Sigma-Aldrich, United Kingdom) plates (100 μL/well) in triplicate. After 1.5 hours incubation at room temperature, the plate was washed six times with PBS-T (PBS containing 0.05% Tween 20).

With the indirect ELISA, the binding of the IgG antibody delivered into the skin samples to the plate was detected by the addition of a secondary antibody specific for the species (human or rabbit) and isotype of the delivered IgG. Since the 'IgG-FITC Study' and the other three repeat studies ('IgG Repeat Studies 1-3') used different IgG molecules as the model delivery antibody, different secondary antibodies were required for detection. For 'IgG-FITC Study' an anti-human IgG produced in rabbit

(A8792, Sigma-Aldrich, United Kingdom) was added at a 1:50,000 dilution, to target any IgG-FITC attached to the ELISA plate. For 'IgG Repeat Studies 1-3', anti-rabbit IgG (whole antibody) produced in goat (A6154, Sigma-Aldrich, United Kingdom) was added at a 1:10,000 dilution, to target any rabbit IgG attached on the ELISA plate. Both the secondary antibodies were conjugated to a Horseradish Peroxidase (HRP) enzyme and showed negligible cross-reactivity with any pig IgG which may have been present in the skin.

After a one-hour incubation of the secondary antibody, the plate was washed six times with PBS-T to remove any unbound secondary antibody. The reaction was visualised by adding 50 µL/well of HRP substrate (Ultra-TMB, Thermo Scientific, United Kingdom). The HRP substrate was modified by the HRP enzyme on the secondary antibody inducing a blue colour change. The addition of 0.5 M sulphuric acid stopped the reaction and changed the colour to yellow. The absorbance was measured at 450 nm with the FLUOstar Omega plate reader (BMG Labtech, Germany).

The intensity of the colour was directly proportional to the amount of secondary antibodies bound to the IgG present in the skin homogenate, as demonstrated by the linear calibration curve. For this curve, a dilution series was prepared by spiking a blank skin sample with a known amount of IgG from the stock solution. This sample was subsequently diluted with blank skin homogenate to prepare in total five different calibration samples. Furthermore, a negative and positive control was added to every ELISA plate. To check for non-specific binding and false positive results, blank skin homogenate without IgG was used as a negative control.

To verify whether the procedure was performed correctly, a positive control sample was added in triplicate containing the IgG molecule from the stock solution.

Protocol specification: For 'IgG Repeat Studies 2' and '3', the positive control was further refined by adding homogenised skin spiked with a known amount of IgG, which helped to validate the calibration curve.

2.2.6.7 Data analysis ELISA

After performing the ELISA, the calibration curve of the absorbance values against known IgG concentration in skin homogenate was plotted. The data points were fitted with a linear regression curve with the formula in the form of $y=ax + b$, with 'a' the slope (AU per µg/mL skin homogenate) and 'b' the intercept (AU) of the curve. In regression, the coefficient of determination (R^2) indicates how well the linear regression curve follows the real data points. R^2 of 1 corresponds to a perfect fit of the curve to the data points and therefore indicates that the dependent variable (IgG in skin homogenate) can be predicted without error from independent variables. The absorbance values from the experimental samples were then converted with the linear regression formula into IgG concentration present in the skin homogenate.

In order to establish how much IgG was delivered into the exposed skin, an additional step had to be performed to relate the measured level back to the amount of skin excised. Specially, before homogenising the skin samples, PBS was added to the skin samples to achieve a total volume of 1000 µL solution/100 mg skin. Due to the variation in skin weight, the IgG concentration in the skin homogenate was multiplied by the total volume (µL), which corresponds to 10x skin weight (mg).

Therefore, the formula used to calculate the IgG dose delivered into the exposed skin was:

$$\text{IgG in the skin (µg)} = \left(\frac{Absorbance - \text{b}}{\text{a}}\right) \cdot (10 \cdot \text{skin weight (mg)}) \qquad (2.3)$$

with 'a' the slope and 'b' the intercept of the calibration curve.

To determine how much of the applied dose was delivered into the skin, the following formula was used:

$$\text{dose delivery in skin (\%)} = \left(\frac{\text{IgG in the skin}}{\text{total applied dose}}\right) \cdot 100\% \qquad (2.4)$$

with 'total applied dose' meaning the amount present in the formulation holder, which is the product of the IgG concentration in the formulation and the applied volume required to fill the formulation holder. For 'IgG-FITC Study', the volume of the formulation holder was first determined to be 2.5 mL. Generally, this volume was required when filling the formulation holder with a viscous formulation containing Anagel®, NCs, and water (no drugs). However, new insights were obtained after repeatedly measuring the volume required in the *ex vivo* studies to fill the formulation holder with the pipettable formulation containing Anagel®, NCs, and IgG-FITC. Hence, the pipettable volume applied was found to be 1.5 mL, corresponding to a total applied dose of 900 µg IgG-FITC. This volume was therefore used to calculate the total applied dose in all four *ex vivo* studies.

2.2.7 Histology on porcine skin

To visually observe the position and depth of the deposition of fluorescently labelled IgG and NCs into the porcine skin after treatment, histology was performed in 'IgG-FITC Study' on half the resected skin of one pig skin sample per experimental group. The prepared skin samples were fixed in formalin and the histology was performed at

the histology service at the Sir William Dunn School of Pathology (University of Oxford, United Kingdom). Ten cross-sections were sliced (slice thickness: 15 μm), from which alternating five slices were stained with hematoxylin and eosin (H&E) stain to enable visualisation of the different skin layers and structures within them. The other alternating five histology slices were treated without any further staining protocols to observe the delivery depth and location of the fluorescently labelled IgG-FITC and Nile Red NCs. The bright field and fluorescent images were captured using a Nikon Eclipse Ti microscope at 4x magnification.

2.2.8 Statistical analysis

Statistical analysis was carried out if the sample size per condition was three or more. The experimental values were represented as mean ± standard deviation (SD). Statistical significance was assessed using one-way analysis of variance (ANOVA) at 95% confidence limit. Bonferroni's multiple comparison post-test was used to determine statistical significance between groups.

2.3 Results

2.3.1 IgG-FITC Study

In the first *ex vivo* IgG study, fluorescently labelled IgG-FITC and Nile Red NCs were used. The results from the recorded acoustic activity will be described first and followed by the dermal delivery results. After indicating the dose delivery efficiency, the position and depth of the fluorescently labelled IgG and NCs into the skin are evaluated.

2.3.1.1 IgG-FITC Study - Cavitation detection

In the first IgG study, the acoustic emission originating from within the drug formulation and skin were isolated as described in section 2.2.4. The acoustic emission spectrograms were characterised and presented in Figure 2.7.

In Figure 2.7(a) it can be observed that insonating the gel formulation without any NCs ('Anagel® + IgG' group) caused only sporadic acoustic emissions (detected as light blue bands) perhaps due to the gas entrapped in the formulation. In the presence of NCs but the absence of IgG (Figure 2.7(b)), stronger broadband acoustic emissions (red bands) were observed in the first 100 seconds before the signal depleted. The presence of broadband emissions (wide frequency spectrum) indicates the occurrence of inertial cavitation. Similar acoustic emission spectrograms were observed for the treatment group containing Anagel®, IgG and NCs (Figure 2.7(d)). Notably, when Anagel® was replaced by water (Figure 2.7(c)), sustained broadband acoustic emissions were detected over the total five-minutes exposure. These results indicate that the presence of Anagel® in the formulation may suppress the NC activity. The influence of the recorded acoustic emissions on the dermal IgG-FITC delivery will be described in the next section.

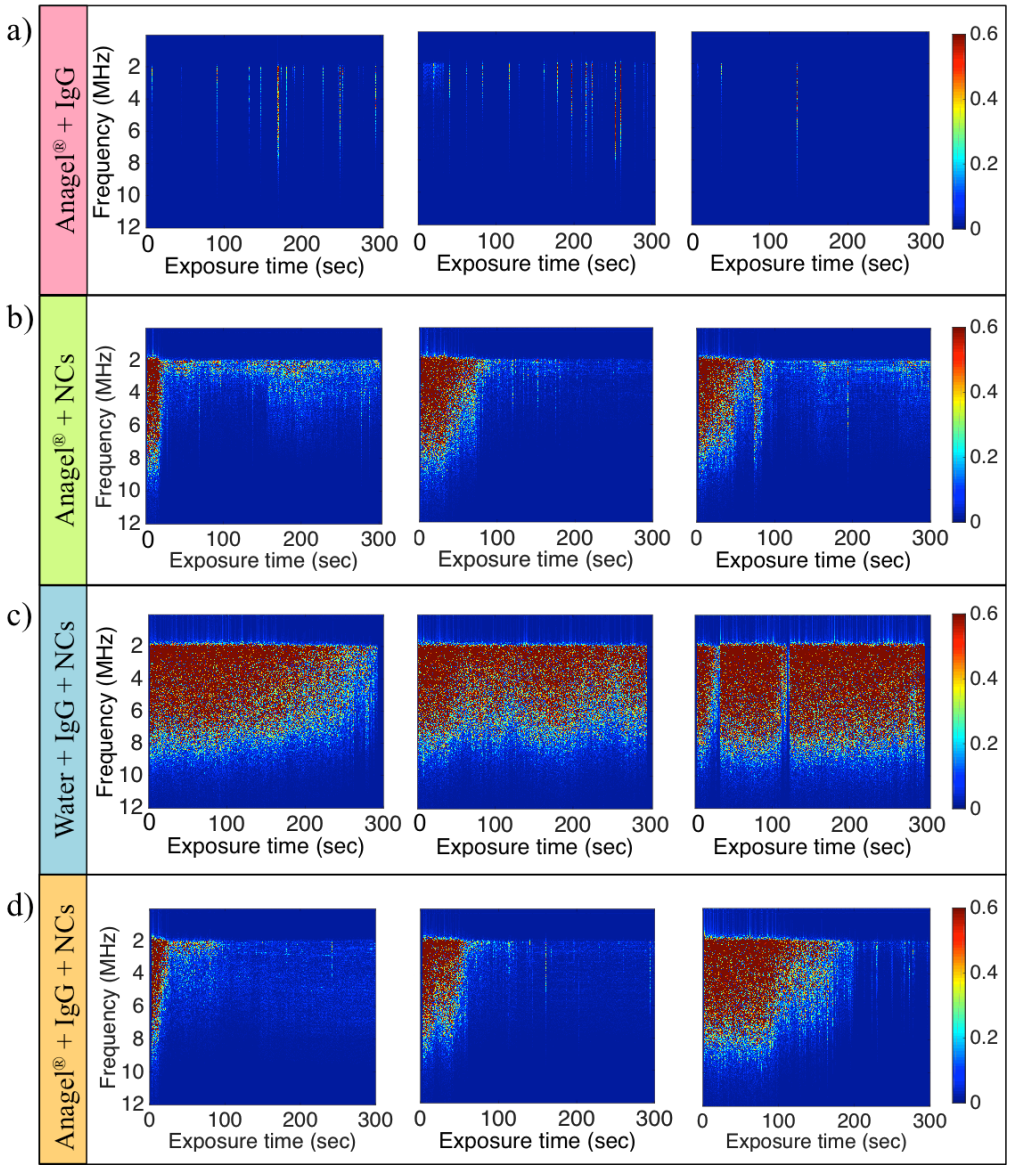

Figure 2.7: Acoustic emission spectrograms from formulation exposed to 1.0 MPa acoustic pressure – IgG-FITC Study. The acoustic emissions were recorded for the formulation containing (a) Anagel® + IgG, (b) Anagel® + NCs, (c) water + IgG + NCs, and (d) Anagel® + IgG + NCs. The data from three repeat experiments for each condition are shown. In the absence of ultrasound no acoustic emissions were detected and therefore no acoustic spectrograms are presented for the 'No Ultrasound' group. The colour bar on the right axis represents the power spectral density (mV^2/Hz).

2.3.1.2 IgG-FITC Study - Dermal delivery

To investigate the amount of IgG-FITC delivered into the skin after treatment, the exposed skin samples were homogenised and analysed by ELISA (as described in section 2.2.6.6). The dermal results are presented in Figure 2.8.

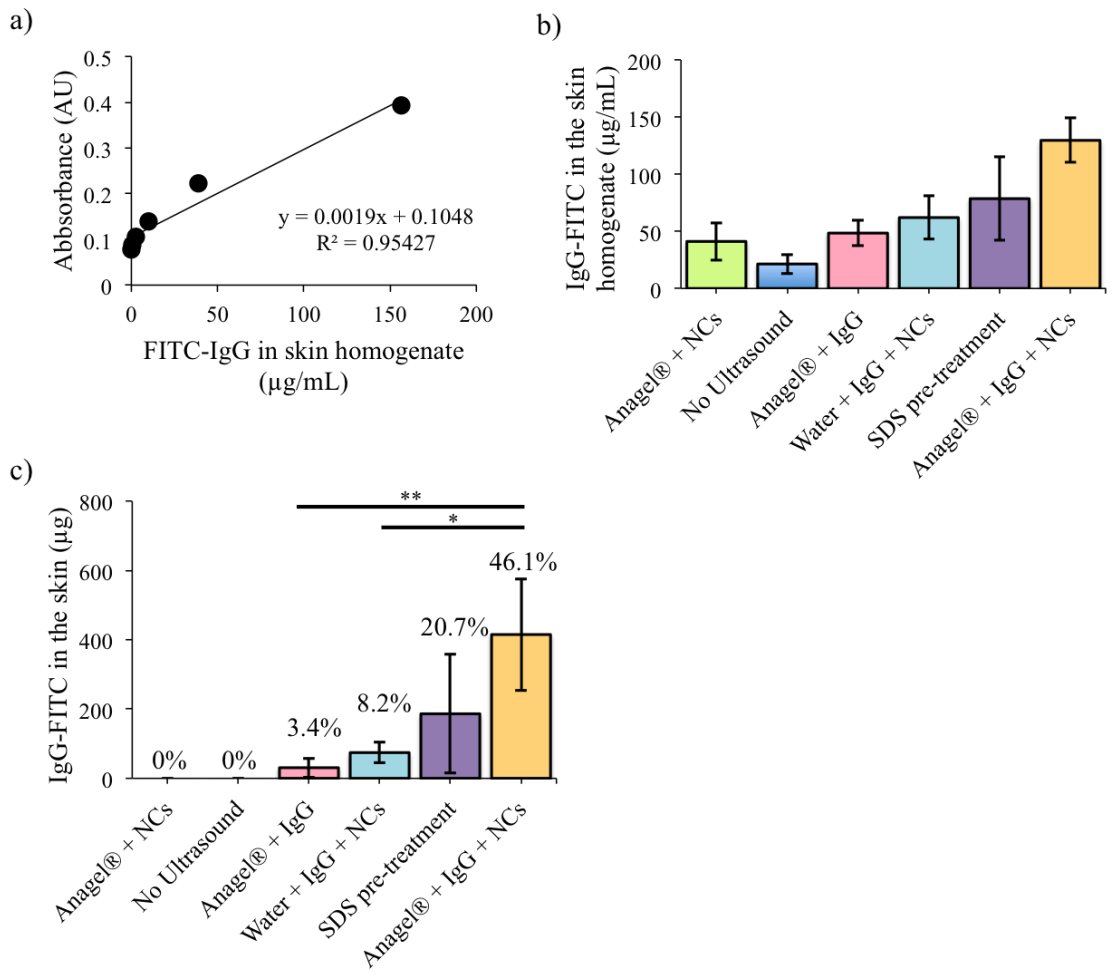

Figure 2.8: IgG-FITC delivery into the skin – IgG-FITC Study. The concentration of IgG-FITC in skin homogenate was calculated with the calibration curve presented in (a). Since the negative control group ('Anagel® + NCs') showed amounts of IgG-FITC present in the skin homogenate in panel (b), an extra background subtraction was performed. c) The delivered amount of IgG-FITC in the skin was calculated with formula 2.3, section 2.2.6.7. The percentage above the bars correspond to the IgG-FITC dose delivered in the skin (formula 2.4, section 2.2.6.7). The error bars in (b) and (c) represent the standard deviation for n=3 samples. The significant difference was determined by one-way ANOVA Bonferroni multiple comparison tests and *,** correspond to $p<0.05$ and $p<0.01$, respectively.

The absorbance values from the experimental samples were converted with the linear regression formula from the calibration curve (R^2 value of 0.954, Figure 2.8(a)) into IgG-FITC concentration present in the skin homogenate (Figure 2.8(b)). It was observed that in all the experimental samples IgG-FITC was present, including the IgG negative group 'Anagel® + NCs'. Therefore, an extra background subtraction was performed by removal of the IgG-FITC amount found in the skin homogenate from the 'Anagel® + NCs' group. Then, the total IgG amount delivered into the exposed skin was calculated for n=3 samples with formula 2.3 (section 2.2.6.7) and presented in Figure 2.8(c).

The dose delivery efficiency was determined with formula 2.4 (section 2.2.6.7) to give an indication on how efficient the drug delivery was on average per treatment and the percentages are presented above the bar chart in Figure 2.8(c). For one sample per treatment group, half the resected skin was used for the ELISA and the other half for histology, the total mass of the resected skin was used to determine the IgG dose in the skin, assuming homogeneous delivery throughout the resected skin sample.

Based on the bar chart in Figure 2.8(c), it can be observed that after exposing the skin to 'No Ultrasound', no IgG-FITC was recovered from the exposed skin. Higher delivery levels were found in the 'Anagel® + IgG' group (30.6 ± 27.8 μg IgG-FITC, corresponding to 3.4% of the 900 μg total applied dose), indicating ultrasound without cavitation may provide marginal benefit. In the absence of Anagel®, 74.2 ± 29.1 μg IgG-FITC (or 8.2% of the applied dose) was found present in the skin. SDS pre-treatment enhanced the delivery further to 186.2 ± 171.9 μg IgG-FITC (corresponding with 20.7% of the applied dose). Notably, substantial delivery levels of 414.9 ± 161.1 μg IgG-FITC (corresponding with 46.1% of the applied dose) were found in the skin after treatment with 'Anagel® + IgG + NCs'.

This high delivery efficiency achieved using inertial cavitation is unprecedented. Also, in previous work, extremely low efficiency (at best, nearly 1 μg, 0.04% of the applied dosage) was found when delivering a model vaccine into murine skin using cavitation-enhanced ultrasound during 90 seconds ultrasound exposure [151].

It is important to note that the ELISA was performed on skin homogenate containing two fluorescent dyes, FITC and Nile Red. When performing the ELISA, the colour

change made by the HPR reaction was determined by measuring the absorbance in the wells at 450 nm. By inspecting the excitation and emission spectra of these two fluorescent dyes Nile Red (Figure 2.9(a)) and FITC (Figure 2.9 (b)), it can be observed that at 450 nm both the fluorescent dyes absorb the light (indicated by the blue arrow in Figure 2.9). In case the fluorescently labelled IgG-FITC and/or the Nile Red NCs had stuck on the ELISA plate, it is possible that the measured absorbance values originated from the light absorbance by the HPR reaction and from the light absorbed by the present fluorescent dyes. Since the calibration curve was made of only IgG-FITC and not the Nile Red labelled NCs, the influence of the light absorbed by the Nile Red NCs in the experimental samples was neglected. This could explain the observation that the absorbance measured from the 'Anagel® + NCs' group was higher than the baseline.

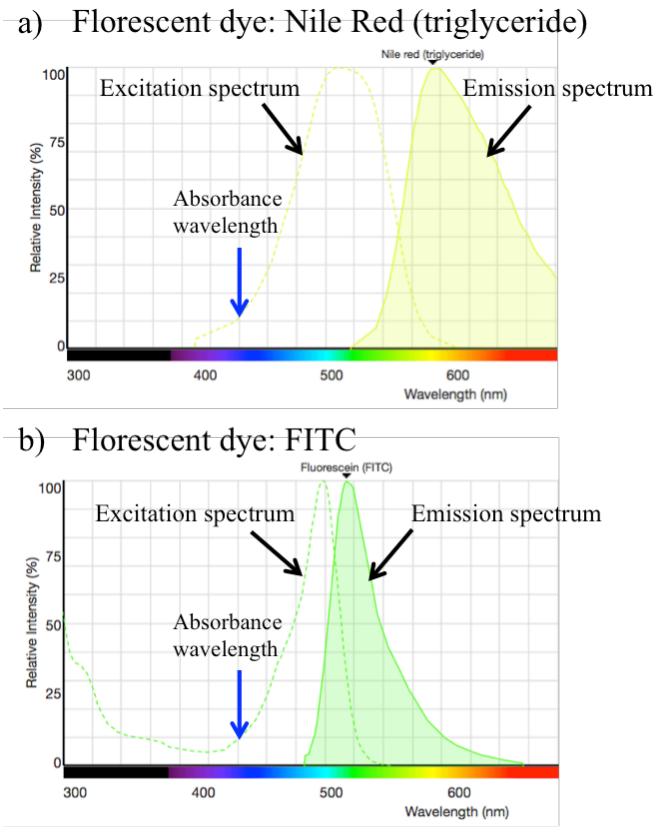

Figure 2.9: Excitation and emission spectra of the two fluorescent dyes a) Nile Red, and b) FITC. The blue arrow indicates the absorbance wavelength of the ELISA. Source: ThermoFisher Scientific Fluorescence SpectraViewer [171].

2.3.1.3 IgG-FITC Study – Localisation delivery by histology

To visually observe the position and depth of the deposition of fluorescently labelled IgG and NCs in the skin after treatment, histology was performed on half the resected skin of one porcine skin sample per experimental group. The other half of the resected skin was used to determine the IgG-FITC dose using ELISA. The bright field images and fluorescent images were overlaid as presented in Figure 2.10 with the bright field (blue), IgG-FITC (green), and Nile Red NCs (red). The images are orientated such that the SC is the uppermost layer of the skin and the ultrasound is being applied from the top of the images downwards. To correlate the calculated IgG-FITC dose with the fluorescent signal, the corresponding IgG dose for each sample is stated in Figure 2.10.

Figure 2.10(a) shows that after exposing the skin to the 'No Ultrasound' conditions, IgG-FITC and Nile Red labelled NCs were found to be co-localised only in the SC of the skin (coloured in orange, indicated by yellow arrow in Figure 2.10(a)). However, no IgG-FITC was found in this sample using the ELISA. In the absence of the Nile Red labelled NCs ('Anagel® + IgG', Figure 2.10(b)), IgG-FITC was found in the whole thickness of the epidermis.

Furthermore, Figure 2.10(c) shows that after treating the skin with 'Water + IgG + NCs', the red fluorescent signal from the NCs was only found locally in the uppermost layer of the epidermis (yellow arrow, Figure 2.10(c)) with a weak green signal from the IgG-FITC. Also, the SDS pre-treatment showed a band of the green fluorescent signal of the IgG-FITC at the uppermost layer of the epidermis with minimal penetration deeper into the epidermis.

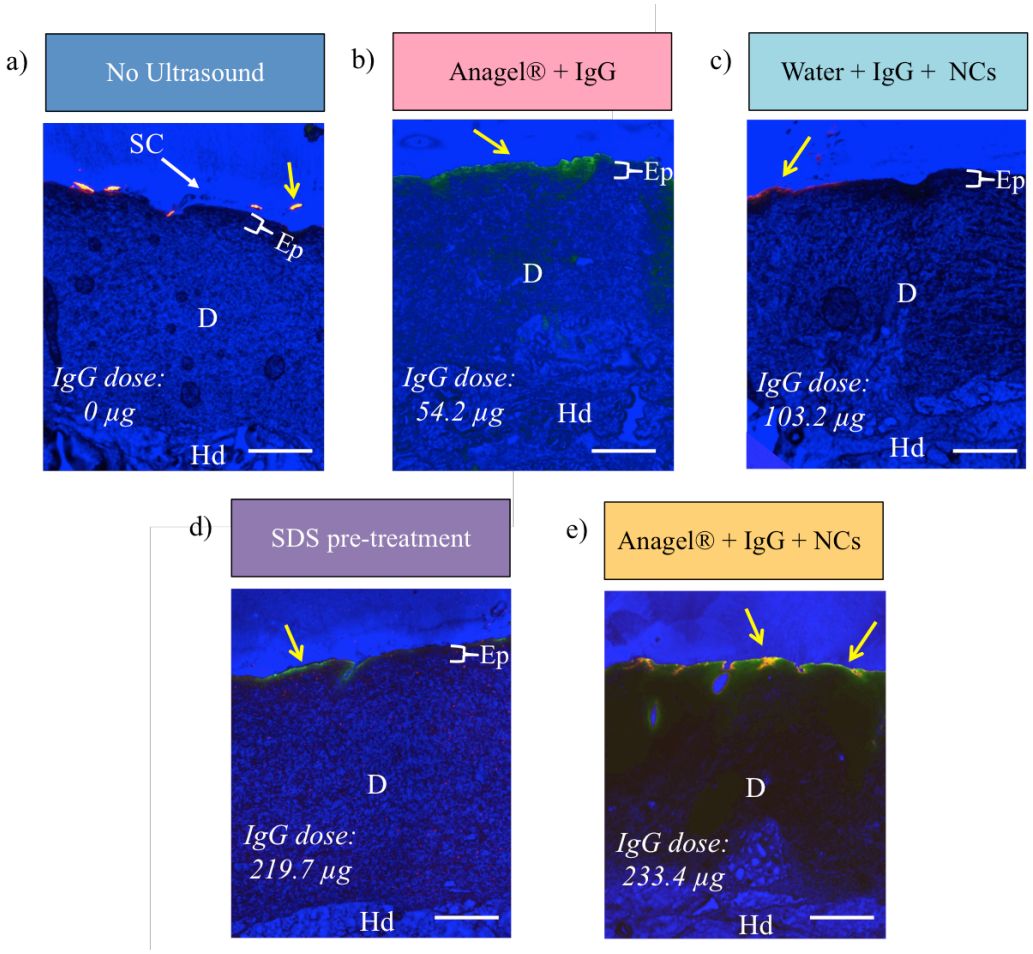

Figure 2.10: Representative co-registered histological sections of the fluorescent labelled IgG-FITC (green), and/or NCs (red) in the porcine skin after the specific treatment (n=1). The yellow arrows highlight the location of the fluorescent signal. a) and e) Co-localisation of IgG and NCs are observed as yellow. The direction of ultrasound is from top to bottom. Please note: the IgG dose indicates the amount of IgG-FITC in the skin determined by ELISA for this specific sample. The images illustrate the skin structure with SC = stratum corneum, Ep = Epidermis, D=dermis, Hp=hypodermis. The scale bar corresponds to 500 µm.

Following treatment of the skin with 'Anagel® + IgG + NCs', fluorescence from the IgG-FITC and Nile Red labelled NCs was found in the uppermost layer of the epidermis as well as deeper into the epidermis, with the co-localisation of IgG and NCs appearing orange in colour (indicated by yellow arrows, Figure 2.10(e)). However, the histology slice for this sample was thicker (20 µm thick) than the other samples (15 µm thick) to prevent tearing of the tissue section during slicing. As a result, the epidermis and the dermis appeared to be darker on the bright field image. No fluorescent signal was found deeper into the dermis or hypodermis.

The IgG-FITC dose found in the single samples of 'SDS pre-treatment' and 'Anagel® + IgG + NCs' was determined by ELISA to have corresponding dose deliveries of 219.7 μg and 233.4 μg IgG-FITC, respectively. Yet, the fluorescent intensity and the location of the fluorescent signal of IgG-FITC were noticeably different in the histology sections for these two samples (compare Figure 2.10(d) and (e)), with stronger and deeper penetration of IgG-FITC in the 'Anagel® + IgG + NCs' sample. This observation could suggest that the delivery may occur heterogeneously in the skin sample and that the observed delivery profile is dependent on the location of the histology section. The ELISA only determined the total amount of IgG found in the homogenised skin without providing information on the distribution of the delivery in the treated skin area. Therefore, it is recommended for further studies, ideally multiple histology sections at different locations of the treatment area would be taken to establish the delivery profile.

2.3.1.4 IgG-FITC Study - Conclusion

Based on these results, it was concluded that inertial cavitation is required to provide marked enhancement of the dermal delivery of IgG-FITC. However, the direct correlation between the level of acoustic emissions and the level of delivery was difficult to establish from these experimental data. This is because the highest level of broadband acoustic emissions was observed in water rather than Anagel® (Figure 2.7(c)), but the level of delivery was highest in the 'Anagel® + IgG + NCs' group (Figure 2.8(c)). This may reflect an advantage of using a viscous medium, which may provide a greater relative benefit than inertial cavitation levels. Notably, the 'Anagel® + IgG + NCs' group showed enhanced IgG-FITC delivery into the epidermis layer of the skin compared to the benchmark approach of applying a chemical penetration enhancer to disrupt the skin barrier and to facilitate dermal delivery to the uppermost part of the epidermis by passive diffusion. The average level shown with the chemical penetration

enhancer (186.2 ± 171.9 μg IgG-FITC, 20.7% of the applied dosage, (Figure 2.8(c))) substantially differs from previously reported levels (~300 ng, 0.013% of the applied dosage) [151].

Overall, the data in 'IgG-FITC Study' demonstrated that substantial delivery levels (414.9 ± 161.1 μg IgG-FITC, 46.1% of the applied dosage, (Figure 2.8(c))) of a large therapeutic agent can be achieved using inertial cavitation. However, it is clear that more data is required to define the acoustic emission and dose delivery relationship. The unprecedented high level of delivery achieved here requires repeat experiments to verify and validate these results, as described in the next section.

2.3.2 IgG Repeat Studies

In subsequent repeat experiments, greater emphasis was placed on the uniformity of skin preparation and processing of the skin prior to the ELISA. Furthermore, to remove concerns about the influence of fluorophores on the activity and detection of the components involved, an unlabelled alternative to IgG-FITC (i.e. anti-mouse IgG produced in rabbit), and unlabelled (i.e. no Nile Red) NCs were used. The three repeat studies described in this section were performed on three separate occasions, with n=3 each time and the cavitation and delivery data are presented below.

2.3.2.1 IgG Repeat Studies - Cavitation detection

The acoustic emissions originating from within the drug formulation and skin were isolated. The acoustic emission spectrograms were characterised for the experimental groups exposed to ultrasound and the results are presented in Figure 2.11 for the three experiments denoted as 'IgG Repeat Study 1', '2', or '3'. The corresponding TASE values are presented in Figure 2.11.

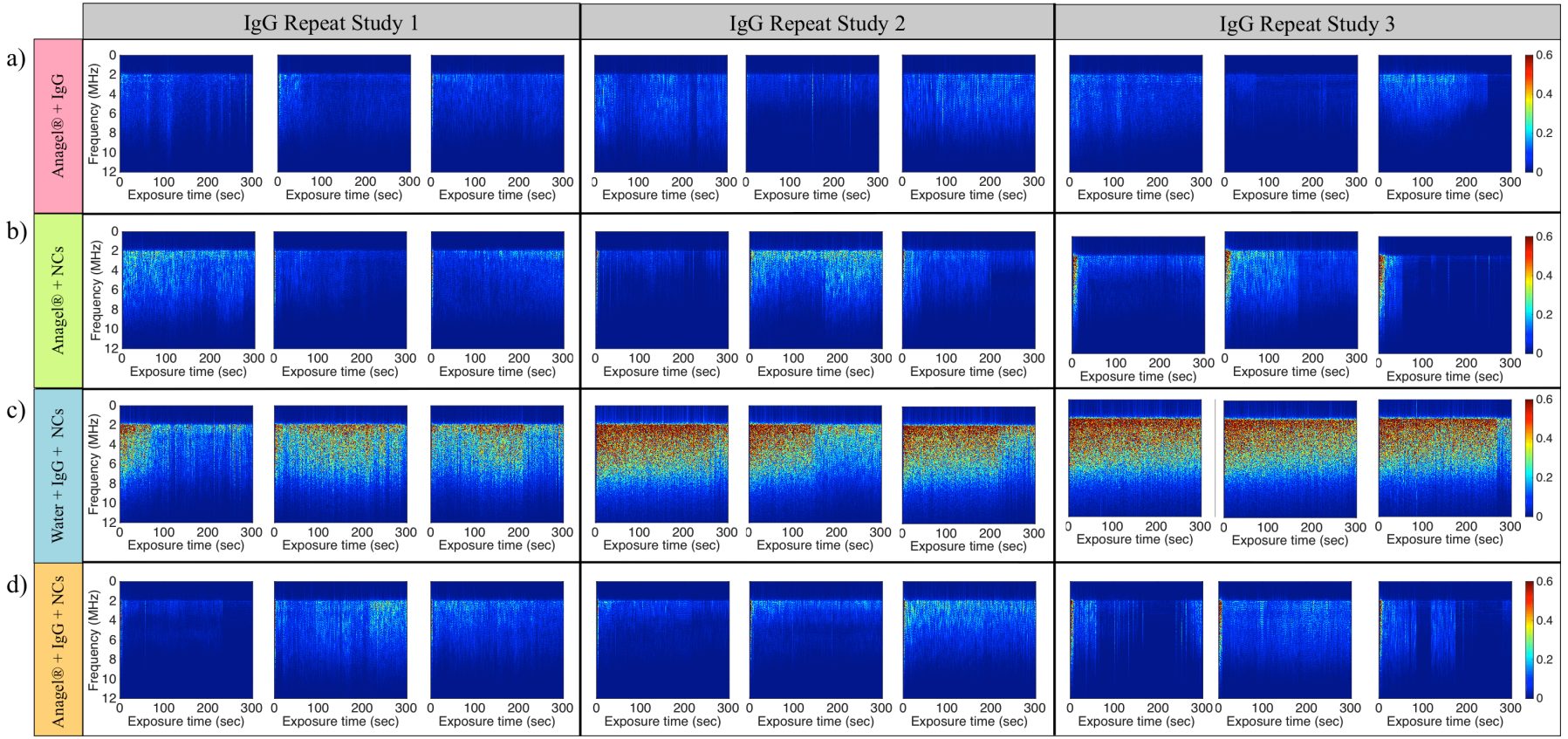

Figure 2.11: Acoustic emission spectrograms after insonation at 1.0 MPa of *ex vivo* IgG Repeat Study 1, 2, and 3. Four different formulations were tested in triplicate containing (a) Anagel® with IgG, (b) Anagel® + NCs, (c) Water with IgG and NCs, or (d) Anagel® with IgG and NCs. The colour bar on the right axis represents the power spectral density (mV^2/Hz).

Figure 2.11(a) shows that without the presence of NCs in the gel formulation, only sporadic acoustic emissions (light blue bands) were detected in all the three repeat studies. Without the presence of IgG (Figure 2.11(b)), slightly stronger broadband acoustic emissions (light blue/green bands), and spectrograms very similar to the spectrograms from the 'Anagel® + IgG' group (Figure 2.11(a)), were observed. In the absence of Anagel® ('Water + IgG + NCs', Figure 2.11(c)), strong broadband acoustic emissions (red bands) were detected over the total exposure time in 'IgG Repeat Study 2' and '3', and red/green bands in 'IgG Repeat Study 1'.

The acoustic emission spectrograms obtained from the 'Anagel® + IgG + NCs' group (Figure 2.11(d)) showed for all the three repeat studies low broadband emissions (light blue bands). These spectrograms were similar to the 'Anagel® + NCs' group (Figure 2.11(b)). In accordance with the 'IgG-FITC Study', these data indicate that seeding the formulation with NCs can provide a means of producing sustained levels of cavitation upon insonation. Yet, the use of Anagel® can reduce the acoustic activity. This may be the result of the presence of surfactants in the Anagel® that reduce the surface tension at the liquid-gas interface that may lead to the dissolution of the gas bubble in the NC crevice.

To quantify the acoustic emissions recorded during the three 'IgG Repeat Studies', the TASE value was calculated for each acoustic emission spectrogram and presented in the bar chart in Figure 2.11.

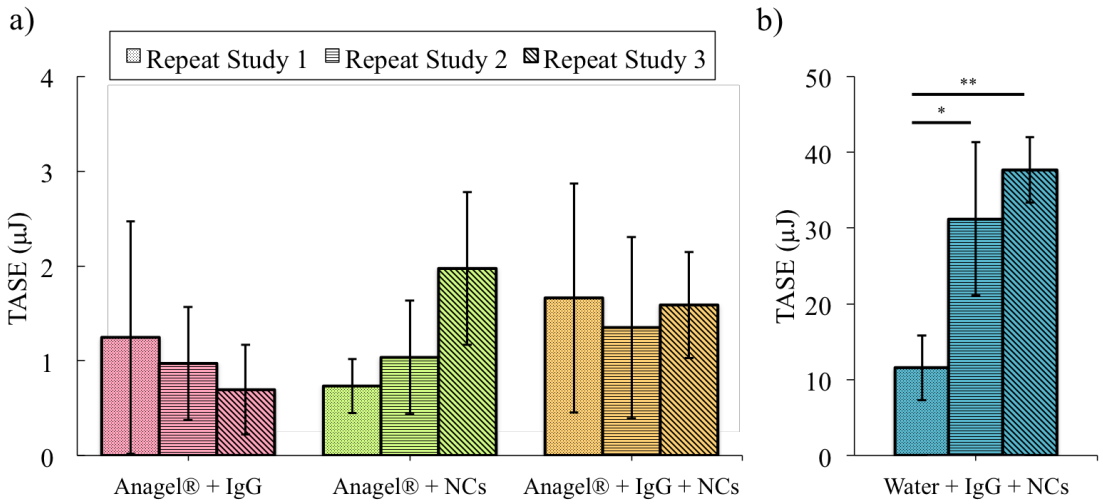

Figure 2.11: The bar chart showing the mean energy of acoustic emissions detected per experimental group for the three 'IgG Repeat Studies'. Since the total acoustic sensor energies (TASE) were substantially higher in the in the absence of Anagel®, the energies of the 'Water + IgG + NCs' group are presented in a separate bar chart (b) from the experimental groups (a) 'Anagel® + IgG', 'Anagel® + NCs', and 'Anagel® + IgG + NCs'. The error bars represent the standard deviation for n=3 samples. The significant difference was determined by one-way ANOVA Bonferroni multiple comparison tests and *,**, correspond to $p<0.05$ and $p<0.01$, respectively.

In Figure 2.11(a) it can be seen that the calculated acoustic emission energies were similar for 'Anagel® + IgG', 'Anagel® + NCs', and 'Anagel® + IgG + NCs' groups, regardless of the study number. No significant difference ($p>0.05$) was found between and within these three experimental groups. The data in Figure 2.11(a) showed that even in the absence of NCs (i.e. 'Anagel® + IgG' group) similar acoustic emission levels were detected, in contrast to earlier results (see Figure 2.5 and Figure 2.6). The gel formulation used for the Anagel® characterisation (Figure 2.5) and the NC concentration optimisation (Figure 2.6) did not contain any therapeutic agent such as IgG. It could be possible that the addition of IgG to the Anagel® reduced the gas content of the formulation.

Without the presence of Anagel® (Figure 2.11(b)), substantial (more than five-fold) TASE values were calculated. This agrees with the findings in the 'IgG-FITC Study' (Figure 2.7(c)). It is also apparent that the removal of Anagel® has led to greater

inter-experiment variability leading to higher but less reproducible values of TASE. Indeed, the NCs batch in 'IgG Repeat Study 2' and '3' induced significantly ($p<0.05$) higher energies (31.2 ± 10.1 μJ and 37.7 ± 4.3 μJ, respectively) than the NCs batch from 'IgG Repeat Study 1' (11.6 ± 4.3 μJ). Furthermore, the TASE values calculated for 'IgG Repeat Study 2' and '3' in the 'Water + IgG + NCs' group were significantly ($p<0.0001$) higher than all the energies recorded for the samples in Figure 2.11(a)).

2.3.2.2 IgG Repeat Studies – Dermal delivery of IgG

In this section, the dermal delivery of IgG was investigated. The homogenised skin samples were analysed by ELISA. The calibration curves for 'IgG Repeat Study 1', '2', and '3' are shown in Figure 2.12(a-c), respectively. These calibration curves were used to calculate the total IgG amount delivered into the exposed skin as well as the dose delivery efficiency (see section 2.2.6.7). In 'IgG Repeat Study 2' and '3' the calibration curves had improved R^2 values compared to the 'IgG-FITC Study', and no additional background subtraction was required in any of the repeat studies. The dermal results of the three 'IgG Repeat Studies' are presented in Figure 2.12(d) and the percentages above the bar chart represent the mean proportion of the applied IgG dose (total dosage: 900 μg IgG) delivered into the skin after the treatment.

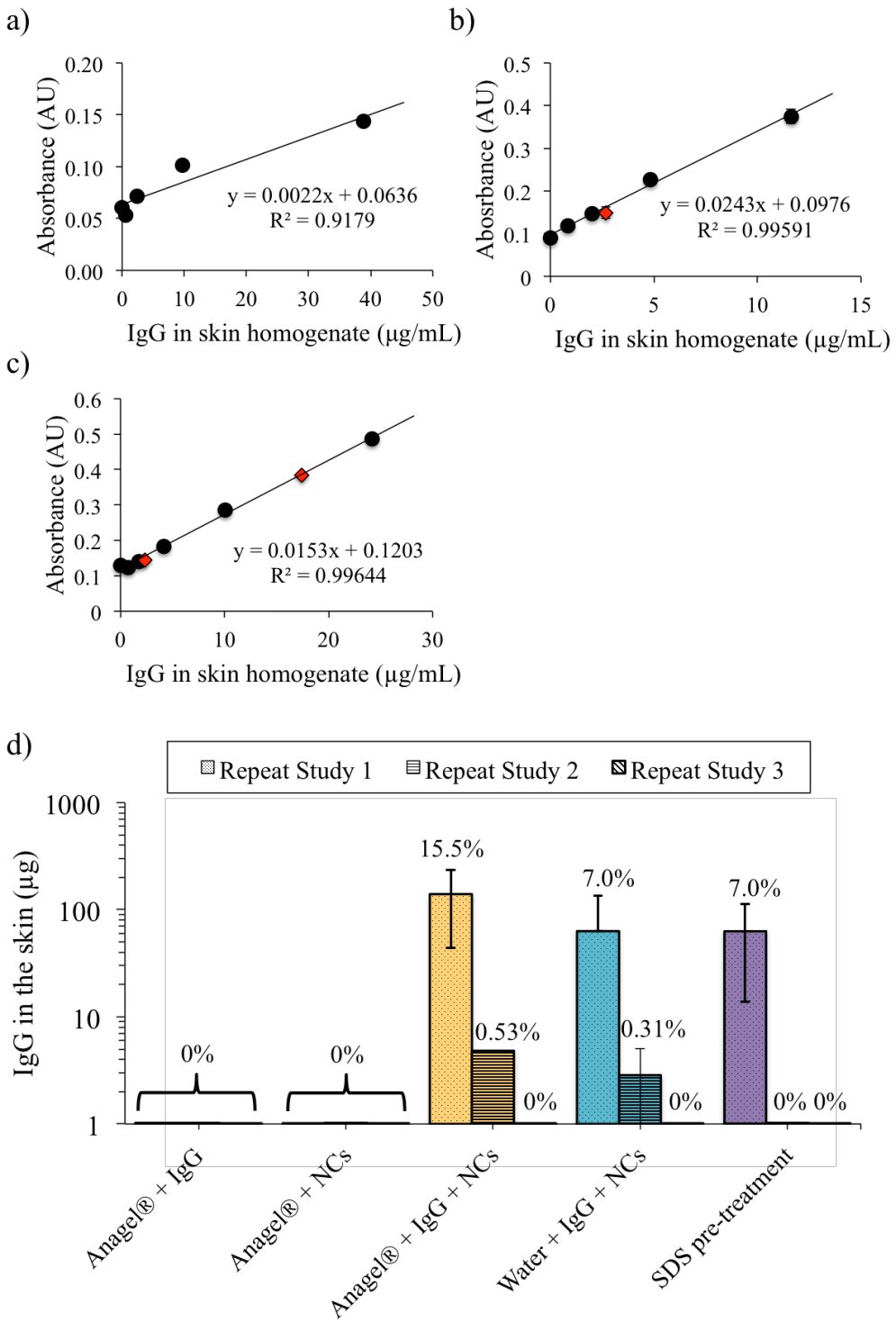

Figure 2.12: IgG delivery into the skin – IgG Repeat Studies 1-3. Bar chart showing the mean delivered IgG dose in the skin. The percentage values shown above the bars represent the mean proportion of the 900 µg applied IgG dose delivered into the skin after the specific treatment. The error bars represent the standard deviation for n=3 samples. One out of three skin samples from the 'Anagel® + IgG + NCs' in 'Repeat Study 2' showed the presence of IgG in the skin and this single delivery is shown. No significant difference was found ($p>0.05$).

In ‘IgG Repeat Study 1’, the calibration curve was prepared with lower IgG concentrations in skin homogenate in comparison to the calibration curve made in the ‘IgG-FITC Study’ (compare Figure 2.8(a) and Figure 2.12(a)). This was done to obtain a better fit of the linear regression curve to the data points at lower IgG concentrations in the skin homogenate. Although R^2>0.9 in Figure 2.12(a), the slope of the curve is very shallow and slight changes in the absorbance value can have a large influence on the IgG concentration calculated to be in the skin homogenate. As previously seen in Figure 2.8(a), there appears to be a loss of linearity at higher IgG concentrations.

In the first repeat study, three out of the six experimental groups had detectable IgG levels in the skin as shown in Figure 2.12(d). The highest dermal delivery was found after treating the skin samples with ‘Anagel®+ IgG + NCs’ (139.65 ± 95.67 µg IgG, 15.5% of the applied dose), which was almost three-fold lower than the IgG-FITC amount found for the same group in the ‘IgG-FITC Study’ (Figure 2.8(b)). In absence of Anagel®, strong sustained broadband emissions were detected (‘Water + IgG + NCs’, Figure 2.11(b)) and 63.04 ± 62.90 µg of IgG was found to be present in the exposed skin. Performing an SDS pre-treatment on the skin also enhanced the delivery of IgG into the skin and reached similar levels of 63.19 ± 49.36 µg of IgG (corresponding to 7.0% of the applied dose). This IgG level was almost three-fold lower than found in the same group in the ‘IgG-FITC Study’.

In ‘IgG Repeat Study 2’ several steps were taken to improve the ELISA assay procedure and to reduce the error at higher concentrations evident in ‘IgG-FITC Study’ and ‘IgG Repeat Study 1’. The calibration curve in ‘IgG Repeat Study 2’ (see Figure 2.12(b)) was improved by incorporating a positive control sample by spiking

non-treated skin with a known amount of IgG before homogenising the skin. The positive control sample was added to the calibration curve to validate the accuracy of the calibration curve.

Further adjustments were made to the ELISA protocol, including the extension of the incubation time of the IgG in the experimental and calibration samples on the ELISA plate from 1.5 hours to overnight incubation. In addition, the HRP reaction was continually monitored and stopped after one hour rather than 10 minutes to enable optimal detection of low IgG concentrations. As a result, it can be observed in Figure 2.12(b) that the linear regression curve fits the calibration data points well ($R^2 = 0.996$), and at higher concentrations the data points do not saturate or bend off the linear regression curve. Furthermore, the positive control sample (2.68 μg/mL IgG in skin homogenate, red diamante in Figure 2.12(b)) fits the linear regression accurately, which gave a calculated value of 2.41 μg/mL IgG. The experimental data points were within the linear range of the calibration curve and all together, the IgG concentration in the experimental skin homogenates can be predicted from the measured absorbance values with more confidence than in previous 'IgG-FITC Study' (Figure 2.8(a)) and 'IgG Repeat Study 1' (Figure 2.12(a)).

In 'IgG Repeat Study 2' successful delivery was found in only two out of the six experimental groups (Figure 2.12(d)). All the three treated skin samples from the 'Water + IgG + NCs' group showed IgG delivery with a total delivery of 2.84 ± 2.17 μg IgG. This was substantially less (over 26-fold) than found in 'IgG-FITC Study' and 'IgG Repeat Study 1' (over 22-fold). Treating the skin samples with 'Anagel®+ IgG + NCs' gave delivery of IgG (4.82 μg IgG) in only one out of three skin samples,

which was at a substantially lower level than the results obtained in 'IgG-FITC Study' (more than 86-fold) and 'IgG Repeat Study 1' (almost 30-fold).

The third repeat study was performed with the optimised ELISA protocol from 'IgG Repeat Study 2' and the obtained calibration curve is presented in Figure 2.12(c) and contains two positive control samples (red diamonds in Figure 2.12(c)). It can be observed that the two positive control samples (2.32 and 17.40 μg/mL IgG in skin homogenate) fit the linear regression curve (R^2 = 0.996) accurately, which gave a calculated value of 2.00 and 17.25 μg/mL, respectively. With the linear regression formula from Figure 2.12(c), no detectable IgG levels were found in any of the six experimental groups as indicated by the 0% in Figure 2.12(d).

Due to high intra-replicate and inter-experiment variability in Figure 2.12, no significant difference ($p>0.05$) was found between the repeat studies and within the experimental groups. Analysis of the acoustic emission recorded in this study ('IgG Repeat Study 3', Figure 2.11) showed similar energies calculated for the groups 'Anagel® + IgG', 'Anagel® + NCs', and 'Anagel® + IgG + NCs'. Stronger broadband acoustic emissions (37.68 ± 4.32 μJ) were recorded in the experimental group 'Water + IgG + NCs'. The same pattern was observed in the other two repeat studies ('IgG Repeat Study 1' and '2', Figure 2.11). However, the IgG levels delivered into the skin samples were inconsistent and dramatically different between the repeat studies. In addition, these repeat studies did not support the high delivery results found in 'IgG-FITC Study'. Also, in contradiction to a previous study [149], these four IgG studies did not demonstrate that ultrasound-mediated cavitation has a significantly enhanced transdermal delivery effect over SDS pre-treatment.

2.4 Conclusions and Discussion

Ex vivo skin models are required to validate and optimise cavitation-mediated delivery before it can be tested *in vivo*. Excised pig skin offers a potential model for such testing as it is readily available, inexpensive and a physiologically relevant mimic for the skin of living mice and humans. The experiments in this chapter were designed to assess the suitability of pig skin as a model system to develop transdermal delivery technologies. An initial study ('IgG-FITC Study') was performed to establish the exposure setup and conditions and validate the detection method (ELISA) by which delivery could be quantified. With this protocol refined and standardised, it was then repeated on three separate occasions to assess the reproducibility.

The 'IgG-FITC Study' highlighted the changes that needed to be made to the size of the formulation holder, the coupling hydrogel used, and the NCs concentration in the formulation. This study also helped to build evidence for the link between the detection of inertial cavitation and the recovery of substantial amounts of IgG dose from the skin. The ELISA results showed that 46.1% of the applied dose was delivered into the porcine skin when insonating a gel formulation with IgG and NCs. This level of delivery far exceeded expectations and previous reports [151, 172]. Methods to refine and validate the calibration curves and to improve sample handling were therefore introduced before investigating the reproducibility of the results by repeating the *ex vivo* experiment three more times.

In all three repeat experiments, when no cavitation was instigated (i.e. no NCs were included) there was no detectable IgG delivery. In contrast, IgG delivery was evident in both repeat studies '1' and '2' whenever cavitation was detected.

However, the dermal delivery levels were not consistent and showed widely different results, with 'IgG Repeat Study 1' showing up to 15.5% dose delivered, 'IgG Repeat Study 2' showing up to 0.53%, and 'IgG Repeat Study 3' showing no detectable IgG delivery in any skin sample. Notably, the acoustic emission energies calculated for the 'Anagel® + IgG' and 'Anagel® + IgG + NCs' were similar (Figure 2.11(a)), but the dermal delivery profiles were remarkably different.

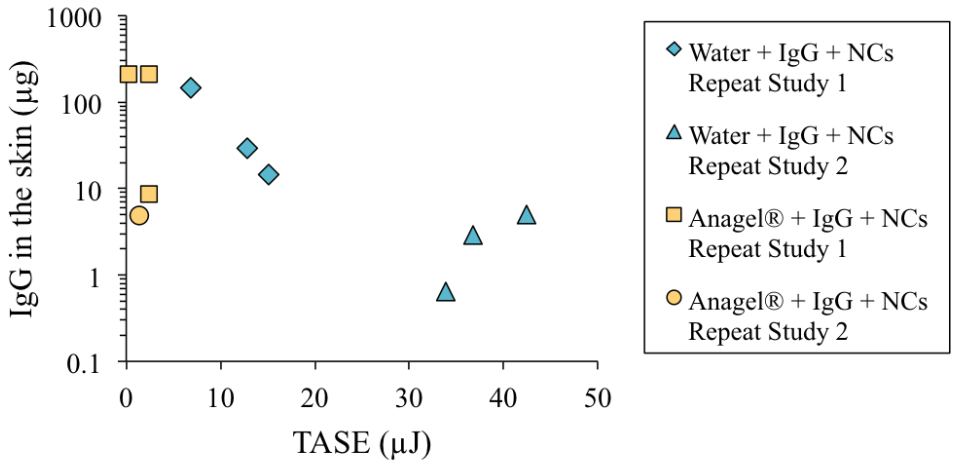

Figure 2.13: Plot of the relationship between the calculated TASE value per sample by passive monitoring and the delivered IgG into the skin. Only the experimental samples are shown that had detectable IgG levels in the skin in 'IgG Repeat Study 1' and '2'.

Indeed, when attempting to correlate the level of cavitation (TASE) with delivery achieved for each individual sample (see Figure 2.13) that contained detectable levels of IgG, it can be seen that there is a high intra-replicate and inter-experiment variability, with little obvious correlation evident. The source of this variability and lack of reproducibility in delivery could be due to several factors, which will be addressed in the following sections.

2.4.1 Cavitation activity

The first possibility is that variability in delivery was a consequence of variability in the levels of cavitation achieved. In the 'IgG Repeat Studies', the recorded acoustic emission showed a consistent pattern between sample groups (Figure 2.11).

Specifically, similar acoustic emission energies were determined for 'Anagel® + IgG', 'Anagel® + NCs', and 'Anagel® + IgG + NCs' and stronger broadband acoustic emissions were recorded in the absence of Anagel® in the experimental group 'Water + IgG + NCs'.

However, although in general, the calculated TASE values within and between groups were similar within each study (producing an order of 'Water + IgG + NCs' > 'Anagel® + IgG + NCs' > 'Anagel® + NCs' > 'Anagel® + IgG'), it was clear that the overall levels obtained in 'IgG Repeat Study 1' were lower than in repeat studies 2 and 3 (see Figure 2.11). This could be a consequence of variation in the source of fabricated NC batches. Although the NCs in every small-scale fabricated batch were characterised on the basis of their shape and size (as described in section 2.2.3), the depth of the depression of the cup cavity could be a crucial determinant of the amount of gas entrapped on the NCs, and therefore its response [162]. Furthermore, the NCs solution may also contain particles that were less or not acoustic active due to the presence of multiple depressions, spheres, or residual contaminating beads. Therefore, determining the NCs concentration based on their dried-weight information did not provide information about the actual amount of 'active' NCs present in the solution. Consequently, improvement is required for the NC fabrication and characterisation. In further studies, NC supply was changed to OxSonics Ltd., which provided large-scale process-validated batches. Such steps should improve the study-to-study variation in cavitation response and therefore decrease the variation in delivery.

2.4.2 Method of detection

The second potential source of variation could be inaccuracies during measurement. The accuracy of ELISA methods is dependent on being able to establish a linear

calibration curve with a dynamic range covering the range of the readings produced by the samples. It is notable that refinements to the ELISA protocol enhanced the linearity and R^2 value of the calibration curves in 'IgG Repeat Study 2' and '3'. As a result, the calibration curve fitted the data points well in both repeat studies and the obtained calibration curves had similar gradients and intercepts to each other (demonstrating the reproducibility of the detection process).

A further requirement of an accurate ELISA is to match the components and processing of the calibration curve as closely as possible to that of the experimental samples. However, this was unfeasible in these experiments, as it would have required four different calibration curves for every experiment. This would have meant too much tissue processing and leaving insufficient wells on each ELISA plate to run all the samples at the same time. As an alternative, a calibration curve was established in homogenised skin and then validated with two 'positive control samples'. These 'positive control samples' were known amounts of IgG spiked into the skin and then processed and measured in the exact same way as the 'unknown' experimental samples. Back-calculation of the absorbance values obtained from the 'positive control samples' using the calibration curve gave IgG values which very closely matched (within 10% margin) the amount spiked into these 'positive control samples' at the start. Hence, although the accuracy of the ELISA protocol was initially a cause for concern, the good R^2 values, reproducibility across 'IgG Repeat Study 2' and '3', and successful positive control validation make it unlikely that the highly variable delivery results are simply an artefact of a failure to accurately measure the output of the delivery by ELISA.

In addition, the labour-intensive skin homogenisation process could also be an additional source of variation, where slight variations occur due to inconsistent homogenisation of the skin samples, loss of small sample volumes, and the presence of variable amounts of skin debris in the sample when added to the ELISA plate.

Overall, it is clear that the methodology has weaknesses relating to its time and labour intensive nature, and also the difficulty in precisely matching calibration curves to all the experimental groups being evaluated. For these reasons, in the further research, ELISA is replaced by High Performance Liquid Chromatography (HPLC).

2.4.3 Ex vivo skin model

The third possible source of variation in the level of delivery between studies is the porcine skin itself. For every experiment, a large area of the abdomen was obtained from the abattoir and the full-thickness skin was prepared. Due to the time between the repeat experiments, the skin was obtained from different pigs. Consequently, there was variability in the harvested skin due to the age of the pig, the location of the skin area excised, the living environment of the pig, as well as the fat composition underneath the skin. In particular, the skin thickness varies considerably on the abdomen, where the skin is very thin near the nipple and thicker towards the spine. The thickness and integrity of the SC and the dermal layer have a direct and crucial impact on the ease in which drug molecules can penetrate the skin [7-9]. Inconsistency in the skin samples would therefore be expected to have a considerable negative influence on the reproducibility of the experiments. In addition, the *ex vivo* skin samples do not have a working blood circulation to mimic the human skin. The difficulties faced in obtaining pig skin with a uniformity of thickness and integrity and the other weaknesses of this model led to future experiments being performed *in vivo* using murine models.

2.5 Summary

The work reported in this chapter aimed to investigate the utility of a pig skin as a model for testing the reproducibility of cavitation-mediated transdermal transport of a large therapeutic agent (IgG). Certain formulation conditions were refined in an attempt to reduce the intra-replicate and inter-experiment variability between formulation batches (replacing Carbopol® with ready-to-use Angel®, and optimising NC concentration). However, despite considerable improvements to the methodologies employed through successive studies, the levels of IgG dose delivered into the pig skin were not consistent between the four *ex vivo* studies and showed widely different results (from 46.1% dose delivery efficiency to 0% delivery). In contradiction to a previous study [149], these four IgG studies did not demonstrate that ultrasound-mediated cavitation has a significantly enhanced transdermal delivery effect over SDS pre-treatment. Variability in the uniformity of thickness and integrity of the obtained pig skin, the level of cavitation, and the method of IgG detection were addressed as important factors that influenced the reproducibility of the delivery results. Further testing clearly required a more robust/reliable test and assay system to further identify the (in)dependent parameters that influence the consistency of the results. Indeed, to move this work forward it was clear that several challenges needed to be met:

1) To validate and standardise a more reliable method of detection of the therapeutic agent in the skin.
2) To perform testing using a vascularised skin model with reproducible skin thicknesses (i.e. *in vivo* studies).
3) To increase the reproducibility of NC activity by using larger NCs batches produced at scale to GMP by OxSonics Ltd. (Oxford, United Kingdom).

Chapter 3: *In vivo* cavitation-enhanced transdermal delivery of Sumatriptan

3.1 Introduction

In the previous chapter, *ex vivo* experiments were performed with a large therapeutic agent (IgG). The levels of IgG dose delivered into the skin samples were not consistent and showed widely different results ranging from detecting a substantial amount of 46.1% of the applied dose in the porcine skin after insonating a gel formulation with IgG and NCs for five minutes, to no detectable IgG levels in one of the repeat studies. The large differences in the doses delivered were believed to be dependent on several factors, including variability in the uniformity of thickness and integrity of the obtained pig skin, the level of cavitation, and the method of IgG detection.

To address the challenges found in Chapter 2, it was expedient to set up a more reliable system and to take the opportunity of studying the uptake of the therapeutic agent into the circulation as a clinical endpoint in addition to just a skin extraction endpoint as seen in Chapter 2. Therefore, *in vivo* studies were performed using mice, which were kept under standardised and controlled living environments in accordance with Home Office Legislation and Oxford University Gold Standard requirements. Care was taken in the *in vivo* studies to expose the same skin region in all mice and pre-treat the mice and skin in the same way. Furthermore, NCs produced at industrial scale were obtained from OxSonics Ltd. (Oxford, United Kingdom) instead of being prepared in small lab-scale batches to reduce the variability in cavitation activity between experiments.

In addition, a small hydrophilic therapeutic agent against migraine (Sumatriptan, 413 Da) was chosen. Sumatriptan is a highly soluble in water (water solubility at 20°C is 101 mg/mL [173]), and the partition coefficient in n-octanol/water is log P = 0.74 at pH 7.4 [174]). This means that Sumatriptan cannot easily cross the highly lipophilic layer of the SC by diffusion alone. However, in the literature, Sumatriptan is a well-studied and validated therapeutic agent to be delivered across the skin in the presence of active enhancement techniques [182-184]. Also, Sumatriptan is an easily measurable drug to allow selective separation and detection by a validated and standardised technique called High Performance Liquid Chromatography (HPLC).

Unfortunately, Sumatriptan in combination with the Anagel® lead to the formulation of macroscopic aggregations, and therefore these experiments are performed in water rather than in Anagel®. With all the adjustments in place, this chapter aims to investigate *in vivo* the feasibility and reproducibility of transdermal delivery of Sumatriptan by cavitation-enhanced transport.

3.1.1 Migraine

Migraine is a common condition that affects an estimated one in every seven adults worldwide [175]. Most commonly, migraine begins at puberty and mostly affects adults between the age of 35 and 45 years [176]. Migraine is unique from other headache disorders and is diagnosed as recurrent and characterised by episodic attacks. Attacks are associated with severe pain, nausea, vomiting, and/or sensitivity to light and sound [177], and may last from a couple of hours to up to 2-3 days [176]. In some cases, the migraine attack is preceded by an aura, which consists of fully reversible visual, sensory, or linguistic symptoms [178].

Migraine headaches are the result of dilatation of the blood vessels in the head. A drug commonly used to treat migraines is Sumatriptan (3-[2-(dimethylamino)ethyl]-N-methyl-indole-5-methanesulfonamide), a 5HT1-receptor agonist [179]. Triptans work by binding agonistically to serotonin receptors, primarily to the $5HT_{1B}$ and $5\text{-}HT_{1D}$ receptors, present in the intracranial blood vessels and the trigeminal nerve fibres, respectively [180]. By acting as an agonist on these receptors, they instigate vasoconstriction and the vascular inflammation is reduced, relieving the migraine symptoms [179]. Clinical trials have demonstrated that early intervention with Sumatriptan blocks the development of central sensitisation [181], thereby emphasising the benefit of the patient taking the medication as soon as the symptoms arise.

3.1.2 Sumatriptan administration routes

Sumatriptan (413 Da) is commercially available in four different delivery forms: oral tablets (25, 50, and 100 mg), s.c. injection (6 mg/0.5 mL), nasal spray (10 or 20 mg/activation) [182], and suppositories (25 mg) [183]. Furthermore, buccal tablets (35 mg) are currently under development [184-186]. One of the primary issues with oral delivery is that patients who suffer from gastrointestinal symptoms postpone or even avoid taking oral medication for migraine attacks [187]. Furthermore, the gastrointestinal dysfunction results in a delay in the absorption into the bloodstream and causes lower bioavailability (in some case just 15%) [173]. Although s.c. injection has a much higher bioavailability (97%) [188], this painful and invasive method causes tissue damage and triggers numerous adverse events [188]. The nasal delivery formulation has the advantage that the onset of action is faster than by oral tablet, but the taste is unpleasant and the bioavailability is similar to oral Sumatriptan (17%) [182]. Therefore, the need to develop a non-oral and non-invasive delivery system to treat a migraine is essential for more rapid and consistent pain relief.

Without any intervention, molecules which are larger than 500 Da or strongly hydrophilic cannot cross the SC. Disruption or perturbation of the SC can help to improve the drug delivery of the hydrophilic Sumatriptan into the skin.

Currently, the use of microneedles [189, 190], and iontophoresis [191] are under investigation for delivering triptans transdermally. Even so, in January 2013, the FDA (U.S. Food & Drug Administration) approved an iontophoretic Sumatriptan transdermal patch (Zecuity®, Teva Pharmaceuticals Industry Ltd, Israel). The transdermal system is designed for patient self-administration to the upper arm or thigh. A low electrical current is used to deliver up to 6.5 mg of Sumatriptan over four hours non-invasively through the skin into the bloodstream [191]. Unfortunately, due to serious application site reactions, the patch was withdrawn from the market in June 2016 [192].

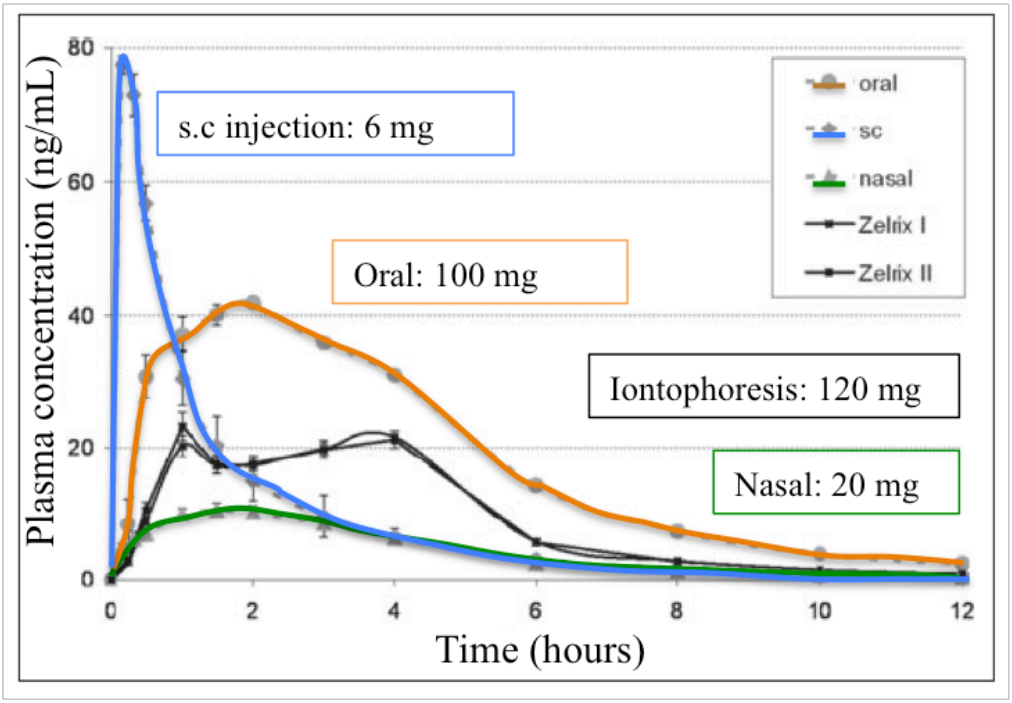

Figure 3.1: Sumatriptan plasma concentration over time measured in humans after different administration routes: s.c. injection (sc. blue), oral tablet (orange), transdermal (iontophoretic patch, black), or nasal spray (green). The total dose of Sumatriptan in the formulation is presented in the coloured boxes. The graph is reproduced from Pierce et al. [177].

Pierce et al. have compared the pharmacokinetic profiles in humans of oral (100 mg), subcutaneous (6 mg), or intranasal (20 mg) Sumatriptan with the iontophoretic transdermal Sumatriptan delivery system (120 mg) (Zelrix™, later commercialised as Zecuity®) (see Figure 3.1). The study was performed in 25 healthy volunteers aged 21-57 years [177]. Sumatriptan was detected in the blood plasma within 15 minutes after activation of the iontophoretic patch and reached a plasma concentration of 10 ng/mL by 30 minutes. The maximum levels of 24.8 ng/mL were detected 1.7 hours post-activation, which corresponds at that time point with 0.1% of the total applied dose (assuming 5.0 L blood volume in humans). Other forms of transdermal or intradermal administration were not tested, although s.c. injection showed a rapid clearance profile, which suggests rapid transfer from this compartment into the bloodstream. Furthermore, different clinical studies have been published that only reported the efficacy and safety of different Sumatriptan delivery systems without including any pharmacokinetic data [193-196].

In literature, it has been reported that the therapeutic blood concentration of Sumatriptan in humans is 18-60 ng/mL [197]. Currently, there are no studies published that have investigated the delivery of Sumatriptan in mice. To determine what the therapeutic concentration of Sumatriptan in the mice blood must be to be equivalent to humans, the therapeutic concentrations in humans is extrapolated to mice by considering the allometric scaling dose as an empirical approach [198]. This method is based on the principle that physiological parameters between mammal species are related to their body surface area for therapeutic agents metabolized by oxidation, like Sumatriptan [199].

A typical human (70 kg, 5.0 L blood volume, 1.62 m^2 body surface area) with a therapeutic concentration range of 18-60 ng/mL has a human dose range of 1.28 – 4.29 µg/kg. To convert between human and mice (0.02 kg, 1.4 mL blood volume, 0.007 m^2 body surface area), a correction factor K_m is estimated by dividing the average body weight (kg) of the species to its body surface area (m^2), which are 37 kg/m^2 for humans and 3 kg/m^2 for mice. This was achieved using the following formula:

$$\text{Mouse dose } \left(\frac{\mu g}{kg}\right) = \text{Human dose } \left(\frac{\mu g}{kg}\right) \cdot \frac{\text{Human } K_M}{\text{Mouse } K_m} \quad (3.1)$$

$$\text{Mouse blood concentration } \left(\frac{\mu g}{mL}\right) = \frac{\text{Mouse dose } \left(\frac{\mu g}{kg}\right) \cdot Mouse\ weight\ (kg)}{blood\ volume\ mouse\ (mL)} \quad (3.2)$$

With formula 3.1 and 3.2 the therapeutic Sumatriptan concentration range in mice was calculated to be 0.23 – 0.76 µg/mL (or in the total 1.4 mL murine blood **0.32 – 1.05 µg**). Even though the calculation is very simplistic, this provides an indication what the corresponding therapeutic Sumatriptan levels are in the murine blood.

3.1.3 Ultrasound-enhanced transdermal delivery

The use of low-frequency ultrasound has been shown to increase skin permeability to a wide range of therapeutic agents. In the early-mid 1990s, it was found that the main mechanism for ultrasound-enhanced delivery was induced by the presence of cavitation. One way to increase the probability of cavitation formation during sonication is by using low-frequency ultrasound (20-100 kHz) and high negative pressure [99, 200], which causes the cavitation of bubbles entrapped on the skin surface. In the presence of low-frequency ultrasound, it induces a slowly fluctuating pressure field that simulates different size bubbles to cavitate.

In the field of low-frequency ultrasound, different studies by Mitragotri et al. have shown the enhanced delivery effect of various low-molecular-weight therapeutics (e.g. aldosterone, butanol, calcium, corticosterone, estradiol, mannitol, salicylic acid, and sucrose [109, 201]), as well as high-molecular weight-molecules (e.g. heparin and insulin [202, 203]) by using 20 kHz, 10% duty cycle and 125 mV/cm^2 acoustic intensity.

Another approach to increasing cavitation activity during ultrasound exposure is to use microbubbles with narrow size destruction. In the presence of cavitation nuclei, the acoustic energy is lowered to induce cavitation upon insonation. Park et al. investigated the use of a microbubble contrast agent (Definity®) as cavitation nuclei in the delivery of glycerol (92 Da) for the purpose of optical clearance. They found that insonated at 1.1 MHz, 600 kPa, 10% duty cycle for 60 minutes, increased the transparency of the *ex vivo* porcine skin by 80% in contrast to insonation without cavitation nuclei [204]. In a second study by Park et al., the transdermal delivery of fluorescent molecules (FITC-dextrans, 4, 20, and 150 kDa) was evaluated *in vivo* in rats using high frequency ultrasound (1.12 MHz and 2.47 MHz, 10 ms pulse length, 1% duty cycle, 1 MPa, 30 minutes exposure time) with two different types of microbubble contrast agents (Definity® and SonoVue®) [205]. It was found that the skin permeability was two-fold enhanced by the addition of 0.1 wt.% contrast agents to the formulation without any visual mechanical or thermal skin damage, while no enhanced delivery was observed without cavitation nuclei. It was stated that the mechanical interaction between the cavitation nuclei and the applied ultrasound is the main mechanism that significantly influences the increase in the FITC-dextrans at the tested frequency range.

Based on these findings it is hypothesized that insonation of the *in vivo* skin under sustained inertial cavitation induced by the NCs can enhance the delivery of a small therapeutic agent into the skin. However, for the clinical relevance of Sumatriptan, therapeutic levels have to be reached into the bloodstream without inducing skin damage. To date, there are no publications that have measured the delivered therapeutic dose in the blood after transdermal treatment of ultrasound-medicated cavitation.

In addition, the skin is a heterogeneous tissue and therefore its properties vary with body location, age, hydration level, gender, and ethnic origin. This increases the uncertainty regarding how much Sumatriptan is delivered under the influence of a physical stimulus such as cavitation. A real-time non-invasive feedback system would therefore be incorporated into any ideal delivery system to allow live monitoring and quantification of the dose delivered into the skin. Passive cavitation detection may provide a method of achieving such feedback [206].

Therefore, the aims of this chapter are:

1) To verify the feasibility of the transdermal delivery of Sumatriptan *in vivo* using cavitation-enhanced transport.
2) To investigate the potential to quantify the amount delivered into the skin through passive monitoring of the acoustic emissions.
3) To characterise and attempt to reduce the physiological impact on the skin caused by exposure to inertial cavitation.

3.2 Materials and Methods

After addressing the challenges identified in Chapter 2, the therapeutic ultrasound setup (described in Chapter 2, Figure 2.1) was optimised and a new coupling cone and formulation holder were designed and characterised. With the optimised acoustic field, further *in vivo* studies were performed in mice to investigate the feasibility and reproducibility of delivering Sumatriptan transdermally.

The first study was a 'Safety Study' with the aim of identifying the maximum acoustic pressure that could generate inertial cavitation and provide efficacious delivery without causing skin damage. The influence of different acoustic pressures on the delivery of Sumatriptan into the mice after 10-minutes exposure period ('Cavitation') was compared to a group where the Sumatriptan was placed on the skin surface and left to rest for 10 minutes (i.e. 'No Ultrasound' group).

The second and third studies were repeat studies (called 'Sumatriptan Repeat Study 1' and 'Sumatriptan Repeat Study 2', respectively). These two repeat studies included one additional experimental group (i.e. 'Sub Cavitation' group), whereby the skin was exposed to Sumatriptan and insonated at lower acoustic pressures (below 1.0 MPa, i.e. too low to produce sustained inertial cavitation). This group characterises the influence of acoustic pressure alone. In other words, what happens in the presence of ultrasound but in the absence of the strong acoustic broadband emission energy that is present in the 'Cavitation' group. Furthermore, to investigate the influence of hair follicles and the hair removal procedure on the transdermal delivery, 'Sumatriptan Repeat Study 1' was performed on CD1 nude mice and the 'Sumatriptan Repeat Study 2' on hairy BALB/c mice.

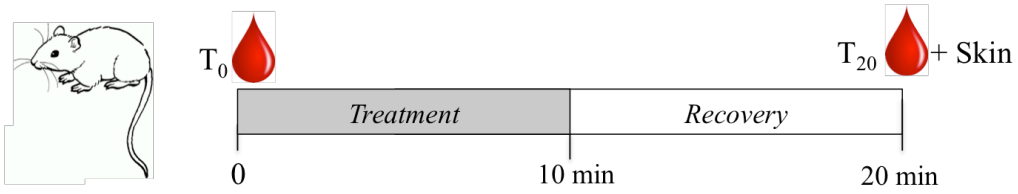

Figure 3.2: Schematic overview of the sample collection timeframe of the animal study. Blood was collected before the treatment (T_0) and after 20 minutes (T_{20}) the mouse was sacrificed and blood was sampled and the exposed skin area was rescued.

As can be observed in Figure 3.2, blood samples were collected from every mouse before the experiment (T_0). Mice were then treated for 10 minutes (the type of treatment dependent on the experimental group) and the acoustic emissions were recorded whilst exposing to 265 kHz therapeutic ultrasound. The skin and blood samples were collected 10 minutes after the treatment was finished (T_{20}). In all the three studies, the rescued skin samples were investigated for skin damage using photographic images. The levels of Sumatriptan delivery achieved into the skin and bloodstream were determined using HPLC. Only on the samples from 'Sumatriptan Repeat Study 2' was histology performed (on one sample per experimental group).

3.2.1 Therapeutic ultrasound setup

The therapeutic ultrasound setup and the ultrasound parameters were kept constant between Chapter 2 and the *in vivo* studies in this chapter. However, it was found in the manufacture calibration sheets of the HIFU transducer that the fundamental frequency of the transducer is 265 kHz and not 256 kHz, as was stated by Bhatnagar [149]. This was verified by sending a pulse to the HIFU transducer and recording the pulse-echo with a hydrophone (data not shown). After determining the harmonic frequencies in the pulse-echo signal, the frequency interval between the harmonics was the same as the fundamental wave, 265 kHz.

The influence of the change in driving frequency to 265 kHz on the pressure profile was evaluated by characterising the ultrasound field by point-by-point scanning with a hydrophone (Onda HNA-0400, Onda Corp, USA). A similar setup was used as shown in Chapter 2, Figure 2.1), but with the HIFU transducer and the coupling cone totally submerged in the degassed water tank (Figure 3.3(a)). A longitudinal pressure scan was performed inside the coupling cone as well as underneath the coupling cone. The normalised pressure profile is presented in Figure 3.3(b), with Z=0 mm corresponding to the end of the coupling cone as indicated in Figure 3.3(a).

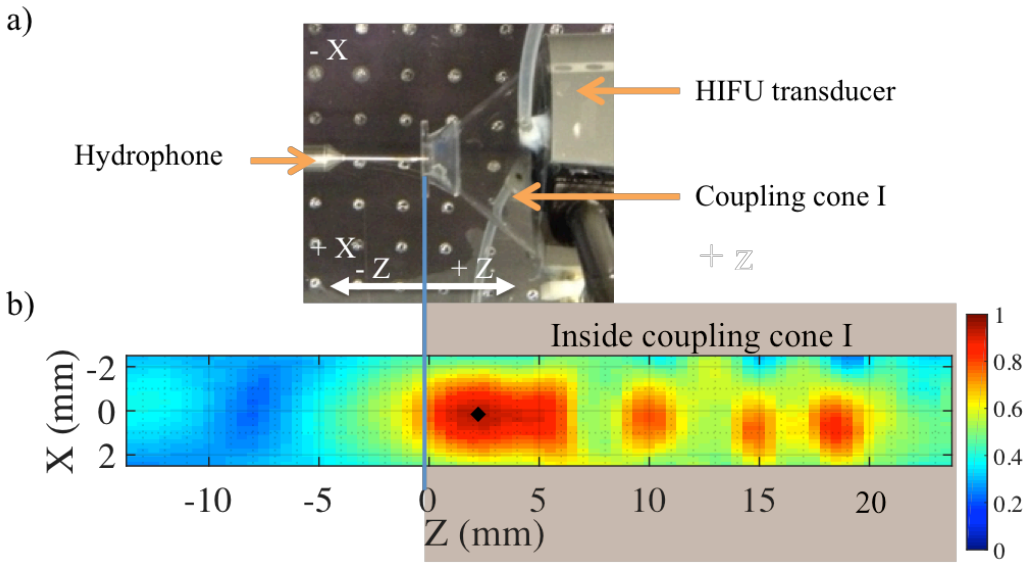

Figure 3.3: Characterisation pressure profile of the HIFU transducer with the coupling cone used in Chapter 2. a) Photographic top view image of the HIFU transducer with the mounted coupling cone in the water tank and the hydrophone on the left-hand side pointing inwards towards the coupling cone. b) Normalised transverse pressure profile of the HIFU transducer driven at 265 kHz with Z=0 the end of the coupling cone.

Notably, Figure 3.3(b) shows the detection of the normalised acoustic pressure field within the coupling cone with the pressure focus at Z=3 mm (highlighted by ◆ in Figure 3.3), instead of having the large ultrasound focus at the interface of the holder and skin (as claimed by previous study [147]). It was estimated that with an input voltage of 160 Vpp to the transducer, the pressure in the ultrasound focus at Z=3 mm would be > 2.0 MPa. To improve the energy efficiency of the therapeutic system with the ultrasound

focus at the interface between the formulation holder and the skin, the therapeutic ultrasound setup (described in Chapter 2, Figure 2.1) was optimised and a new coupling cone and formulation holder were designed and characterised as shown in Figure 3.3.

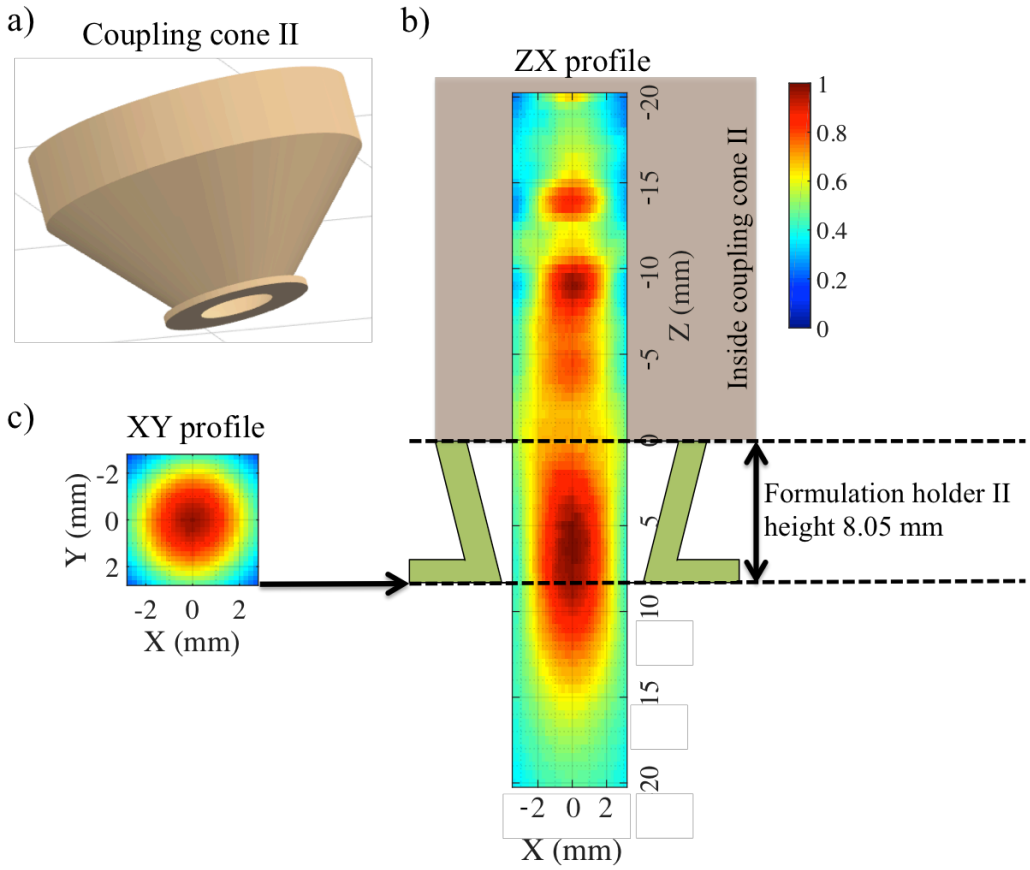

Figure 3.4: Re-design and characterisation of coupling cone II. a) 3D conical design of the coupling cone II where the HIFU transducer can fit from the top and focuses the ultrasound through the lower aperture into the formulation holder. b) Normalised longitudinal pressure profile of the ultrasound within the coupling cone (Z=-20:0 mm), formulation holder (Z=0:8.05 mm), and beyond (Z=8.05:20 mm). c) Normalised transverse pressure profile performed underneath the formulation holder (Z=8.05 mm).

Without any coupling cone, the HIFU focus was found to be 52.5 mm away from the transducer face, with -3dB focal width 6.04 mm, and focal length 39.49 mm. Based on these findings a shorter coupling cone (named coupling cone II) was designed in such a way that the conical shape matched with the outer envelope of the spherically focussed ultrasound field and that the ultrasound focus was predominantly within the formulation and mouse skin (Figure 3.4(a)). The coupling cone II was 3D printed with the Form2 stereolithography 3D printer (Formlabs, United Kingdom) with clear photoresins.

The coupling cone was mounted over the face of the HIFU transducer and the location of the ultrasound focus was verified by point-by-point scanning with a hydrophone. The normalised longitudinal and transverse pressure profiles are presented in Figure 3.4(b) and (c), respectively.

With the addition of coupling cone II, the predominant ultrasound focus is located outside the coupling cone (Figure 3.4(b)). Based on this pressure profile, a conically shaped formulation holder was designed (2.0 mL volume) and 3D printed to localise this ultrasound focus in the formulation holder and skin surface. The transverse pressure profile in Figure 3.4(c), measured at the end of the formulation holder, showed a circular focussed beam. With the new coupling cone II and formulation holder II, the input voltage to the transducer could be reduced six-fold to 60 Vpp to obtain a PRFP within the formulation of 1.0 MPa peak negative.

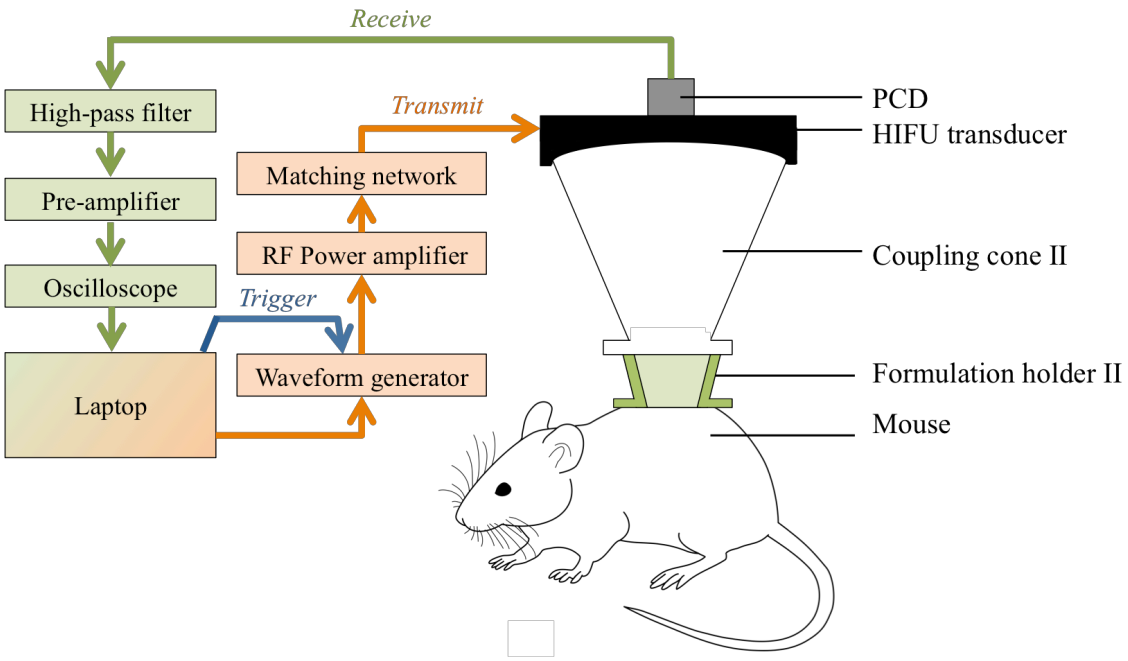

Figure 3.5: Schematic representation of the therapeutic ultrasound setup used for the *in vivo* studies. The sonication loop is presented on the left-hand side and includes transmit, receive, trigger and monitoring pathway as described in section 2.2.1. On the right-hand side is the ultrasonic delivery system presented with the newly designed coupling cone (II) and formulation holder (II). Source mouse image [207].

For the *in vivo* experiments, the therapeutic ultrasound setup as shown in Figure 3.5 was used. The sonication loop is similar as described in Chapter 2, section 2.2.1, but with some adjustments to the receive pathway to make the setup portable. Instead of using a desktop computer, the pre-amplified PCD signal was digitised by an 8-bit digital oscilloscope (Handyscope HS3 100 MHz, TiePie Engineering, The Netherlands) and saved onto a laptop (Toshiba, United Kingdom). The ultrasonic delivery system on the right side of Figure 3.5 included the newly designed coupling cone II and formulation holder II. The ultrasound settings used in this chapter are presented in Table 3.1.

Table 3.1: Overview of ultrasound parameters for *in vivo* experiments.

Ultrasound parameters	Settings
Driving frequency	265 kHz
Duty cycle	10%
PRF	10 Hz
Pulse length	10 ms
Ultrasound exposure	10 minutes
PRFP range	0 – 2.1 MPa

3.2.2 Passive cavitation monitoring

For every ultrasound experiment, the acoustic emissions from the ultrasound focus were recorded by the PCD and analysed as described in Chapter 2, section 2.2.4. Since the length of coupling cone II and formulation holder II were different from the previous chapter, the time window was also defined differently in the *in vivo* experiments. As shown in Figure 3.6, a 16 µs time frame (99.4 - 115.6 µs) was windowed to look at the acoustic emissions originating from within the formulation holder and mouse skin.

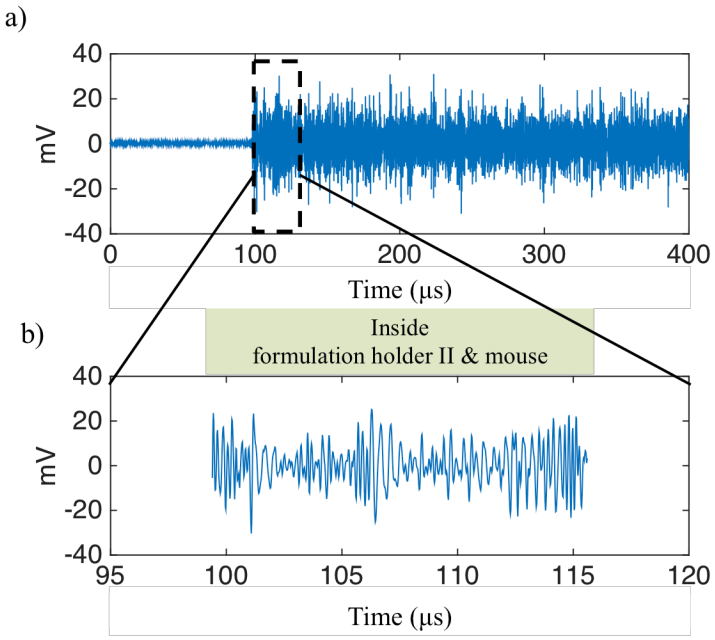

Figure 3.6: Example of recorded raw PCD voltage trace (a) and windowed signal (b). The windowed signal contains acoustic emissions originating from the formulation holder II and mouse skin.

The windowed signal was Fourier-transformed and the power spectral density was plotted as a time-frequency diagram. The TASE value was calculated in the same way as described in Chapter 2, section 2.2.4.

3.2.3 Experimental groups

3.2.3.1 Safety Study

For the 'Safety Study', ten female BALB/c mice (6 months old) were obtained from the Biomedical Service Unit at the John Radcliffe Hospital (Oxford, United Kingdom). These ten mice were randomly divided into two groups of five mice: the 'Cavitation' group received ultrasound at different acoustic pressure generating sustained inertial cavitation, and the negative control group 'No Ultrasound' did not receive any ultrasound. This second group was used as a negative control to investigate the delivery of Sumatriptan into the skin and blood by passive diffusion alone.

Three different acoustic pressures were used in the 'Cavitation' group as specified in Table 3.2.

Table 3.2: Overview of experimental groups in the 'Safety Study'.

Experimental group	Description of Treatment	Acoustic pressure
No Ultrasound	Sumatriptan + NCs in water No exposure to ultrasound.	0 MPa (n=5)
Cavitation	Sumatriptan + NCs in water Generation of sustained inertial cavitation during the exposure to ultrasound.	1.5 MPa (n=1) 1.7 MPa (n=1) 2.1 MPa (n=3)

These three pressures were chosen to be well above the inertial cavitation threshold of the NCs at 265 kHz [162], but were gradually increased in an attempt to identify the highest pressure that would result in substantial cavitation without causing skin damage. Once this point (2.1 MPa) was identified it was repeated to give three replicates in total.

3.2.3.2 Sumatriptan Repeat Studies

With the optimised acoustic pressure from the 'Safety Study', two more *in vivo* experiments were performed. 'Sumatriptan Repeat Study 1' and '2' were repeat experiments of the 'Safety Study', except that one extra control group was included whereby the skin was exposed to lower acoustic pressures without the detection of strong acoustic broadband emission energy ('Sub Cavitation' group). To clarify the difference between 'Sub Cavitation' and 'Cavitation' better, closer examination is needed of the recorded acoustic emissions detected when exposing the Sumatriptan + NCs formulation to increasing acoustic pressures (Figure 3.7).

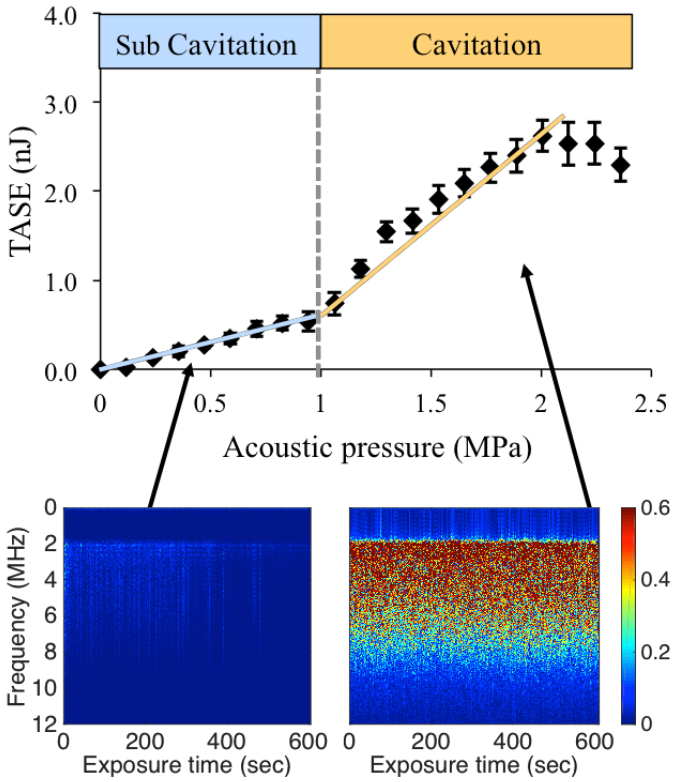

Figure 3.7: Plot defining the 'Sub Cavitation' and 'Cavitation' regime together with representative spectrograms.

Figure 3.7 shows the calculated TASE value recorded from the 16 µs timeframe window that corresponds to the acoustic emissions originating from within the formulation holder (as described in section 3.2.2) as a function of the acoustic pressure. By performing a ramping up study of the formulation (containing Sumatriptan + NCs) and recording the acoustic broadband emissions of 10 pulses per acoustic pressure (10% duty cycle, individual pulse consisting of 2650 cycles (10 ms on, 90 ms off)), a threshold can be observed at an acoustic pressure of 1.0 MPa peak negative.

As observed in Figure 3.7, up to 1.0 MPa the TASE value is increased and relates to sporadic activity of cavitating NCs inside the formulation ('Sub Cavitation') as well as the presence of larger gas pockets trapped inside the formulation. Furthermore, the sporadic activity can be clearly monitored in the acoustic emission spectrogram by seeing light blue bands in Figure 3.7.

Yet, the detected sensor energy sharply increases above 1.0 MPa acoustic pressure when the acoustic pressure reaches the minimum acoustic pressure required to 'activate' the bubble inside the NC crevice ('Cavitation' regime) [162]. Since the formulation contains a normal distribution of bubble sizes (NCs and entrapped bubbles during formulation preparation), an increase in the TASE value is recorded for increasing acoustic pressure until all possible air pockets cavitate in the acoustic pressure field. Consequently, some bubbles grow by rectified diffusion to larger sizes forming a bubble cloud and cause scattering and absorption of the incoming ultrasound waves and thereby shield the ultrasound from reaching further into the formulation [208] as well as preventing the detection of acoustic emissions from within the formulation holder and mouse skin. This may cause the TASE value to reach a plateau beyond 2.0 MPa. Nevertheless, the presence of broadband acoustic emissions (associated with inertial cavitation) can be identified in the acoustic emission spectrum by its vertical band of coloured pixels.

The optimal control group would be to use inactivated NCs that would not cavitate at the acoustic pressures used for the 'Cavitation' group. However, several repeat experiments demonstrated that obtaining completely inactivated NCs, which no longer cavitate at acoustic pressures above 1.0 MPa, was impossible (data not shown). Therefore, inactivated NCs could not be used in such a way and a 'Sub Cavitation' pressure was used as a control instead. This was the most appropriate technically possible control condition to validate whether sustained inertial cavitation could be used for transdermal Sumatriptan delivery.

In ‘Sumatriptan Repeat Study 1’, 15 female CD1 nude mice (6 months old) were obtained and 18 female BALB/c mice (8 weeks old) for ‘Sumatriptan Repeat Study 2’. The mice were randomly divided into three groups: ‘Cavitation’, ‘Sub Cavitation’, and the negative control group ‘No Ultrasound’. An overview of the experimental groups of these two repeat studies is outlined in Table 3.3.

Table 3.3: Overview of experimental groups for ‘Sumatriptan Repeat Study 1’ and ‘2’. One of the samples highlighted with * was used for Histology.

Experimental group	**Description of Treatment**	**Acoustic pressure**	
		Repeat Study 1: Nude mice	*Repeat Study 2: BALB/c mice*
No Ultrasound	Sumatriptan + NCs in water. No exposure to ultrasound.	0 MPa (n=5)	0 MPa (n=6) *
Sub Cavitation	Sumatriptan + NCs in water. Generation of sub cavitation levels during the exposure to ultrasound.	1.0 MPa (n=5)	0.5 MPa (n=4) * 0.7 MPa (n=2)
Cavitation	Sumatriptan + NCs in water. Generation of inertial cavitation during the exposure to ultrasound.	1.6 MPa (n=5)	1.6 MPa (n=1) 1.8 MPa (n=5) *

The results of ‘Safety Study’ identified the maximum effective acoustic pressure to deliver Sumatriptan, without inducing skin damage, to be in the range of 1.6-2.1 MPa acoustic pressure. This acoustic pressure of 1.6 MPa was therefore used for the ‘Cavitation’ group in ‘Sumatriptan Repeat Study 1’ using nude mice. 1.0 MPa was chosen to represent the highest pressure that could be deployed without causing significant inertial cavitation activity. ‘Sumatriptan Repeat Study 2’ required some refinement of these pressure levels (possibly due to the change in mouse strain or NCs batches) and histology was performed on one mouse per group (indicated by the asterisk in Table 3.3).

3.2.4 Formulation preparation

The drug formulation was prepared containing ultrasound gel Anagel®, NCs (obtained from OxSonics Ltd., United Kingdom), and therapeutic antibody solution in the composition of 50:25:25 wt.%, respectively. In the *in vivo* experiments described in this chapter, the same formulation composition was used. However, visual precipitation in the formulation was observed when mixing high concentrations of Sumatriptan with the Anagel®. Therefore, Anagel® was replaced by DI water making the final formulation a liquid form.

Sumatriptan succinate (413.49 MW, 1642201 USP (United States Pharmacopeia) grade, Sigma-Aldrich, United Kingdom) was dissolved in DI water to a concentration of 50 mg/mL before addition to the NCs and DI water, making up a final concentration of 5.2 mg/mL. The formulation holder II was filled with 2 mL of the formulation, which corresponds with a total dose of 10.4 mg Sumatriptan succinate (i.e. the recommended therapeutic dose [209]). The formulation was made on the day of the *in vivo* experiments and stored at room temperature before use. Different NCs batches were used to prepare the formulation for different experiments. Although care was taken to characterise these batches, because the manufacturing process was not yet GMP (Good Manufacturing Practise) certified, their acoustic activity often showed slight variation.

3.2.5 Animal model

Mice were used as an *in vivo* skin model due to their availability, small size, and relatively low cost in comparison with larger rodents. Two strains of mice were investigated; the hairy BALB/c and the nude CD1 mice. The nude mice strain lacks the FOXN1 gene, which results in the absence of fur and thymus (important for efficient immune responses) [210].

Since the *in vivo* Sumatriptan studies do not investigate the effect on the immune system, both mice strains were suitable. For the placement of the formulation holder, a relatively flat and stable surface was required and therefore the dorsal area around the hip joint was selected as the treatment area.

3.2.6 General experimental protocol

All the animal studies were performed in accordance with Home Office Legislation and Oxford University Gold Standard requirements under an approved project licence. On the day of the experiment, the fur of the BALB/c mice was removed at the treatment area using an electric razor and depilatory cream (VEET) (i.e. pre-treatment). This was not required for the hairless CD1 mice. Prior to the treatment, blood samples (T_0) were collected from the tail vein and then diluted in PBS (1:5 dilution). The samples were centrifuged for three minutes at 3,000x g and the supernatant (blood serum/PBS) was collected and stored at -20°C.

The mice were sedated with 2% isoflurane and 98% oxygen (2 L/min flow rate). The formulation holder was placed on the hairless treatment area and filled with ~2 mL of the drug formulation. The transducer was then coupled with the formulation holder (see Figure 3.5). Depending on the experimental group, ultrasound was applied for 10 minutes or not.

After the treatment, the transducer was removed from the treatment area and the remaining formulation in the holder was recovered. The treated skin was thoroughly washed with tap water to remove any remaining formulation from the skin surface. Next, the skin was dried with a clean tissue and the treatment area was marked with a permanent marker. The mice were placed back in the warmed cage to recover from

the anaesthetics and to increase their blood pressure to normal levels again. After 10-minute recovery time (see Figure 3.2), the mice were sacrificed by cervical dislocation. The exposed skin area was rescued and blood was collected from the chest cavity post-cull (T_{20}) and diluted, centrifuged and stored in the same way as the T_0 blood serum samples.

For the calibration curves, skin and blood serum from untreated mice were collected and directly spiked with different defined amounts of Sumatriptan formulation and stored at -20°C with the other samples.

3.2.7 Histology on BALB/c skin

To investigate the effect on the skin at the microscopic level, histology was performed on the skin from one BALB/c mouse per experimental group from 'Sumatriptan Repeat Study 2'. The skin samples were fixed in formalin directly after harvest. The histology was performed at the histology service at the Kennedy Institute of Rheumatology (University of Oxford, United Kingdom). Ten alternating sections were sliced from the centre of the exposed skin and Masson's trichrome staining was applied to visualise the different skin layers and to identify damage of the skin layers due to treatment. Images were captured with a Nikon Eclipse Ti microscope (Detector Nikon Sight D5-Fi1, 119430) at 20x magnification. As a control, sample of non-treated skin was rescued from a BALB/c mouse that only received the pre-treatment to remove the fur from the skin.

3.2.8 Detection Sumatriptan by HPLC

The level of Sumatriptan in the skin and blood serum was measured using HPLC. The Varian Pro Star HPLC instrument (Varian Corporation, USA) was equipped with

two ProStar 210 solvent delivery modules: ProStar 410 autosampler, and ProStar 330 UV photodiode detector. In the HPLC, the liquid solvent (i.e. mobile phase) is mechanically pumped through a column (i.e. stationary phase). The individual solutes are separated, depending on their interaction with the stationary phase.

In the case of reverse-phase HPLC, a column filled with silicon beads (ZORBAX Eclipse Plus C18, 4.6 x 150 mm, 5 μm, Agilent, United Kingdom) that strongly interact with solutes that preferentially associate with the non-polar organic phase, was used. Therefore, polar components flow faster through the column and elute before the non-polar solutes. With an analytical guard column in place (ZORBAX Eclipse Plus-C18, 4.6 x 12.5 mm, 5 μm, Agilent, United Kingdom), the reverse-phase HPLC column was protected from large impurities entering the column.

3.2.8.1 Internal standard

The skin and blood serum samples are a heterogeneous mixture of biological components that are likely to block and increase backpressure on the HPLC column. Therefore, the biological samples were purified before analysis by HPLC. However, with every sample preparation step, the initial and final recovered sample volumes were seldom exactly the same for every sample. By including an internal standard to the samples, loss of analyte during the sample preparation can be corrected during the data analysis.

Zolmitriptan (≥98% HPLC grade, 287.36 MW, Sigma-Aldrich, United Kingdom) was chosen as the internal standard because it is structurally very similar to Sumatriptan but sufficiently different so as to elute as a distinct peak after the Sumatriptan peak (see Figure 3.10(b)). The internal standard solution was prepared in water (0.1 mg/mL) and

added to the sample for the generation of a sufficient peak size (e.g., S/N>100) to be measured with suitable precision and accuracy [211].

3.2.9 Sample preparation

3.2.9.1 Skin - Homogenising

To investigate the amount of Sumatriptan present in the skin after treatment, the rescued skin was homogenised and purified before analysis by HPLC. Firstly, photographic images were taken with a mobile device (12 mega-pixels mobile camera) from the thawed skin samples. The skin samples were weighed and cut into smaller pieces to facilitate faster homogenisation. PBS was added to the skin samples to achieve a concentration of 1 mL solution/100 mg skin and homogenised on ice using an Ultra-Turrax homogenizer (T25, Ika Works Inc., USA). The homogenates were sonicated on ice using an ultrasonic cell disruptor (Microson Ultrasonic cell disruptor, Misonix, USA) four times for 10 seconds at level six with an interval of 10 seconds between each repeat, and then centrifuged for seven minutes at 14,000x g (Sorvall Legend X1R, Thermo Scientific, Germany). The supernatants were collected and stored at -20°C. For the Sumatriptan calibration curve, the spiked skin samples were processed in the same way and on the same day as the experimental samples. For the negative controls, untreated skin was homogenised and used as blanks.

3.2.9.2 Skin – Extraction protocol

Before running skin samples through the HPLC, the Sumatriptan was extracted from the skin homogenate by preparing aliquots of 800 µL in eppendorf tubes containing 150 µL skin homogenate, 10 µL of internal standard and 640 µL acetonitrile. The mixtures were shaken for five seconds, vortexed for 15 minutes at 1,400x g at 4°C (HCM100-Pro, Scilogex, USA) and finally centrifuged for five minutes at 14,000x g

(Sorvall Legend X1R, Thermo Scientific, Germany). 750 µL of the supernatant was transferred into 15 mL tubes. The calibration samples were prepared in the same way and on the same day. For the calibration curve, the skin homogenate of the spiked skin samples were diluted (if required) with blank skin homogenate. At least five calibration samples were prepared including one blank ('0') sample containing skin but no Sumatriptan. All experimental and calibration samples were blow-dried using a nitrogen (N_2) line and stored at -20°C overnight.

The next day, the thawed skin extract was dissolved in 220 µL of solvent A (i.e. DI water:acetonitrile, 90:10 v/v), vortexed for five minutes at 800x g at room temperature (HCM100-Pro, Scilogex) and centrifuged for five minutes at 14,000x g at room temperature (Beckman Coulter J26XP, JA 14.50 Rotor, USA). 200 µL of the solution was transferred into 0.3 mL PP snap ring Micro-vial (VWR international).

3.2.9.3 Blood serum - Extraction protocol

From every mouse, blood serum samples were taken before the experiment (T_0) and at 10 minutes after completion of the 10-minutes treatment (T_{20}). The extraction procedure for blood was similar to the protocol described for the homogenised skin. However, the volumes were slightly different as described below.

For the extraction of the blood serum samples in the 'Safety Study', aliquots of 700 µL final volume were prepared in eppendorf tubes containing 130 µL blood serum, by the addition of 10 µL of internal standard and 560 µL acetonitrile. After shaking the sample for five seconds, vortexing for 15 minutes at 1,400x g at 4°C, and centrifuging for five minutes at 14,000x g, 650 µL was transferred to 15 mL tube and blow-dried under

N_2 gas. This protocol was also used for the blood samples from the 'No Ultrasound' and 'Sub Cavitation' groups from 'Sumatriptan Repeat Study 2' with BALB/c mice.

For the experimental groups 'No Ultrasound' and 'Sub Cavitation' in 'Sumatriptan Repeat Study 1', aliquots of 690 µL were prepared containing; 120 µL blood serum instead of 130 µL, because this was the maximum volume found in one of the T_0 blood samples. In addition, 560 µL acetonitrile was added together with 10 µL of 10x diluted Zolmitriptan internal standard (working solution 0.01 mg/mL). A lower amount of internal standard was used to reduce the interference of the internal standard peak with the detection of low-intensity signal peaks from the Sumatriptan. After shaking, vortexing and centrifuging the sample, 650 µL was transferred to 15 mL tube, blow-dried under N_2 gas and stored at -20°C overnight.

The blood samples collected from the mice in the 'Cavitation' group from 'Sumatriptan Repeat Study 1' and '2' were analysed after preparing aliquots of 500 µL containing 80 µL blood serum, 20 µL internal standard and 400 µL acetonitrile. After shaking, vortexing and centrifuging the sample, 450 µL was transferred to 15 mL tube, blow-dried under N_2 gas and stored at -20°C overnight. For every set of extracted samples, the calibration samples were prepared in the same way and on the same day. Spiked mouse blood serum was diluted (if required) with mouse serum from an untreated mouse or with purchased mouse serum (M5905, Sigma-Aldrich, United Kingdom). At least five calibration samples were prepared per calibration curve including one blank sample.

The blow-dried samples and their calibration samples were thawed the next day and the residue was dissolved in 120 µL of solvent A. The samples were vortexed for five minutes at 800x g at room temperature (HCM100-Pro, Scilogex, USA) and centrifuged for five minutes at 14,000x g at room temperature (J26XP, JA 14.50 Rotor, Beckman Coulter, USA). 100 µL of the solution was transferred into 0.3 mL micro-vial.

3.2.10 HPLC method

As shown in Figure 3.8, a gradient method was used that contained two mobile phases: solvent A (green) and solvent B (blue). Solvent A contained a mixture of DI water:acetonitrile (90:10, v/v) with 0.1% Trifluoroacetic acid (TFA, 99%, Fluka) and solvent B contained 0.1% TFA in acetonitrile.

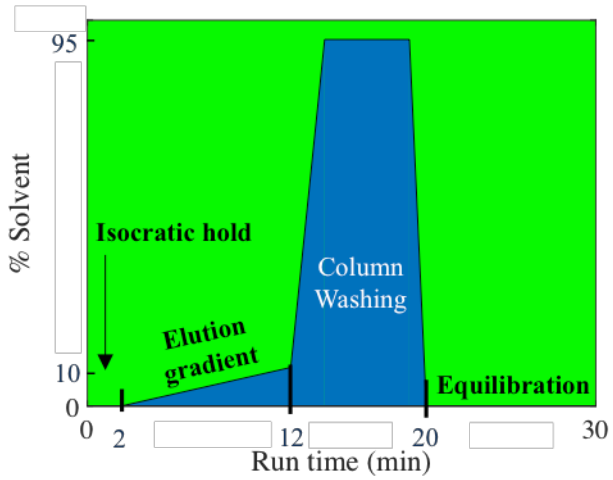

Figure 3.8: Pumps gradient chart with percentage solvent B (acetonitrile with 0.1% TFA) presented in blue and the remaining percentage of solvent A (DI water:acetonitrile (90:10, v/v)) in green.

The first two minutes of the HPLC method (Figure 3.8) were used as an isocratic hold to stabilise the baseline, before starting the elution gradient. During the 10-minutes elution gradient, the mobile phase solvent strength was enhanced to ensure the Sumatriptan and the internal standard (Zolmitriptan) had clearly distinguishable elution profiles. The following 18 minutes column washing enabled all the remaining solutes in

the column to elute. It was found that without this washing step, remaining solutes collected in the (pre) column and caused high backpressure and ultimately column blockage. The last 10 minutes of the method run was used to re-equilibrate the solvent composition before the next run. Between every sample run, a blank run was performed by injecting 20 µL solvent A. This prevented any crossover between samples. The total run time, including the blank run, was 60 min/sample.

The solvents A and B were freshly prepared before running a sample batch and vacuum filtered through a 0.45 µm pore size Nylon 66 filter membrane (Sigma-Aldrich, United Kingdom), and simultaneously degassed by placing the bottle in an ultrasonic bath during vacuum filtering. 20 µL was injected into the system at a flow rate of 1.0 mL/min and the detection wavelength was set to 230 nm. An example chromatogram is shown in Figure 3.9(a) after injecting 20 µL of clean solvent A into the system. The plots in Figure 3.9 show the absorbance intensity as a function of the retention time.

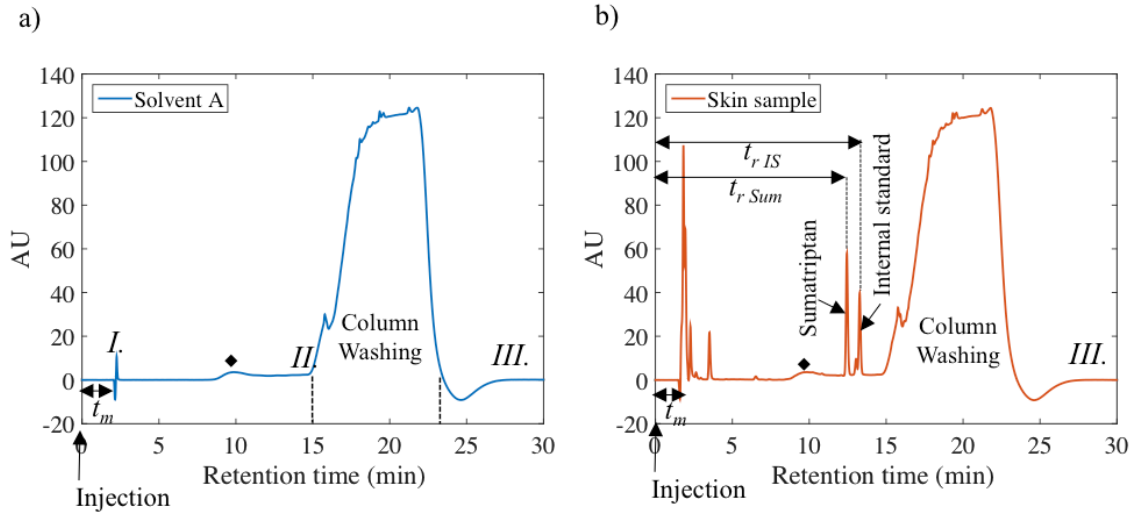

Figure 3.9: Representative chromatograms of a blank run by injection of solvent A into the system (a) or a skin sample (b). a) Chromatogram from a blank run with solvent A, showing the time of injection (t=0 min), void time (t_m) with corresponding band (*I.*), bulge in detector signal (◆, ± t=10 min), column washing starting at time point (*II.*), and re-equilibrated baseline (*III.*). b) Chromatogram from a representative skin sample showing the elution peaks of Sumatriptan and the internal standard, the retention times of Sumatriptan ($t_{r\ Sum}$) and the internal standard ($t_{r\ IS}$), the bulge in detector signal (◆, ± t=10 min), and re-equilibrated baseline (*III.*).

The recording of the chromatogram started at the moment a sample was injected into the HPLC. As the injected sample migrates down the column, the separation of the individual solutes is dependent on their interaction with the stationary phase. More polar components flowed faster through the column and eluted before more non-polar solutes. Provided the interaction strength of each solute with the stationary phase was sufficiently different, then each solute was separated into individual bands with a Gaussian profile [212].

Despite the precautions taken, evidence of baseline drift was still apparent over time in Figure 3.9(a). For example, soon after the sample injection, a small peak elutes (peak *I.* in Figure 3.9(a)). This peak originates from solutes (present in the mobile phase) that do not interact with the column and travel at the same rate as the mobile phase. The time it takes for these un-retained solutes to move from the injector to the detector is called void time (t_m). Furthermore, during the gradient method the composition of the mobile phase changes. Since the absorbance properties of water and acetonitrile are different at 230 nm [211], the baseline increases with the increase in percentage acetonitrile in the mobile phase. These effects caused a shallow positive baseline drift to be observed up to point *II.* (Figure 3.9(a)), and steeper positive and then negative slopes during the column washing until the baseline was in equilibrium again (i.e. at 100% solvent A) at the end of the run (point *III.* in Figure 3.9(a))

Figure 3.9(b) shows a representative chromatogram recorded after injecting a skin sample containing multiple solutes. The same baseline pattern is observed as in Figure 3.9(a) with un-retained solutes eluting after t_m, baseline increase and decrease due to the column washing, and the equilibrium state at the end of the run (point *III.*).

In addition, the solutes of interest (i.e. analytes) Sumatriptan and the internal standard elute sequentially in clearly distinguishable elution profiles. The time it takes for an analyte to move from the point of injection to its peak maximum is called the retention time (t_r). The retention times are designated in Figure 3.9(b) as $t_{r\ Sum}$ and $t_{r\ IS}$ for Sumatriptan and the internal standard, respectively. The concentration of the solute available in the sample is proportional to its peak height.

In both the chromatograms presented in Figure 3.9, a small bulge (designated with ◆) in the baseline occurred at ± 10 minutes during the elution gradient. This bulge appeared during every single run at the same retention time, but it did not interfere with the retention time of the analytes as shown in Figure 3.9(b).

Quantitative analysis of Sumatriptan in a biological sample relies on comparing the retention time of the peak in an unknown sample with that of $t_{r\ Sum}$ in a calibration sample. Yet, over the course of several runs, the retention time of the analytes drifted to longer retention times as can be seen in Figure 3.10.

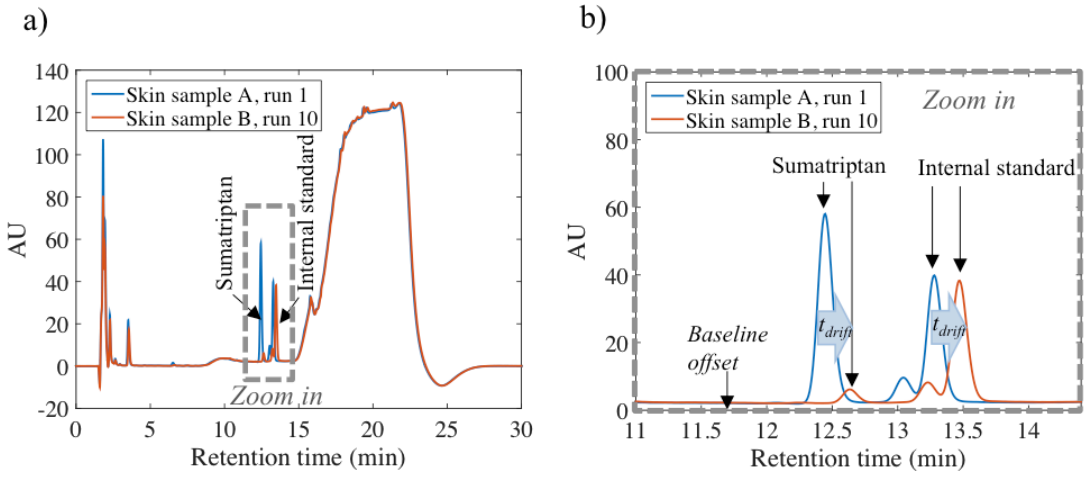

Figure 3.10: The drift in retention time of analytes over a 10-hour period. a) Showing an example of the retention drift illustrated with two skin samples A (blue) and B (red) recorded in the first run and the 10th run (10 hours later), respectively. b) Zoom-in of the grey dotted square in panel a) reveals the time drift of the analyte peaks over time (t_{drift}) as well as the baseline offset.

Figure 3.10(a) shows the chromatograms of two individual skin samples. Skin sample A (blue) detected in the first run and skin sample B (red) taken nine runs later (i.e. 10 hours). By taking a closer look at the region where Sumatriptan and the internal standard elutes (Figure 3.10(b)), it can be observed that Sumatriptan and the internal standard have the same drift in retention time (t_{drift}) and so the internal standard (Zolmitriptan) peak is important to verify the identity of the Sumatriptan peak.

Furthermore, it can be observed in Figure 3.9(b) that the chromatogram from skin sample B is shifted to longer retention times than skin sample A. This is caused by the slow loss of volatile components like acetonitrile to the headspace above the liquid surface. As a result, the percentage of acetonitrile decreases in the pre-mixed solvent A. Therefore, more solvent B is required to get the desired mobile phase mixture to elute Sumatriptan and the internal standard out of the column and consequently results in longer retention times.

By adding a known amount of internal standard to every sample, the internal standard peak can always be identified in a chromatogram. This is not always the case for Sumatriptan, because the presence and the amount of Sumatriptan are unknown in the experimental samples. Therefore, the chromatograms were post-processed using MATLAB software, with the internal standards being re-aligned and the location of the Sumatriptan peak being determined and quantified as described in the next section.

3.2.11 Data analysis of chromatograms

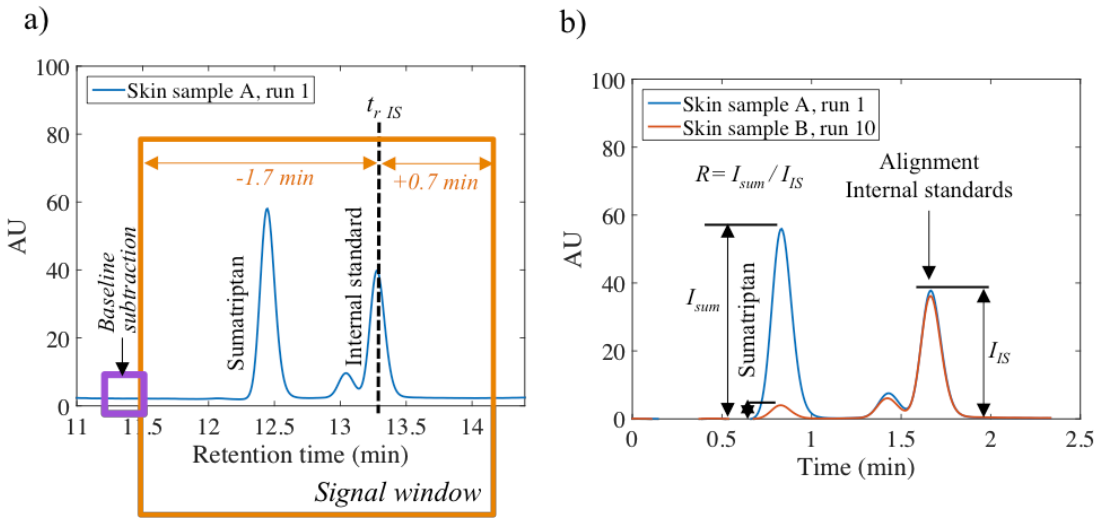

Figure 3.11: Re-aligning the chromatogram using the internal standard to correct for the retention drift. a) Post-processing of the raw chromatograms by windowing the signal based on the retention time of the internal standard ($t_{r\ IS}$), and subtracting the baseline with the average intensity calculated in the purple box. b) Aligning the internal standard band by overlaying the windowed and baseline corrected signals.

Figure 3.11(a) shows the two actions that were performed on every raw chromatogram to correct for the retention drift. The first action was to identify $t_{r\ IS}$ and to window the signal around this retention time. In the second action, the baseline offset was calculated and subtracted from the windowed signal. The baseline offset was determined as the average absorbance of a 30 seconds duration chromatogram trace (free from any eluting solutes) located 1.6 minutes before $t_{r\ IS}$ (purple box in Figure 3.11(a)).

Figure 3.11(b) shows the overlay of the two chromatograms from skin sample A and B after retention drift and baseline correction. It can be seen that the internal standard peaks overlay well with each other. Even though the retention drift changed the retention time of the analytes between runs, it did not have any influence on the retention time difference between Sumatriptan and the internal standard within a single run. As a result, the time location of Sumatriptan was identified and the peaks appearing

at this location were confirmed to be Sumatriptan. In the following figures, only the post-processed chromatograms will be shown and not the raw chromatograms.

By including an internal standard to the samples, loss of analyte during the sample preparation can be corrected during the data analysis (presuming loss of internal standard and Sumatriptan would be equivalent). As specified in Figure 3.11(b), the maximum absorbance intensity of Sumatriptan (I_{Sum}) and the internal standard (I_{IS}) were determined and the ratio was calculated:

$$R = \frac{I_{Sum}}{I_{IS}} \tag{3.3}$$

For the calibration curve, the R-values were calculated and plotted against the standard linear regression curve of known Sumatriptan concentrations in skin homogenate (Figure 3.12) and blood serum (Figure 3.13). To calculate the total amount of Sumatriptan delivered into the rescued skin, the R-value from the experimental sample was converted into concentration with the linear regression formula y= a*x* + b, with 'a' the slope (AU per µg/mL) and 'b' the intercept (AU).

Before homogenising the rescued skin tissue, PBS was added to the skin samples to achieve a concentration of 1000 µL solution/100 mg skin. To calculate the total amount of Sumatriptan in the rescued skin tissue, the concentration was multiplied by the total volume (µL) PBS added, which corresponds to 10x skin weight (mg). Therefore,

$$\text{Sumatriptan in the skin (µg)} = \left(\frac{\text{R}-\text{b}}{\text{a}}\right) \cdot (10 \cdot \text{skin weight (mg)}) \tag{3.4}$$

with *R* the ratio of $\frac{I_{Sum}}{I_{IS}}$, 'a' the slope and 'b' the intercept of the calibration curve.

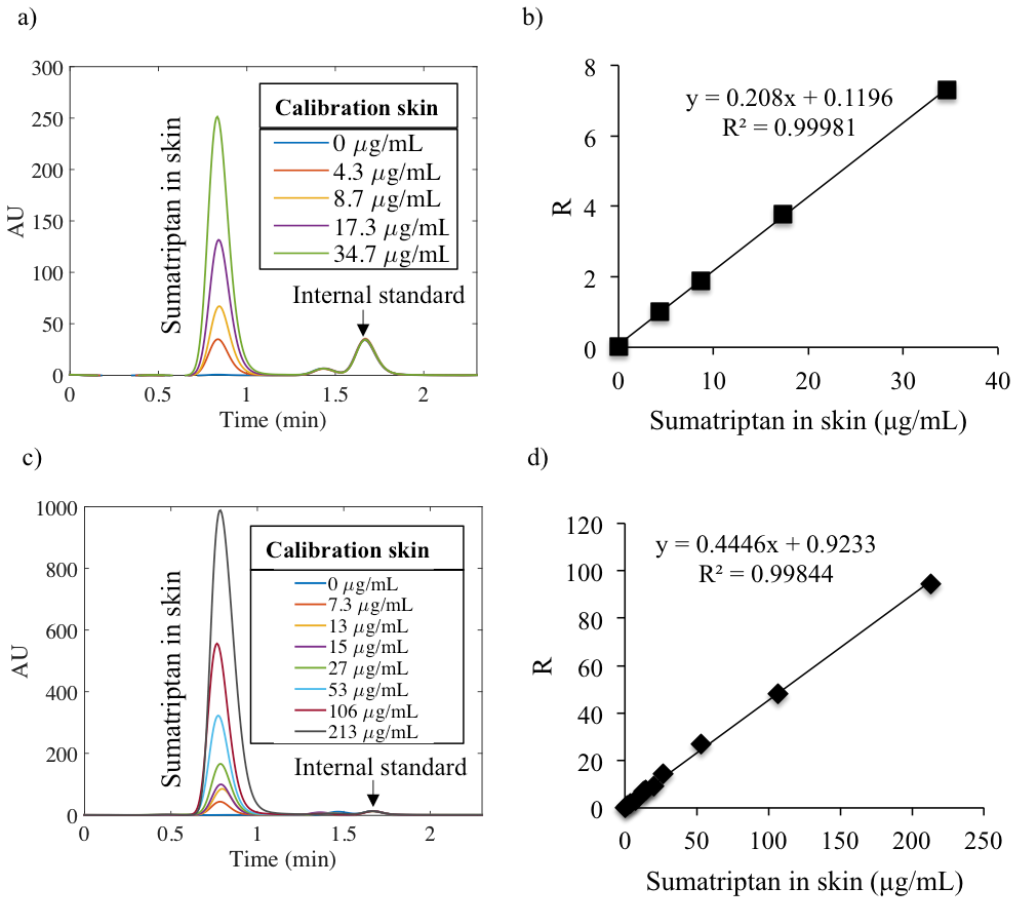

Figure 3.12: Calibration samples of Sumatriptan and internal standard in the skin. a) and c) The chromatograms of the calibration samples and b) and d) the corresponding calibration curve. a) and b) Calibration curve of blank skin samples spiked with known Sumatriptan amounts used to analyse Sumatriptan levels in the skin samples from the 'Safety Study' and 'Sumatriptan Repeat Study 1'. c) and d) Calibration curve of blank skin samples spiked with known Sumatriptan amounts made to quantify Sumatriptan levels in the skin samples from 'Sumatriptan Repeat Study 2'.

To determine how much of the applied dose was delivered into the skin (and therefore the delivery efficiency of the technology), the following formula was used:

$$\text{Dose delivery in skin (\%)} = \left(\frac{\text{µg Sumatriptan in skin}}{\text{10.4 mg applied dose}}\right) \cdot 100\% \qquad (3.5)$$

with 'applied dose' meaning the amount present in the formulation holder, calculated as the product of the Sumatriptan concentration in the formulation and the applied volume required to fill the formulation holder.

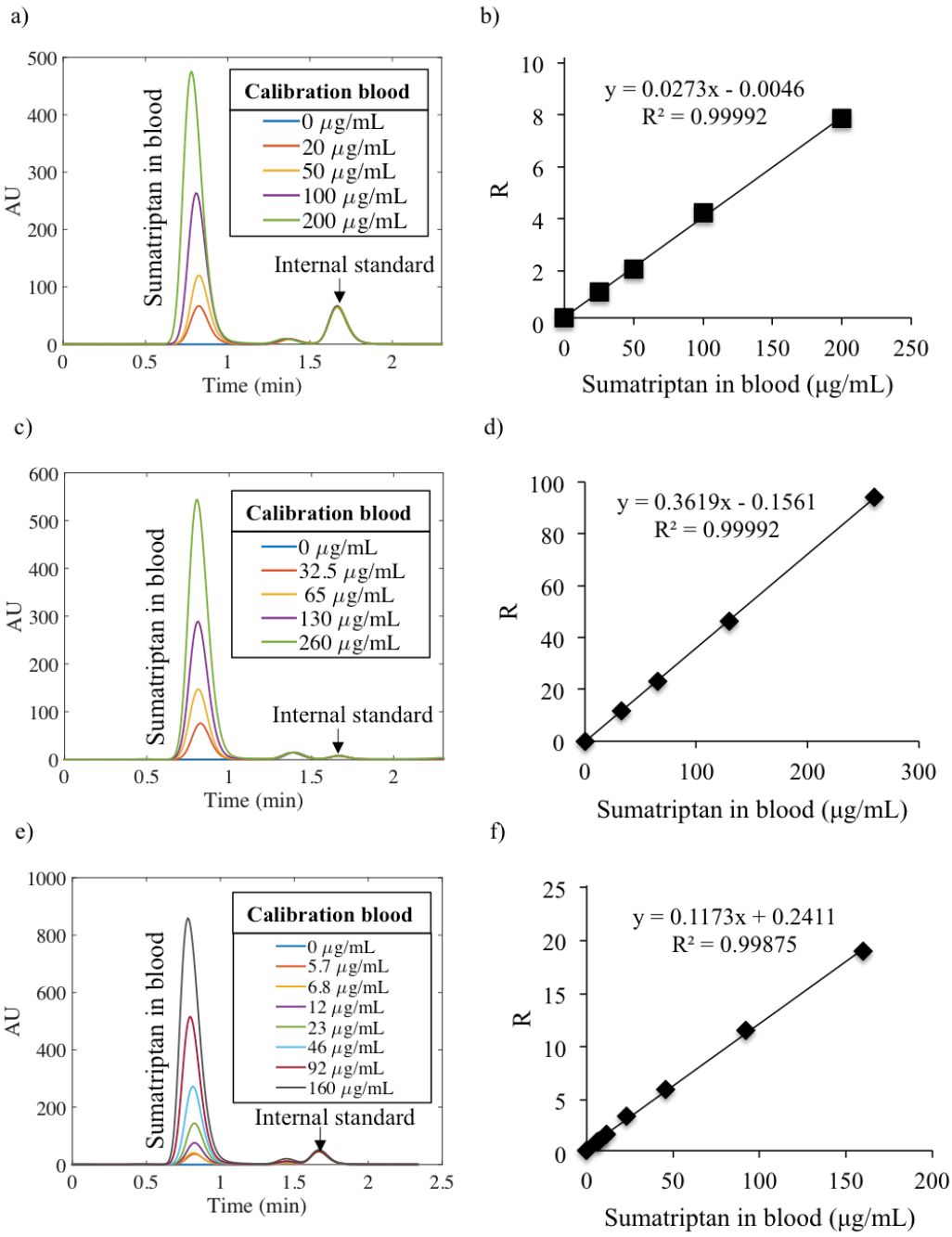

Figure 3.13: Calibration samples of Sumatriptan and internal standard in blood. a), c) and e) The chromatograms of the blood calibration samples and b), d) and f) the corresponding calibration curves calculated from the chromatograms. a) and b) Calibration curve of blank blood samples spiked with known Sumatriptan amounts and used to quantify Sumatriptan in blood samples from the 'Safety Study'. c) and d) Calibration curve made up with the blood samples from the 'Sumatriptan Repeat Study 1' and e) and f) for the 'Sumatriptan Repeat Study 2'.

The same calculation method was applied to the blood samples, but with the R-value plotted against the Sumatriptan concentration in blood serum (µg/mL) as shown in Figure 3.13.

The blood from the mouse was diluted with PBS (dilution factor 5) to obtain the blood serum. By assuming the total blood volume of a mouse to be 1.4 mL, the total Sumatriptan in the whole blood was calculated as following:

$$\text{Sumatriptan in whole mouse blood (µg)} = 5 \cdot \left(\frac{R-\text{b}}{\text{a}}\right) \cdot 1.4 \qquad (3.6)$$

with R the ratio of $\frac{I_{Sum}}{I_{IS}}$, 'a' the slope, and 'b' the intercept of the linear regression curve.

The dose delivery in blood was determined in the same way as formula 3.5, but with the total Sumatriptan delivery into the blood instead of skin. Although this method was substantially more labour intensive than the ELISA used for assaying antibody delivery in the previous chapter, the improved R^2 values and reproducibility across experiments, as well as the switch from *ex vivo* pig skin to *in vivo* mouse skin, provided confidence that more robust data could be obtained.

3.3 Results

3.3.1 In vivo Sumatriptan delivery – Safety Study

In the first Sumatriptan *in vivo* study, different acoustic pressures were used to identify the effective acoustic pressure to deliver Sumatriptan, without inducing skin damage. Firstly, the results from the recorded acoustic activity are described and then the effect on skin damage assessed. Next, the Sumatriptan delivery into the skin and bloodstream are evaluated.

3.3.1.1 Safety Study – Characterisation of pre-focal cavitation

Before post-processing the recorded PCD traces into acoustic emission spectrograms (see methods section 3.2.2), the raw PCD trace was closely inspected. An example of the envelope signal of the voltage trace recorded during 2.1 MPa acoustic pressure is presented in Figure 3.14(a).

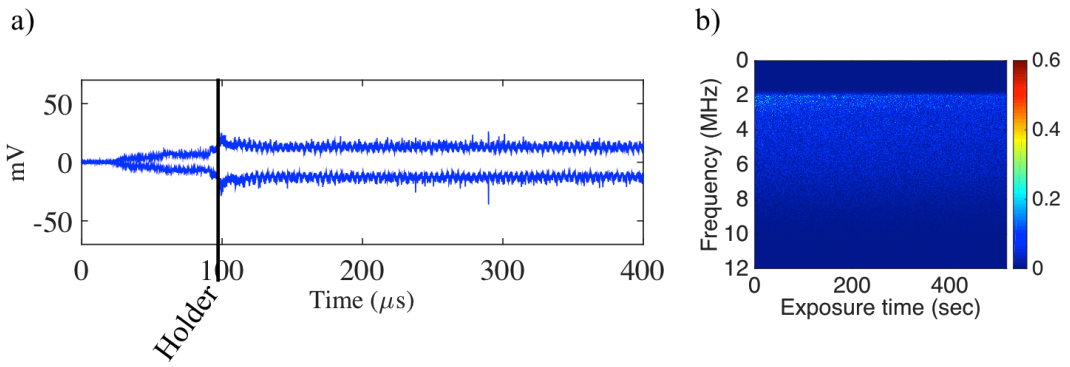

Figure 3.14: Characterisation of the raw PCD trace for pre-focal acoustic activity – Safety Study. a) Envelope signal of PCD voltage trace recorded from the 'Cavitation' group from the safety study acquired at 2.1 MPa peak negative. The line at 99.4 μs indicates the time-of-flight corresponding to the end of the cone - formulation holder interface ('Holder'). b) Acoustic emission spectrograms of the pre-focal signal (0-99.4 μs). The colour bar on the right axis represents the power spectral density (mV^2/Hz).

Notably, the PCD trace showed increasing voltage between 0 μs and where the holder starts (99.4 μs) (Figure 3.14(a)). This was not observed in the *ex vivo* study performed on pig skin (Chapter 2, Figure 2.4). To investigate the origin of the acoustic activity in the coupling cone (i.e. pre-focal cavitation), the frequency composition of the time

window 0-99.4 μs was characterised and the frequency spectra are presented in Figure 3.14(b). In the acoustic emission spectrogram, there are light blue speckles visible from 2.0 MHz to around 6.0 MHz for the entire exposure duration. Such broadband acoustic emissions are typically associated with the presence of inertial cavitation [213]. Therefore, the location and frequency spectra of this inertial cavitation activity indicate it originates pre-focally in the coupling cone, possibly due to incomplete degassing of the water in the cone.

Typically, the coupling cone is filled with degassed water to enhance the acoustic coupling between the transducer and the skin, and to instigate inertial cavitation only at the ultrasound focus (within the formulation and the skin, see Figure 3.4(b)), where the acoustic pressure crosses the cavitation threshold of the NCs. In case of incomplete degassing of the water in the coupling cone, the low acoustic pressures induced inside the coupling cone could be sufficient to cross the cavitation threshold of the air-rich water and the present bubbles to cavitate (leading to the detection of pre-focal activity). As a result, it is possible that inertial cavitation inside the cone generated a bubble cloud that reduced the acoustic energy entering the formulation. Ultimately, this may have resulted in lower acoustic pressure levels inside the formulation holder than desired. This pre-focal cavitation was observed in all the PCD traces in the 'Safety Study'.

3.3.1.2 Safety Study – Cavitation detection

The acoustic emissions originating from within the formulation holder and mouse skin were isolated as described in section 3.2.2. The acoustic emission spectrograms were characterised (Figure 3.15(a)) and the average TASE value was determined for the three acoustic pressures (Figure 3.15(b)).

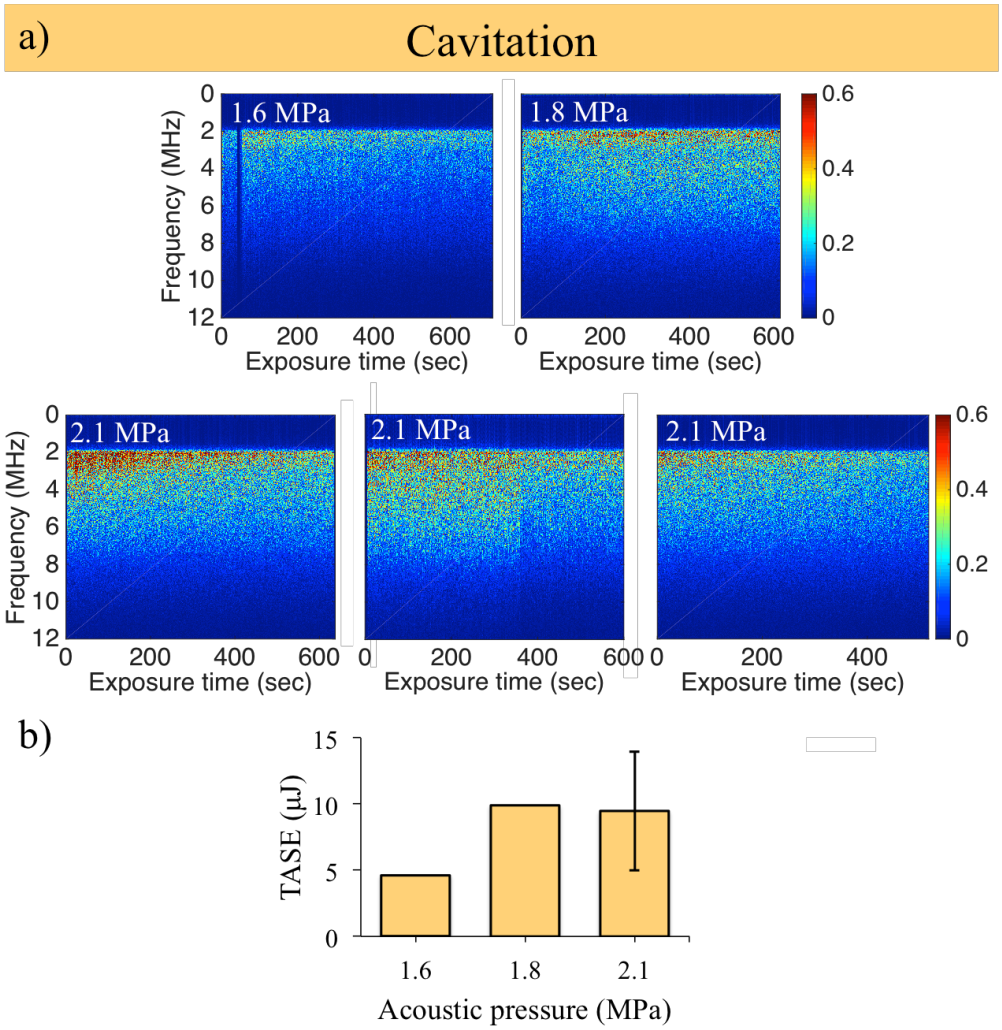

Figure 3.15: Acoustic emission spectrograms from NCs exposed to 1.6, 1.8 and 2.1 MPa acoustic pressure – Safety Study. a) The acoustic emissions were recorded for the 'Cavitation' treatment group only (in the absence of ultrasound there is nothing to record). The colour bar on the right axis represents the power spectral density (mV^2/Hz). b) The bar chart shows the TASE level determined per treatment group and the error bar represent the standard deviation for n=3 mice at 2.1 MPa.

In all the five acoustic emission spectrograms shown in Figure 3.15(a), sustained broadband acoustic emissions (green/red band) were recorded over the total 10-minutes treatment time indicating the presence of sustained inertial cavitation in the windowed signal. From visual assessment of Figure 3.15(a) it is clear that the acoustic emission spectrogram at 1.6 MPa exhibits weaker broadband acoustic emissions than at 2.1 MPa. To quantify this observation, the TASE value was calculated for each acoustic emission spectrogram and presented in the bar chart (Figure 3.15 (b)). The TASE value calculated for the single case of 1.6 MPa was two-fold less (4.64 µJ) than determined

for 1.8 MPa (9.90 μJ). The average of the three samples exposed to 2.1 MPa was 9.48 ± 4.48 μJ.

3.3.1.3 Safety Study – Investigation of skin damage

In this section, the effect of sustained inertial cavitation on the skin damage was assessed using the photographic images of the rescued mouse skin for the two exposure conditions (Figure 3.16).

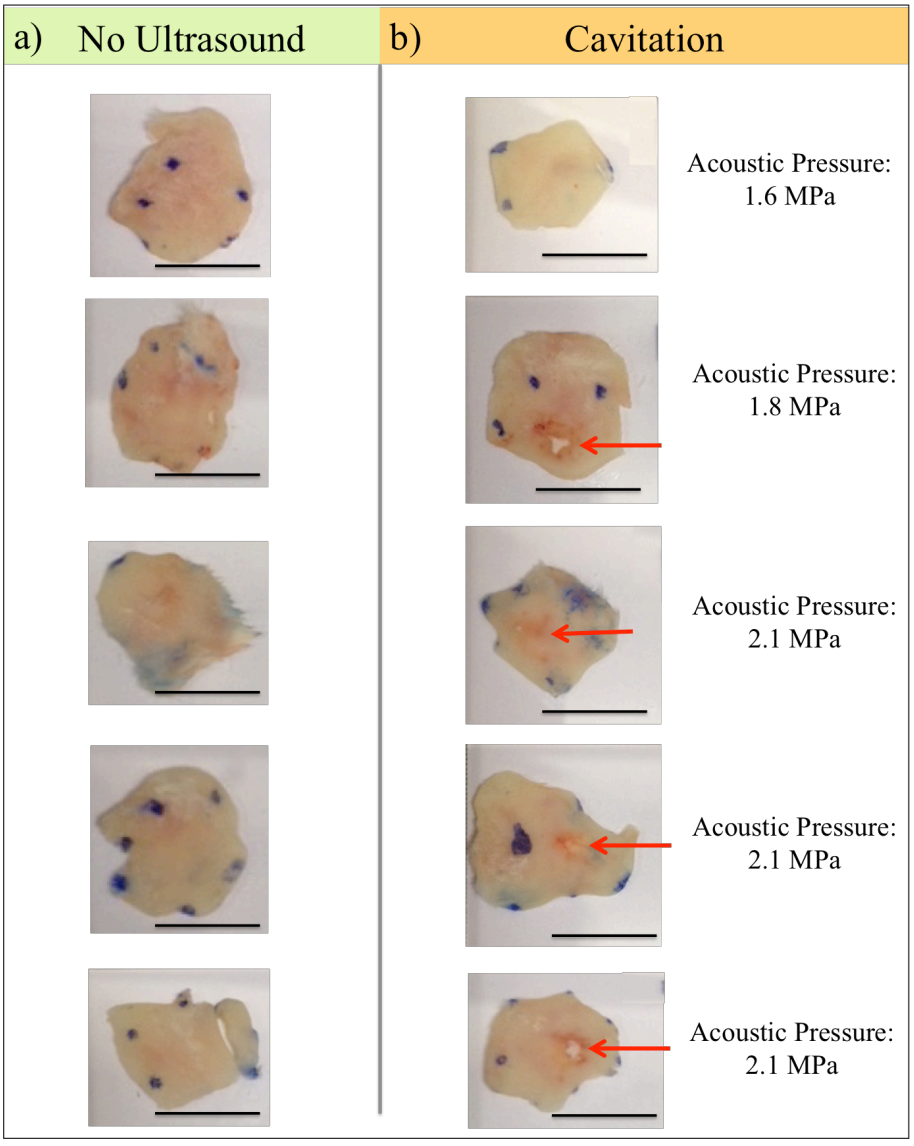

Figure 3.16: Assessment of skin damage after treatment of BALB/c mice – Safety Study. Photographic images are shown from rescued skin from BALB/c mice with (a) 'No Ultrasound', and (b) from mice treated with ultrasound-mediated cavitation ('Cavitation') at different stated acoustic pressures. After 10-minutes treatment and 10-minutes recovery time, the skin was rescued and processed as described in section 3.2.9. The blue dots on the skin mark the treatment area and the scale bar corresponds to 1 cm. Skin damage in the form of reddening and white spots (marked with the red arrow) was observed in the mice exposed to acoustic pressures above 1.6 MPa peak negative.

Figure 3.16 shows the photographic images of the rescued skin collected at T_{20}. No skin damage was observed within the treated area of the mice that were not exposed to ultrasound (Figure 3.16(a)). Applying ultrasound to the skin and generating sustained inertial cavitation was not visibly harmful to the skin at a peak negative pressure of 1.6 MPa (Figure 3.16(b)). However, higher acoustic pressures produced redness and white marks on the skin (see red arrows in Figure 3.16(b)). Given that previous experimentation had shown that temperature rises at these frequencies and pressures are negligible [149], the white marks were most probably induced by surface cavitation caused by bubbles trapped on the skin surface at these pressures, or may even represent the presence of opaque NCs.

3.3.1.4 Safety Study – Sumatriptan delivery into the skin

Next, the dermal delivery of Sumatriptan was investigated. The homogenised skin samples were analysed by HPLC (as described in section 3.2.9) and the chromatograms are presented in Figure 3.17(a) and (b). The dermal delivery results for each acoustic pressure as well as the percentage of the total dose delivered into the skin are shown in Figure 3.17(c).

It can be seen that in the 'No Ultrasound' group (Figure 3.17(a)), three out of five mice have maximum absorbance values above 130 AU at the time corresponding to the elution of Sumatriptan, and two mice have values around 40 AU. Figure 3.17(b) shows that the mice exposed to acoustic pressures of 1.8 and 2.1 MPa have Sumatriptan peak values around 80 AU. The lowest Sumatriptan peak value was observed for the mouse exposed to 1.6 MPa.

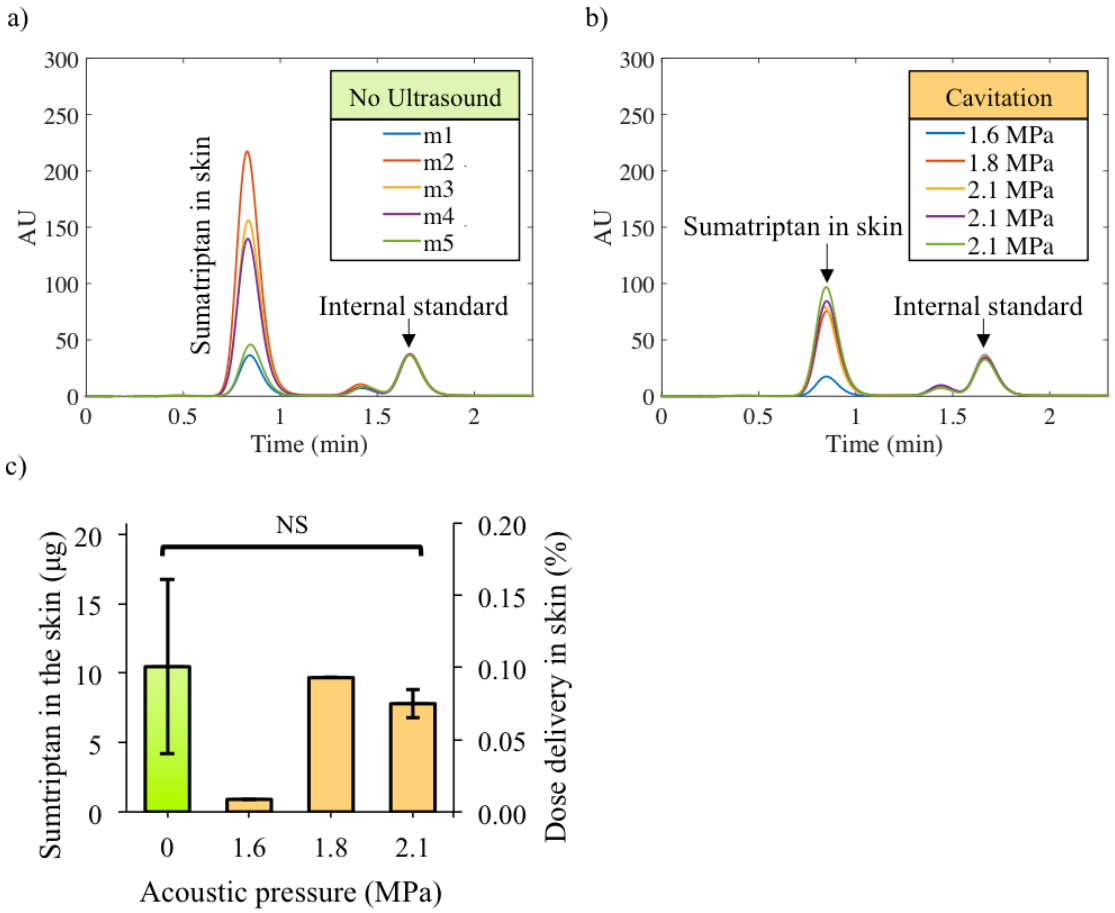

Figure 3.17: Sumatriptan delivery into the skin – Safety Study. Chromatograms of the skin samples from the mice treated (a) without ('No Ultrasound') and (b) with ultrasound ('Cavitation'). The HPLC traces are re-aligned to the internal standard peak and the baseline is corrected as described in section 3.2.11. c) Bar chart showing the total Sumatriptan amount in the skin on the left axis and percentage dose delivery into the skin on the right axis. Error bar represents the standard deviation for n=5 at 0 MPa and n=3 for 2.1 MPa. The significant difference was determined by t-test. NS: no significance**.**

The calculated R-value for every mouse was converted into Sumatriptan concentration in the skin samples (based on the calibration curve Figure 3.12(b)) and the total Sumatriptan amount delivered into the rescued skin as well as the percentage dose delivery was calculated with the formulas 3.5 and 3.6 (described in section 3.2.11). The delivery results are presented per exposed acoustic pressure in Figure 3.17(c). Since the 'No Ultrasound' group had five mice treated at 0 MPa and the 'Cavitation' group three mice treated with 2.1 MPa, the significance was calculated between these two groups.

Without applying any ultrasound to the mice, 10.46 ± 6.28 μg (corresponding with 0.10 ± 0.06% applied dose) Sumatriptan was found in the rescued skin at T_{20}. Similar levels were found after exposing the mice to 1.8 MPa (9.7 μg, 0.09% applied dose) or 2.1 MPa (7.8 ± 1.0 μg, 0.07 ± 0.01% applied dose). Notably, exposing the mouse to 1.6 MPa delivered 11-fold less Sumatriptan in the skin (0.9 μg, 0.01% applied dose) than the 'No Ultrasound' group. Examination of Figure 3.16(b) showed no visual damage to the skin of this 1.6 MPa insonated mouse.

There was no significant difference ($p>0.05$) between the Sumatriptan delivery into the skin after applying 2.1 MPa and recording broadband emissions, or no ultrasound at all. Therefore, this data shows that there is no enhanced delivery into the skin after applying cavitation-enhanced ultrasound, in contradiction with a published study [149]. The measured levels of Sumatriptan in the skin homogenate by HPLC represented the amount of Sumatriptan above the SC layer as well as in or below. No distinction can be made on the location of the drug after skin harvest. Therefore, the drug that was merely associated with the skin surface may overwhelm lower more specific levels of delivery. As a consequence, in further repeat studies, a more thorough washing of skin was performed before the skin was rescued.

3.3.1.5 *Safety Study – Sumatriptan delivery into the bloodstream*

The collected blood samples at T_{20} were analysed by HPLC and the chromatograms of the two experimental groups are presented in Figure 3.18.

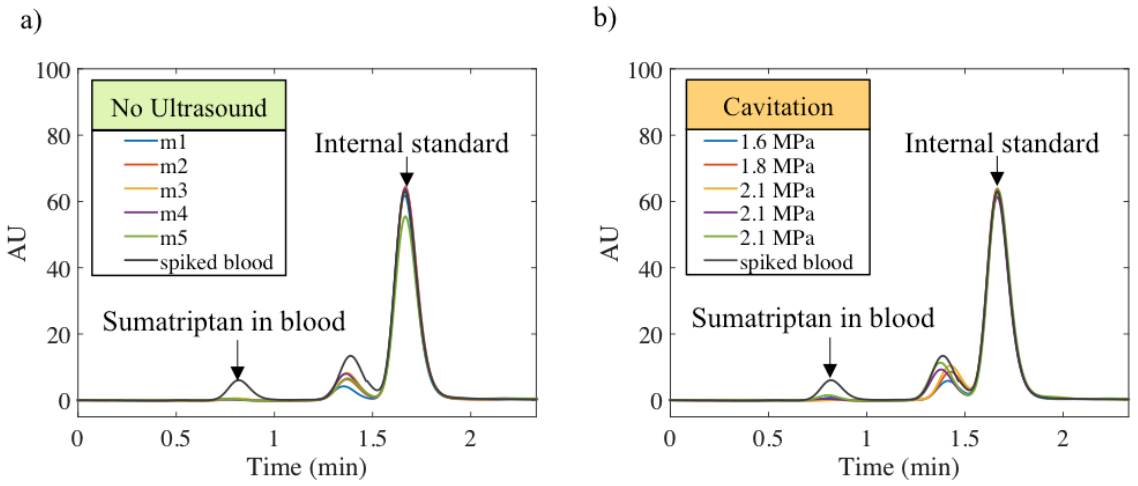

Figure 3.18: Sumatriptan delivery into the blood – Safety Study. Chromatograms of the blood samples from the mice treated (a) without ('No Ultrasound') and (b) with ultrasound ('Cavitation'). Methodology for rescue and analysis of the blood samples is described in section 3.2.9. To confirm the location of the Sumatriptan peak, an extra sample of known Sumatriptan concentration spiked into the blood was added ('spiked blood'). For elution protocol and calibration curve protocol, see section 3.2.11.

Figure 3.18 shows the chromatograms of the blood samples taken at T_{20}. An extra chromatogram of spiked blood was added to the chromatograms to confirm the location of Sumatriptan. No discernible Sumatriptan peaks were found in the blood samples in either of the experimental groups, even when comparing with the traces from the T_0 blood samples (data not shown). Therefore, Figure 3.18 shows that both treatments were unsuccessful in delivering Sumatriptan into the bloodstream 20 minutes post-treatment.

Notably, it can be observed in Figure 3.18 that a third peak is visible between Sumatriptan and the internal standard at ~1.2 min. This peak corresponds to a blood component that is present in every mouse but different in quantity (peak heights). This peak has no influence on the detection of Sumatriptan or the internal standard.

3.3.1.6 Safety Study – Discussion

The aim of the 'Safety Study' was to demonstrate the safety and feasibility of the delivery of Sumatriptan *in vivo* using cavitation-enhanced transport. The results showed a relationship between the level of cavitation recorded by PCD and the level of visible reddening of the skin within the exposed region. It is notable that this reddening did not develop into a permanent bruise, caused no loss in mouse activity or change in behaviour, and was shown in subsequent experiments to resolve within 24 hours with no impact on mouse welfare, health or weight.

Contrary to expectations there was no correlation between enhanced Sumatriptan delivery into the skin and raised cavitation levels. Indeed, the sumatriptan delivery levels found in the 'Safety Study' were equivalent at 2.1 MPa (recording TASE value of 9.48 ± 4.48 μJ) and 0 MPa. Furthermore, Sumatriptan was not detected in any of the blood samples from the BALB/c mice. These findings show that there was no enhanced delivery effect after ultrasound-mediated cavitation and are therefore in contradiction with published studies [109, 172, 201-203] as well as previous e*x vivo* IgG Studies (Chapter 2) and can be explained by the following factors.

Firstly, the failure to achieve delivery could be a result of the pre-focal cavitation evident in the PCD traces (Figure 3.14). Ideally, there would be no pre-focal cavitation activity, and the acoustic emissions recorded from 99.4 μs onwards would originate only from within the formulation holder and the mouse skin. However, acoustic emissions were recorded prior to the holder and their acoustic emissions overlapped with the emissions originating from within the formulation holder and the mouse skin during 2650 cycles long ultrasound pulse.

As a result, the windowed signal contained acoustic information from the formulation, the mouse as well as from the pre-focal cavitation activity. However, there is a slight increase in voltage at 99.4 μs in Figure 3.14(a) at the time-of-flight corresponding with the start of the holder. This increase in signal could originate from the cavitating NCs in the formulation. Unfortunately, with a single PCD element little spatial resolution can be determined and it is not certain how much of the calculated TASE value in Figure 3.14(c) is contributed by pre-focal cavitation.

Secondly, the pre-focal cavitation could generate a bubble cloud in front of the transducer (shielding) reducing the acoustic energy entering the formulation. Ultimately, this may have resulted in lower acoustic pressure levels inside the formulation and caused insufficient NCs activity in the holder formulation and mouse skin. In order to prevent pre-focal cavitation, the degassing time of the water in the coupling cone was prolonged in subsequent experiments.

Thirdly, there are concerns regarding how effectively the skin samples were washed post-exposure, perhaps leading to surface contamination of all skin samples to a level which overwhelmed any genuine delivery into the skin. Therefore, in subsequent studies the exposed skin area was more effectively washed post-exposure to remove any formulation residue on the skin surface.

Finally, it was notable that the BALB/c mice used here in the ‘Safety Study’ required the fur to be thoroughly removed using an electric razor and then depilatory cream just prior to the experiment. Despite thorough washing to remove the cream and residual fur, it is possible that this process could have changed the hydrophobicity of the skin.

This may have led to the entrapment of bubbles on the surface when the formulation was applied. When turning on the ultrasound, the entrapped bubbles could undergo inertial cavitation causing skin damage in the form of redness and white marks (Figure 3.16(b)) due to mechanical cavitation effects. However, for the ultimate clinical application, skin damage is not desirable. Therefore, the lowest pressure that could result in delivery without causing skin damage (1.6 MPa) was chosen for the next study. Furthermore, to remove the possibility that mouse fur was detrimentally impacting on the delivery, the experiment was repeated for the first time using CD1 nude (see next section).

3.3.2 In vivo Sumatriptan Repeat Study 1

In this first repeat study, the Sumatriptan delivery experiment was performed with the inclusion of one additional experimental group 'Sub Cavitation', whereby the drug formulation on the skin was exposed to 1.0 MPa acoustic pressure. With the therapeutic ultrasound setup described in section 3.2.1, this acoustic pressure was below the threshold to generate inertial cavitation activity. Nude mice were used for the study to eliminate the influence of hair and fur removal agents on transdermal delivery. These changes and the addition of the extra control group ensured that all experimental limitations identified in the 'Safety Study' were addressed.

3.3.2.1 Sumatriptan Repeat Study 1 – Inspection of pre-focal cavitation

In the 'Safety Study', pre-focal cavitation was identified as a possible factor in the lack of transdermal delivery achieved. Therefore, for successful delivery it is important that the raw PCD traces do not show acoustic emissions originating pre-focally. As a result of prolonged degassing time of the water in the cone, no pre-focal cavitation was observed in either this repeat study, or any subsequent studies.

An example of the envelope signal of the voltage trace (recorded during insonation at 1.6 MPa) is presented in Figure 3.19.

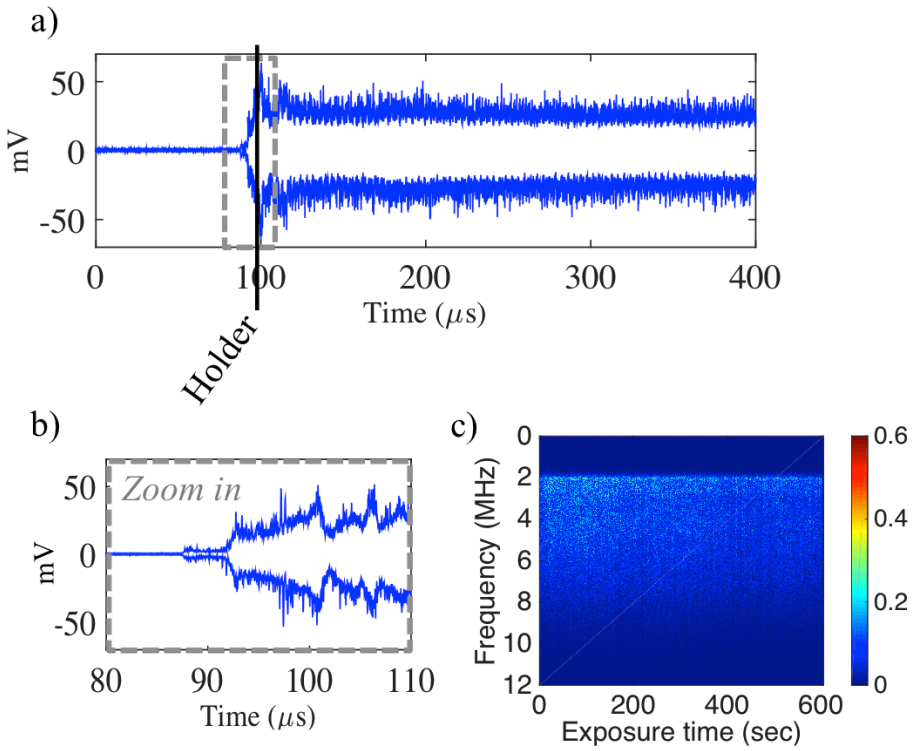

Figure 3.19: Characterisation of raw PCD trace for pre-focal acoustic activity – Sumatriptan Repeat Study 1. a) Enveloped signal of a representative PCD trace recorded from the 'Cavitation' group acquired at 1.6 MPa peak negative. The black line indicates the time-of-flight corresponding to the end of the cone-formulation holder interface ('Holder') and b) a zoom-in of the grey dotted window. c) Acoustic emission spectrograms of the pre-focal trace (0 – 94.08 μs window) with the colour bar representing the power spectral density (mV^2/Hz).

Figure 3.19(a) shows the envelope of a representative PCD voltage trace from the 'Cavitation' group. Between the transducer (0 μs) and where the formulation holder starts (99.4 μs) the voltage trace appeared to be flat (i.e. absence of pre-focal cavitation), and then increased sharply at the time point that corresponds to acoustic emissions originating from within the formulation holder. However, a closer analysis of the zoomed-in trace in Figure 3.19(b) showed that low voltages (± 8 mVpp) were observed in the window 89.46-94.08 μs, just before where the holder starts (i.e. pre-holder trace). To investigate the cause of the pre-holder trace, the spectral content over the time

window 0-94.08 μs was calculated and the acoustic emission spectrogram is presented in Figure 3.19(c).

The acoustic emission spectrogram in Figure 3.19(c) shows the presence of a broad range of frequencies present in the pre-holder trace over the total duration. Broadband acoustic emissions were observed which relate to the occurrence of inertial cavitation in the region between the transducer and the formulation holder. Yet, the pre-holder trace occurred almost instantly at 89.45 μs and it was not observed closer to the transducer as was in the 'Safety Study' (Figure 3.14(a)). This indicates that the acoustic pressure in the coupling cone at 89.45 μs crossed the cavitation threshold of the degassed water to start inertial cavitation. When taking a closer look at the normalised pressure profile of the ultrasound within the coupling cone II (Figure 3.3(b)), the start of the pre-holder activity can be related to the presence of a small ultrasound focus located at Z=-10 mm.

In conclusion, the precaution of extending the degassing time of the water in the cone has helped to permanently remove the pre-focal cavitation activity.

3.3.2.2 Sumatriptan Repeat Study 1 – Cavitation detection

From the recorded PCD traces, the acoustic emissions originating from within the formulation holder and mouse skin were isolated as described in section 3.2.2. The acoustic emission spectrograms were characterised (Figure 3.20(a) and (b)) and the TASE values were determined (Figure 3.20(c)) for the 'Sub Cavitation' and 'Cavitation' group.

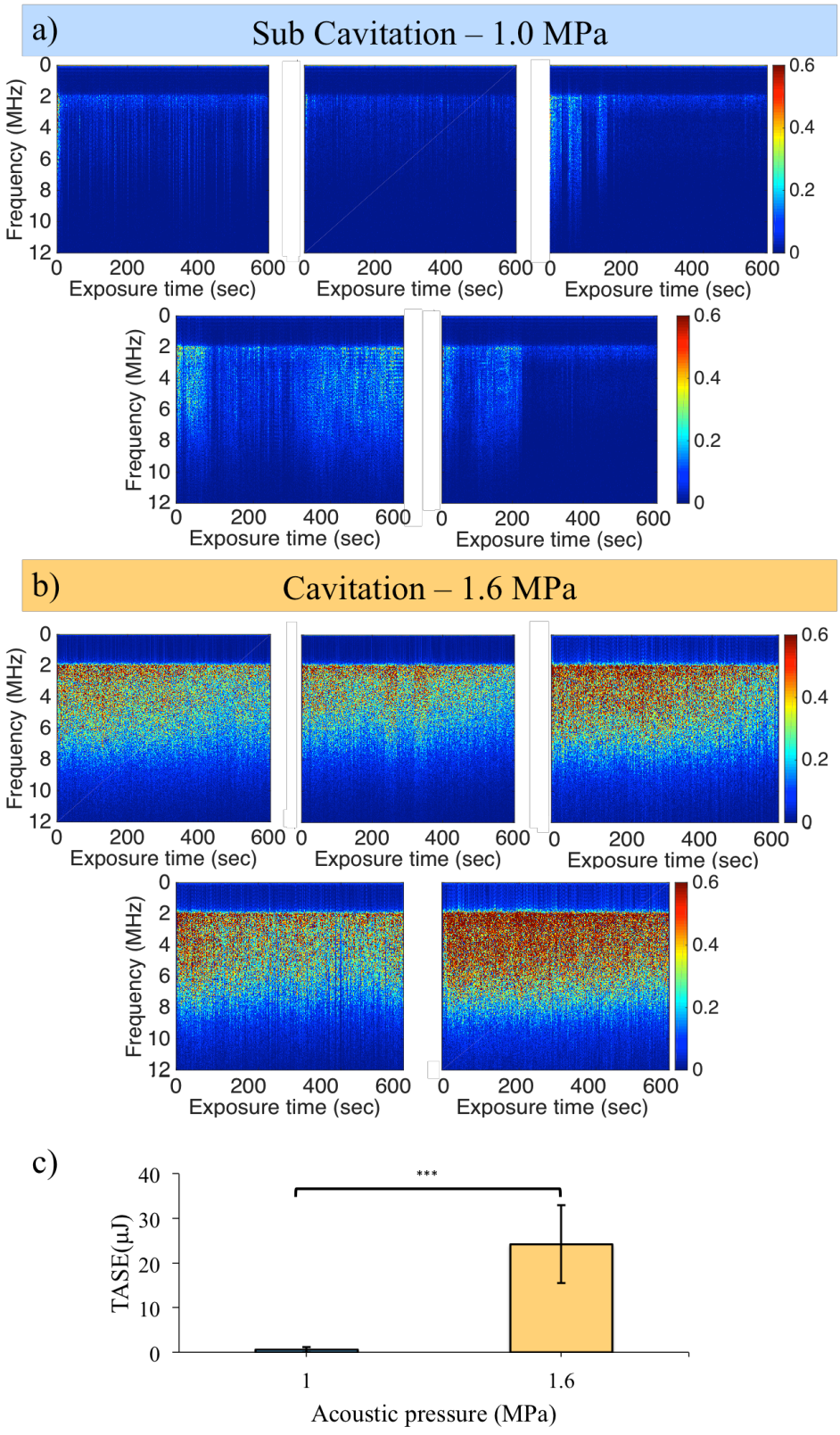

Figure 3.20: Acoustic emission spectrograms from NCs exposed to (a) 1.0 MPa ('Sub Cavitation') and (b) 1.6 MPa ('Cavitation') – Sumatriptan Repeat Study 1. The colour bar on the right axis represents the power spectral density (mV^2/Hz). c) The bar chart shows the mean of the Total Acoustic Sensor Energy (TASE) determined per treatment group with the exclusion of the 'No Ultrasound' group. In the absence of ultrasound there is nothing to record. The error bars represent the standard deviation for n=5 mice. The significant difference was determined by t-test and *** corresponds to $p<0.001$.

Figure 3.20(a) shows that exposing the formulation to 1.0 MPa caused only sporadic broadband acoustic emissions to be detected (light blue bands) and some harmonics (horizontal bands), attributed to gas entrapped in the formulation as well as sporadic activity of NCs. Stronger and sustained broadband acoustic emissions (red bands) were recorded for all the five mice over the full 10-minutes exposure time when the mice were insonated at 1.6 MPa (Figure 3.20(b)). This indicates the presence of sustained inertial cavitation within the formulation during the 'Cavitation' treatment.

Figure 3.20(c) shows the TASE value detected over the 10-minutes exposure time for the two acoustic pressures. Substantially (40-fold) and significantly ($p<0.01$) stronger energy (24.19 ± 8.73 μJ) was detected in the 'Cavitation' group than in the 'Sub Cavitation' group (0.62 ± 0.61 μJ). Notably, these cavitation levels were substantially higher than those recorded in the 'Safety Study' (9.48 ± 4.48 μJ at 2.1 MPa, Figure 3.20(b)). This improvement is perhaps a consequence of reduced 'shielding' by pre-focal cavitation.

3.3.2.3 Sumatriptan Repeat Study 1 – Investigation of skin damage

The effect of sustained inertial cavitation on the skin damage was assessed using the photographic images of the rescued nude mouse skin for the three exposure conditions (Figure 3.21). No skin damage was observed within the treated area of the nude mice that were exposed to 'No Ultrasound' (Figure 3.21(a)) and 'Sub Cavitation' (Figure 3.21(b)). In agreement with the skin samples in the 'Safety Study' (Figure 3.16(b)), no effects suggesting major irreversible skin damage were observed after exposing the skin to 1.6 MPa. Only sporadic, transient, very minor reddening of the skin was observed in two out of the five mice (highlighted by the red arrows, Figure 3.21(c)). In subsequent studies, this reddening was shown to resolve in less than 24 hours.

Notably, despite levels of cavitation being substantially (~ 2.5 fold) higher than in the 'Safety Study' (compare 24.19 ± 8.73 µJ in Figure 3.20(c) versus 9.48 ± 4.48 µJ in Figure 3.14(b)), the level of reddening was lower. This perhaps indicates that concerns over entrapment of bubbles on the skin permitting surface cavitation had been successfully addressed by the change in mouse model.

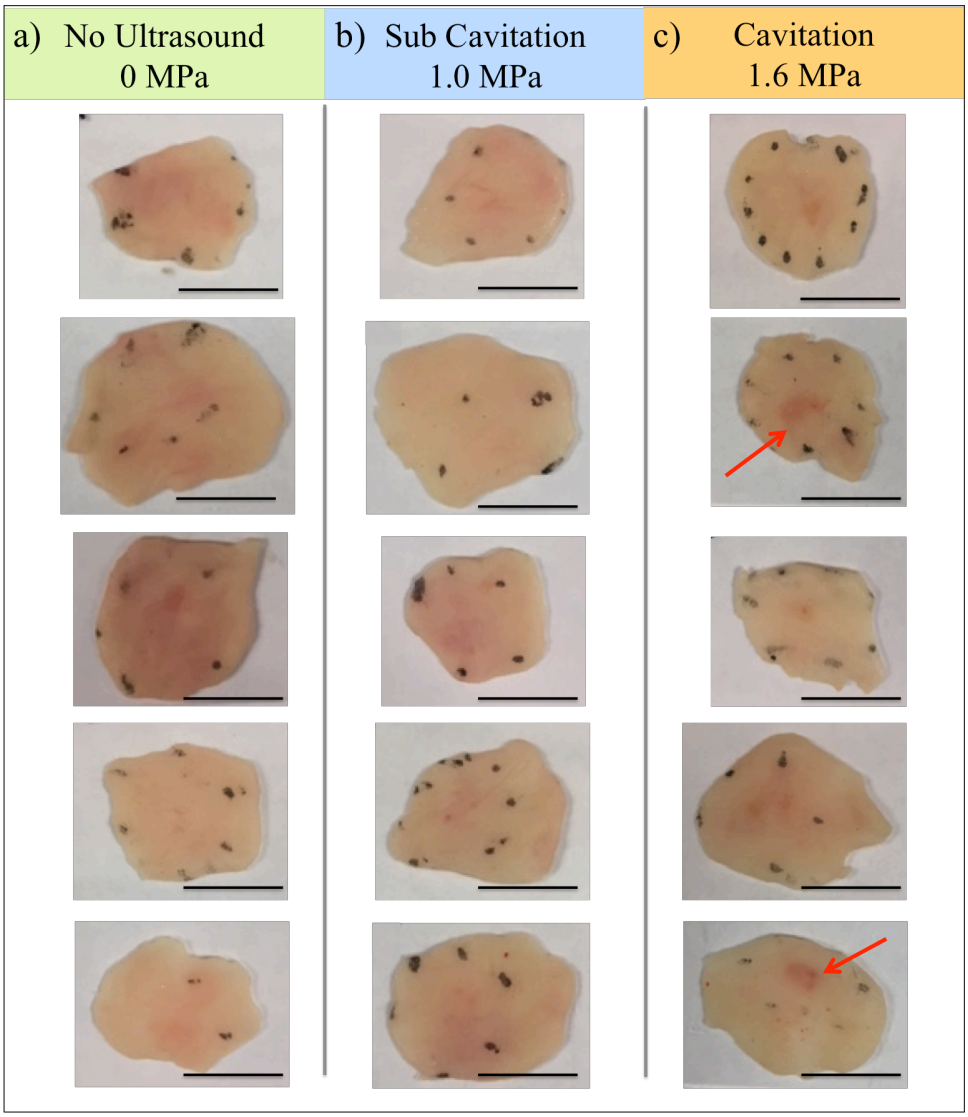

Figure 3.21: Assessment of skin damage after treatment of nude mice – Sumatriptan Repeat Study 1. Photographic images are shown from rescued skin from hairless mice treated with (a) 'No Ultrasound', (b) 'Sub Cavitation', or (c) 'Cavitation'. After 10-minutes treatment and 10-minutes recovery time, the skin was rescued and processed as described in section 3.2.9. The red arrows highlight minor areas of reddening on the skin after cavitation. The black dots on the skin mark the treatment area and the scale bar corresponds to 1 cm.

3.3.2.4 Sumatriptan Repeat Study 1 – Sumatriptan delivery into the skin

In this section, the dermal delivery of Sumatriptan was investigated and the post-processed chromatograms are presented in Figure 3.22(a-c). The calibration curve (shown in Figure 3.12(b)) was used to calculate the total amount of Sumatriptan in the skin as well as the percentage of the total dose delivered into the skin, both presented in Figure 3.22(d).

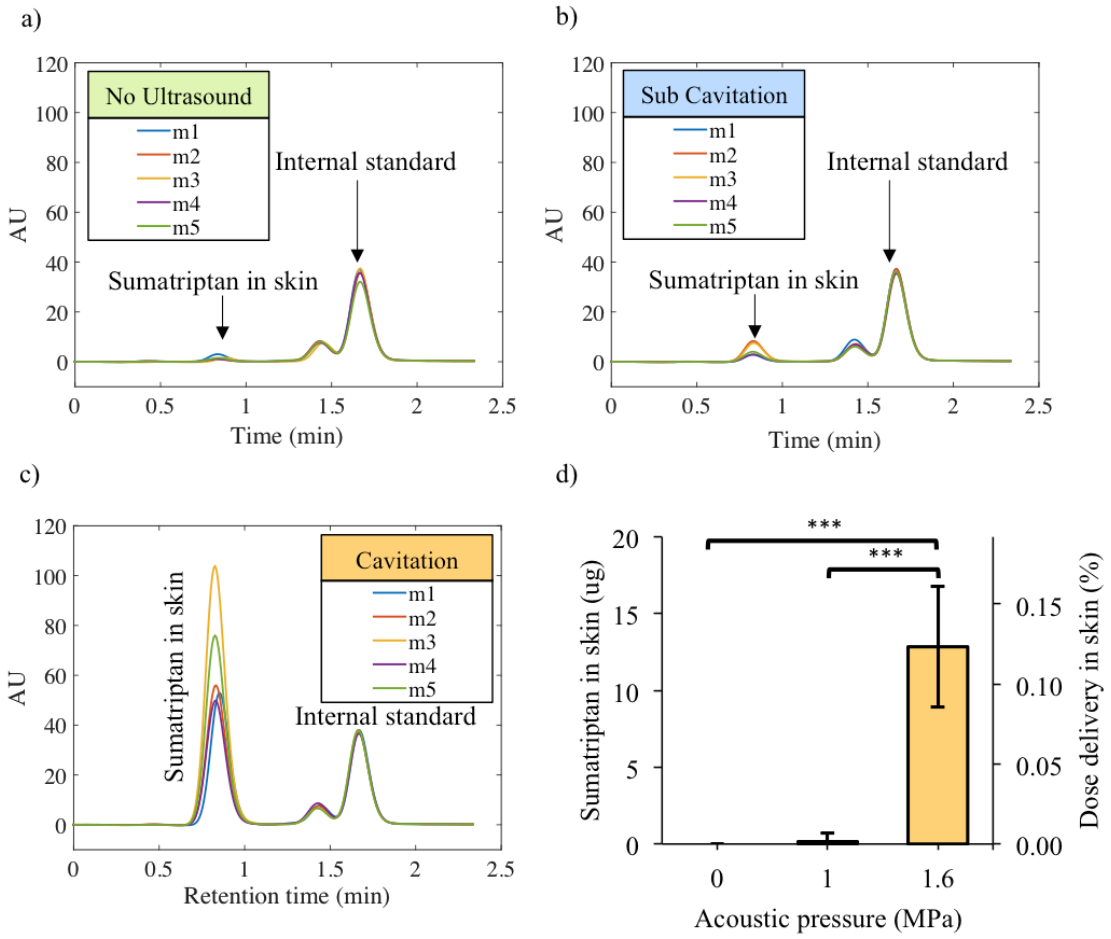

Figure 3.22: Sumatriptan delivery into the skin – Sumatriptan Repeat Study 1. Chromatograms of the skin samples from the mice treated with (a) 'No Ultrasound', (b) 'Sub Cavitation', or (c) 'Cavitation'. The traces are re-aligned to the internal standard peak and the baseline is corrected as described in section 3.2.11. d) Bar chart showing the total Sumatriptan amount in the skin on the left axis and percentage dose delivery into the skin on the right axis. Error bar represents the standard deviation. The significant difference was determined by one-way ANOVA Bonferroni multiple comparison tests. *** corresponds to $p<0.001$.

Figure 3.22(a) demonstrates that of the five skin samples that were exposed to 'No Ultrasound', only one skin sample (m1) yielded detectable levels of Sumatriptan. In the 'Sub Cavitation' group (Figure 3.22(b)), two out of five mice had slightly higher absorbance peak values, in the order of 10 AU. These dermal levels are much reduced compared to those found in the 'No Ultrasound' group in the 'Safety Study' (Figure 3.17). This could indicate that the more stringent post-exposure washing procedure was successful in removing Sumatriptan formulation residue from the skin surface after treatment. This enhanced the reliability of the measured signal that the detected Sumatriptan in the skin homogenate did not include a false-positive result from the formulation residue on the skin surface, but represented the Sumatriptan amount delivered beyond the SC.

The average amount of Sumatriptan detected in the skin at T_{20} was negligible for the 'No Ultrasound' group. Slightly enhanced delivery was observed in the 'Sub Cavitation' group with 0.44 ± 0.31 μg Sumatriptan. However, the highest amount was calculated to be 12.82 ± 3.93 μg Sumatriptan in the 'Cavitation' group. These levels correspond to 0.004% ± 0.003%, or 0.123% ± 0.038% of the applied dose for the 'Sub Cavitation' or the 'Cavitation' group, respectively. The mean Sumatriptan level recovered from the 'Cavitation' group was therefore substantially (~30-fold) and significantly ($p<0.001$) higher than in the 'No Ultrasound' and 'Sub Cavitation' groups.

3.3.2.5 Sumatriptan Repeat Study 1 - Sumatriptan delivery into the bloodstream

The collected blood samples at T_{20} were analysed by HPLC and the chromatograms are presented in Figure 3.23(a-c). The total amount of Sumatriptan found in the blood as well as the percentage of the total dose delivered into the blood, are shown in Figure 3.23(d).

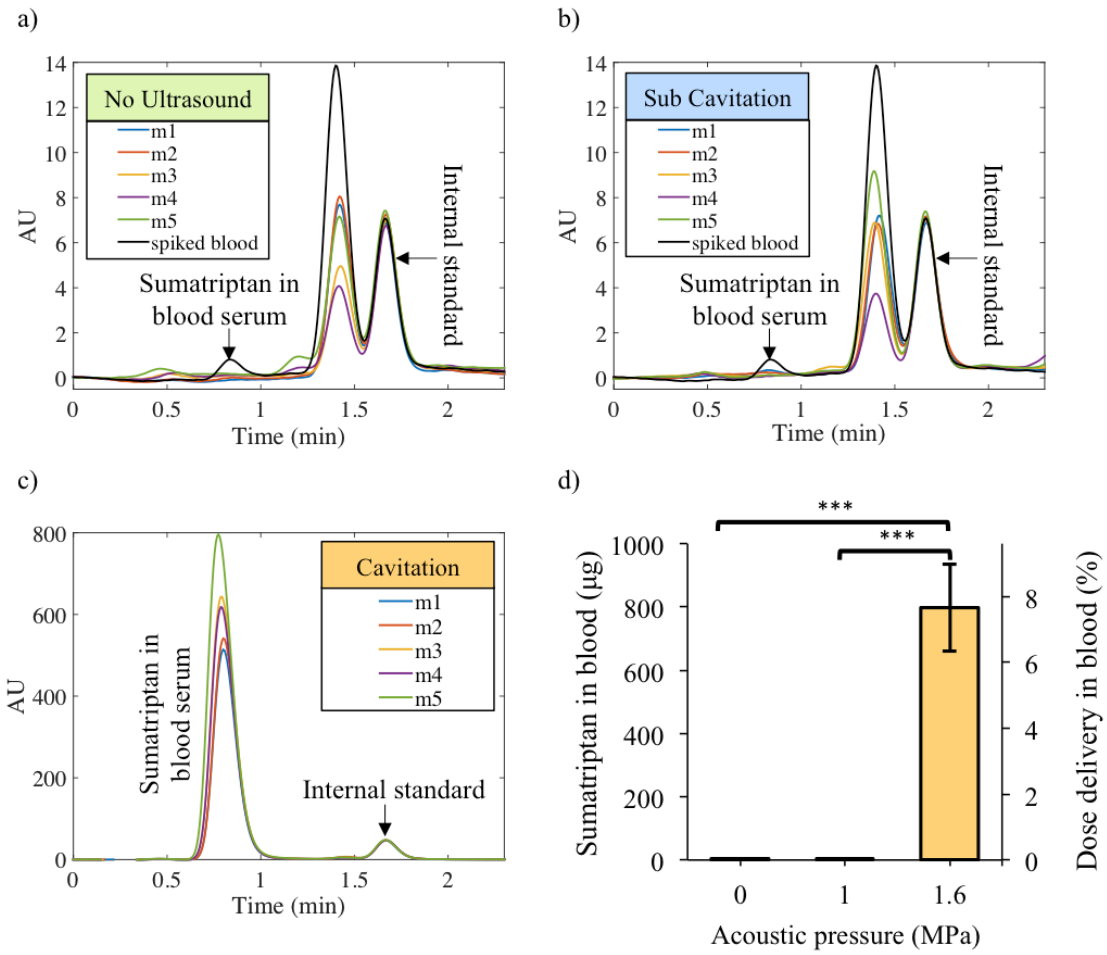

Figure 3.23: Sumatriptan delivery into the blood – Sumatriptan Repeat Study 1. Chromatograms of blood serum samples from the mice treated with (a) 'No Ultrasound', (b) 'Sub Cavitation', or (c) 'Cavitation'). The traces are re-aligned to the internal standard peak and the baseline is corrected (see section 3.2.11). a) and b) To identify the location of Sumatriptan, an extra elution was added with a known amount of Sumatriptan spiked into the blood. d) Bar chart showing the total Sumatriptan amount in 1.4 mL blood on the left axis and percentage dose delivery into the blood on the right axis. Error bar represents the standard deviation for n=5 mice. The significant difference was determined by one-way ANOVA Bonferroni multiple comparison tests. *** corresponds to $p<0.001$.

In Figure 3.23(a) and (b) it can be seen that no discernible Sumatriptan peaks were found in the 'No Ultrasound' and 'Sub Cavitation' groups, respectively. An extra elution of Sumatriptan spiked blood was added to the chromatograms in Figure 3.23(a) and (b) to clarify the location of Sumatriptan. Due to the zoomed-in scale of Figure 3.23(a) and (b), all the chromatograms show a peak of different intensities at 1.4 minutes. This is a blood specific component and the intensity of this peak does not change over time (when comparing to the T_0 blood samples) and is therefore not of interest in this experiment.

In sharp contrast, peak values of Sumatriptan beyond 850 AU were found in the blood samples from the 'Cavitation' group (Figure 3.23(c)). Using the calibration curve shown in Figure 3.13(d), it was calculated that a total of 795.0 ± 137.1 μg Sumatriptan (or 7.64 ± 1.32% of the applied dose) was found in the 1.4 mL total blood volume at T_{20}. This was significantly higher ($p<0.001$) than the other two groups and these data therefore support the potential of inertial cavitation to enhance transdermal delivery of small molecules such as Sumatriptan into the bloodstream.

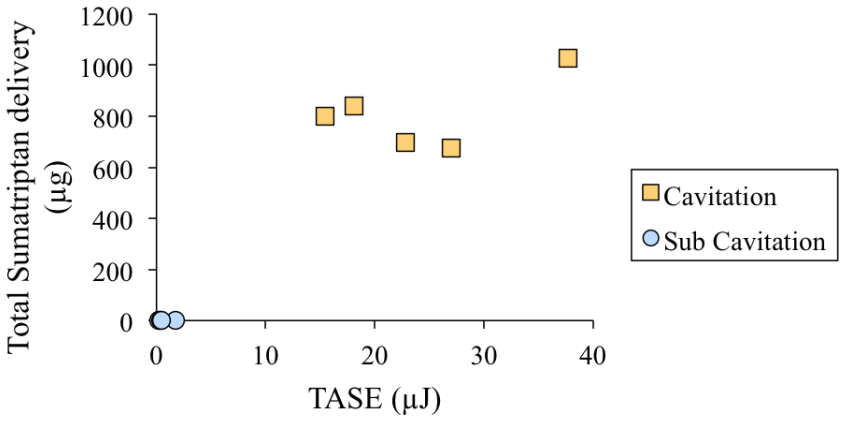

Figure 3.24: Plot of recorded TASE value per sample (as measured by passive monitoring) against the total amount of Sumatriptan delivered into the nude skin and bloodstream for the 'Sub Cavitation' and 'Cavitation' samples in 'Sumatriptan Repeat Study 1'.

When attempting to correlate the level of cavitation with the total delivery achieved for each individual sample exposed to ultrasound (see Figure 3.24), it can be seen that only in the presence of sustained inertial cavitation with TASE > 15 μJ was substantial Sumatriptan delivery (> 675 μg) detected in the skin and bloodstream. These data demonstrate the potential of using TASE value acquired from the passive monitoring as a feedback system to identify the presence of inertial cavitation during treatment to provide assurance of Sumatriptan delivery.

3.3.2.6 Sumatriptan Repeat Study 1 – Discussion

The aim of this study was to demonstrate the feasibility of delivering Sumatriptan *in vivo* by cavitation-enhanced transport. In contrast to the 'Safety Study' (see section 3.3.1) and in accordance to literature, the results showed successful Sumatriptan delivery into the skin and bloodstream only in the presence of sustained inertial cavitation.

In contrast to the 'Safety Study', there was no pre-focal cavitation recorded in the PCD trace in this repeat study at 1.6 MPa (Figure 3.19). By removing the pre-focal cavitation, the acoustic energy was not shielded from entering the holder and the acoustic pressure inside the holder was increased. As a result, the TASE values from the 'Sumatriptan Repeat Study 1' at 1.6 MPa was five-fold higher than the TASE values calculated at the same pressure in the 'Safety Study' (Figure 3.25). Since the acoustic emissions were only recorded at the time point corresponding to the location just prior to the holder, the contribution of the low pre-holder activity to the calculated TASE value determined from within the formulation and mouse skin was substantially lower than seen in the 'Safety Study'. Therefore it can be assumed that the calculated TASE values were the sole result of the inertial cavitation of the NCs in the formulation and skin. This shows the importance of degassing the water in the cone as well as the potential of using PCD as a feedback system to detect and prevent errors in the system.

To investigate the influence of the pre-focal cavitation on the acoustic emissions recorded from within the formulation and mouse skin, the TASE values calculated from the PCD traces from the 'Safety Study' and 'Sumatriptan Repeat Study 1' are compared in Figure 3.25. Overall, it can be seen that the TASE values recorded in 'Sumatriptan

Repeat Study 1' was substantially (~ 2.5 fold) and significantly ($p<0.01$) higher than the energies recorded in the 'Safety Study'. Notably, despite this increase in TASE value no major damage of the skin was observed in 'Sumatriptan Repeat Study 1' (Figure 3.21).

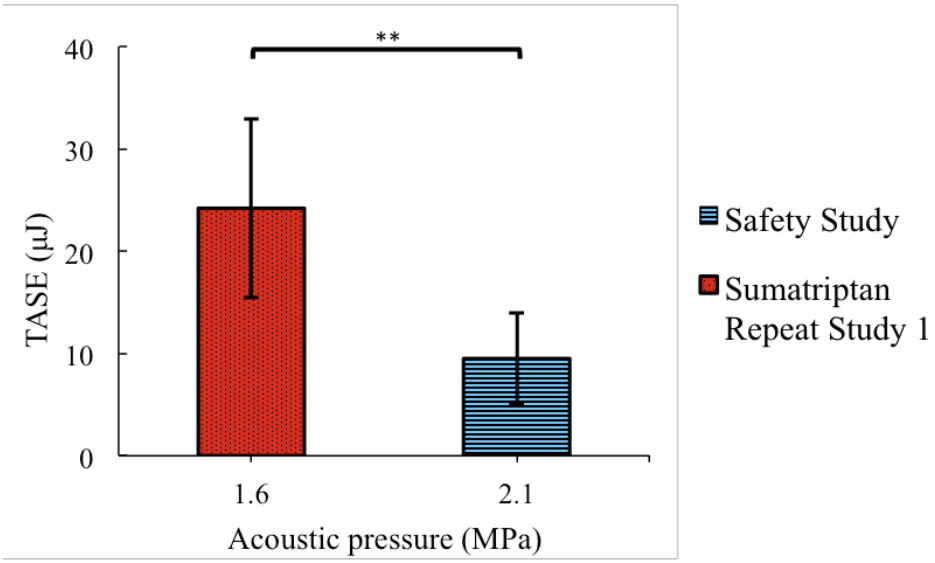

Figure 3.25: Comparison of the TASE values calculated in the 'Safety Study' and 'Sumatriptan Repeat Study 1'. Acoustic emissions were detected using a PCD as described in section 3.2.2. The bar chart showing the mean TASE value calculated for the 'Cavitation' group of both studies. The error bars represent the standard deviation for n=5 mice in 'Sumatriptan Repeat Study 1' and n=3 for the 'Safety Study'. The significant difference was determined by t-test and ** correspond to $p<0.01$.

It was shown that exposing the nude mice skin in 'Sumatriptan Repeat Study 1' to 0 MPa or 1.0 MPa, resulted in negligible amounts of Sumatriptan being recovered from the skin and blood serum. Only exposure to 1.6 MPa achieved substantial cavitation and Sumatriptan delivery into the skin and blood, delivering a total of ~8% of the applied dose. These results demonstrated the feasibility of delivering Sumatriptan by cavitation-enhanced transport.

3.3.3 In vivo Sumatriptan Repeat Study 2

In the first Sumatriptan repeat study, it was observed that substantial Sumatriptan delivery into the skin and (for the first time) in the blood circulation was achieved only following ultrasound exposure to 1.6 MPa and by treating nude mice rather than hairy BALB/c mice. Since pre-focal cavitation and better washing of the skin after the exposure was shown to play a crucial role in the success of the delivery, the experiment was repeated (i.e. 'Sumatriptan Repeat Study 2') on BALB/c mice to investigate the influence of hair and fur removal on the delivery.

3.3.3.1 Sumatriptan Repeat Study 2 – Cavitation detection

The acoustic emission spectrograms were characterised for the 'Sub Cavitation' and 'Cavitation' groups and presented in Figure 3.26(a) and (b), respectively. In Figure 3.26(a) it can be observed that exposing the formulation to 0.5 and 0.7 MPa resulted in sporadic broadband emissions (light blue bands) and some harmonics (horizontal bands). Since the TASE values for the two 0.7 MPa exposures were lower than the average TASE value from the four traces at 0.5 MPa (0.13 ± 0.07 μJ), the six samples were pooled together and presented in a single bar in Figure 3.26(c) under ≤0.7 MPa.

Stronger and consistent broadband acoustic emissions (red bands) were recorded over the full 10-minutes exposure time for all mice insonated at 1.6 or 1.8 MPa (Figure 3.26(b)). Because there was no difference in delivery (see Figure 3.30(c) and Figure 3.31(c)) when insonating at 1.6 or 1.8 MPa, all the samples in the 'Cavitation' group were pooled together under ≥1.6 MPa in Figure 3.26(c). The TASE value of 49.41±14.24 μJ was significantly ($p<0.0001$) higher than the energies found at ≤0.7 MPa (0.11±0.07 μJ) and also two-fold higher than 'Cavitation' group in Figure 3.20(c).

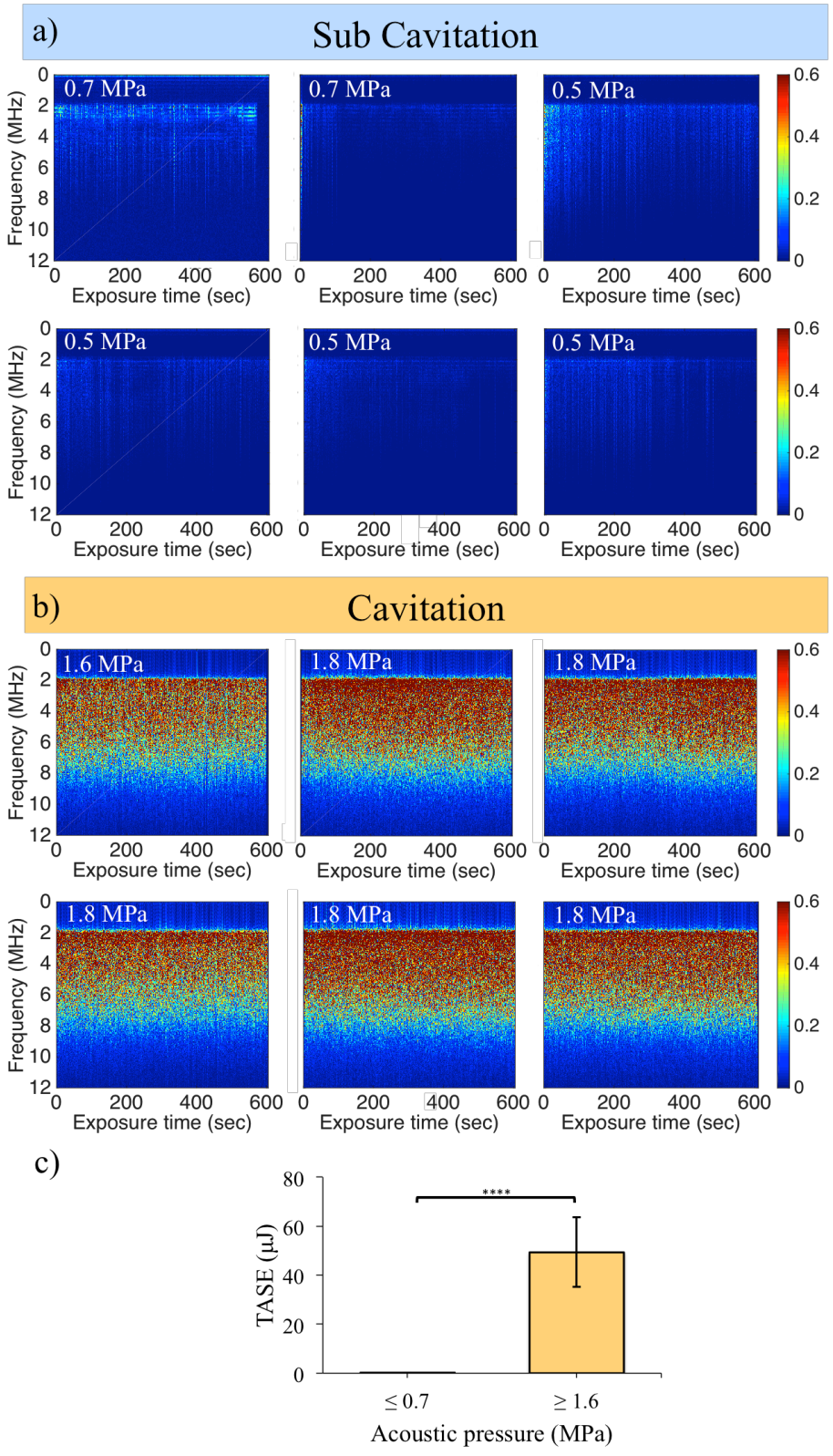

Figure 3.26: Acoustic emission spectrograms from NCs exposed to ≤0.7 MPa and ≥1.6 MPa acoustic pressure – Sumatriptan Repeat Study 2. a) The acoustic emissions were recorded for the 'Sub Cavitation' treatment group and (b) the 'Cavitation' treatment group. The colour bar on the right axis represents the power spectral density (mV^2/Hz). c) The bar chart shows the mean of the Total Acoustic Sensor Energy (TASE) determined per treatment group with the exclusion of the 'No Ultrasound' group. In the absence of ultrasound, there is nothing to record. The error bar represents the standard deviation for n=6 mice. The significant difference was determined by t-test. **** corresponds to $p<0.0001$.

3.3.3.2 *Sumatriptan Repeat Study 2 - Investigation of skin damage*

The skin damage was then assessed by taking a close examination of the photographic images of the rescued mouse skin for the three exposure conditions (Figure 3.27).

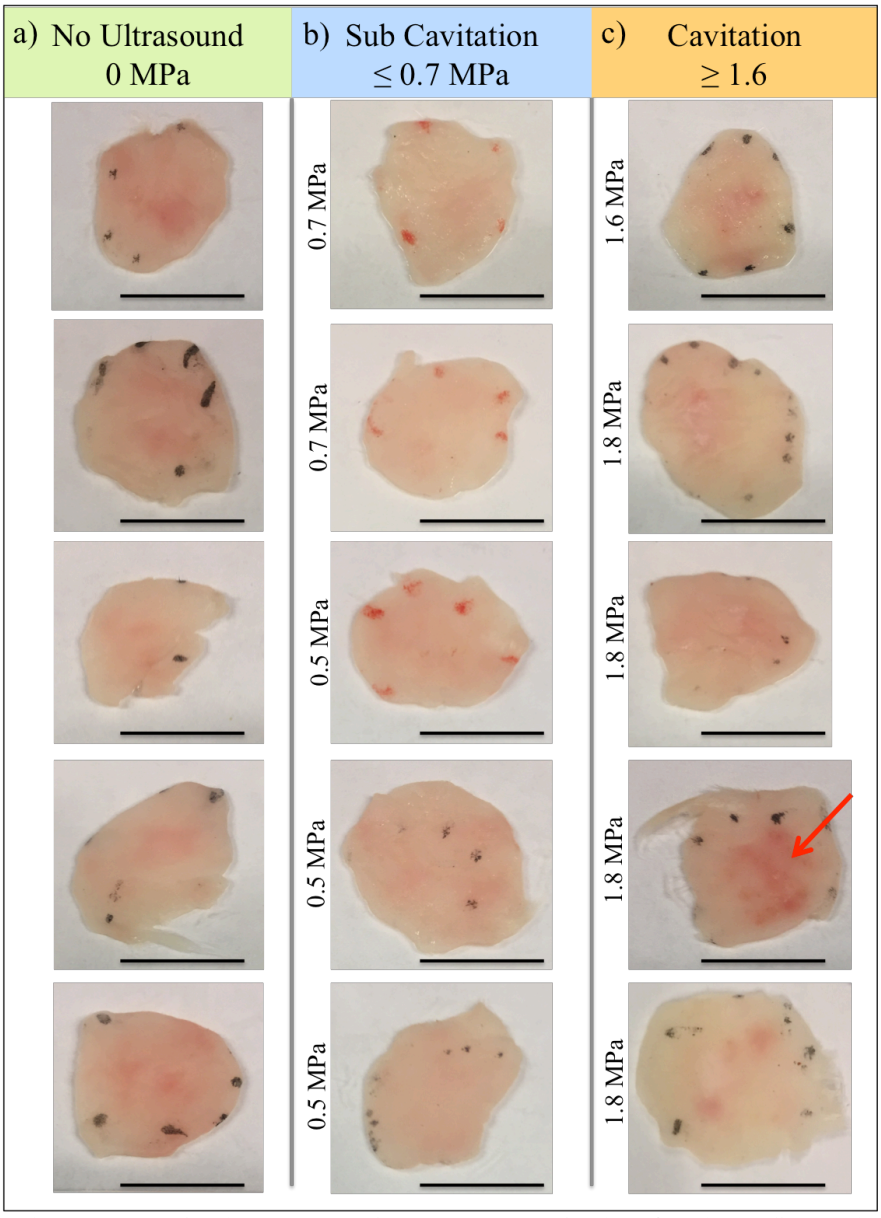

Figure 3.27: Assessment of skin damage after treatment of BALB/c mice – Sumatriptan Repeat Study 2. Photographic images are shown from rescued skin from BALB/c mice treated with (a) 'No Ultrasound', (b) 'Sub Cavitation', (c) or 'Cavitation' at the different stated acoustic pressures. After 10-minutes treatment and 10-minutes recovery time, the skin was rescued and processed as described in section 3.2.9. The blue dots on the skin mark the exposed area and the scale bar corresponds to 1 cm. The red arrow highlights minor areas of reddening on the skin after cavitation. The black and red marker dots on the skin mark the exposed area and the scale bar corresponds to 1 cm.

The skin samples from mice exposed to 'No Ultrasound' (Figure 3.27(a)) and 'Sub Cavitation' (Figure 3.27(b)) showed similar appearance. Only one mouse in the 'Cavitation' group (highlighted with the red arrow, Figure 3.27(c)) showed a red patch over the whole exposure region. By contrast to the skin samples in the 'Safety Study' (Figure 3.16(b)), no major skin damage or white dots were observed in this second repeat study after exposing the skin beyond 1.6 MPa.

3.3.3.3 Sumatriptan Repeat Study 2 - Histology of skin

To investigate potential skin damage after treatment in more detail, histology was performed on the rescued skin of one mouse per group. For the clinical application of the technology, it is important that the treatment does not cause irreversible or functional damage to the skin. Therefore, the integrity of the epidermis was assessed with histology. To visualise the different skin layers and structures within them, Masson's trichrome stain was used that selectively stained collagen fibres (green/blue), erythrocytes and muscle fibres (red) and cell nuclei (dark brown). In Figure 3.28 the histology slide of a non-treated skin sample is shown for comparison and to highlight the important skin features.

In general, the three skin layers can be observed in Figure 3.28, the epidermis, dermis and hypodermis. The dark blue band shows the top layer of the skin (epidermis) with the flaky SC on top. The underlying light blue band (colouring the collagen fibres) is the dermis that contains the sweat glands, hair follicles, and sebaceous glands. The red colour inside the blood vessels represents red blood cells. The third layer is the hypodermis, which mostly contains adipocytes and some blood vessels. Hydrophobic fat-rich structures like the adipocytes tend to remain clear in histology image, as visible in Figure 3.28.

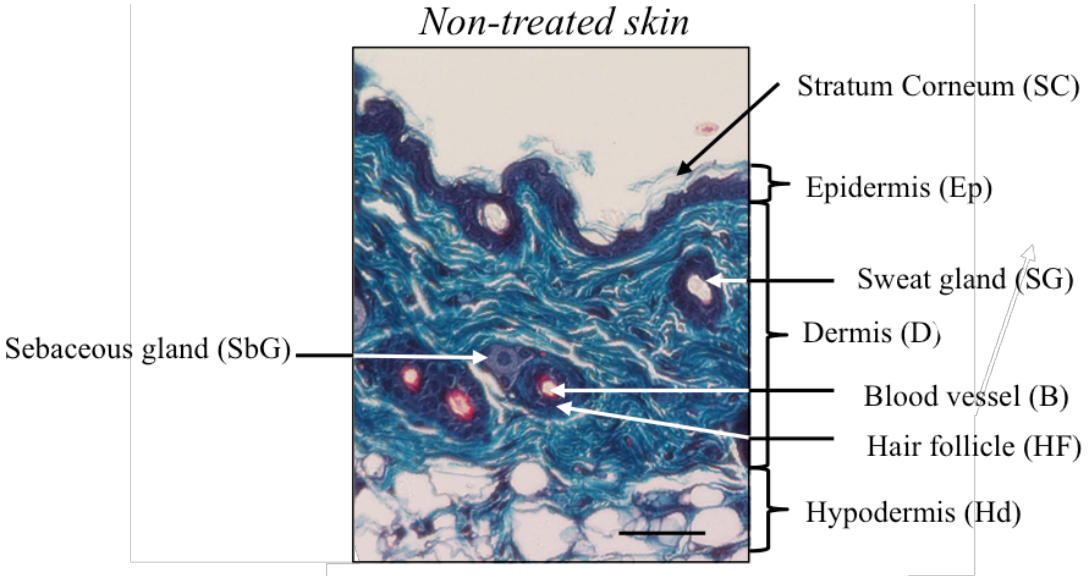

Figure 3.28: Histology cross-section of non-treated BALB/c mouse skin. The skin was rescued from a BALB/c mouse that only received the pre-treatment to remove the fur from the skin area. Masson's trichrome stain was applied to visualise the different skin layers. The important skin features are labelled and the scale bar corresponds to 50 µm (20x magnification).

Figure 3.29 shows images of the skin samples taken directly after the 10-minutes treatment alongside the same sample post-fixation, staining and analysis under the microscope. For every histology image, the three skin layers were indicated as well as important skin features.

After exposing the skin to 0 MPa (Figure 3.29(a)) or ≤ 0.7 MPa acoustic pressure (Figure 3.29(b)), no indications of skin damage such as redness were observed in the photographic images. This was confirmed by histology. The three skin layers were well defined. The flaky SC can be observed in both the 'No Ultrasound' (Figure 3.29(a)) and 'Sub Cavitation' (Figure 3.29(b)) groups. However, in comparison to the non-treated skin in Figure 3.28, the SC is marginally harder to observe. These minor disruptions of the upper layers of the SC could be caused by the pre-treatment of the skin using the electric razor and depilatory cream and the application/removal of the formulation from the skin surface. The extent of disruption was apparent on careful inspection of the images taken directly after the treatment (Figure 3.29(a) and (b)) and following skin

rescue (Figure 3.27(a) and (b)). In both cases, light red shades/irritation spots were observed. These minor SC disruptions heal within hours and are not classified as harmful.

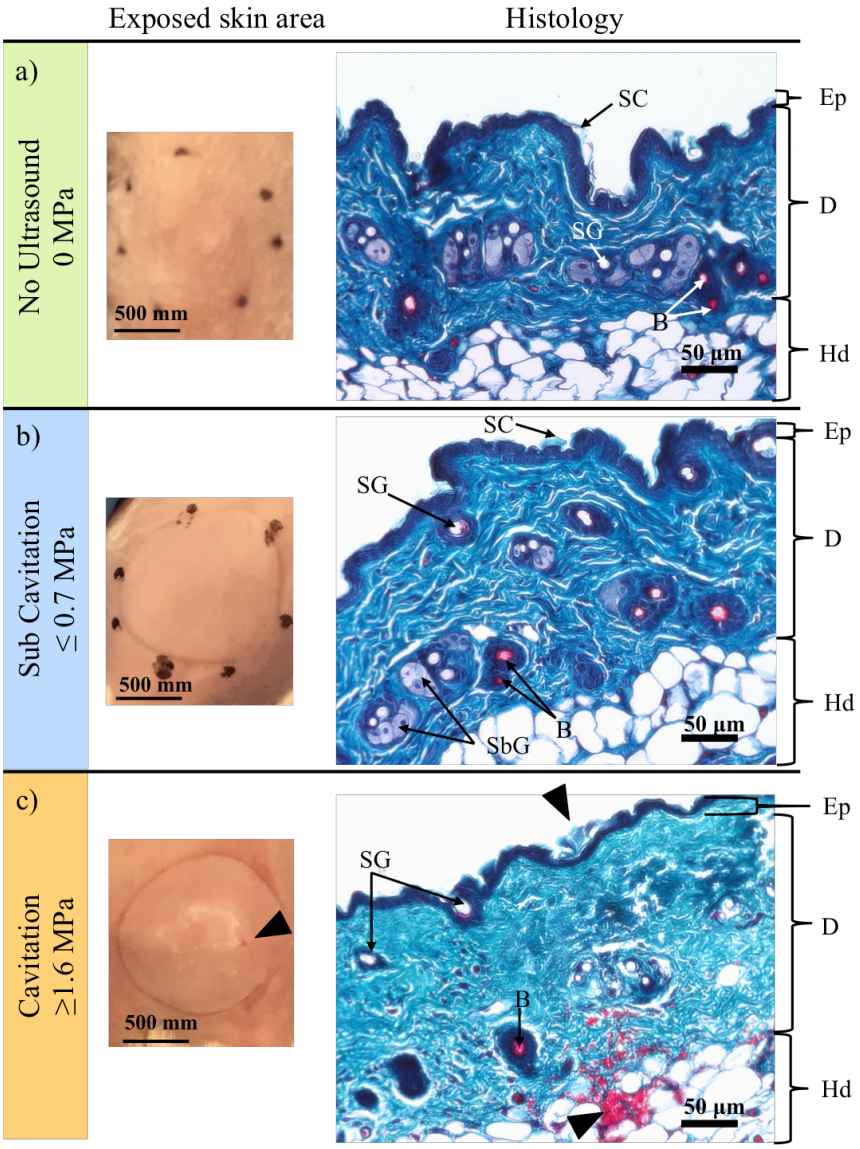

Figure 3.29: Assessment of skin damage after treatment on macroscopic (left column) and microscopic level (right column). In the left column photographic images are shown of the treated area directly taken after the 10-minutes treatment of 'No Ultrasound' (b) 'Sub Cavitation', or (c) 'Cavitation'. The black marker dots on the skin mark the treatment area, the black arrow in the 'Cavitation' group highlights a small red dot, and the scale bar corresponds to 500 mm. In the right column, cross-sectional images of Masson's trichrome stained histology slides of the skin sample are shown for each treatment group. In the histology images (b) and (c), the ultrasound was applied from the top downwards onto the skin surface. The scale bar corresponds to 50 µm. SC = Stratum Corneum, SG= Sweat glands, SbG = Sebaceous glands, B= blood vessel, Ep=epidermis, D=Dermis, Hd=Hypodermis.

Significant changes to the skin were observed after exposing to ≥1.6 MPa (Figure 3.29(c)). Due to the sustained inertial cavitation, the epidermis was occasionally disrupted (not full thickness, indicated by the arrow in Figure 3.28(c)), but still protects the underlying dermis. In addition, it can be clearly observed that at the interface of the dermis and the hypodermis red blood cells are present. The blood cells appear to originate from a blood vessel in the hypodermis and not from the labelled blood vessel ('B' in Figure 3.28(c)) in the dermis. Bleeding inside the tissue could be the result of mechanical perturbation by the ultrasound exposure and inertial cavitation inside the skin. Such bleeding could be classified as bruising, which heals without scar formation within 24 hours and therefore is assumed to be non-harmful [214].

3.3.3.4 Sumatriptan Repeat Study 2 - Sumatriptan delivery into the skin

Next, the dermal delivery of Sumatriptan was investigated. Since one out of the six samples was used for histology, the dermal delivery of Sumatriptan was analysed in the remaining five skin samples per group using the calibration curve shown in Figure 3.12(d). The chromatograms are presented in Figure 3.30(a-c) and the calculated amounts of Sumatriptan in the skin, as well as the percentage of the total dose delivered into the skin, are presented in Figure 3.30(d).

All the skin samples had detectable Sumatriptan levels. The 'No Ultrasound' group (Figure 3.30(a)) had Sumatriptan peak values between 2-7 AU (corresponds to a total amount of 0.50 ± 0.28 μg Sumatriptan, or 0.005 ± 0.003% of the applied dose). Higher levels were found in the 'Sub Cavitation' group (Figure 3.30(b)) with peak values between 7-25 AU. Although two skin samples were exposed to 0.7 MPa, their peak values were similar to the samples exposed to 0.5 MPa. Therefore, the total delivered Sumatriptan into the skin was 1.62 ± 0.85 μg (or 0.016 ± 0.008% of the applied dose).

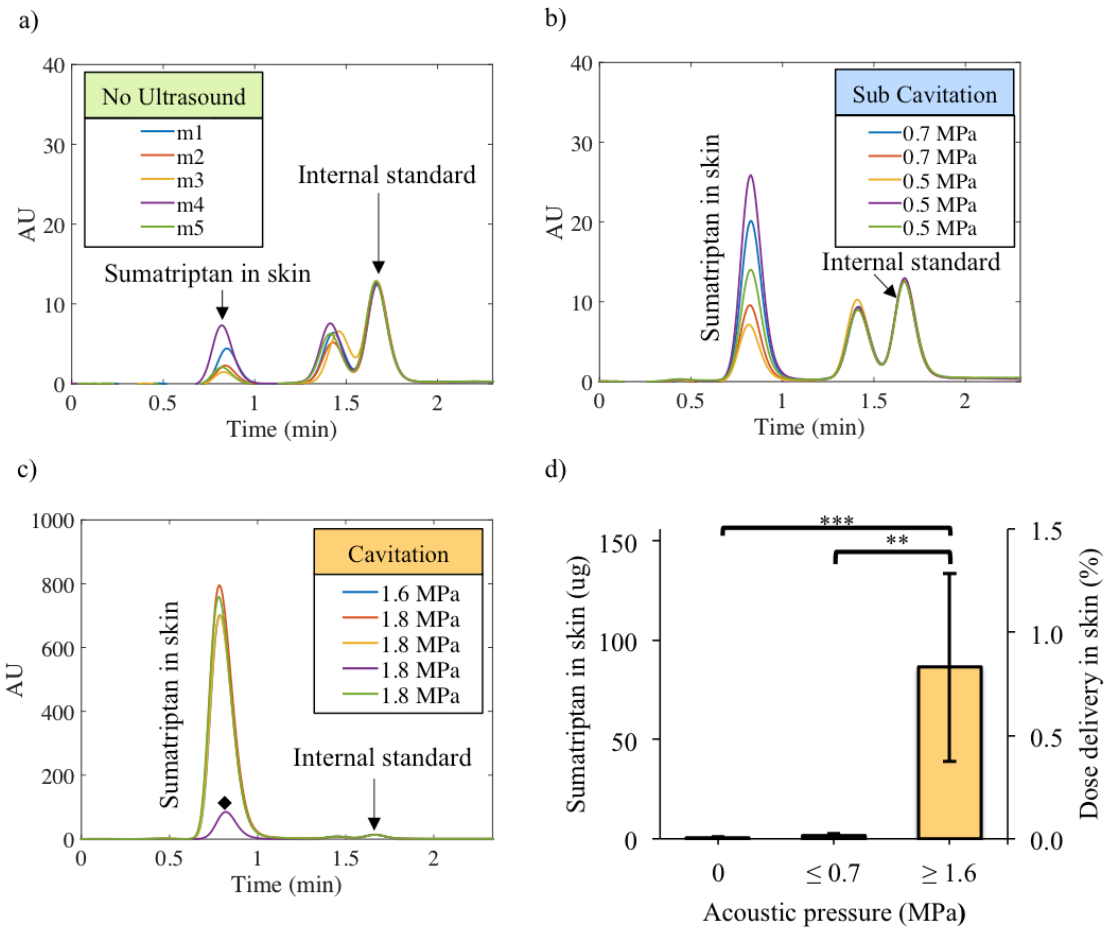

Figure 3.30: Sumatriptan delivery into the skin – Sumatriptan Repeat Study 2. Chromatograms of skin samples from the BALB/c mice treated with (a) 'No Ultrasound', (b) 'Sub Cavitation', or (c) 'Cavitation'. The traces are re-aligned to the internal standard peak and the baseline is corrected as described in section 3.2.11. The ◆ in c) highlights an outlier. d) Bar chart showing the total Sumatriptan amount in the skin on the left axis and percentage dose delivery into the skin on the right axis. The error bars representing the standard deviations and are shown for n=5 mice. The significant difference was determined by one-way ANOVA Bonferroni multiple comparison tests. ** and *** correspond to $p<0.01$ and $p<0.001$, respectively.

Substantially higher Sumatriptan peak values were measured for the 'Cavitation' group where four out of the five samples had peak values exceeding 700 AU. The total amounts of Sumatriptan found in the skin after exposing to ≥1.6 MPa was 86.32 ± 47.42 µg Sumatriptan (or 0.830 ± 0.456% of the applied dose). This was 53-fold more delivery than achieved after exposing to sub-cavitation acoustic pressures. Also, the delivery level after 'Cavitation' treatment was almost seven-fold higher than the same group in 'Sumatriptan Repeat Study 1'.

Notably, one skin sample (highlighted ◆ in Figure 3.30(c)) had a peak value of only 84 AU after exposing to 1.8 MPa, which corresponds to a delivery of 8.75 μg Sumatriptan into the skin. Since the peak of this sample is higher than the Sumatriptan peaks found at lower acoustic pressures, the sample cannot be marked as an outlier. This explains the large standard deviation in Figure 3.30(c). Nevertheless, these results demonstrate the feasibility of delivering Sumatriptan into the skin using cavitation-enhanced transport.

3.3.3.5 Sumatriptan Repeat Study 2 - Sumatriptan delivery into the bloodstream

The amount of Sumatriptan delivered into the blood after treatment was also measured. The blood samples collected at T_{20} were analysed by HPLC and the chromatograms of the three experimental groups are presented in Figure 3.31(a-c). The total amount of Sumatriptan found in the blood, as well as the percentage of the total delivered dose in the blood, are shown in Figure 3.31(d).

Figure 3.31(a) shows that no discernible Sumatriptan peaks were found in the 'No Ultrasound' group. Only one out of six blood samples had a detectable Sumatriptan level after treatment at 0.7 MPa (Figure 3.31(b)). In contrast, five out of the six mice had substantial peak values of Sumatriptan, giving between 180 and 570 AU, after being treated at ≥1.6 MPa (Figure 3.31(c)). However, a single mouse had no detectable Sumatriptan levels in the blood at 1.8 MPa (as highlighted ◆ in Figure 3.31(c)). Notably, this mouse also had lower levels in the skin as highlighted ◆ in Figure 3.30(c). No reason for this low delivery was found in the PCD trace. The PCD trace of this mouse looked similar to the other 'Cavitation' traces (as shown in Figure 3.26(b)). It is possible that in this mouse the formulation holder contained a substantial air bubble at the side of the holder (outside the focus for the PCD), which changed the pressure field. However, no data is available to confirm this hypothesis.

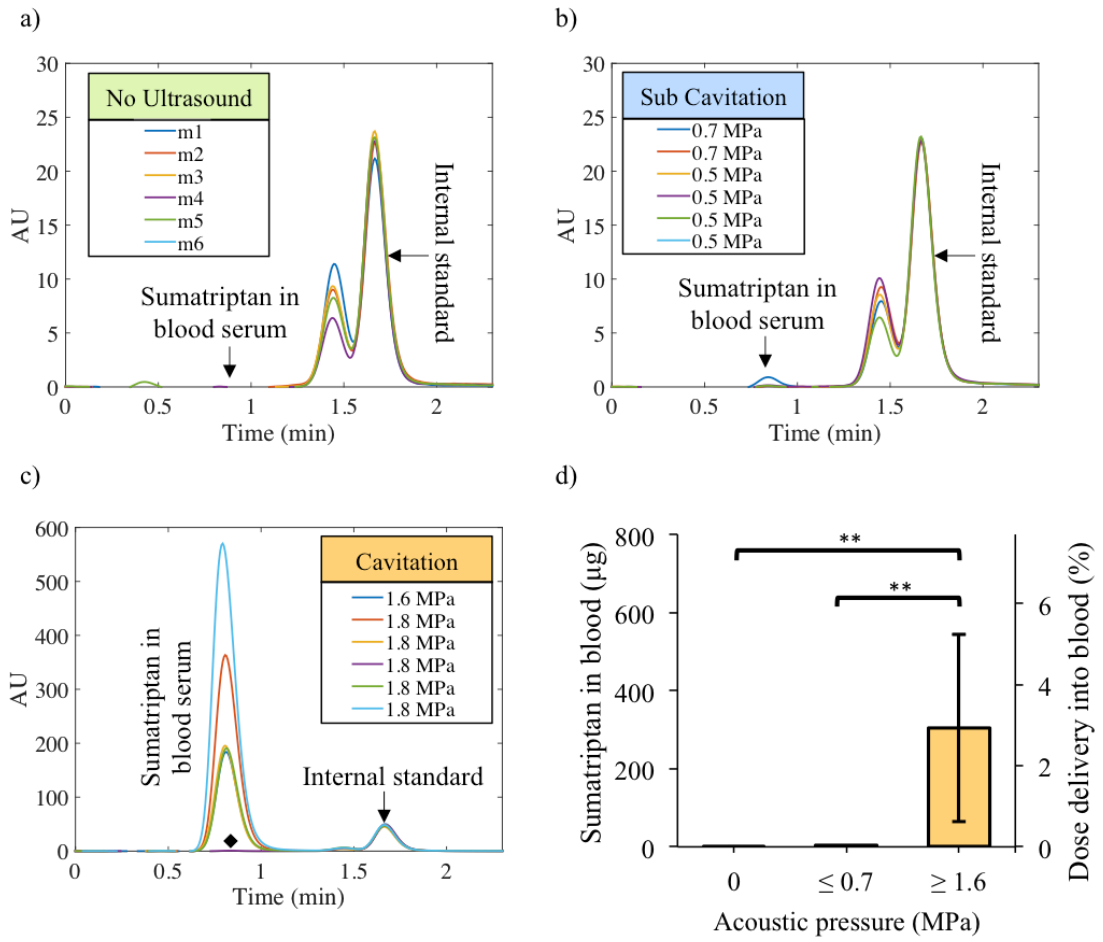

Figure 3.31: Sumatriptan delivery into the blood – Sumatriptan Repeat Study 2. Chromatograms of blood serum samples from the BALB/c mice treated with (a) 'No Ultrasound', (b) 'Sub Cavitation', or (c) 'Cavitation). The traces are re-aligned to the internal standard peak and the baseline is corrected (see section 3.2.11). The ◆ in c) highlights an outlier. d) Bar chart showing the total Sumatriptan amount in 1.4 mL blood on the left axis and percentage dose delivery into the blood on the right axis. Error bar represents the standard deviation for n=6 mice. The significant difference was determined by one-way ANOVA Bonferroni multiple comparison tests. ** corresponds to $p<0.01$.

Using the calibration curve shown in Figure 3.13(f), it was calculated that a total of 304.5 ± 239.7 µg Sumatriptan (or 3.11 ± 2.53% of the applied dose) was found in the 1.4 mL blood volume at T_{20} at ≥ 1.6 MPa. This was significantly higher ($p<0.01$) than the other two groups and these data again show the benefit of using inertial cavitation to enhance transdermal delivery of Sumatriptan. However, this level was also three-fold lower than the blood levels observed in the same group in 'Sumatriptan Repeat Study 1' (Figure 3.22(d)).

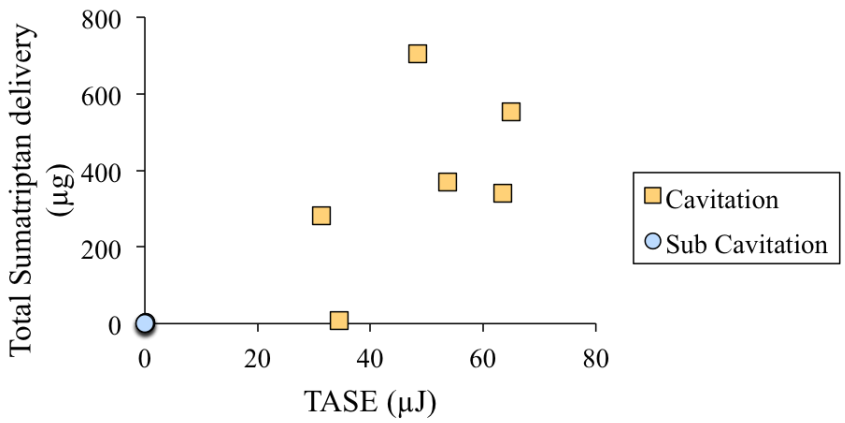

Figure 3.32: Plot of recorded TASE value per sample (as measured by passive monitoring) against the total amount of Sumatriptan delivered into the nude skin and bloodstream for the 'Sub Cavitation' and 'Cavitation' samples in 'Sumatriptan Repeat Study 2'. The ◆ highlights the sample that had no detectable Sumatriptan levels in the blood at 1.8 MPa.

Figure 3.23 shows an attempt to correlate the level of cavitation with the total Sumatriptan delivery achieved for each individual sample exposed to ultrasound. It can be seen that only in the presence of sustained inertial cavitation, with TASE values in excess of 31 µJ, Sumatriptan delivery was detected in the skin and bloodstream (except sample ◆ in Figure 3.32). These data demonstrate the potential of using the TASE value from passive cavitation monitoring as a feedback system to provide assurance of successful Sumatriptan delivery.

3.3.3.6 Sumatriptan Repeat Study 2 - Discussion

In response to the issues identified in the 'Safety Study', several changes were made to optimise the experimental procedures. Notably, the successful delivery of Sumatriptan into the skin and blood in 'Sumatriptan Repeat Study 1' was achieved as a result of the removal of pre-focal cavitation and better washing of the skin after the exposure. The optimised experimental procedures were then used in 'Sumatriptan Repeat Study 2' to investigate the influence of hair and fur removal on the delivery of Sumatriptan.

In Figure 3.33, the TASE values from the 'Cavitation' group from 'Sumatriptan Repeat Study 1' (nude CD1 mice) and 'Sumatriptan Repeat Study 2' (hairy BALB/c mice) are compared. It can be observed that the TASE values recorded in 'Sumatriptan Repeat Study 2' were significantly higher (two-fold, $p<0.01$) than those recorded in 'Sumatriptan Repeat Study 1'. This increase could be explained by the fact that in 'Sumatriptan Repeat Study 2' higher acoustic pressures were used (1.6 MPa versus 1.8 MPa).

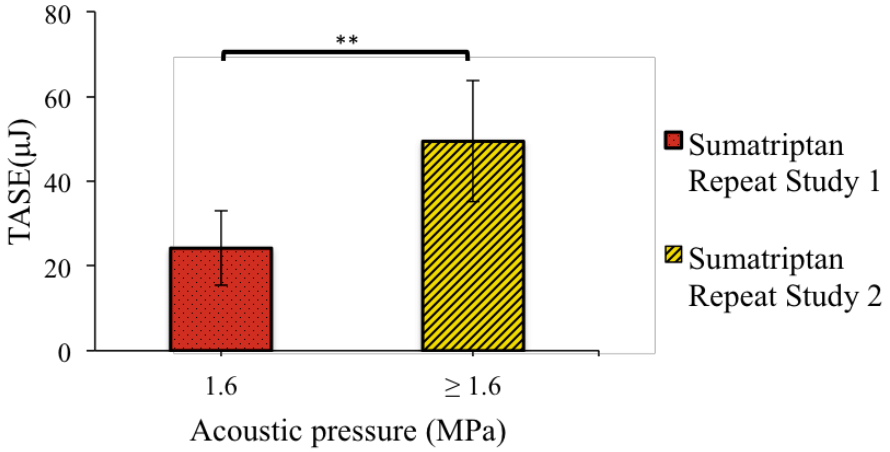

Figure 3.33: Comparison of the TASE values detected in the 'Cavitation' group from 'Sumatriptan Repeat Study 1' (nude mice) and 'Sumatriptan Repeat Study 2' (hairy BALB/c mice). The bar chart shows the mean of the TASE of the 'Cavitation' group from 'Sumatriptan Repeat Study 1' and '2'. The error bars represent the standard deviation for n=5 nude mice in 'Sumatriptan Repeat Study 1', and n=6 BALB/c mice in 'Sumatriptan Repeat Study 2'. The significant difference was determined by t-test and ** corresponds to $p<0.01$.

Despite these increases in acoustic pressure and TASE values, no major skin damage was observed in 'Sumatriptan Repeat Study 2'. Minor irritation in the form of a red patch was observed in a single mouse (Figure 3.27(c)), similar to the minor irritation observed in 'Sumatriptan Repeat Study 1' (Figure 3.21(b)). Therefore, it can be concluded that there is no obvious correlation between the detected TASE value and the amount of cavitation-induced skin damage observed macroscopically. The marked skin damage observed in the 'Safety Study' (Figure 3.16(b)) is most likely to be the result of the pre-focal cavitation activity.

This observation shows again the importance of degassing the water in the coupling cone as well as the potential of using PCD as a feedback system to detect and prevent errors in the system.

Notably, microscopic evaluation of stained-tissue sections did reveal cavitation-associated minor disruption to the SC and rare instances of minor red blood cell leakage from vasculature supplying the skin (Figure 3.29). Since these skin disruptions heal without lasting bruising or scar formation within 24 hours [214], the technology is therefore still assumed to be non-harmful to the skin.

To investigate the influence of hair and fur removal on the delivery of Sumatriptan, the differences in Sumatriptan delivery between the two repeat studies are explored in Figure 3.34. In Figure 3.34(b) it can be observed that treating nude mice ('Sumatriptan Repeat Study 1') with 'No Ultrasound' and 'Sub Cavitation' has led to a negligible amount of Sumatriptan being recovered from the skin. In contrast, detectable levels were found in the BALB/c mice (0.50 ± 0.28 μg Sumatriptan, 'Sumatriptan Repeat Study 2') even without applying ultrasound. In the literature, it is reported that the thickness of the mouse skin is not influenced by the presence or absence of fur (see Table 2.1). Hence, the difference in delivery between the two mouse models could be explained by the differences in the protocol to prepare the skin prior to the treatment. Specifically, the use of hair removal cream may have increased the skin permeability and enhanced the uptake of Sumatriptan into the skin by passive diffusion when using BALB/c mice. This was not evident in 'Sumatriptan Repeat Study 1' where no de-epilation was required.

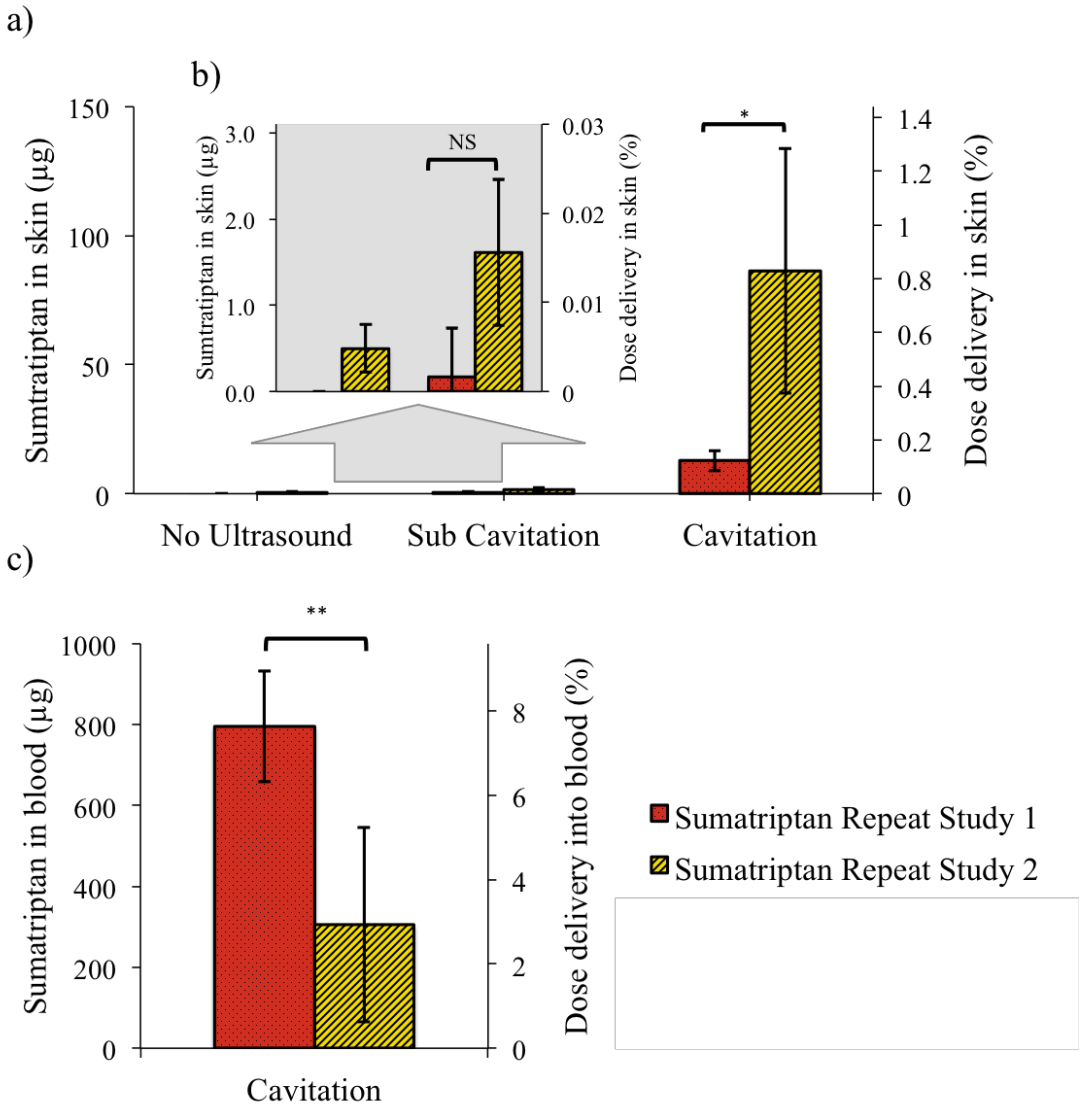

Figure 3.34: Influence of mice strain on Sumatriptan delivery. a) Bar chart showing the total Sumatriptan amount in the skin on the left axis and percentage dose delivery into the skin on the right axis for nude mice ('Sumatriptan Repeat Study 1') and BALB/c mice ('Sumatriptan Repeat Study 2'). b) Zoom-in to the Sumatriptan delivery found into the skin after treatment of 'No Ultrasound' and 'Sub Cavitation'. c) Bar chart showing the total Sumatriptan amount in 1.4 mL blood on the left axis and percentage dose delivery into the blood on the right axis for the 'Cavitation' group in the nude and BALB/c mice. Error bars represent the standard deviation and the significant difference was determined by t-test. *, and ** correspond to $p<0.05$ and $p<0.01$, respectively.

In accordance with the analysis of the active ingredient of the depilatory cream, thioglycolic acid breaks down the sulphide bonds in the keratin structures that are present in hair filaments and corneocytes (making up the SC) [215]. As a result, thioglycolic acid disrupts the structural integrity of the SC and removal of the corneocytes enhances transepidermal delivery as long as one day after

application [215-217]. The histology images of the 'No Ultrasound' group confirmed the reduction of the flaky SC (Figure 3.29(a)).

When exposing the BALB/c skin to 'Sub Cavitation' in 'Sumatriptan Repeat Study 2', the dermal delivery was not significantly enhanced to 1.62 ± 0.85 μg Sumatriptan in comparison to the same group in 'Sumatriptan Repeat Study 1' (Figure 3.34(b)). As a result of sub-cavitation activity in the formulation, it could be possible that the diffusion gradient between the formulation and the skin was preserved as a result of microstreaming and enabling more Sumatriptan to diffuse into the skin. Nevertheless, exposing both mouse strains to 'No Ultrasound' or 'Sub Cavitation' was not sufficient enough to deliver Sumatriptan into the bloodstream (Figure 3.34(c)). This indicates that at time point T_{20} Sumatriptan did not reach the blood vessels in the dermis. Or alternatively, Sumatriptan did reach the blood vessels in the dermis, but the resulting Sumatriptan concentrations in the systemic circulation were too low to give detectable Sumatriptan peaks on the HPLC chromatograms.

In both repeat studies, substantial Sumatriptan delivery was detected in the skin (Figure 3.34(a)) and bloodstream (Figure 3.34(c)), only when sustained inertial cavitation was achieved, with plasma concentration in the order of μg/mL (568 μg/mL Sumatriptan in the first repeat study, 217.5 μg/mL Sumatriptan in the second repeat study). The therapeutic blood concentrations required in human are 18–60 ng/mL [197], corresponding to 228 - 755 ng/mL in murine model (see section 3.1.2). This shows that cavitation-enhanced transdermal delivery was able to deliver 1000-fold more Sumatriptan into the bloodstream than the therapeutic required dose, and also already within 20 minutes after the start of the treatment.

In contrast to other needle-free technologies, the iontophoretic patch (Zecuity®) reached Sumatriptan plasma concentrations of 10 ng/mL in humans within ~30 minutes [177], and nasal delivery formulations have shown maximal systemic concentrations of 20 ng/mL at 20 minutes post inhalation [218]. Furthermore, the pharmacokinetic parameters of Sumatriptan in mice have not been published before, but articles have shown *in vivo* results in rabbits and rats (see Table 3.4). The maximum plasma concentration found in rabbits and rats were at least 54-fold lower than found in this chapter, but the total applied dose in this chapter was also higher (10.4 mg Sumatriptan). Hence, whilst these results show a promising level of dose that can be achieved using the technology described here, there are still substantial issues regarding the amount of dose that remains in the formulation holder after the treatment and is in essence 'wasted'.

Table 3.4: Pharmacokinetic parameters obtained from literature of Sumatriptan delivery via different administration routes in rabbit, rats, and clinical studies. The maximal plasma concentration (C_{max}) and the corresponding time to achieve the maximum concentration (Tmax) are shown after single treatment. s.c. = subcutaneous.

Mammal species	Administration route	Dose (mg)	C_{max} (µg/mL)	T_{max} (min)
Rabbit [219]	Oral	50	0.51 ± 0.22	92.4 ± 50.4
Rat [189]	Oral	1.3	0.2 ± 0.1	26.3 ± 3.8
	s.c. injection	1.3	3.9 ± 0.3	15.0 ±0.0
	Microneedle	2.5	4.0 ± 0.5	52.5 ± 6.7
Human [177, 220]	Oral	100	0.051	132
	s.c. injection	6	0.082	18
	Intranasal	20	0.012	90
	Iontophoresis	120	0.025	102

It has been previously reported that ultrasound-enhanced permeability does not occur homogeneously over the total exposed skin area, but in localised transport regions after exposure to low-frequency ultrasound [221-223] (as discussed in section 1.4.5). It was hypothesised that collapsing cavitation bubbles close to the skin surface caused the localised regions due to the mechanical mixing effects of cavitation. However, Ueda et al. observed that no change in surface confirmation was found after exposing a gelatine surface to 158 kHz ultrasound, but deeper tissue penetration of a fluorescent dye (rhodamine B) was evident [224]. This could indicate that at higher acoustic frequencies the localised regions are smaller (and invisible by histology (Figure 3.29(c))), but still effective enough to deliver the drug into the skin. In other *in vivo* tumour model studies, Kwan et al. have shown that ultrasound-propelled NCs travel further into the tumour than co-delivered model therapeutics and deposit up to hundreds of microns from the blood vessel wall [152]. Bhatnagar et al. reported similar findings for the NC assisted transdermal delivery of Ovalbumin [172].

Notably, between the two mouse strains, the nude mice showed significantly less Sumatriptan delivery into the skin than the BALB/c mice. The nude mice did not receive any pre-treatment with depilatory cream and therefore can be assumed to have had a fully intact SC. During sustained inertial cavitation, it is possible that the NCs create microstreaming and shockwaves thereby increasing the convective transport of Sumatriptan. It has also been observed that NCs can propel themselves into the skin [152], a process which may leave behind small short-lasting localised disruptions to the SC through which the Sumatriptan can more readily enter the lower skin layers.

Indeed, these ‘tunnels’ have been reported to reach depths sufficient to reach the blood vessels feeding the dermal layers. The very high vascularisation of the skin and the sustained duration of the cavitation events may explain how ~ 8% of the applied dose can enter into the bloodstream. These tunnel formations are potentially similar to the ones visualised in agar phantoms after ultrasound-induced cavitation of a cavitation nuclei [225]. In this way, the influence of cavitation on the skin and Sumatriptan over the 10-minute exposure allows effective passage of the drug into the skin, which then serves as a well-perfused drug reservoir from which the Sumatriptan can then enter the bloodstream over the subsequent 10 minutes of the recovery period. It is hard to ascertain whether this is in accordance with the rate of Sumatriptan transfer from a dermal compartment as there is little published information about the pharmacokinetics of transdermally delivered Sumatriptan and animal or clinical studies comparing different administration routes are scarce.

Notably, the variation in delivery profiles between the two repeat studies (performed on very similar animal models), do serve to emphasise the challenges of accurately predicting levels of transdermal delivery across a human population. Furthermore, the differences in skin model, blood volume, pharmacokinetics, and the number of sampling points make it difficult to extrapolate between the clinical studies and those reported in this thesis. Moreover, in this chapter the total dose delivered is presented from calculations of the level of Sumatriptan found in the skin and blood at T_{20} relatively to the amount present in the formulation holder at the start of the exposure. No loss of drug via degradation, metabolism, or clearance by the kidneys was included.

Therefore, for further testing of the potential of cavitation-enhanced Sumatriptan delivery system, it is suggested to perform delivery studies on larger animal models to obtain insight into the pharmacokinetic profile of the system. Furthermore, studies comparing the delivery performance of cavitation-enhanced Sumatriptan to other administration routes and/or delivery devices would be of value.

3.4 Summary

In this chapter, the challenges found in Chapter 2 were addressed to enhance the reproducibility of the experiments. As a result, *in vivo* studies on mice were performed using a vascularised skin model with reproducible skin thicknesses. Furthermore, larger NC batches were obtained from OxSonics Ltd. to reduce the variability in NC activity between experiments. In addition, Sumatriptan was used as a small therapeutic agent to allow selective separation and detection by a validated and standardised detection method (HPLC). Also, the location of the ultrasound focus was optimised with a new coupling cone and formulation holder. With all these adjustments in place, three *in vivo* studies were performed.

Table 3.5: Summary Sumatriptan delivery of the three *in vivo* studies (total applied dose 10.4 mg).

Study	Mouse strain	Pressure (MPa)	TASE (µJ)	Sumatriptan delivery		Total delivery (%)
				Skin (µg)	Blood (µg)	
Safety Study	BALB/c	0	0	10.46 ± 6.28	-	0.10
		1.6	4.64	0.9	-	0.01
		1.8	9.90	9.67	-	0.09
		2.1	9.48 ± 4.48	7.80 ± 1.03	-	0.07
Sumatriptan Repeat Study 1	CD1	0	0	-	-	0
		1	0.62 ± 0.61	0.44 ± 0.31	-	< 0.01
		1.6	24.19 ± 8.73	12.82 ± 3.93	795.0 ± 137.1	7.77
Sumatriptan Repeat Study 2	BALB/c	0	0	0.50 ± 0.28	-	< 0.01
		≤0.7	0.11 ± 0.07	1.62 ± 0.85	-	0.02
		≥1.6	49.41 ± 14.24	86.32 ± 47.42	304.5 ± 239.7	3.62

In the first study ('Safety Study'), there was no significant difference ($p>0.05$) found between the Sumatriptan delivery into the skin after applying 2.1 MPa (up to 0.07% dose delivery) or no ultrasound at all (up to 0.10% dose delivery).

More thorough washing of the skin post–exposure and longer degassing time of the coupling cone water to remove pre-focal cavitation events were identified as possible areas of protocol improvement. Enhanced washing substantially decreased the background delivery signal due to Sumatriptan left on the skin surface. Extended degassing served to emphasise the value of cavitation detection and ultimately enhanced the cavitation energy within the desired region. Furthermore, these measures also reduced the detrimental impact on the skin.

With these protocol enhancements in place, 'Sumatriptan Repeat Study 1' on CD1 nude mice showed substantial Sumatriptan delivery into the skin and blood (in total 7.77% of the total applied dose) only in the presence of sustained inertial cavitation at 1.6 MPa ('Cavitation' group). Significantly ($p<0.001$) lower dermal deliveries were detected in the 'Sub Cavitation' group (up to 0.004% of the applied dose). No Sumatriptan was found in the bloodstream after the treatment of 'No Ultrasound' or 'Sub Cavitation'.

Even when repeating the experiment on hairy BALB/c mice ('Sumatriptan Repeat Study 2'), inertial cavitation showed again to have a benefit on Sumatriptan delivery over 'Sub Cavitation' and 'No Ultrasound' treatment. Up to 3.62% of the applied dose was in total delivered after exposing to ≥ 1.6 MPa.

To address the second aim of this chapter, an attempt was made to correlate the level of cavitation with the total Sumatriptan delivery achieved. Overall, it was observed that substantial (up to ~8% of the applied dose) and significant Sumatriptan delivery into the skin and bloodstream was only achieved when sustained inertial cavitation (> 15 μJ) was detected over the 10-minutes exposure.

These studies have therefore demonstrated that inertial cavitation can be used to enhance and monitor delivery of a small molecule, but that many challenges remain in fully standardising and understanding the relationship between cavitation and delivery. Nevertheless, the detected blood concentration was 1000-fold higher than the therapeutic concentration required in mice and already detected within 20 minutes after the start of the treatment, which is substantially more efficient than other needle-free technologies.

The last aim of this chapter was to reduce the physiological impact on the skin after insonation. In the 'Safety Study' redness and white marks on the skin were observed after applying ultrasound at 1.8 MPa. By removing the pre-focal cavitation by extending the degassing time of the water in the cone, no severe skin damage was observed in the two Sumatriptan repeat studies. Occasionally, some sporadic very minor reddening of the skin was observed which resolved in less than 24 hours. Furthermore, the histology in 'Sumatriptan Repeat Study 2' in Figure 3.29 showed local bleeding (bruising) in the hypodermis after inertial cavitation. However, bruising of the tissue heals without scar formation within a couple of days. Therefore, it is assumed that the cavitation-enhanced transdermal device is non-harmful and the absence of pre-focal cavitation essential in preventing severe skin damage at these acoustic pressures.

In the next chapter, the potential of cavitation-enhanced delivery of nucleotide-based therapeutic material is investigated.

Chapter 4: *In vivo* cavitation-enhanced epidermal vaccine delivery

4.1 Introduction

In the previous chapter, cavitation-enhanced transdermal delivery was shown to be of use in the delivery of a small therapeutic agent (i.e. Sumatriptan) into the skin and bloodstream of mouse models. The skin is a dendritic cell-rich environment [23] and is therefore an attractive site for therapy, for example in vaccination. In contrast to drugs such as Sumatriptan or antibodies, which need to achieve delivery into the bloodstream, vaccines typically only have to reach the dermal layers where these dendritic cells reside. Furthermore, much lower levels of vaccine need to be delivered to trigger the immune cells to instigate an immune response. The aim of this study is to investigate if an immune response can be induced by ultrasound-assisted transdermal vaccination of a DNA 'vaccine' construct against influenza (flu) virus. Firstly, the composition of DNA vaccines and their importance to healthcare is described. Secondly, the current challenges and proposed solutions for developing a vaccine against influenza are discussed. Thirdly, an overview is given of how DNA vaccines work and ultimately the aims of this chapter are described.

4.1.1 Vaccination

Vaccination can be considered to be the most effective and cost-beneficial intervention for reducing the morbidity and mortality associated with a whole range of human pathogens in many millions of people. Although the principles of vaccination were understood before the 17th century, with some reports even dating back to 430 BC,

work by the British medical doctor Edward Jenner (1749-1823) represented the first scientifically methodological attempt to control an infectious disease (i.e. smallpox) by vaccination [226]. Vaccination involves the use of an infectious agent or components of an infectious agent [227]. The agents are modified in such a way that the immune system is activated and long-lasting protection is then provided against subsequent exposure to the 'live' pathogen, without instigation of severe ill-effects.

4.1.2 Type of vaccines

Depending on the type of pathogen and its method of infecting cells, there are five main classes of vaccines that can be used and they are described below.

4.1.2.1 Live attenuated vaccines

Live attenuated vaccines (LAV) have been available since the 1950's and are made from disease-causing pathogens (living virus or bacteria) that have been weakened under laboratory conditions [227]. Since LAV are the closest mimic of a natural infection, they can induce strong cellular and antibody responses within a single dose whilst causing no or very mild disease. One limitation of LAV is that the weakened microbe in the vaccine can undergo slight changes or mutations, raising the possibility of a re-establishment of full virulence [228]. Furthermore, LAV need to be refrigerated to stay potent [227, 229]. However, LAV are relatively easy to generate and are commonly used as vaccines against tuberculosis, polio, measles, and yellow fever.

4.1.2.2 Inactivated vaccines

Inactivated vaccines are made from microorganisms that have been killed through physical or chemical processes [230]. This vaccine contains no living components and there is no risk of introducing the disease into the host. The inactive vaccine may induce less strong immune response compared to LAV and possibly require multiple

doses [227]. However, they are safer and more stable than LAV and often do not require refrigeration as they can be stored and transported in a freeze-dried form.

4.1.2.3 Subunit vaccines

Subunit vaccines contain only the antigenic part of the pathogens that is necessary to induce a protective immune response [231]. However, identifying a particular subunit that can elicit an effective immune response with long-lasting memory is a challenging and time-consuming process.

4.1.2.4 Toxoid vaccines

Toxoid vaccines are based on the secreted toxins of bacteria [230, 232]. The toxins are inactivated and used in a vaccine when the bacterial toxin is the main cause of the illness. Diphtheria and tetanus are examples of toxoid vaccines [231].

4.1.2.5 Conjugate vaccines

Conjugate vaccines typically use the sugar molecules (i.e. polysaccharides) on the outside bacterium membrane conjugated to a protein carrier molecule to enhance immunogenicity [231], but the principle of combining separate immunogens into one molecule can be applied more broadly.

4.1.3 Influenza virus

Influenza (or also knows as the flu) is a highly contagious respiratory illness caused by the influenza viruses type A or B that cause annual seasonal epidemics [233]. Influenza virus type C also circulates in humans but causes less severe illness than either types A or B, with symptoms similar to a cold [234]. The natural hosts for influenza A viruses are wild birds, but various mammals including humans, horses, dogs, and pigs have also been infected by the influenza A virus and become a natural host [235].

The influenza vaccines provide a level of efficacy in preventing the spread of the seasonal influenza epidemic. However, unlike many other vaccines they cannot initiate a life-long immunity, and so achieving immunity against influenza requires annual re-vaccination. This is because the high mutation rate of the influenza virus leads to the surface antigenic proteins undergoing rapid change through successive generations of the virus [236]. This means the body cannot neutralise the altered antigenic regions using the antibodies generated against influenza from the previous year or the years before [233, 236]. Therefore, the composition of the influenza vaccine must be updated every year to keep up with the continuous evolution of the virus. Notably, mutations in influenza A viruses occur three times faster than in influenza B viruses, and influenza A viruses lead to higher morbidity and mortality. As a consequence more effort and more resources have been directed at developing vaccines to influenza A.

The major targets of the immune response are the two important surface proteins on the virus surface [236]. Hemagglutinin (H) is responsible for the binding of the virus to the target host cells and mediates the entry of the virus to the cell. Neuraminidase (N) is an enzyme that is essential for the release of recently formed virus particles and the further spread of the virus [237]. There are 18 H-subtypes and 11 N-subtypes [238] and the combination of these two surface glycoproteins typically forms the foreign antigenic material that characterises the influenza strain and comprises the targets for vaccination [233].

There are two types of influenza A combinations (i.e. A/H1N1 and A/H3N2) that circulate widely in humans and are responsible for the seasonal flu as well as for global pandemics in the past [235]. For example, in 1918 the A/H1N1 Spanish flu pandemic

caused more than 50 million deaths worldwide and the mortality induced by the A/H3N2 Hong Kong flu in 1968 was estimated to be over a million deaths worldwide [239].

Influenza epidemics represent a dramatic and recurring public health problem to which governments have responded by introducing widespread yearly vaccination programmes to protect against infection, particularly for people that are predicted to be at higher risk of associated morbidity and mortality if they were to develop an influenza infection. In the United Kingdom, the annual influenza vaccination has been recommended for those aged over 65 years, pregnant women, children under six months, and those that have underlying health conditions [240]. The vaccines used are typically inactivated or live attenuated versions of influenza.

4.1.4 Production of influenza vaccines

The World Health Organisation (WHO) monitors the epidemiology of the circulating influenza viruses worldwide. Twice a year, the WHO reviews the surveillance data with the current virus strains circulating in the Northern (reviewed in February) and Southern (reviewed in September) hemispheres and determines which virus variants are likely to cause the next seasonal flu [241]. The seasonal influenza epidemics are caused by at least one of the influenza A and B subtypes. Since it is difficult to predict which one will cause the next seasonal flu, three or four circulating influenza virus strains are selected by the WHO to be included in the next influenza vaccine. From the moment this information is published, vaccine-producing companies have six months to manufacture large enough vaccine quantities and to deliver the seasonal influenza vaccines to the health care providers [241].

Three different technologies are used to produce influenza vaccines: egg-based, cell-based, and recombinant vaccines and these will be discussed in the next sections.

4.1.4.1 Egg-based vaccine

This process is a time- and resource-intensive method that is critically dependent on the supply of fertilised hens eggs, which might be limited in the case of pandemics. Furthermore, there is a risk of microbial contaminations and unintended change in antigenicity of the virus strain during the manufacturing process [242]. Also, during the six-month production time, mutations in the circulating virus may occur or new virus variants can emerge that reduce the efficacy of the newly produced vaccine. Therefore, there is a pressing need for a technology that can generate sufficient vaccines in decreased manufacturing time.

4.1.4.2 Cell-based vaccine

This technology uses mammalian cells instead of embryonic eggs and was developed as an alternative to the egg-based manufacturing process. The mammalian cells are cultured in synthetic media to avoid animal serum and they can be frozen in advance. Therefore, this technology has a faster start-up and scale-up time than the egg-based vaccines and is also suitable for people with egg allergies [243]. In November 2012, the FDA approved, for the first time, a cell-culture derived influenza vaccine called Flucelvax® (Novartis Vaccines and Diagnostics, USA) [244].

4.1.4.3 Recombinant Vector Vaccines

Another alternative to egg-based vaccine production involves the use of recombinant DNA technology where a section of the target virus genome encoding a particular antigenic epitope is selected and expressed in a heterologous expression system (i.e. E. coli bacteria, yeast, or insect cells) [229]. With a recombinant vaccine, the produced

recombinant (i.e. subunits) proteins are purified and used as antigens to trigger the immune system when administrated. The first recombinant influenza vaccine produced with insect cells (FluBlok®, Protein Science Corporation, USA) was FDA approved in 2013 [245, 246].

4.1.4.4 DNA vaccine

Once the genetic code from a pathogen has been sequenced, the sequence encoding a particular antigen can be used to prepare DNA vaccines. Similar to the production of recombinant protein vaccines, the gene encoding the antigen is selected and is typically incorporated into an expression plasmid and transformed into bacteria [172]. During bacterial growth, multiple plasmid copies are produced and the purified DNA plasmids are administrated as a vaccine. The encoded antigens are produced inside the host to instigate the desired immune response.

The DNA vaccine manufacturing process has the advantages of rapid production (weeks instead of months) and the potential for efficient scale-up in response to a pandemic [247]. Furthermore, DNA vaccines induce a long-lasting immunity and have improved stability for transport and storage. The FDA has yet to approve any DNA vaccines for human use, but the first phase I clinical trial using this approach for influenza A/H1N1 virus has shown the generation of a strong immune response which encourages the further development of this technique [248].

The production of large volumes of plasmids encoding viral proteins still requires the growth of large-scale batches of bacteria in which the plasmids are produced. Rigorous cell lysis and cleaning procedures are then required to ensure no bacterial contaminants are co-delivered [249]. There are also issues with the longevity of the expression that

can be achieved as high levels of CpG repeats (i.e. DNA region where CG:GC ratio is more than 0.6) marks bacterially produced DNA for silencing [250]. Furthermore, there is a concern that the antibiotic resistance genes used in recombinant DNA plasmids can potentially contribute to the development of multi-drug resistant organisms as well as integrate into the human chromosomes [251]. Although these bacterial methods of DNA vaccine production are not ideal, the rationale for the use of DNA vaccines remains strong.

4.1.4.5 Cell-free DNA vaccine

To date, the need for large-scale production of DNA vaccines using high volume bacterial cultures and laborious isolation and purification procedures has proven prohibitive. Whilst DNA vaccines have been proven to be safe in a number of animal studies and early phase clinical trials, and although there are DNA vaccines licensed for veterinary use [252, 253], there are currently none licensed for use in humans [254].

Recently, a novel DNA vaccine technology has emerged which enables the synthesis of large quantities of DNA vaccines in a cell-free way (i.e. without the need for bacteria). Touchlight Genetics Ltd. has developed a proprietary method to synthetically produce DNA on a commercial scale in a two-week process [255]. Due to the shape of the cell-free fabricated DNA vectors, the linear closed DNA constructs are referred to as 'doggy bones' DNA (dbDNA™). In a recent study, the dbDNA™ construct used for DNA vaccines were able to produce comparable expression and immunogenicity as conventional DNA plasmids [256]. Indeed, in mouse model studies this cell-free technology has generated DNA vaccines which can provide protection against a lethal influenza A/H5N1 virus challenge when injected intramuscularly [228]. In this study, BALB/c mice were vaccination intramuscularly (50 μg/mouse) on day 0, 14, and 28,

and showed two weeks after the third vaccination dose titre dilution levels of 6250, which were sufficient to protect 93% of the mice against lethal infection with virulent influenza A/H5N1. The mice containing titre dilution levels of 250 did not survive the lethal challenge. Therefore, it is important that the titre dilution levels are above 250 to successfully protect the mice against lethal influenza.

4.1.5 Working mechanism of DNA vaccine

The exact mechanism by which a DNA vaccine can produce antigen-specific immunity is still unclear. However, in the literature, at least three different routes have been proposed to contribute to the activity of DNA vaccines in the skin [247, 257, 258]. These routes are presented in Figure 4.1.

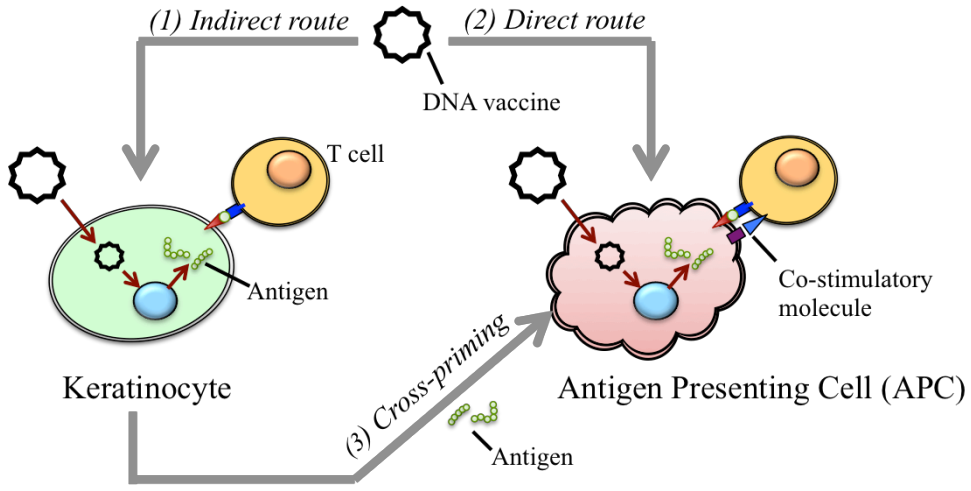

Figure 4.1: Three routes of antigen presentation following DNA immunisation.

Via the indirect route (1) in Figure 4.1, DNA vaccine is taken up by keratinocytes in the skin. Using the host cellular machinery, the DNA vaccine is transcribed and translated inside these cells [258]. The foreign proteins are then degraded into smaller peptide building blocks. These antigens are presented on the cell membrane via Major Histocompatibility Complex (MHC) and recognised by cytotoxic T-cells [257]. Upon binding, the cytotoxic T-cells secrete enzymes that lyse and kill the transfected cell.

The released antigens from the keratinocytes can then 'cross-prime' antigen presenting cells (APC) (route (3) in Figure 4.1).

Via the direct route (2) (Figure 4.1), the DNA vaccine directly transfects the APCs, which are prevalent in the skin. The antigen is expressed by the APC and presented on the cell membrane. The antigen-loaded APCs (via route 2 or 3) move to the draining lymph node where they present the antigens to T-cells in combination with co-stimulatory molecules [259]. These interactions initiate the necessary secondary signals required to induce an immune response cascade, including the activation of B-cells and the production of antibodies specifically against the viral antigens [257]. When antibodies specifically bind to their matching antigen, B-cells are stimulated to produce larger quantities of the specific antibody to further inactivate the pathogen.

After the elimination of the antigen, a small number of B- and T-cells are transformed into memory cells [260]. Upon re-exposure, the memory cells can recognise the antigens and reactivate the immune system resulting in a rapid and effective immune response to neutralise the virus before it causes major ill effects.

4.1.6 DNA vaccine delivery methods

The vectors used for vaccination and the methods for their production have developed and improved considerably since the work of the British medical doctor Edward Jenner in 1796. However, the technologies primarily used for the delivery of vaccines remain rather unsophisticated. The use of hypodermic needle and syringe offers good validation of delivery success but is associated with pain, non-compliance, the risk of needle-stick injuries and poor amenability to non-cold-chain transportation. Many alternative needle-free vaccination methods have been explored and only a couple of them are FDA

approved. For example, Flumist® (MedImmune, LLC, USA) was the first live attenuated intranasal influenza vaccine that was successfully approved by the FDA in 2003 and commercialised in America and Europe under the name Fluenz® [261]. In 2014, the powder jet injector Alfuria® (developed by PharmaJet®) was approved by the FDA to vaccinate against Influenza by shooting vaccine through the skin into the muscle, without a needle but not necessarily without the pain [262]. Furthermore, other needle-free transdermal delivery technologies (see section 1.3.2) have yet to meet the challenges of providing efficacy and validation of dose delivered.

Gene delivery requires the artificial introduction of foreign genes into target cells, where the cellular machinery translates the foreign material and produces the encoded protein. Since DNA is negatively charged like the cell membrane, the electrostatic forces have to be overcome for the DNA to enter the cell. The transfection efficiency into target cells is the highest when encapsulating the genetic material in a viral vector (66.8%) [263]. However, safety concerns (i.e. immunogenicity and cytotoxicity) and misdirection of the resulting immune response has stimulated the development of safer non-viral DNA plasmids [264]. In comparison to the viral vectors, non-viral DNA plasmids are weakly immunogenic (about 18.3% transfection efficiency) and face major delivery challenges. Plasmid DNA is a hydrophilic macromolecule that has limiting capacity to extravasate into the target tissue and successfully transfect the target cells after intravenous injection [265]. In addition, the plasma DNA is subject to rapid degradation *in vivo* by nucleases in the blood plasma or tissue [266].

The use of ultrasound as a transfection method has been studied in literature over a couple of decades as a physical approach to address the shortcomings of alternatives.

In 1987 Fechheimer et al. demonstrated for the first time that plasmid DNA could be successfully transfected *in vitro* to cultured mouse fibroblasts using ultrasound [267]. Also, Tata et al. [268] and Kim et al. [269] demonstrated successful transfection in mammalian cells using exposure to 1.0 MHz (around 15% transfection efficiency). Kim et al. showed that the presence of cavitation played a crucial role in successful transfection, especially because of concomitant cell lysis and the failure of gene expression at 3.5 MHz [269]. Indeed, ultrasound-mediated transfection was significantly enhanced to 50% when introducing encapsulated gas microbubbles (developed as ultrasound contrast agents) to cultured cells [270, 271] and also showed the potential for *in vivo* studies. Anwer et al. showed that localised application of ultrasound (1.5 W/cm^2 for 5 minutes at 1.0 kHz) on skin tumours before or after the injection of contrast agents resulted in the significant enhancement in gene expression to inhibit tumour growth compared to control conditions [272]. The magnitude of enhanced expression was in the range of three to 270-fold but was dependent on the administrated dose (range 15 – 90 μg administrated by tail vein).

Most *in vivo* studies have used ultrasound-mediated gene delivery on organs and tissues that were easy to image by diagnostic ultrasound machines, including heart [273, 274], kidney [275], and skeletal muscles [276-278]. Since higher concentrations of the plasmid DNA at the target tissue result in higher transfection efficiencies [279], many pre-clinical studies have injected the DNA plasmid encoding the reporter genes into the target tissue prior to ultrasound exposure [263, 277, 280-282]. These studies have used different ultrasound parameters such as intensity (0.5 to 3 W/cm^2), duty cycle, frequency (mostly 1-3 MHz), different contrast agents, and in particular short application times (less than 15 minutes) due to the rapid disruption/destruction of the

microbubbles upon insonation. Up to 22-fold enhanced gene expression was observed using the contrast agent Definity® with ultrasound over DNA plasmid injection alone [282]. Perhaps most interesting is the consistent observation that the expression of the reporter gene was only seen in the insonated tissue without the detection of significant expressions in other organs. Unfortunately, direct injection of the plasmid DNA is invasive and also technically difficult to perform. These results show the importance of inducing cavitation during treatment to enhance the gene delivery. However, caution has to be taken that sonoporation can induce cell apoptosis, especially when using continuous ultrasound waves [283].

Currently, it has been found that the most limiting parameter in ultrasound-mediated gene delivery is the number of microbubbles and the duration of generating cavitation. Therefore, inducing sustained inertial cavitation with the NCs was suggested to enhance the duration of inertial cavitation and thereby enhance the cutaneous DNA delivery. In addition, different publications have shown the potential of delivering small and macromolecules into the skin. Furthermore, Tezel et al. has used tetanus toxoid (150 kDa) as a strong immunogenic vaccine and showed in mice that by pre-treating the skin with low-frequency ultrasound (20 kHz, 2.4 W/cm^2, 50% duty cycle, 10 seconds pulse length) that vaccine delivery was enhanced (about 1% of the 100 µg topically applied dose) compared to topical administration [284]. Furthermore, when insonating with an energy of 300 J/cm^2, the induced immune response was comparable to that induced by s.c. injection of 10 µg tetanus toxoid. The application of low-frequency ultrasound permeates the skin, but also stimulated the immune system by the activation of the Langerhans cells in the epidermis [284]. Dahlan et al. also showed the generation of anti-tetanus toxoid IgG and neutralizing antibody titres after sonication pre-treatment

(20 kHz, sonication period 45 seconds, pulse length one second) [285]. Furthermore, it was found that a 10% duty cycle generated a two-fold higher immune response and lower skin damage in comparison to 20% duty cycle. Nevertheless, the immune response was more than 30-fold lower than those obtained after intramuscular injection.

However, there are no published studies available that have shown the potential of inducing an immune response after delivering a DNA vaccine into the skin by cavitation-enhanced transport. The potential to non-invasively deliver genetic material and locally treat the target area with sustained inertial cavitation is novel and therefore the aim is to investigate if an immune response can be induced by cavitation-enhanced epidermal delivery of a DNA vaccine

4.1.7 Validating successful immunity induced by DNA vaccine

As can be seen in Figure 4.2, in summary, there are three main hurdles that need to be overcome to successfully induce immunisation using a DNA vector.

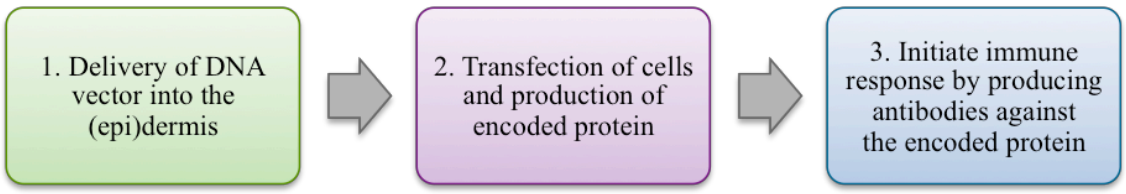

Figure 4.2: Schematic representation of the important steps in immunisation by DNA vaccine.

At first, the DNA vector has to be delivered into the (epi)dermis. Secondly, the DNA vector has to transfect the cells at the inoculation site and express the encoded protein. Thirdly, the immune system needs to produce antibodies against the viral antigen. The production of antibodies can only be initiated when the previous two steps are successfully performed.

Ex vivo and *in vivo* experiments in previous chapters showed the potential of ultrasound technology for delivering small molecule therapeutics (i.e. Sumatriptan in Chapter 3) as well as large therapeutic antibodies (i.e. IgG in Chapter 2) into the skin by cavitation-enhanced delivery. These findings, as well as results found in the literature [286], indicate that a DNA vaccine may be amenable to be delivered into the skin and that the first hurdle shown in Figure 4.2 can be overcome.

To verify if cavitation-enhanced delivery can overcome the second hurdle in Figure 4.2, a study was performed with a DNA construct encoding a luciferase reporter gene (i.e. dbDNA™/Luc). Subsequent delivery of the luciferin substrate for the encoded luciferase protein allows the success of the delivery and expression of the dbDNA™/Luc to be measured. Only the transfected cells express the luciferase enzyme and therefore catalyse the conversion of the substrate (luciferin) leading to the emission of photons of light. This detection method is well-established, rapid, easy to perform and can be repeated over a time course. With this method, it is possible to test and provide an answer to the question of whether cavitation-enhanced delivery can enable transfection of cells and can lead to the production of an encoded protein.

Two *in vivo* studies ('Luciferase Study 1' and '2') were performed to investigate the feasibility of transfecting the cells with the luciferase reporter gene by cavitation-induced transfection. In addition, 'Luciferase Study 2' explored the delivery profile of the dbDNA™ construct post-treatment as well as the transfection efficiency. In the last study (i.e. 'Influenza Vaccination'), the dbDNA™ construct encoding the reporter gene was replaced by a therapeutic DNA vaccine encoding for HA1 protein specific for the influenza A/California/07/2009)(H1N1) type virus (i.e. dbDNA™/Cal09) to show

the clinical potential of cavitation-enhanced transport. The studies performed in this chapter employed the *in vivo* therapeutic ultrasound system developed and optimised in Chapter 3 (Figure 3.4) and the ultrasound settings as defined in Table 3.1.

In summary, the aims of this chapter are:

1) To demonstrate the feasibility of transfecting cells within the epidermis and producing encoded transgenic protein using cavitation-enhanced epidermal delivery.
2) To determine the transfection and dose delivery efficiency of the dbDNA™ vector by cavitation-enhanced transport.
3) To attain and characterize *in vivo* the generation of a specific antibody response against a therapeutic DNA vaccine when delivered into the (epi)dermis using ultrasound-mediated cavitation.

4.2 Materials and Methods

4.2.1 Luciferase Studies

To investigate the first aim of this chapter, two *in vivo* luciferase studies were performed ('Luciferase Study 1' and '2'). In collaboration with Touchlight Genetics Ltd, a dbDNA™ construct encoding a luciferase reporter gene (i.e. dbDNA™/Luc, 2555 bp) was fabricated using a similar method as described in [256] and used for both luciferase studies. In addition, 'Luciferase Study 2' also explored the second aim of this chapter by using qPCR to determine the transfection and delivery efficiencies of cavitation-enhanced transport in the skin.

4.2.1.1 Luciferase Study 1 - Experimental groups

Five female CD1 nude mice (six months old) were obtained from the Biomedical Service Unit at the John Radcliffe Hospital (Oxford, United Kingdom) and were kept (like all other mice in this chapter) under standardised and controlled living environments in accordance with Home Office Legislation and Oxford University Gold Standard.

Since the luciferase assay visualises local expression of the reporter gene, multiple (non-overlapping) regions on the mouse can be treated without cross-contaminating the signal. Therefore, multiple experimental groups were tested on a single mouse reducing the total number of mice required for the experimental study.

As can be observed in Figure 4.3, every mouse received three different treatments in the following order; (1) 'No Ultrasound' - passive diffusion over 10 minutes by placing dbDNA^{TM}/Luc on the right flank and then allowing to rest for 10 minutes,

(2) 'Cavitation' insonation of the right flank for 10 minutes at 1.6 MPa acoustic pressure (sufficient to induce inertial cavitation at acoustic pressures that would result in delivery without causing skin damage as defined in Chapter 3), and (3) 'ID injection' into the neck scruff as positive control.

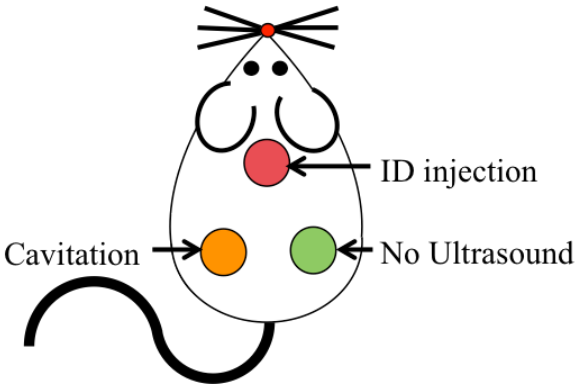

Figure 4.3: Schematic representation of the dbDNA™/Luc treatment locations on the CD1 nude mice. Cutaneous delivery at 1.6 MPa acoustic pressures ('Cavitation') was performed on the left flank and no ultrasound on the right flank. As a positive control, 20 µg dbDNA™/Luc was ID injected into the neck scruff.

4.2.1.2 Luciferase Study 1 - Formulation preparation

The drug formulation for the dermal application (i.e. 'No Ultrasound' and 'Cavitation' groups) contained DI water, NCs and dbDNA™/Luc solution in the composition ratio of 50:25:25 wt.%, respectively. This ratio was used throughout this chapter. The dbDNA™/Luc was diluted with DI water to 35.2 µg/mL before adding to the NCs (20 mg/mL, OxSonics Ltd., United Kingdom), making up a final concentration of 26.4 µg/mL dbDNA™/Luc (corresponding with a total dose of 52.8 µg dbDNA™/Luc per treatment). For the positive control 'ID injection' group, the dbDNA™/Luc was diluted in sterile 20 mM HBS and 100 µL was administrated into the neck scruff delivering a total dose of 20 µg dbDNA™/Luc. The lower dosage was chosen for the positive control group to induce a strong positive luminescent signal that would not overwhelm the signal from the lower level of delivery achieved by cavitation-enhanced transport.

All the formulations were made on the day of the *in vivo* experiments and stored at room temperature before use.

4.2.1.3 Luciferase Study 1 - Experimental protocol

Prior to the procedure, the mice were sedated with 2% isoflurane and 98% oxygen (2 L/min flow rate). To prevent cross-contamination between the three treatment areas on the mouse, the treatment sequence was started with the 'No Ultrasound' treatment on the left flank. The mouse was placed on its side to enhance the stability of the formulation holder on the flank. The holder was filled with ~2 mL of drug formulation before coupling the transducer with the holder. For the 'No Ultrasound' treatment, the formulation was placed on the right flank and left to rest for 10 minutes without ultrasound exposure. Afterwards, the transducer was decoupled from the formulation holder and the remaining formulation left in the holder was discarded. The treated skin was thoroughly washed with tap water to remove any remaining formulation on the skin surface. Then, the skin was dried with a clean tissue and the treatment area was marked with a permanent marker.

The mouse was placed back again under anaesthetics before treating the right flank with 1.6 MPa. During the 10-minute ultrasound treatment (at the acoustic settings outlined in Table 3.1), the PCD was recorded and analysed as described in Chapter 3, section 3.2.2. After thorough washing and drying of the second exposed skin area, the mouse received a single ID injection into the neck scruff and was placed back into a warmed cage to recover. This procedure was performed on all the five mice.

4.2.1.4 Luciferase Study 1 - Bioluminescence Imaging

The expression of luciferase was evaluated 18 hours post-treatment, facilitated by D-luciferin (Thermo Scientific, United Kingdom) injection (100 µL of a 15 mg/mL solution) into the tail of the mice under isoflurane anaesthesia. The mice were imaged 10 minutes later using an In Vivo Imaging System (IVIS, PerkinElmer, USA) and the photons emitted were acquired over a period of 60 seconds.

The images were post-processed with the IVIS software (Living Image®, Perkin Elmer®, USA). For all images, the bioluminescence intensity colour bars were scaled to the radiance range from violet (least intense) to red (most intense) and the three treatment areas ('ID injection', 'Cavitation', and 'No Ultrasound' group) were selected on the mice as outlined in Figure 4.3. To correct for the collecting area size, the results were expressed in photons per second per cm^2. Furthermore, from every mouse, the background signal was acquired and an average background signal over all the tested mice was established. This value was subtracted from the bioluminescence detected from the treatment areas.

4.2.2 Luciferase Study 2

In the second luciferase study, twenty-four female BALB/c mice (six weeks old) were obtained and randomly divided into six groups of four mice: the positive control group 'ID injection' received 50 µg dbDNA™/Luc by ID injection into the flank, the 'Sub Cavitation' group received ultrasound at low acoustic pressures (up to 1.0 MPa), the 'Cavitation' group received ultrasound for 10 minutes generating sustained inertial cavitation at 1.6 MPa acoustic pressure. In a variation to the 'Cavitation' group, the treatment time was extended from 10 minutes to 15 minutes ultrasound exposure in the 'Cavitation – 15 min' group.

The 'Cavitation – Double dose' group received a formulation with two-fold higher dbDNA™/Luc dosage (100 µg/treatment) and was insonated for 10-minutes at 1.6 MPa. The negative control group 'No Ultrasound' investigated the delivery and expression of the dbDNA™/Luc vector by passive diffusion alone by placing a double dose dbDNA™/Luc (100 µg/treatment) on the flank and then allowing it to rest for 10 minutes. An overview of the experimental groups is given in Figure 4.4.

Table 4.1: Overview of experimental groups - Luciferase Study 2.

Experimental group (n=4)	Description of Treatment	Acoustic pressure
No Ultrasound (Negative control)	100 µg dbDNA™/Luc + NCs in water. Applying formulation with double dose dbDNA™/Luc, but no exposure to ultrasound.	0 MPa
Sub Cavitation	50µg dbDNA™/Luc + NCs in water. Exposure to sub cavitation pressure levels during the 10-minutes exposure to ultrasound.	0.7 MPa
Cavitation	50µg dbDNA™/Luc + NCs in water. Generation of sustained inertial cavitation during the 10-minutes exposure to ultrasound.	1.6 MPa
Cavitation - 15 min	50 µg dbDNA™/Luc + NCs in water. Generation of sustained inertial cavitation during the 15-minutes exposure to ultrasound.	1.6 MPa
Cavitation – Double dose	100 µg dbDNA™/Luc + NCs in water. Generation of sustained inertial cavitation during the 10-minutes exposure to ultrasound with double dose dbDNA™/Luc (100 µg/treatment).	1.6 MPa
ID injection (Positive control)	ID injection of dbDNA™/Luc (50µg/100µL) in PBS.	N.A.

Two formulation batches were prepared prior to the experiment as described in section 4.2.1.2, with a single (50 µg) or double (100 µg) dosage of dbDNA™/Luc. For the positive control 'ID injection', the dbDNA™/Luc was diluted in sterile PBS

and 100 µL was administrated into the flank, delivering a total dose of 50 µg dbDNA™/Luc. All the formulations were made on the day of the *in vivo* experiments and stored at room temperature before use.

4.2.2.1 Luciferase Study 2 - Experimental protocol

On the day of the experiment, the fur of the BALB/c mice was removed at the treatment area by using an electric razor and depilatory cream (VEET). Prior to the treatment, the mice were anaesthetised with isoflurane. With the exception of the 'ID injection' group, the formulation holder was placed on the flank and filled with the formulation before coupling the transducer with the formulation holder. Dependent on the experimental group (see Table 4.1), ultrasound was applied at 0, 0.7 or 1.6 MPa for 10 or 15 minutes and the acoustic emissions were recorded with the PCD. After the treatment, the exposed skin was thoroughly washed with tap water, dried, and finally, the treated area was marked with a permanent pen before placing the mouse back into the warmed cage to recover. The anaesthetised mice in the 'ID injection' group received a single 100 µL injection into the flank.

The expression of the luciferase reporter gene was investigated 24 hours post-treatment instead of 18 hours post-treatment as in 'Luciferase Study 1' due to experimental scheduling. The same protocol was used as described in section 4.2.1.4. The mice were imaged 3.5 minutes after injecting the D-luciferin and the photon emissions were collected over 90 seconds. The data was analysed in the same way as described in section 4.2.1.4.

4.2.2.2 Luciferase Study 2 - Skin preparation

After imaging the mice 24 hours post-treatment, the mice were sacrificed by cervical dislocation and the exposed skin area was rescued and stored at -20°C. For the calibration curve, skin from an untreated mouse was collected and directly spiked with different known amounts of formulation and stored at -20°C.

The delivery of dbDNA™/Luc into the rescued skin 24 hours post-treatment was determined by quantitative Polymerase Chain Reaction (qPCR). Before performing qPCR, the rescued skin was homogenised and the DNA was isolated from the skin homogenate. Similar protocol for homogenising skin was used as described in Chapter 3, section 3.2.9.1. Briefly, skin samples were weighed and cut into smaller pieces. PBS was added to the skin samples to achieve a concentration of 1 mL solution/100 mg skin. The skin was homogenised on ice and stored at -20°C. For the calibration curve, a five-fold serial dilution was prepared by diluting spiked skin with non-treated skin homogenate. The genomic DNA was extracted from the homogenised experimental and calibration samples with the GenElute^{TM} Mammalian Genomic DNA Miniprep Kit (Sigma, United Kingdom). The samples were stored at -20°C.

4.2.2.3 Luciferase Study 2 - qPCR protocol

A real-time analysis, that used a fluorescent-based PCR, was performed to quantify how many dbDNA™/Luc copies were delivered into the skin after treatment. This technique can selectively generate billions of copies of a specific sequence within a DNA template (i.e. target DNA).

In the luciferase studies, the delivered dbDNA™/Luc contained a specific gene for the enzyme luciferase. Since these mice were not exposed to this gene before,

their cells should not contain this gene. Therefore, the presence of the luciferase gene in the rescued skin can only occur after treatment with dbDNA™/Luc.

The fluorescent-based PCR was performed on the StepOnePlus™ Real-Time PCR System (ThermoFisher, United Kingdom). The specifically designed probe (purified by HPLC) and the forward and reverse primers (desalted) for the target DNA in the dbDNA™/Luc were purchased from Sigma-Aldrich. The probe contained on either side a fluorescent dye, 6FAM (6-carboxyfluorescein) receptor dye and TAMRA (tetramethylrhodamine) quencher dye. The sequences of the probe and two primers are provided in Table 4.2.

Table 4.2: qPCR primers and probe for dbDNA™/Luc.

	Sequence (5'-3')
Probe	[6FAM] TGCTGGTGCCCACACTATTTAGCT[TAMRA]
Reverse primer	GTCGTACTTGTCGATGAGAGTG
Forward primer	CTTCGAGGAGGAGCTATTCTTG

The master mix was prepared using qPCRBIO Probe Mix Hi-ROX (PCR Biosystems Ltd., United Kingdom) and according to the manufacturer's instructions containing a final concentration of 200 nM TAM-FAMRA labelled probe and 400 nM forward and reverse primers, PCR grade water, nucleotides, polymerase, buffers, and ROX dye. To every well in the MicroAmp™ Fast Optical 96-well reaction plate (ThermoFisher, United Kingdom), 5 µL template DNA rescued from the skin samples (or from spiked calibration samples) was mixed with 15 µL master mix. The plate was coated with adhesive PCR plate seal (ThermoFisher, United Kingdom). All the experimental and calibration samples were tested in triplicate.

The qPCR conditions were 95°C for polymerase activation and denaturing for two minutes followed by the amplification cycles consisting of 95°C for five seconds, and 60°C for 30 seconds that was repeated for 40 cycles.

4.2.2.4 Luciferase Study 2 –qPCR data analysis

The raw qPCR data, as well as the determined C_T values, were obtained from the StepOnePlus™ Real-Time PCR System. For the calibration curve, the C_T values of the calibration samples were plotted against the known number of DNA copies in the 5 µL template DNA solution and fitted with an exponential regression curve (Figure 4.4(b)).

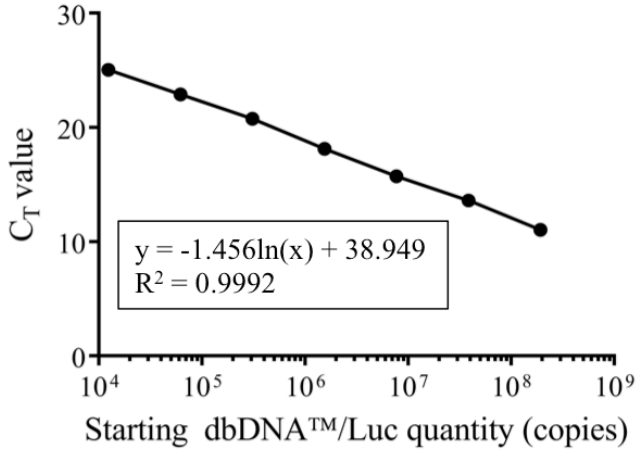

Figure 4.4: Calibration samples of dbDNA™/Luc in the skin. a) Amplification plot of five-fold dilution series of dbDNA™/Luc copies in the skin. b) The calibration curve with the C_T value of the calibration samples plotted against the natural logarithm (ln) of each known dbDNA™/Luc copies.

To calculate the total amount of DNA copies delivered into the rescued skin, the C_T values from the experimental samples were converted into the amount of DNA copies added to the 96-wells plate at the start of the run by using the exponential regression formula in the form of $y=a \ln(x) + b$, with y the C_T values, 'a' the slope, $\ln(x)$ the natural logarithm, and 'b' the intercept from the calibration curve (Figure 4.4(b)).

Before homogenising the rescued skin tissue, PBS was added to the skin samples to achieve a concentration of 1000 µL solution/100 mg skin. Subsequently, the DNA was extracted from the homogenate, assuming no dilution or loss of DNA from the sample above the level seen with the identically treated calibration curve samples.

To calculate the total amount of DNA copies in the rescued skin, the number of DNA copies in the skin homogenate was multiplied by the total volume (µL) PBS added, which corresponds to 10x skin weight (mg). Therefore,

$$\text{dbDNA™ copies in the skin} = e^{\left(\frac{C_T - b}{a}\right)} \cdot (10 \cdot \text{skin weight (mg)}) \quad (4.1)$$

with the C_T value, 'a' the slope, and 'b' the intercept of the calibration curve.

To determine how much of the applied dose was delivered into the skin, the following formula was used:

$$\text{Dose delivery in the skin (\%)} = \left(\frac{\text{DNA copies in the skin}}{\text{total applied DNA copies}}\right) \cdot 100\% \quad (4.2)$$

4.2.3 Dose Delivery Efficiency

To evaluate the dose delivery efficiency 10 minutes post-treatment, this *in vivo* study was performed containing nine female BALB/c mice (six-weeks old) that were obtained and randomly divided into three experimental groups of three mice: 'Sub Cavitation', 'Cavitation' or 'ID injection' group, with an overview of the conditions outlined in Table 4.3. The negative control group 'No Ultrasound' was not included, because it was found in 'Luciferase Study 1' that the delivery by passive diffusion alone was not sufficient to initiate successful cell transfection and gene expression.

Table 4.3: Overview of experimental groups – Dose Delivery Efficiency.

Experimental group (n=3)	Description of Treatment	Acoustic pressure
Sub Cavitation	50 µg dbDNA™/Cal09 + NCs in water. Exposure to sub cavitation pressure levels during the 10-minutes exposure to ultrasound.	0.7 MPa
Cavitation	50 µg dbDNA™/Cal09 + NCs in water. Generation of sustained inertial cavitation during the 10-minutes exposing to ultrasound.	1.6 MPa
ID injection (Positive control)	ID injection of dbDNA™/Cal09 (50µg/100µL) in PBS.	N.A.

The formulations for the three experimental groups were prepared as described in section 4.2.1.2. For this study, a second dbDNA™ construct was provided by Touchlight Genetics Ltd, encoding a therapeutic DNA vaccine against the HA1 protein specific for influenza A/California/07/2009 (H1N1) type virus (i.e. dbDNA™/Cal09, 2603 bp). This dbDNA™ construct was fabricated in the same way and of similar size to the dbDNA™/Luc construct. Since the delivery efficiency was investigated 10 minutes after treatment, the delivery profile of the dbDNA™/Cal09 construct was assumed to be essentially the same as for the dbDNA™/Luc vector.

On the day of the experiment, the BALB/c mice were prepared as described in section 4.2.2.1. Depending on the experimental group (Table 4.3), the mice received an ID injection or were insonated at 0.7 or 1.6 MPa for 10 minutes. The mice were sacrificed by cervical dislocation 10 minutes after finishing the treatment. The exposed skin area was rescued, homogenised, and the DNA was isolated from the homogenate by DNA extraction (as described in section 4.2.2.2). Due to the high concentration of DNA templates in the skin samples collected from the 'ID injection' group,

these samples were 10,000-fold diluted with skin extract from a non-treated skin sample. Furthermore, for the calibration curve, a five-fold serial dilution was prepared by diluting spiked skin with non-treated skin homogenate. The delivery of the dbDNA™/Cal09 into the rescued skin 10 minutes post-treatment was analysed by qPCR (as described in section 4.2.2.3).

Since the DNA sequence of the dbDNA™/Cal09 was different from the dbDNA™/Luc, the 6FAM-TAMRA labelled probe and the two primers were specifically designed for the target DNA in the dbDNA™/Cal09 vector and purchased from Sigma-Aldrich. The sequences of the probe (purified by HPLC) and the two primers (desalted) are presented in Table 4.4.

Table 4.4: qPCR primers and probe for dbDNA™/Cal09.

	Sequence (5'-3')
Probe	[6FAM] CGGAGCCAACTGAAGAACAACG[TAMRA]
Reverse primer	CTTCCTCGCTGTACTTAG
Forward primer	CAACGTGAAGAACCTGTA

The linear regression curve from the calibration curve (Figure 4.5) was used to calculate the total amount of DNA copies delivered into the rescued skin (as described in section 4.2.2.4). For the skin samples collected from the 'ID injection' group, the calculated quantities were corrected for the 10,000-fold dilution factor. Based on the cutaneous delivery calculated at 10 minutes and 24 hours post-treatment, the delivery efficiencies were determined with formula 4.2.

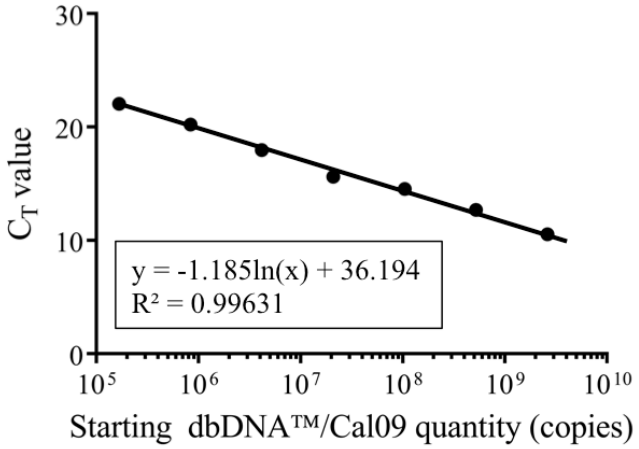

Figure 4.5: Calibration curve of dbDNA™/Cal09 in murine skin. The C_T values of the calibration samples are plotted against the natural logarithm (ln) of each known dbDNA™/Cal09 copies.

To determine how much of the delivered dbDNA™ copies were still remaining in the skin 24 hours post-treatment, the following formula was used:

$$\text{Transfection efficiency (\%)} = \left(\frac{\text{DNA copies 24 hours}}{\text{DNA copies 10 min}}\right) \cdot 100\% \qquad (4.3)$$

This formula assumes that all dbDNA™ copies are cleared from the tissue within 24 hours post-treatment, unless the dbDNA™ construct was successfully transfected in the cells and protected from clearance/degradation by nucleases [287].

4.2.4 Influenza Vaccination

To study the last aim of this chapter, the 'Influenza Vaccination' study assessed if cavitation-mediated delivery can induce an immune response against a therapeutic dbDNA™/Cal09 vaccine. For this study, 15 female BALB/c mice (seven-weeks-old) were obtained and randomly divided into three experimental groups of five mice; 'Sub Cavitation', 'Cavitation' or 'ID injection' group (see Table 4.3). The formulations for the three experimental groups were prepared as described in section 4.2.1.2, with a total dose of 50 µg dbDNA™/Cal09 per treatment.

4.2.4.1 *Influenza Vaccination - Experimental protocol*

As can be observed in Figure 4.6, at the start of the 'Influenza Vaccination' (day 0), the mice received their first vaccination ('Prime') and on day 20 their second ('Boost'). On the day of the 'Prime' and 'Boost' treatment, the BALB/c mice were prepared and the experiments were performed as described in section 4.2.2.1. Depending on the experimental group (Table 4.3), ultrasound was applied at 0.7 or 1.6 MPa for 10 minutes. The mice in the 'ID injection' group received a single 100 µL injection into the flank.

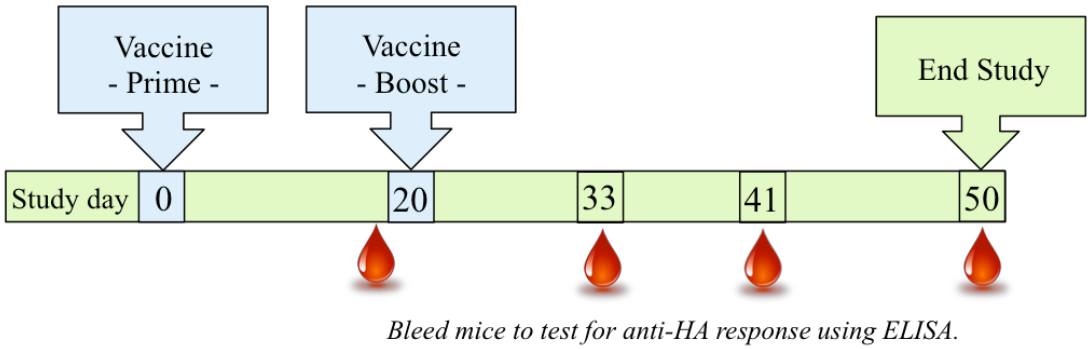

Figure 4.6: Timeline of ultrasound-assisted epidermal vaccination study.

The immune response generated against the HA1 protein encoded by the dbDNA™/Cal09 vector was characterised by taking blood samples from the tail vein on day 16 (prior to the 'Boost' treatment), day 33, 41, and 50 (see Figure 4.6). The blood was diluted in PBS (1:50 dilution) and centrifuged for three minutes at 3,000x g. The supernatant (blood serum/PBS) was collected and stored at -20°C until further analysis by ELISA. The mice were sacrificed on day 50 by cervical dislocation.

4.2.4.2 *Influenza Vaccination - Detection of antibody levels in blood serum*

The amount of antibodies present in the collected blood was calculated by ELISA. The titre levels in the blood serum were determined by diluting the blood samples in

a two-fold series until no detectable signal was measured. Briefly, 96 well-Nunc ImmunoPlates (MaxiSorp) were coated with recombinant HA1 protein (A/California/07/2009)(H1N1) (Immune Technology Corp., USA) at 100 ng/well. The coating was performed by overnight incubation at 4°C. The following day, the plate was washed six times with PBS-T (i.e. PBS containing 0.05% Tween 20) and blocked with 10% FBS in PBS for one hour at room temperature. The collected blood samples were diluted with PBS in a dilution series of 1:50, 1:100, 1:200 etc. After washing the plate six times with PBS-T, 50 µL of diluted blood samples were added to the well in duplicate. After two hours incubation at room temperature, the plate was washed again and HRP-labelled anti-mouse IgG (whole antibody) produced in goat (A4416, Sigma-Aldrich, United Kingdom) was added in 1:10,000 dilution to target any anti-influenza A(H1NI)Cal09 antibodies attached to the HA1 proteins on the plate. After a final washing step, the reaction was visualised by adding 50 µL/well of HRP substrate (Ultra-TMB, Alpha Thermo Scientific) and stopped after 20 minutes by adding 50 µL/well of stop solution (0.5M H_2SO_4 solution). The absorbance was measured at 450 nm with the FLUOstar Omega plate reader (BMG Labtech, Germany).

To every ELISA plate, a negative control was added that contained blood from a non-treated mouse (1:50 dilution). For the positive control, anti-influenza A(H1N1)Cal09, HA1 antibody (Kerafast, USA) was added in 1:10,000 dilution. The titre levels from every mouse were determined at the last dilution that had a signal higher than the mean of negative control wells plus two times the standard deviation. The titre per experimental group was determined by calculating the mean titre and the standard deviation within the group.

4.3 Results

4.3.1 Luciferase Study 1

In this first study, the feasibility of delivering the luciferase reporter gene via cavitation-enhanced transport was investigated. The acoustic emissions recorded by the PCD during treatment are presented first and then the cutaneous expression of the dbDNA™/Luc construct is described.

4.3.1.1 Luciferase Study 1 - Cavitation detection

The acoustic emissions originating from within the formulation and skin were isolated (see section 3.2.2). The acoustic emission spectrograms and the TASE values were determined (see section 2.2.4) for the 'Cavitation' group. Since the acoustic spectrograms were very similar, a representative spectrogram for the 'Cavitation' group is presented in Figure 4.7(a) and shows strong and sustained broadband acoustic emissions over the total 10-minutes treatment time. This successfully indicated the presence of sustained inertial cavitation during the 'Cavitation' treatment. The average TASE value for the 'Cavitation' group was 35.14 ± 11.36 µJ (Figure 4.7(b)).

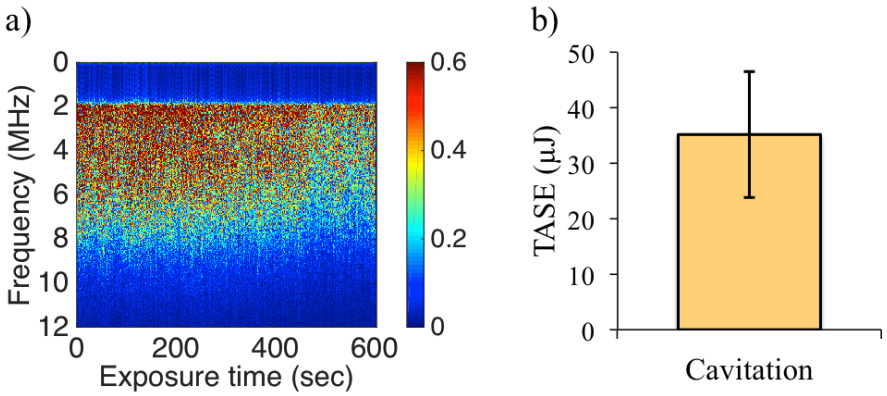

Figure 4.7: Acoustic emission spectrogram from NCs with dbDNA™/Luc exposed to 1.6 MPa. a) Representative spectrogram of the 'Cavitation' group. In the absence of ultrasound, there was nothing to record and therefore only the acoustic emissions from the 'Cavitation' group were analysed. The left axis shows the frequency spectra recorded by the PCD, the colour bar on the right axis represents the power spectral density (mV^2/Hz). b) The bar chart shows the mean TASE value determined in the 'Cavitation' group and the error bar represent the standard deviation for n=5 mice.

4.3.1.2 *Luciferase Study 1 - Expression of dbDNA™/Luc construct*

The effect of the sustained inertial cavitation on the expression of the luciferase reporter gene was investigated by taking IVIS images of the mice 18 hours post-treatment. The results are presented in Figure 4.8.

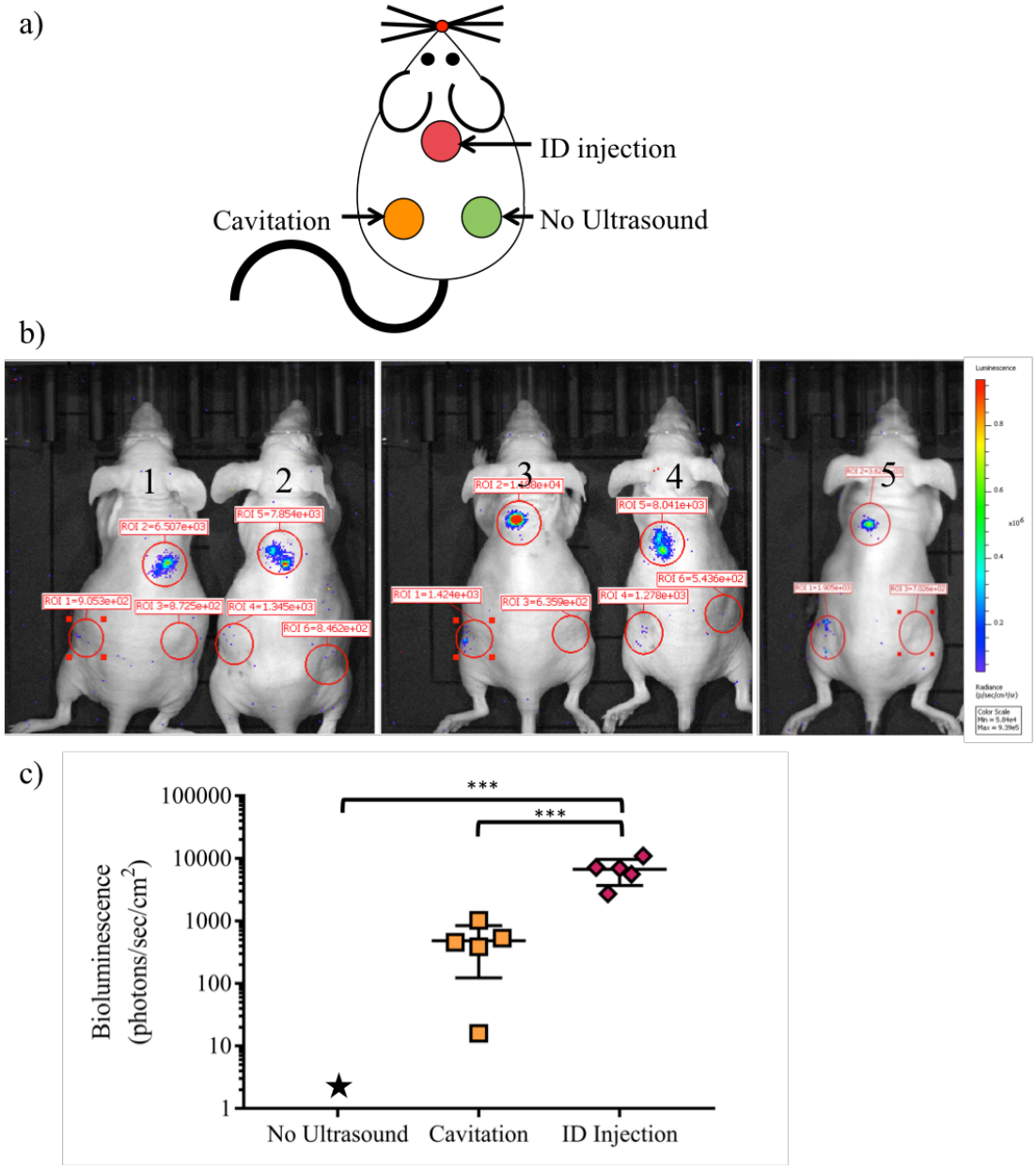

Figure 4.8: Luciferase activity detected 18 hours after treatment. a) Schematic representation of the treatment locations. b) IVIS images of the bioluminescent signal of luciferase expression in the three different treatment location (red circles) in all the five mice. Colour presentation indicates the intensity of the bioluminescence in photons/sec/cm^2, as shown in the bar. c) Quantification of the amount of photons emitted by the luciferase-expressing cells of the five mice per experimental group after background correction with the mean and standard deviation shown. The ★ in (c) highlights the five mice in the 'No Ultrasound' group that had no detectable bioluminescent signal after background correction. The significant difference was determined by one-way ANOVA Bonferroni multiple comparison tests and *** corresponds to $p<0.001$.

Figure 4.8(b) shows the IVIS images of the five mice, where the three red circles on each mouse correspond to the 'ID injection', 'Cavitation', or 'No Ultrasound' group, as indicated in Figure 4.8(a). By using the gold standard of ID injecting 20 μg dbDNA^{TM}/Luc into the neck scruff, strong bioluminescence was detected by luciferase transfected cells as indicated by the green and red coloured pixels in Figure 4.8(b). In the absence of ultrasound, no photons were detected at the treatment area on right flank (indicated by ★ in Figure 4.8(c)). This demonstrates that the delivery of dbDNA^{TM}/Luc into the skin by diffusion alone did not achieve transfection of cells.

After applying 10-minutes inertial cavitation on the left flank ('Cavitation' group), bioluminescence was detected locally within the treatment area as can be observed by the (light) blue pixels scattered inside the red circles on the left flank in Figure 4.8(b). Although the bioluminescence was significantly ($p<0.001$) and substantially (14-fold) lower than after ID injection (Figure 4.8(c)), these results show the feasibility of delivering a dbDNA™/Luc construct into the skin to transfect cells and initiate gene expression by cavitation-enhanced transport *in vivo*.

Figure 4.9 attempts to represent any correlation between the level of cavitation (TASE) and the total bioluminescent signal detected for each individual sample of the 'Cavitation' and 'No Ultrasound' groups. It can be observed that in the absence of ultrasound (★, Figure 4.9), no emitted photons were detected corresponding to a failure in transfection. Only in the presence of sustained inertial cavitation with TASE values beyond 20 μJ, transfection was achieved and the bioluminescent signal from luciferase expressing cells was detected.

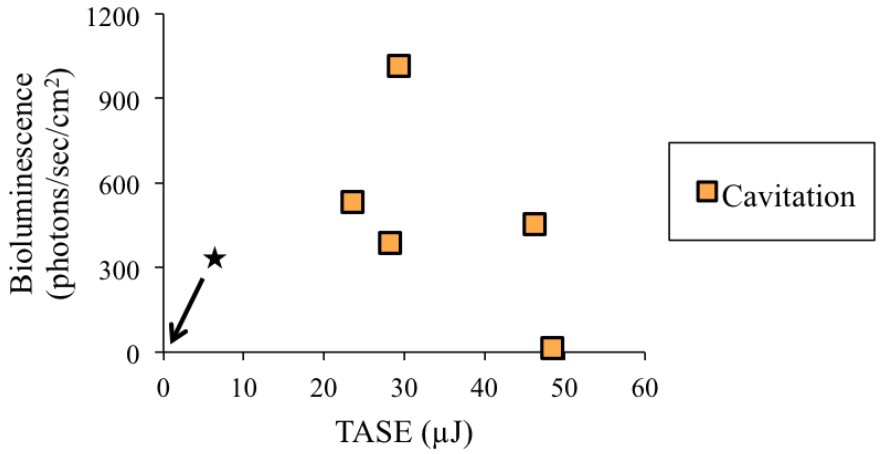

Figure 4.9: Plot between recorded TASE value per sample by passive cavitation monitoring and the bioluminescent signal of luciferase-expressing cells after cavitation treatment. In the absence of ultrasound, no photons were detected in any of the five mice (indicated by ★).

However, the data from the five mice in the 'Cavitation' group (orange squares, Figure 4.9) showed high intra-replicate variability in calculated TASE values, even though all the five mice in this group were consistently insonated at 1.6 MPa. Hence, from these data no detailed correlation between the bioluminescent signal and the TASE value can be attained.

4.3.1.3 Luciferase Study 1 - Conclusion

Overall, these results demonstrated that inertial cavitation rather than passive diffusion alone can provide a mechanism to transfect cells with the dbDNA™/Luc construct leading to the production of the encoded transgenic protein. However, the detected bioluminescent signal 18 hours after the cavitation treatment was 14-fold lower than after injecting 20 µg dbDNA™/Luc. To investigate the reproducibility of these results, the experiment was repeated using eight-weeks old BALB/c mice (see next section).

4.3.2 Luciferase Study 2

In this second luciferase study, three additional experimental groups were included. The mice in the 'Sub Cavitation' group were insonated for 10-minutes at sub cavitation pressure levels (≤ 1.0 MPa). Furthermore, in a variation to the 'Cavitation' group (i.e. generating sustained inertial cavitation at 1.6 MPa), the treatment time was extended from 10 minutes to 15 minutes (i.e. 'Cavitation – 15 min' group), and the 'Cavitation – Double dose' group received a formulation with two-fold higher dbDNA™/Luc dosage (100 μg/treatment) and was insonated for 10-minutes at 1.6 MPa. Firstly, the acoustic emissions recorded by the PCD during treatment are discussed and the expression of the dbDNA™/Luc construct 24 hours post-treatment is then presented.

4.3.2.1 Luciferase Study 2 - Cavitation detection

The acoustic emission spectrograms were characterised for the four experimental groups exposed to ultrasound and representative spectrograms are presented in Figure 4.10(a-d). In addition, the TASE values were determined and presented in Figure 4.10(e).

Figure 4.10(a) shows the spectrogram of one treated mouse in the 'Sub Cavitation' group insonated at 1.0 MPa acoustic pressure (Figure 4.10(a), left-hand side) and one representative spectrogram of the other three mice treated at 0.7 MPa (Figure 4.10(a), right-hand side). The spectrogram recorded at 1.0 MPa showed sporadic broadband acoustic emissions which blue/green bands (TASE value of 1.53 μJ). Lowering the acoustic pressure from 1.0 MPa to 0.7 MPa reduced the recorded power spectral density as can be observed by the light blue bands in the right spectrogram in Figure 4.10(a). The TASE value calculated for the three mice insonated at 0.7 MPa was 0.28 ± 0.04 μJ.

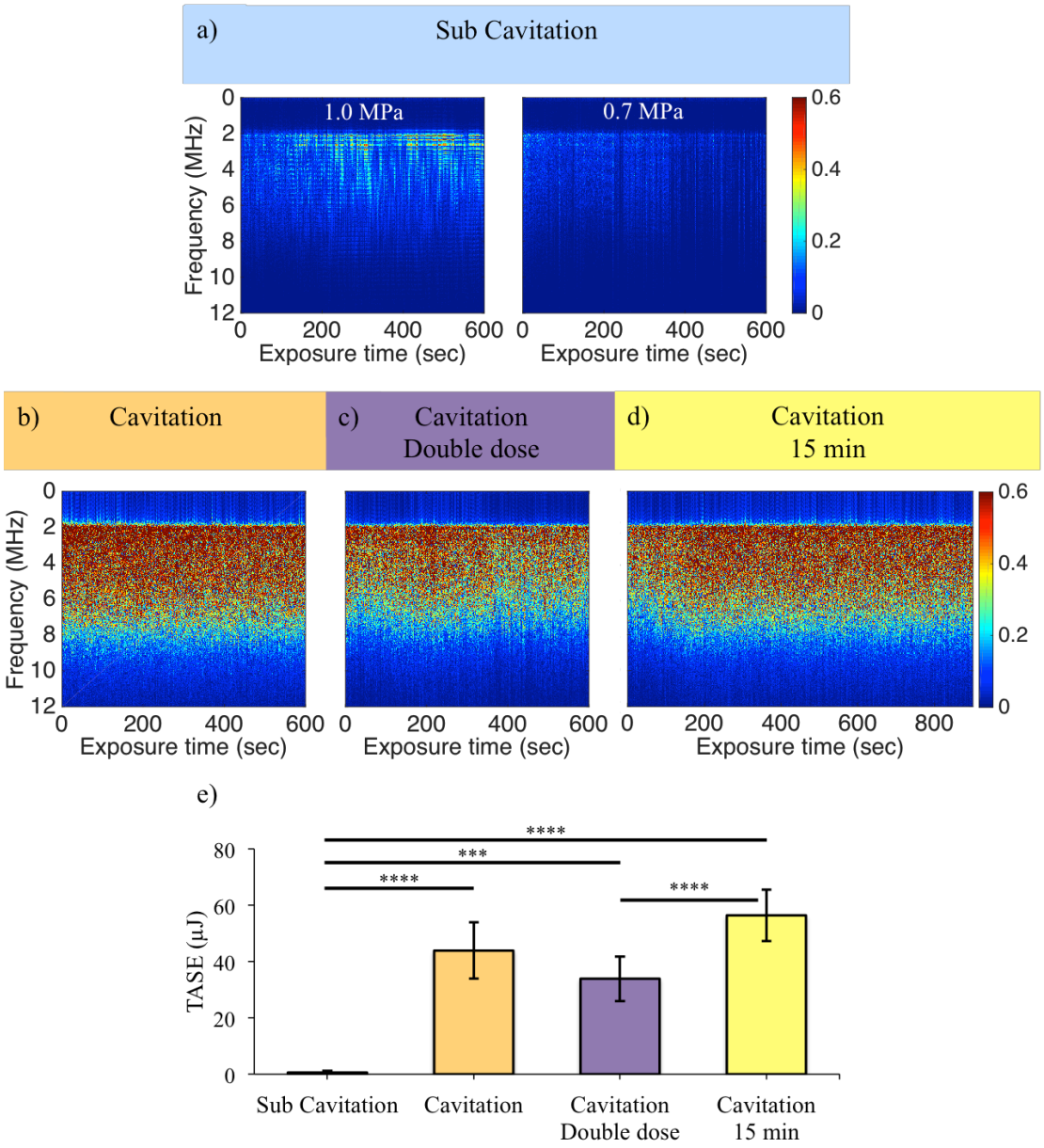

Figure 4.10: Acoustic emission spectrograms from NCs with dbDNA™/Luc exposed to (a) sub cavitation pressure levels of ≥ 1.0 MPa, or (b-d) inertial cavitation at 1.6 MPa. In a variation to the 10 minutes 'Cavitation' treatment (b), the applied dbDNA™ dose was doubled to 100µg/treatment (c), or the insontation time was extended to 15 minutes (d). The left axis shows the frequency spectra recorded by the PCD, the colour bar on the right axis represents the power spectral density (mV^2/Hz). e) The bar chart shows the mean TASE values and the error bar represent the standard deviation for n=4 mice. The significant difference was determined by one-way ANOVA Bonferroni multiple comparison tests with $p<0.001$ (***) and $p<0.0001$ (****).

When insonating the formulation at 1.6 MPa, raised and sustained broadband acoustic emissions were recorded for all the mice in the 'Cavitation', 'Cavitation – Double dose', and 'Cavitation – 15 min' groups (Figure 4.10(b-d)). The TASE value calculated for the 'Cavitation' group was 43.89 ± 9.95 µJ and was significantly ($p<0.0001$) higher than

the ‘Sub Cavitation’ group. Doubling the concentration of dbDNA™/Luc in the formulation slightly reduced, but not significantly ($p>0.05$), the TASE value to 33.92 ± 7.94 μJ. This indicates that the addition of the dbDNA™/Luc to the NCs had no influence on the generation of sustained inertial cavitation. In addition, extending the insonating time to 15 minutes showed sustained inertial cavitation and increased the TASE value to 56.42 ± 9.15 μJ, but not to a significant ($p>0.05$) level compared to the 10-minutes treatment time of the ‘Cavitation’ group. This suggests that extending the exposure duration may not be the simplest method of enhancing delivery.

4.3.2.2 Luciferase Study 2 - Expression of dbDNA™/Luc construct

The effect of the sustained inertial cavitation on the expression of the luciferase reporter gene in the skin was assessed 24 hours post-treatment and the bioluminescent results are shown in Figure 4.11.

Figure 4.11(a) shows that in the absence of ultrasound, no photons were detected in the treatment area. In accordance with ‘Luciferase Study 1’ (Figure 4.8), this indicates that the delivery of dbDNA™/Luc into the skin by diffusion alone was not a successful means of transfecting the cells with the dbDNA™ construct. Furthermore, no bioluminescent signal was detected in three out of the four mice in the ‘Sub Cavitation’ group (Figure 4.11(b)) that were insonated at 0.7 MPa. Interestingly, a single mouse in this group that expressed strong bioluminescence (2.86×10^6 photons/sec/cm^2) in the whole treatment area was insonated at 1.0 MPa. This mouse was the first to be treated in this group and on the basis of the raised cavitation signal observed the subsequent mice were treated at 0.7 MPa. Although this has created a disparity within this treatment group, it does exemplify the value of the feedback provided by cavitation detection and perhaps also helped to identify the TASE threshold for successful delivery.

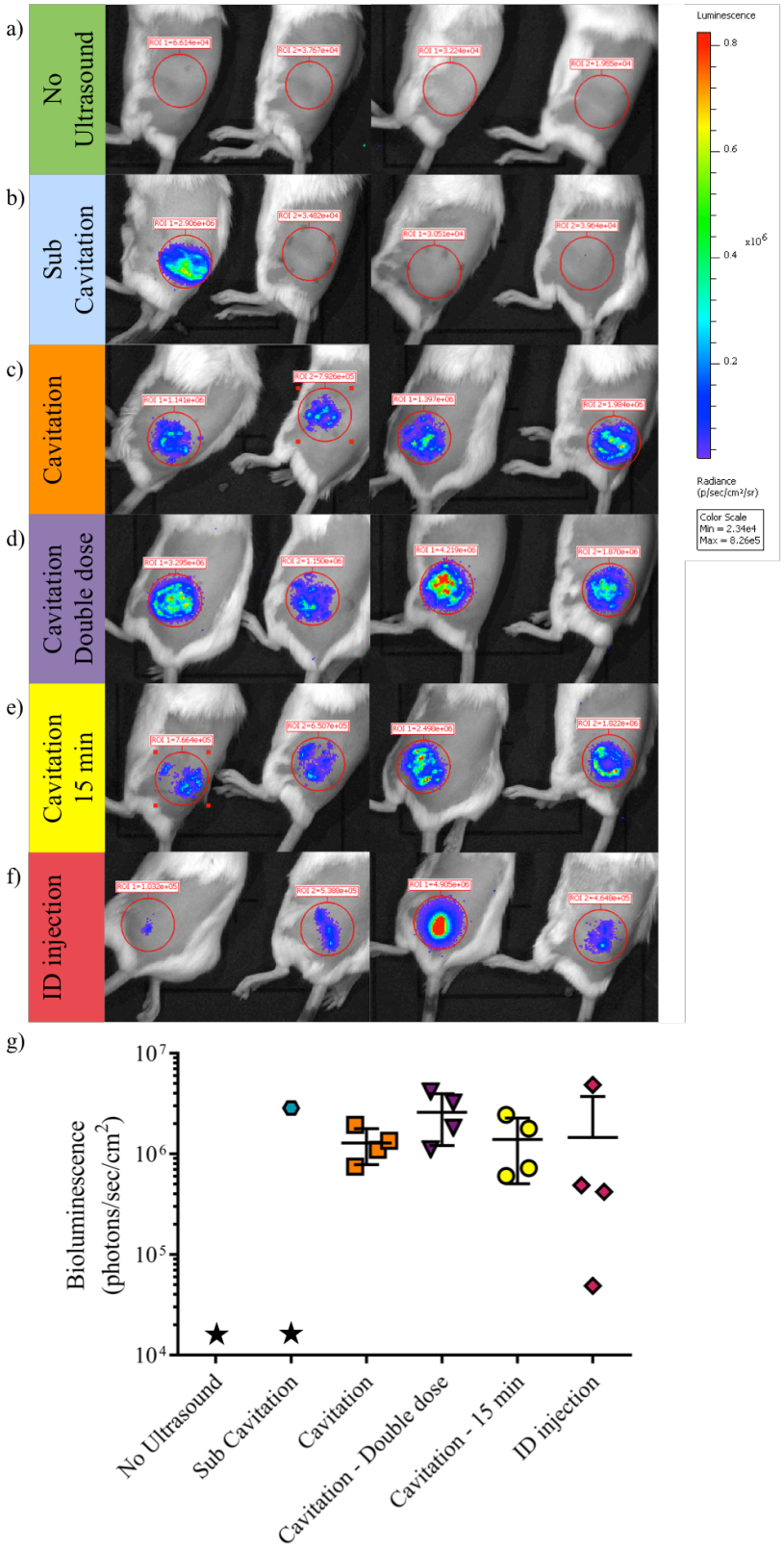

Figure 4.11: *In vivo* bioluminescent imaging of BALB/c mice 24 hours post-treatment with dbDNA™/Luc. The images were taken from the mice (n=4) treated with (a) 'No Ultrasound' (negative control), (b) 'Sub Cavitation', (c) 'Cavitation', (d) 'Cavitation – Double dose', (e) 'Cavitation – 15 min', and (f) 'ID injection' (positive control). The red circle indicates the treatment location on the flank. g) Quantification of the amount of photons emitted by the luciferase-expressing cells of the four mice per experimental group with the mean and standard deviation shown. The ★ in (g) highlights the four mice in the 'No Ultrasound' group and the three mice of the 'Sub Cavitation' group that had no detectable bioluminescent signal. No significant difference was found ($p>0.05$).

After applying 10 minutes inertial cavitation ('Cavitation' group, Figure 4.11(c)), strong bioluminescence ($1.28x10^6 \pm 5.02x10^5$ photons/sec/cm^2) was detected within the whole treatment area as can be observed by the (light) blue pixels inside the red circles. This clearly demonstrates the feasibility of delivering a dbDNA™ construct into the skin to successfully transfect cells and initiate gene expression by cavitation-enhanced transport.

By doubling the dbDNA™/Luc concentration in the formulation, stronger bioluminescent signal ($2.59x10^6 \pm 1.38x10^6$ photons/sec/cm^2) was detected from the 'Cavitation – Double dose' group, as indicated by the green and red pixels inside the red circle in Figure 4.11(d). The bioluminescence was two-fold higher than the 'Cavitation' group, but not significantly ($p>0.05$) different. Furthermore, extending the treatment time to 15 minutes showed no enhancement expression over 10-minute treatment with inertial cavitation (compare Figure 4.11(c) and (e)). These findings indicate that alterations in dbDNA™ concentration rather than exposure time may be a preferable route to optimisation.

Using the gold standard of injecting 50 μg dbDNA™/Luc into the flank, high bioluminescent signal was observed at the location of injection ($1.45x10^6 \pm 2.28x10^6$ photons/sec/cm^2, Figure 4.11(e)). However, the signal was not as spread over the treatment area as the experimental groups receiving a 'Cavitation' treatment (compare Figure 4.11(c-e) with Figure 4.11(f)). Furthermore, the expression levels between the four mice showed high variability. This variation may be due to the technical challenge of administrating the dose into the dermis. Pushing the needle too deep into the skin will result in a subcutaneous injection to the hypodermis.

Nevertheless, when comparing the gold standard to the experimental groups, it was found that similar expressions levels were detected with no significant difference ($p>0.05$) between the 'ID injection' group and the levels found in the 'Cavitation', 'Cavitation – Double dose', and 'Cavitation – 15 min' groups (see Figure 4.11(f)). This promising result indicates that the 'Cavitation' treatment is as effective in the production of the encoded gene as using the needle and syringe and may even provide improved reproducibility and a larger area of transfected cells.

4.3.2.3 Luciferase Study 2 - Cutaneous delivery and transfection efficiency

To address the third aim of this study, the cutaneous delivery in skin recovered 10 minutes ('Dose Delivery Efficiency') or 24 hours post-treatment was quantified using qPCR (see sections 4.2.2.2-4 and 4.2.3). For the 'Dose Delivery Efficiency' study, the TASE values were 0.35 ± 0.17 μJ for the 'Sub Cavitation' group and 41.79 ± 10.77 μJ for the 'Cavitation' group. These levels were similar and not significantly different from the TASE values measured in Figure 4.10(e) from the 'Luciferase Study 2'. The amount of dbDNA™ copies present in the rescued skin 10 minutes and 24 hours post-treatment are shown in Figure 4.12.

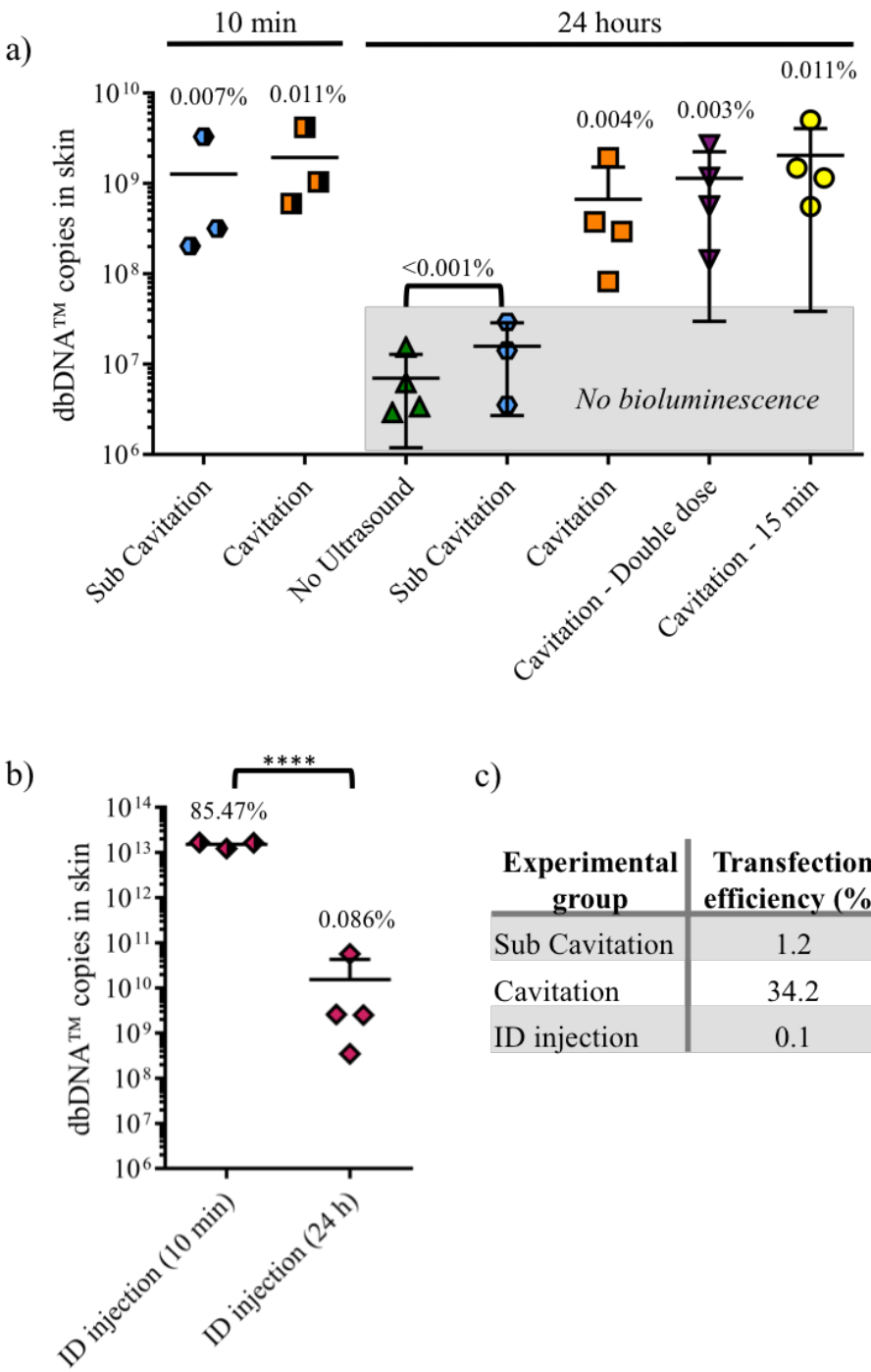

Experimental group	Transfection efficiency (%)
Sub Cavitation	1.2
Cavitation	34.2
ID injection	0.1

Figure 4.12: Presence of dbDNA™ construct in the skin 10 minutes and 24 hours post-treatment analysed by qPCR. a) Amount of dbDNA™ copies delivered into the skin 10 minutes after the 'Sub Cavitation' or 'Cavitation' treatment, and 24 hours post-treatment of all other experimental groups (exclusion of 'ID injection' group). The percentage values represent the mean proportion of the applied dose delivered into the skin after the specific treatment. The total applied dose for the 'No Ultrasound' and 'Cavitation – Double dose' groups was 100 µg dbDNA™ and the applied dose of the other groups was 50 µg dbDNA™. The grey box highlights the murine skin samples that had no detectable bioluminescence. b) dbDNA™ copies detected in the skin 10 minutes and 24 hours after injection. The horizontal bars represent the mean and the standard deviation of n=3 per group. The significant difference was determined by t-test. **** corresponds to $p<0.0001$. c) Table indicating the transfection efficiencies of the different treatment groups (calculated with formula 4.3, section 4.2.3).

In Figure 4.12(b) it can be observed that 10 minutes after injecting 50 µg dbDNA™ construct into the dermis, 85.47 ± 14.56% of the applied dose (or $1.52x10^{13} \pm 2.59x10^{12}$ dbDNA™ copies) was found in the rescued skin. 24 hours post-treatment, significantly ($p<0.0001$) and almost 1000-fold less dbDNA™ copies were detected in the skin ($1.56x10^{10} \pm 2.75x10^{10}$ dbDNA™ copies, 0.086% of the applied dose) of injected mice. This data shows that over 99.9% of the administrated dose was cleared from the inoculation site. This calculation also indicates that the levels of expression evident in the skin at 24 hours are produced from only 0.1% of the injected dose. Although more detailed characterisation of the degradation of the dbDNA™ and the half-life of the luciferase protein is needed before it can be stated that only 0.1% of the injected dose was able to successfully transfect the cells and produce the encoded protein (Figure 4.12(c)), with the other 99.9% being excluded from cells and cleared.

10 minutes after insonating the skin with 'Sub Cavitation' or 'Cavitation', substantially (~8,000-fold) lower delivery levels were detected in the skin (10 min, Figure 4.12(a)) in comparison to the 'ID injection' group (10 min, Figure 4.12(b)). After exposing the mice to 0.7 MPa, $1.27x10^{9} \pm 1.25x10^{9}$ dbDNA™ copies (or 0.007% of the applied dose) were found in the resected skin 10 minutes post-treatment. Higher levels (1.5-fold) were found after exposing the mice to 1.6 MPa ($1.96x10^{9} \pm 1.94x10^{9}$ dbDNA™ copies, 0.011% of the applied dose) (10 min, Figure 4.12(a)).

24 hours after finishing the treatment, negligible amounts of dbDNA™ copies were found in the 'No Ultrasound' group ($6.98x10^{6} \pm 5.79x10^{6}$ dbDNA™ copies, 0.00002% of the 100 µg applied dose) and in the three samples from the 'Sub Cavitation' group that were insonated at 0.7 MPa ($1.58x10^{7} \pm 1.30x10^{7}$ dbDNA™ copies,

0.00009% of the 50 μg applied dose). These dbDNA™ levels were insufficient to produce luciferase-expressing cells (as seen in Figure 4.11 and indicated in Figure 4.12(a) by the grey bar). Notably, the 'Cavitation' groups had 40-fold higher levels of dbDNA™ copies ($6.71x10^8 \pm 8.50x10^8$ dbDNA™ copies, 0.004% of the 50 μg applied dose) compared to the three samples of the 'Sub Cavitation' insonating at 0.7 MPa.

Interestingly, both the 'ID injection' and 'Sub Cavitation' groups demonstrated 100-1000 fold reductions in the levels of dbDNA™ copies between 10 minutes and 24 hours post-treatment, whilst the 'Cavitation' group suffered a mere three-fold reduction during this time. This indicates that although inertial cavitation is only enabling a low percentage of the total dbDNA™ to access the skin, it is delivering the dbDNA™ construct to a compartment where it is protected from clearance/degradation.

The single mouse in the 'Sub Cavitation' group that was insonated at 1.0 MPa had comparable dbDNA™ levels in the skin ($6.37x10^8$ dbDNA™ copies, 0.0035% of the applied dose) as were found in the 'Cavitation' group. Although noting that this is an interesting result, this single mouse was an anomaly by not being exposed to sub cavitation activity (TASE value of 1.53 μJ, Figure 4.10(a)). Therefore, this mouse was excluded from the 'Sub Cavitation' group during this analysis.

In comparison to the 'Cavitation' group, doubling the dose in the formulation enhanced (1.7-fold) the dbDNA™ level present in the rescued skin ('Cavitation – Double dose', $1.14x10^9 \pm 1.11x10^9$ dbDNA™ copies, 0.003% of the 100 μg applied dose), and three-fold enhancement was observed after extending the treatment time to 15 minutes ('Cavitation – 15 min', $2.06x10^9 \pm 2.01x10^9$ dbDNA™ copies, 0.011% of the 50 μg

applied dose). However, there was no significant difference ($p>0.05$) between these three 'Cavitation' groups.

The table in Figure 4.12(c) shows a calculation of the 'transfection efficiency' (calculated with formula 4.3, section 4.2.3). It indicates that 34.2% of the delivered dbDNA™ copies measured 10 minutes after the 'Cavitation' treatment were still detectable 24 hours post-treatment, suggesting that they were successfully transfected into the cells, which is substantially more efficient than 0.1% transfection efficiency found in the 'ID injection' group (Figure 4.12(c)). Intriguingly, despite there being ~8,000-fold less dbDNA™ present at 10 minutes in the 'Cavitation' group compared to the 'ID injection' group and 23-fold less at 24 hours, the levels of expression achieved in these two groups was equivalent. Again indicating that inertial cavitation provides access to a compartment where the dbDNA™ is better protected and more actively transcribed and translated.

4.3.2.4 Luciferase 2 - Discussion

The aim of both the luciferase studies was to demonstrate the feasibility of a dbDNA™ construct to transfect cells and to induce the production of the encoded luciferase protein by cavitation-enhanced delivery. Although both studies successful addressed this aim, the bioluminescence detected in 'Luciferase Study 2' was substantially stronger for both the 'Cavitation group' (4000-fold) and 'ID injection' group (100-fold) than the same groups in 'Luciferase Study 1'. Administrating a higher dose in the 'ID injection' group (50 μg versus 20 μg dbDNA™/Luc), imaging the mice 24 hours instead of 18 hours post-treatment, and using eight-weeks-old BALB/c mice (instead of six months CD1 mice) could all have positively influenced the strength of the detected bioluminescent signal.

In both luciferase studies it was found that in the absence of ultrasound, no emitted photons were detected corresponding to a failure in cell transfection. Furthermore, by increasing the acoustic pressure to 0.7 MPa (TASE < 0.33 μJ), no gene expression was detected in 'Luciferase Study 2' (★, Figure 4.13). Interestingly, increasing the acoustic pressure to 1.0 MPa (TASE value of 1.53 μJ, blue diamante in Figure 4.13) showed successful gene expression and the bioluminescent signal was in the same order as for the experimental groups insonated at 1.6 MPa (Figure 4.13).

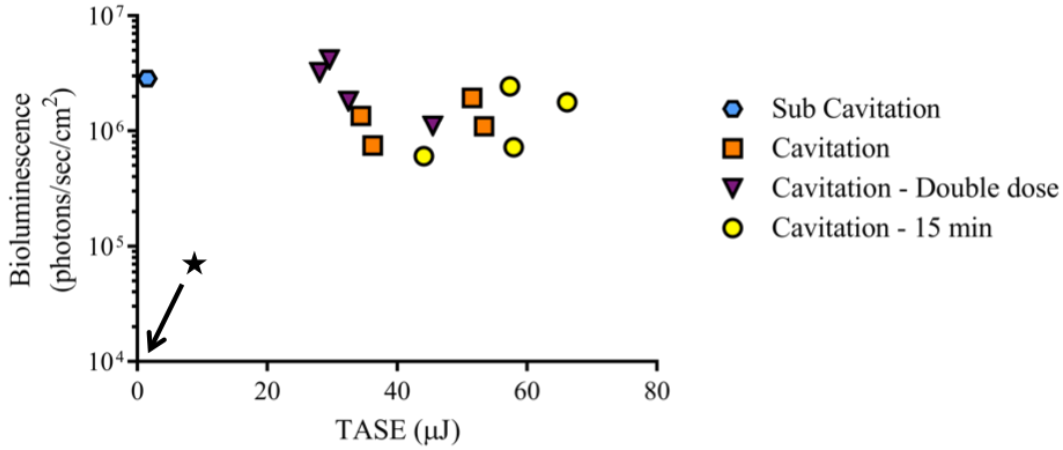

Figure 4.13: Plot between recorded TASE value per sample monitored by passive cavitation detection and the bioluminescent signal detected of the luciferase-expressing cells 24 hours post-treatment. The ★ indicates the three samples from the 'Sub Cavitation' and the four samples from the 'No Ultrasound' group that had no detectable bioluminescent signal.

As defined in Figure 3.7, 0.7 MPa acoustic pressure is in the 'Sub Cavitation' regime of the NCs. Below the cavitation threshold of 1.0 MPa, the NCs generate sporadic activity in the formulation. However, increasing the acoustic pressure to ≥1.0 MPa induced inertial cavitation that was found to be essential in the cell transfection and the production of luciferase. This data may indicate that reducing the acoustic pressure to 1.0 MPa could still be as effective as insonating at higher acoustic pressures and that there may be a delivery threshold related to the insonated pressures which lies somewhere between 0.7 and 1.0 MPa.

Furthermore, it has to be taken into account that the IVIS images only showed bioluminescence in two dimensions with no depth resolution. When transfecting only the cells in the epidermis, the expression of the encoded-gene will not last as long as transfecting the cells deeper into the dermis due to the renewal of the epidermis [21]. Furthermore, it is important to note that the cutaneous delivery of the dbDNA™ construct at 10 minutes and 24 hours post-treatment were determined by sacrificing two different groups of mice at the two different time points. Therefore, the amount of dbDNA™ construct delivered in the skin cannot be followed per mouse over time to better correlate between delivered dose and gene-expression. However, for further research, it would be interesting to evaluate if there is a delivery threshold related to acoustic pressures and for how long the transgene expression lasts.

In 'Luciferase Study 2', two additional experimental groups were included to evaluate the effect of doubling the dbDNA™ dosage or extending the 'Cavitation' treatment time on gene expression. As can be seen in Figure 4.13, doubling the application dose (100 µg) of the dbDNA™ construct (i.e. 'Cavitation – Double dose' group) also doubled the detected bioluminescence over a single dose (50 µg). However, no significance enhancement ($p>0.05$) was found. In addition, it was shown that extending the treatment time to 15 minutes had no significantly enhanced effect on the gene delivery in comparison to 10 minutes 'Cavitation' treatment.

The second aim to determine the transfection and delivery efficiency of the dbDNA™/Luc vector by cavitation-enhanced transport was also addressed in 'Luciferase Study 2'. It was observed that after injecting 50 µg dbDNA™ construct into the skin, 85.47 ± 14.56% of the administrated dose was detected.

Although it was expected that recovery of the injected dose would be close to 100%, the skin contains endonuclease that can degrade about 99% of intradermally injected plasmid DNA within 90 minutes of injection [287].

The transfection efficiency for the 'ID injection group' was in the order of 0.1%, similar to the levels found in the literature [287, 288]. Interestingly, the delivery efficiency of transporting the dbDNA™ construct into the skin by cavitation-enhanced delivery is very low (<0.01%), but the transfection efficiency is as high as 34%. These results are an exciting demonstration that a dramatically lower number of dbDNA™ copies are required to reach the (epi)dermis by cavitation-enhanced transport than by direct injection in order to induce the same gene expression.

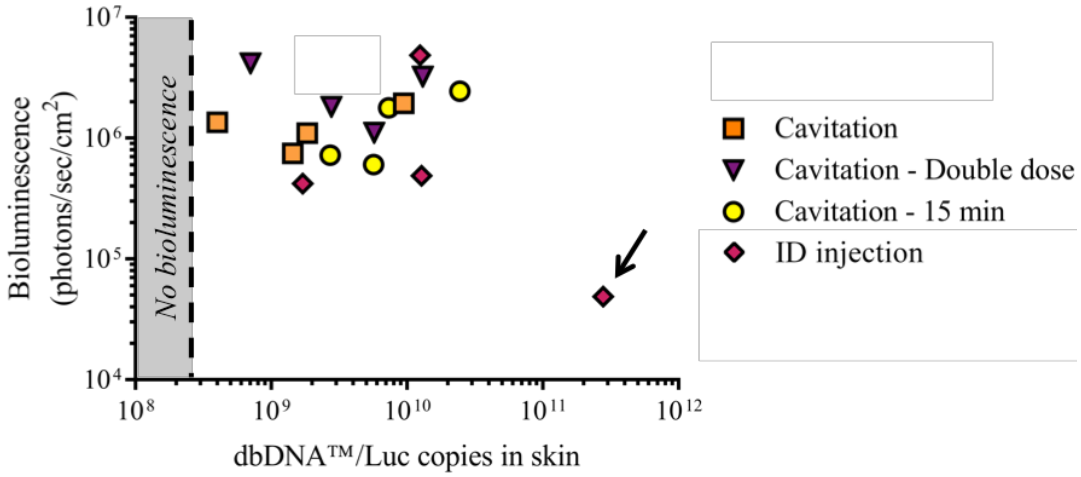

Figure 4.14: Plot of the detected DNA copies in the rescued skin versus the bioluminescent signal imaged 24 hours post-treatment. Delivering up to 1.45×10^8 dbDNA™/Luc copies into the skin did not induce a detectable bioluminescent signal (grey box).

It can be observed in Figure 4.14 that more dbDNA™/Luc copies in the skin do not directly correlate with higher bioluminescent signal. In particular, one mouse in the 'ID injection' group (highlighted by the arrow in Figure 4.14) contained 2.19×10^{11} dbDNA™ copies in the skin (or 0.134% of the applied dose) but emitted a weak

bioluminescent signal (i.e. $4.87x10^4$ photons/sec/cm^2). Assaying the expression of luciferase in cells *in vivo* is subject to confounding factors. For example, the luciferase-luciferin reaction required both the substrate and co-factors (i.e. ATP, oxygen, and magnesium) to measure the luciferase activity by the IVIS system. However, limited availability of any of these components may result in an underestimation of the luciferase activity [289], as may have occurred in this single mouse.

4.3.2.5 Luciferase Study 2 – Conclusion

Overall, these results demonstrated that successful transfection of the reporter gene was induced after insonation at ≥ 1.0 MPa. No significant enhancement was detected by elongation the treatment time to 15 minutes or doubling the applied dosage to 100 µg dbDNA™. Interestingly, the cavitation-induced transfection showed similar expression of the reporter gene to the use of the conventional needle-and-syringe approach.

In addition, the highest dose delivery of dbDNA™ construct was found after ID injection (85.47%) but only with a transfection efficiency of 0.1%. On the other hand, ultrasound-mediated cavitation delivered up to 0.01% of the applied dose from which 34.2% was still present in the rescued skin 24 hours post-treatment. However, it is unknown if the induced transgene expression levels would be sufficient to stimulate the immune system against an immunogenic transgene. Therefore, the experiment was repeated with a therapeutic DNA vaccine as described in the next section.

4.3.3 Influenza Vaccination

In this section, a therapeutic dbDNA™ vaccine against influenza A (i.e. dbDNA™/Cal09) was used to investigate if cavitation-mediated delivery can induce sufficient expression of the viral protein to induce an immune response. Four experimental groups were investigated (n=5); 'Sub Cavitation', 'Cavitation', positive control group 'ID injection', and negative control group 'No Vaccine' (generation of sustained inertial cavitation at 1.6 MPa without the vaccine vector).

4.3.3.1 Influenza Vaccination – Cavitation Detection

For the experimental groups exposed to ultrasound, the acoustic emission spectrograms were characterised for the 'Prime' (day 0) and 'Boost' (day 20) treatments. One representative spectrogram of each group per treatment is presented in Figure 4.15(a-c). The calculated TASE value is presented in Figure 4.15(d) for the 'Prime' and 'Boost' treatment.

Figure 4.15(a) shows that exposing the formulation in the 'Prime' and 'Boost' treatment to 0.7 MPa caused sporadic broadband emissions (light blue band) with no significant difference ($p>0.05$) between the 'Prime' and 'Boost' treatment. Insonating the 'No Vaccine' group at 1.6 MPa showed strong, sustained, and reproducible broadband acoustic emissions (red bands) over the total exposure time during both 'Prime' (39.36 ± 8.12 μJ) and 'Boost' (33.15 ± 9.00 μJ) treatments. Also, similar TASE values were found for the 'Cavitation' group (37.33 ± 7.13 μJ) during the 'Prime' treatment. This indicates that the dbDNA™ vaccine present in the formulation had no effect on the NC activity.

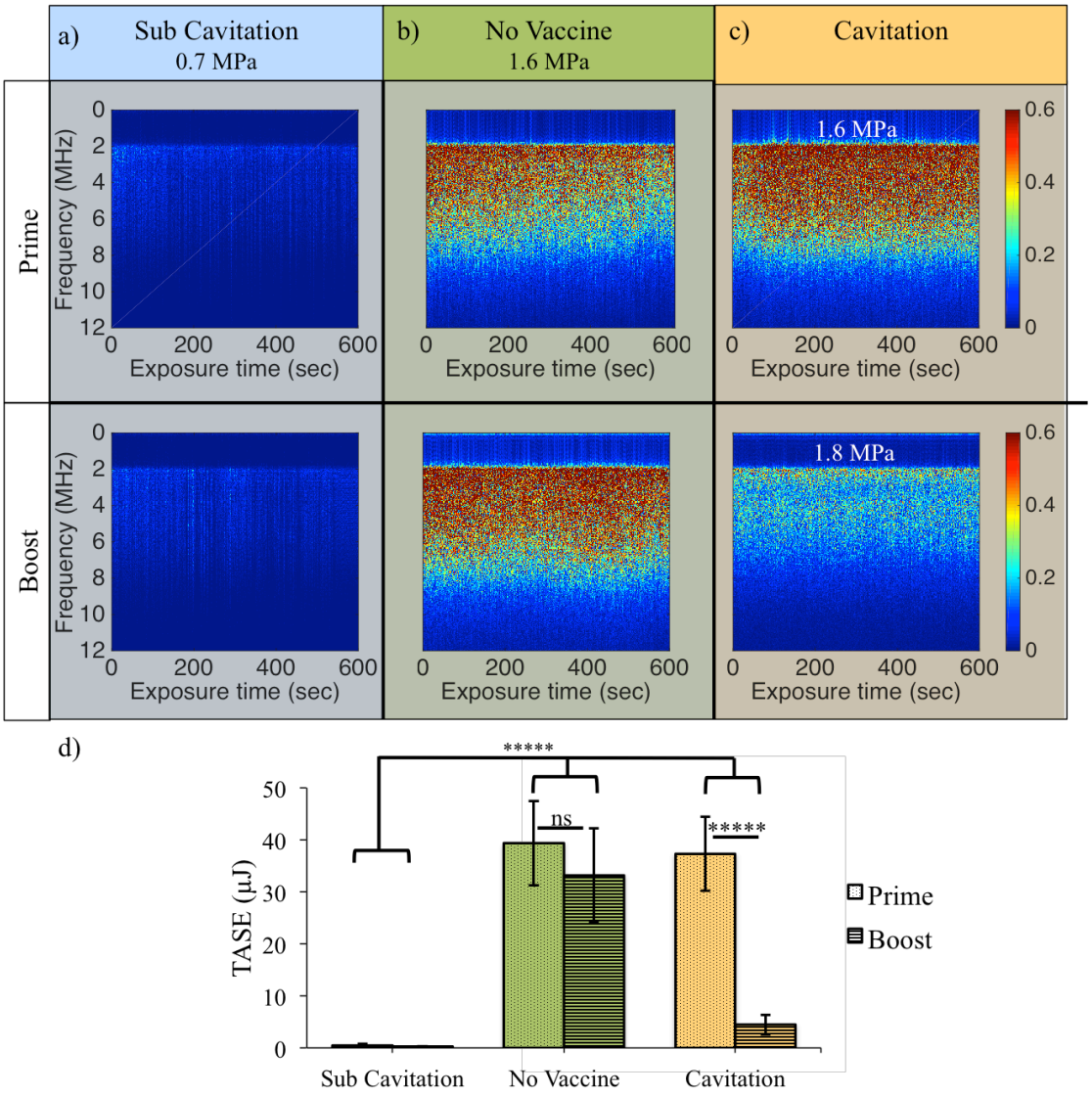

Figure 4.15: Acoustic emission spectrogram from NCs exposed to 0.7 MPa (a) 'Sub Cavitation', 1.6 MPa (b) 'No Vaccine', or (c) 'Cavitation' on day 0 ('Prime') and day 20 ('Boost') – Influenza Vaccination. The colour bar on the right axes represents the power spectral density (mV^2/Hz). d) The bar chart showing the mean TASE value detected per experimental group for both the 'Prime' and 'Boost' treatment. The error bars represent the standard deviation for n=5 mice. The significant difference was determined by one-way ANOVA Bonferroni multiple comparison tests with $p<0.00001$ (*****) and not significant (ns).

During the 'Boost' treatment of the 'Cavitation' group, it was noticed that the amplitude of the recorded PCD trace was lower than observed in the 'Prime' treatment (data not shown). Therefore, the acoustic pressure was immediately increased to 1.8 MPa, but not beyond the value known to potentially cause skin damage. Despite this increase in the acoustic pressure, the acoustic emission spectrograms from the 'Boost' treatment contained less red pixels than the acoustic emission spectrogram determined from the

'Prime' treatment (as can be seen in 'Boost', Figure 4.15(c)). Substantially (eight-fold) and significantly ($p<0.00001$) lower TASE values were recorded in the 'Boost' treatment (4.48 ± 1.91 μJ) in comparison to the 'Prime' treatment (Figure 4.15(d)).

This difference could be explained by the preparation of the formulation. In the 'Prime' treatment, one large NC batch was used from which the three formulations ('No Vaccine', 'Sub Cavitation', and 'Cavitation' groups) were prepared. Due to availability, in the 'Boost' treatment different NC batches were used to prepare the 'No Vaccine' formulation, and the 'Sub Cavitation' and 'Cavitation' formulations. By preparing this last formulation, the highly concentrated dbDNA™/Cal09 construct (1.048 mg/mL) was directly added to the NCs before adding the required volume of DI water. Afterwards, it was visually observed that the formulation contained white clusters of NCs. This could have negatively influenced the activity of the NCs in the formulation.

4.3.3.2 Influenza Vaccination – Antibody levels in the blood

Successful induction of an immune response against the HA1 protein encoded by the therapeutic dbDNA™/Cal09 vaccine was assayed by measuring anti-HA1 antibodies in the blood serum of treated mice (as described in section 4.2.4.2). Such an analysis was performed on blood samples taken at 16, 33, 41 and 50 days after the 'Prime' treatment. The titre levels are presented in Figure 4.16.

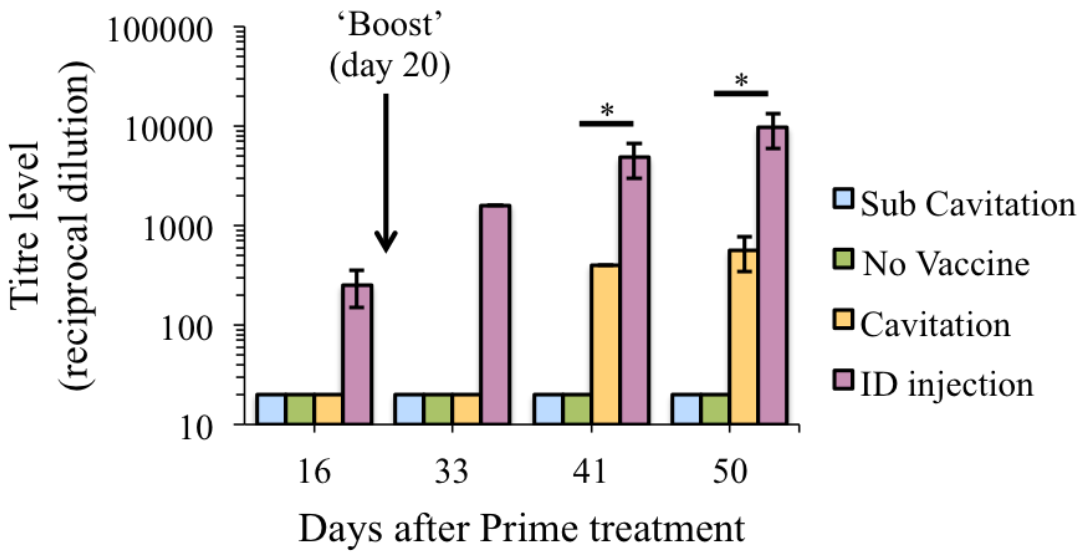

Figure 4.16: The titre levels of antibodies against the encoded dbDNA™/Cal09 – Influenza Vaccination. The titre levels were determined from the blood plasma of the mice that received the gold standard 'ID injection', or 'Cavitation'. On day 0 the mice received their first ('Prime') treatment and on day 20 their 'Boost' treatment (indicated by the arrow). The titre level corresponds to the maximum dilution of the blood that still provided a detectable signal in the ELISA. The bar chart is showing the average titre level determined at the four-time points with the error bar representing the standard deviation for n=5. The significant difference was determined by t-test with * corresponding to $p<0.05$.

The positive control group ('ID injection') showed high anti-HA1 levels in blood just 16 days after the 'Prime' treatment (Figure 4.16). After receiving their second ID injection on day 20, the anti-HA titre levels increased up to 9600 ± 3695 titre level dilution on day 50.

Notably, treating the mice with sustained inertial cavitation during the 'Prime' and 'Boost' treatment has led to the production of specific antibodies against the HA1 after the 'Boost' treatment on day 41. The titre levels increased to 260 ± 219 titre level dilution on day 50 but were substantially (almost 37-fold) and significantly ($p<0.05$) lower than after ID injection. No antibody levels above 1:20 serum dilutions were detected in any of the blood samples from the 'Sub Cavitation' or 'No Vaccine' groups.

Furthermore, it is clear that in this experiment the cavitation-enhanced delivery approach was substantially less efficient at generating antibody responses than the conventional needle-and-syringe approach. Based on the results shown in the research paper by Kendirgi et al. [228], the detected titre levels at day 50 are not sufficient to provide protection against an influenza challenge.

4.3.3.3 Influenza Vaccination - Discussion

In the development of vaccines or novel delivery technologies, it is important to validate if the induced immunization correlates to sufficient protection. In the literature, different antibody and/or cell-mediated immune response assays are performed to characterise the induced immune reaction. However, there are three commonly used serological assays for detecting influenza-specific antibodies in the blood serum; single radial haemolysis (SHR), haemagglutination inhibition (HAI) and microneutralization (MN), of which SRH and HA are the most commonly used [290].

The HAI assay uses the tendency of the HA protein of the influenza virus to bind to red blood cells and causing them to agglutinate [291]. In the presence of specific antibodies, the antigenic sites on the HA protein sites become blocked and therefore unable to bind to red blood cells. The HAI titre is the reciprocal of the highest serum dilution that completely inhibits haemagglutination. In addition, the SHR is based on the radial diffusion of the antibody in an agar gel that contains red blood cells and blood complement and the area of haemolysis are proportional to the antibody concentrations in the blood serum [292].

Different clinical studies have established that an HAI antibody titre of ≥ 40 [293, 294] and SHR tire ≥ 25 mm^2 [290] are associated with 50% or higher protection against

influenza. In future work, to compare the detected anti-HA1 antibodies found in this chapter to other immunisation studies, it is important to use other serological assays to validate the induced outcome.

Furthermore, in the vaccination study, two treatments were performed ('Prime' and 'Boost'). Due to the difference in recorded TASE values on the 'Prime' and the 'Boost' treatment (Figure 4.15), it is difficult to answer if both treatments delivered similar dbDNA™ copies into the skin and produced equal amounts of viral proteins to trigger the immune system. Further research has to be performed to investigate the dependence of TASE value to induced gene expression.

In a previous study by Bhatnagar, it was found that a model vaccine Ovalbumin (42.7 kDa) was delivered (0.04% of the applied dose) into murine skin after cavitation-enhanced transdermal delivery [16]. In this study, comparable delivery efficiencies were found after delivering 2.6 kDa dbDNA™ construct (0.01% of the applied dose). Most interesting, despite all the improvements made in this thesis, the delivery efficiency of a large therapeutic drug into the murine skin was not enhanced over the dermal deliveries found by Bhatnagar [16]. It may be possible that the ultrasound settings used in this thesis cannot enhance the delivery of a large therapeutic agent to be beyond 0.1% of the applied dose. However, the data presented here may indicate that the area and site of deposition is just as an important factor in the generation of transgene and ultimately an immune response as the amount of deposition.

4.4 Summary

The work in this chapter aimed to investigate the feasibility of cavitation-enhanced transport to overcome the three main hurdles in immunisation using a DNA vaccine, as presented in Figure 4.2.

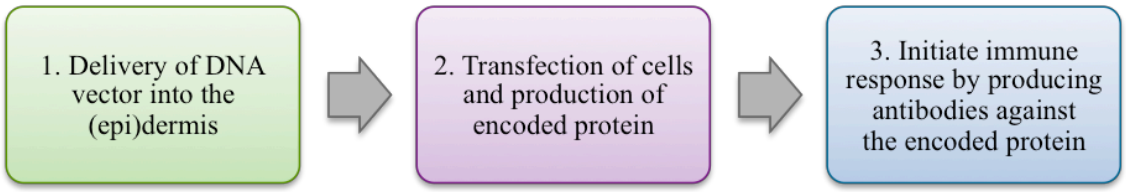

Figure 4.2: Schematic representation of the important steps in immunisation by DNA vaccine.

Since previous *ex vivo* (Chapter 2) and *in vivo* experiments (Chapter 3) have shown the potential of delivering therapeutic agents into the skin, the first hurdle was assumed to be addressable by the use of cavitation-enhanced transport.

The results from the luciferase studies demonstrated that inertial cavitation rather than passive diffusion alone was the key factor in achieving successful transfection of cells with the dbDNA™/Luc construct. The approach has led to a significant increase ($p<0.001$) in the level of expression of the encoded transgenic protein compared to passive diffusion control group ('No Ultrasound'). Notably, in 'Luciferase Study 1', the levels of transgene expression were 14-fold lower than those achieved by direct ID injection. In 'Luciferase Study 2', up to 4000-fold higher bioluminescence levels were detected, with no significant difference between cavitation-induced transfection and ID injection. In addition, no significant enhancement ($p>0.05$) was detected by elongation the cavitation treatment time to 15 minutes or doubling the applied dosage to 100 µg dbDNA™.

Furthermore, the highest dose delivery of the dbDNA™ construct was found after ID injection (85.47%) but only with a transfection efficiency of 0.1%. On the other hand, ultrasound-mediated cavitation delivered up to 0.01% of the applied dose from which 34.2% was still detectable 24 hours later.

During the 'Influenza Vaccination', the *in vivo* experiment was repeated with a therapeutic DNA vaccine (i.e. dbDNA™/Cal09) to investigate if inertial cavitation can achieve sufficient delivery to induce an immune response against the encoded viral protein. When treating the mice with sustained inertial cavitation during the 'Prime' and 'Boost' treatment, specific antibodies against the HA1 were first detected 41 days after the 'Prime' treatment. The titre levels increased to 260 ± 219 titre level dilution on day 50.

Overall, these results showed for the first time that cavitation-enhanced delivery can overcome the three hurdles in immunization by a DNA vaccine and successfully induced an *in vivo* immune response against a therapeutic DNA vaccine. However, the antibody levels achieved so far are unlikely to provide protection against an infectious challenge. Furthermore, although ultrasound-mediated cavitation was a mild procedure with negligible associated damage, it could not match the delivery efficiency and ultimately the antibody levels of the 'gold standard' (i.e. needle-and-syringe approach).

Chapter 5: Conclusions and Future Work

5.1 Research overview

As outlined in Chapter 1, the SC barrier limits the delivery of drugs into or through the skin. Multiple delivery methods have been explored to disrupt or perturb the SC layer, but most of them struggle to meet the challenge of achieving a sufficient dose delivery without causing excessive skin damage. Research into cavitation-enhanced drug delivery using ultrasound and a gel formulation seeded with cavitation nuclei to deliver drugs into the skin has shown early promise [172]. However, the technology is limited by the short lived nature of currently approved cavitation agents, and the lack of real-time monitoring when used across a broad range of therapeutic classes and environmental conditions, especially in situations where defining the dose delivered is important. Therefore, this thesis set out four research aims:

1) To demonstrate the feasibility and reproducibility of transdermal delivery of different therapeutic agents by cavitation-enhanced transport.
2) To establish the utility of *ex vivo* pig skin and *in vivo* mouse skin as model systems for testing transdermal delivery.
3) To investigate the potential to ascertain successful delivery of adequate dose of the therapeutic agent into the skin using passive monitoring of acoustic emissions.
4) To assess the potential of using cavitation-enhanced transport as a delivery system for nucleotide based vaccines in mouse models.

The first three research objectives were investigated in Chapter 2. However, this first required certain delivery conditions to be refined and optimised (such as replacement of Carbopol® with ready-to-use Anagel®, optimisation of NC concentration, and refining of the size of formulation holder) before performing *ex vivo* transdermal delivery experiments on porcine skin. These *ex vivo* studies focussed on the utility of porcine skin as a suitable skin model for testing cavitation-mediated transdermal transport of a large therapeutic agent. IgG was chosen as the 'model' drug to represent antibody-based therapeutics. In the four *ex vivo* experiments, it was found that the cutaneous delivered IgG were not consistent throughout the *ex vivo* experiments and showed regretfully different results with up to 46.1% of the applied dose found in one IgG Study, and no detectable IgG delivery in any skin sample in the final study.

The source of the high intra-replicate and inter-experiment variability in delivery and level of cavitation was believed to be dependent on three main factors. The first possibility was that it was a consequence of variability in the levels of cavitation achieved and originating from variation in the used NC batches that were fabricated in small-scale batches in the laboratory. The second source of variation was identified as being due to the inaccuracies during the ELISA measurement. Even though, improvements were made to the methodology to refine and validate the calibration curves, inaccuracies due to sample preparations were inevitable when using ELISA. The third and most compelling possible source of variation in the level of delivery between the studies was the porcine skin itself. The reasons for such variability in the studies presented here could reflect the differences in the age of the pig, the location of the harvested skin, the variation in skin thickness, and the amount of adipose tissue and hair follicles. Due to the abattoir origins of the skin these factors were hard to control.

In response to variability found in using porcine skin, further studies (Chapter 3 and 4) were performed in murine models. Hence, this switch in the skin model provided a better testing system that allowed the influence of blood perfusion to be accounted for and permitted bloodstream delivery to be assessed. This was especially important for the transdermal delivery study of Sumatriptan (Chapter 3), which is an intravenously active small molecule and an exemplar of a drug that is already transdermally delivered using an approved transdermal technology [177]. Sumatriptan also represented a good choice because a validated and standardised methodology (i.e. HPLC), with enhanced selective separation of the drug from other particles in the skin homogenate, was in place to provide a more reliable detection assay over ELISA. To address the other limitations in the system, large-scale NC batches were sourced from OxSonics Ltd (Oxford, United Kingdom) in order to achieve more consistent cavitation activity from the NCs.

In addition, studies were also performed to profile any detrimental impact of exposure to inertial cavitation on the skin. Initial safety and feasibility studies in mice showed that increasing acoustic pressures beyond 1.6 MPa induced redness and potential bruising on the skin without enhancing the delivery of Sumatriptan into the skin and blood. Since skin damage is not desirable in ultimate clinical application, 1.6 MPa was initially chosen to be the upper limit of ultrasound acoustic pressure. However, subsequent studies indicated that setting a threshold on the detected cavitation activity (i.e. TASE value) rather than on the applied acoustic pressure may be a more robust method of ensuring beneficial delivery without skin damage.

Indeed, refinements to the ultrasound setup and experimental procedures in further studies enabled optimisation of Sumatriptan transport in both hairless and hairy mice, using pressures above 1.6 MPa without causing skin damage. These protocol enhancements included more thorough washing of the skin post-exposure and longer degassing time of the coupling cone water to remove pre-focal cavitation activity. Enhanced washing substantially decreased the background delivery signal due to Sumatriptan left on the skin surface. Extended degassing served to emphasise the value of cavitation detection and ultimately enhanced the cavitation energy within the desired region. Furthermore, removal of pre-focal cavitation events appeared to reduce the occurrence of macroscopically obvious damage to the skin.

In accordance with previous work using the protein Ovalbumin [172], substantial (up to ~8% of the applied dose) and significant Sumatriptan delivery into the skin and bloodstream was achieved only when sustained inertial cavitation (> 15 μJ) from the NCs was evident over the total 10-minutes exposure. These data demonstrate the potential of using the TASE values from the passive monitoring system as a feedback system to identify the presence of inertial cavitation during treatment as well as the assurance of Sumatriptan delivery when detecting TASE values > 15 μJ. The detected blood concentration were 1000-fold higher than the therapeutic required dose in mice as established using recognised allometric calculations [198], and already detected within 20 minutes after the start of the treatment. This is substantially more efficient than other needle-free technologies [177]. A prime example being the clinically approved iontophoretic transdermal patch Zecuity® that uses a low electrical current to deliver up to 6.5 mg of Sumatriptan over four hours non-invasively through the skin into the bloodstream [192]. However, this technology does not include any delivery feedback

system, and due to serious site reaction the patch was withdrawn from the market in 2016 [192].

Enthusiasm over the promising results described in Chapter 3 is tempered by the limitations that remain, primarily issues of reproducibility, consistency of cavitation activity, and the dose wastage resulting from >99% of the drug remaining in the formulation holder after treatment. Such dose wastage indicates further optimisation of the formulation holder to concentrate the drug at the skin interface.

Hence, whilst achieving *in vivo* cutaneous delivery of a maximum of 0.83% of the applied dose for small molecules represented a promising finding, the cutaneous immunisation of a DNA vaccine offered an attractive further application of ultrasound-mediated cavitation. This is because for cutaneous immunisation the immunologically active cells found in the (epi)dermis need to be triggered by the presence of foreign material in the skin. Therefore, the required effective delivery dose and location may be more attainable as passage of large amounts of the dose all the way into the bloodstream may not be required.

To successfully induce immunisation by a DNA vector, there are three main steps. At first, the DNA has to be delivered into the (epi)dermis. Then, the DNA has to transfect the cells to induce the production of the viral protein. Finally, the amount of produced foreign proteins needs to be sufficient to initiate an immune response and trigger the production of antibodies against the viral protein [257].

To characterise DNA delivery, a luciferase encoding dbDNA™ vector was used to assess the level of delivery achieved and the impact of delivery on transgene expression. Two *in vivo* studies showed that cavitation could be used as a stimulus to achieve measurable gene expression of the dbDNA™/Luc construct. Whilst the first luciferase study showed that injecting the dbDNA™ construct was 14-fold more effective than insonating at 1.6 MPa, the second luciferase study found that similar expressions levels were detected using needle and syringe or 'Cavitation' treatment. This variation in data may relate to the differences in the strain and age of the mice.

Notably, the delivery levels 10 minutes post-treatment were in the order of 0.01% of the applied dose after insonating at 0.7 or 1.6 MPa with no correlation with the measured TASE values. However, 24 hours after detecting sustained inertial cavitation, 34.2% of the delivered copies were still detectable, suggesting perhaps that they were successfully transfected into the cells, which is substantially higher than the 0.1% of the delivered dose that was detected 24 hours after directly injecting the dbDNA™ vector.

Substantial luciferase expression was observed at TASE values > 1.53 μJ. Identification of this threshold and our ability to control and monitor acoustic emissions so that this level can be reliably achieved represents an important advance. However, due to the numerous biological variables that influence the gene expression and immunisation, as well as the different TASE values calculated in the 'Boost' and 'Prime' treatment, it was not possible to correlate the TASE value to a specific immune response.

The *in vivo* experiment was repeated with an influenza vaccine construct (dbDNA™/Cal09). When treating the mice with sustained inertial cavitation during the

'Prime' (at day 0) and 20 days later during the 'Boost' administration, specific antibodies against the HA1 were first detected 41 days after the 'Prime' treatment. The titre levels increased to 260 ± 219 titre level dilution on day 50. These results showed for the first time that cavitation-enhanced delivery could overcome the three hurdles in immunisation by a DNA vaccine and induce measurable immune responses against a therapeutic DNA vaccine. Unfortunately, these titre levels are not predicted to be sufficient to protect the immunised mice against a lethal challenge of influenza A/Cal09 [228]. Furthermore, cavitation-enhanced epidermal vaccination was almost 37-fold less efficient in inducing antibody levels as the gold standard of direct injection. Therefore, these results show that ultrasound-mediated cavitation cannot currently induce cavitation-induced immunisation in mice.

The research in this doctoral thesis has been the first to demonstrate:

- The general utility of therapeutic ultrasound (265 kHz) in combination with sustained inertial cavitation produced by NCs as a physical enhancer to transdermally deliver low-molecular-weight drugs (413 kDa) and macromolecules (150 kDa).
- The delivery of 1000-fold higher Sumatriptan blood concentrations than the therapeutically required concentration in murine blood detected 20 minutes after exposure to 10 minutes sustained inertial cavitation.
- The detection of high levels of luciferase expression solely in the treatment area after cavitation-enhanced transfection of a dbDNA™ construct.
- The induction of an antibody response against a dbDNA™ construct encoding a therapeutic DNA flu vaccine.

5.2 Research limitations and future directions

Table 5.1 provides an overview of the experimental outcomes produced over the course of this thesis, during which different variables were identified and optimised to enhance the reproducibility of cavitation-enhanced transdermal delivery. Despite these efforts, this table evidences that the experiments performed resulted in highly variable delivery performance for each and every therapeutic class. To address other factors limiting the reproducibility of this research, different possible sources of variability are addressed in the next section and a number of suggestions are given for potential future work on transdermal drug delivery by ultrasound-mediated cavitation.

5.2.1 Research skills

The most fundamental compelling source of variability in the research outcomes has been found to be highly dependent on the research skills from the researcher. As an engineer, it has been proved again that good time management, discipline, determination, persistence, accuracy, and a high level of precision are crucial to lay a solid fundament to perform reliable research. Since many parameters are influencing cavitation-enhanced delivery, this is essential to reduce the additions of extra variables by human error. Without this fundament or condition, it is impossible to validate the performed research.

In addition, dedication and patience were undoubtedly important to keep a critical eye towards the research outcomes and to not jump to conclusions. These conditions are not only specific to this research, but are also essential for research in general (it is a *condition sine qua non*).

Table 5.1: Overview of drug delivery results found in this thesis.

Drug	Skin Model	Formulation	Pressure (MPa)	TASE (µJ)	Therapeutic outcome	Dose delivery efficiency (%)
IgG 150 kDA 900 µg total dose	*Ex vivo* porcine skin	Water	1.0	Not available	186.2 ± 171.9 µg	20.7
				11.58 ± 4.3	63.04 ± 62.90 µg	7.0
				31.20 ± 10.09	2.84 ± 2.17 µg	0.31
				37.68 ± 4.32	-	-
		Anagel®	1.0	Not available	414.9 ± 161.1 µg	46.1
				1.66 ± 1.21	139.65 ± 95.67 µg	15.5
				1.35 ± 0.96	4.82 µg	0.53
				1.59 ± 0.56	-	-
Sumatriptan 413 kDA 10.4 mg total dose	*In vivo* mouse model	Water	0	-	10.46 ± 6.28 µg	0.10
				-	0.50 ± 0.28 µg	0.005
				-	-	-
			≤0.7	0.11 ± 0.07	1.62 ± 0.85 µg	0.02
			1.0	0.62 ± 0.61	0.44 ± 0.31 µg	0.004
			1.6	4.64	0.9 µg	0.01
				24.19 ± 8.73	807.87±140.67 µg	7.77
			≥ 1.6	49.41 ± 14.24	376.48 ± 238.35 µg	3.62
			1.8	9.9	9.67 µg	0.09
			2.1	9.48 ± 4.48	7.80 ± 1.03 µg	0.02
DNA vaccine 2.6 kDA 50 µg total dose	*In vivo* mouse model	Water	0.7	0.28 ± 0.04	-	-
				0.35 ± 0.17	$1.27x10^9$ ± $1.75x10^9$ copies	0.007 (10 min)
			1.0	1.53 (n=1)	2.86 x 10^6 photons/sec/cm^2	0.003 (24 h)
			1.6	35.14 ± 11.36	$4.79x10^2$ ± $3.59x10^2$ photons/sec/cm^2	
				43.89 ±9.95	$1.28x10^6$ ± $5.02x10^5$ photons/sec/cm^2	0.004 (24 h)
				41.79 ± 10.77	$1.96x10^9$ ± $1.94x10^9$ copies	0.011 (10 min)
		ID injection		-	$6.69x10^3$ ± $2.98x10^3$ photons/sec/cm^2	
				-	$1.45x10^6$ ± $2.28x10^6$ photons/sec/cm^2	0.086 (24 h)
				-	$1.52x10^{13}$ ± $2.59x10^{12}$ copies	86.47 (10 min)

5.2.2 Skin model

The second possible source of variability was found to be the skin itself. In Chapter 2, e*x vivo* pig skin from the abdomen was found as one of the most compelling possible sources of variation in the level of delivery. More consistent delivery results were found in a vascularised skin model like that of mice. This gave the opportunity to perform experiments on reproducible skin thicknesses and to measure the delivery in Chapter 3 of Sumatriptan in the skin and bloodstream up to 10 minutes after treatment. In Chapter 4, the gene expression and antibody response to a therapeutic DNA vaccine could be studied over a total of 50 days by using an *in vivo* skin model.

Although the skin thickness of mice is much thinner than humans (Table 2.1), it is essential to choose the best skin model to test the experimental objectives, in which accessibility, ease of handling, costs, and available facilities play a key role.

In Chapter 3, the Sumatriptan delivery was measured 20 minutes after the start of the treatment. To study the pharmacokinetics of Sumatriptan over time, regular blood sampling is required. Since mice have a low amount of blood volume (~1.5 mL), *in vivo* studies on for example pigs could be a possible next step since porcine was found to be the most relevant animal model for human skin due its similarities in histology, cellular composition, thickness and speed of sound (1720 m/s) to human skin [158]. Furthermore, due to optimised therapeutic setup (obtained in Chapter 3) and the reliable detection and quantification of Sumatriptan in biological tissue using HPLC, the initial *ex vivo* porcine skin model from Chapter 2 can also be used in further studies as an experimental model to better understand the fundamental principles behind the transdermal delivery of Sumatriptan by cavitation-enhanced transport.

In addition, in collaboration with the John Radcliffe Hospital, Oxford, *ex vivo* human skin was available for transdermal delivery experiments. However, due to the irregularity in size and availability, transplanting human skin on mice could be a suitable combination of using a vascularised system with human properties.

Another important factor that can explain the inter-variability in all the studies is that no two experiments were performed in exactly the same way. With every individual experiment, different dependable parameters were observed and learned from when performing the next study (i.e. cybernetic method). For further research, cybernetic knowing means that the negative outcomes will be equally (or even more) important as the positive outcomes.

Furthermore, the size of the experimental groups in this thesis were three samples for the *ex vivo* studies and three to six mice in the *in vivo* studies. In order to reduce the intra-replicate and inter-experiment variability, it is recommended to enlarge the experimental groups. However, the number of mice is restricted due to the animal license, the size of the animal facilities, time, costs, and ethical considerations.

Finally, in Chapter 3 it was found that no delivery studies have been published about Sumatriptan in a murine model. Therefore, it is difficult to compare the published data with the results found in Chapter 3. In addition, the Sumatriptan studies performed here did not include a positive control group or reference group that contained the most commonly used administration method of Sumatriptan delivery (i.e. s.c. injection). With the inclusion of a positive control group, it gives the possibility to relate the

experimental data to a reference point. This will also help to investigate other unknown intra- and inter-experimental variables that may affect its reproducibility.

5.2.3 Ultrasound parameters

The therapeutic setup used in this thesis fills up half a desk space and requires a large car boot to transport it between laboratories. For clinical applications, downsizing the setup is therefore essential. Depending on the application of this technology, a portable and battery-driven device could be a solution when requiring on-demand delivery (i.e. in case of migraine attack).

To increase the cavitation activity, or to reduce the variability in cavitation activity, dual- or multiple-frequency sonication could be of interest. Dual- or multiple-frequency sonication contains a set of frequencies with a range wider than the sum of the spectra of the individual fields. This can lead to an increase in the size range of the cavitation bubbles and consequently increase their total number. Bubbles creased at higher frequencies can act as cavitation nuclei for lower frequency cavitation and consequently increase the permeability of the skin by sonophoresis.

It is highly likely that an optimal compromise exists between the violence and density of cavitation activity and cavitation-enhanced transport. Too many cavitation bubbles can shield the insonating field from reaching deeper into the tissue, possibly reducing the impact of the sonophoresis on the skin surface. Currently, the therapeutic ultrasound setup used in this thesis contains a single PCD transducer that records the cavitation activity only in one dimension. In order to better understand and control the cavitation activity during transdermal delivery, better spatial resolution of the cavitation events is

required. This could be made possible by detecting the cavitation activity in the focal zone by multiple PCD transducers.

5.2.4 Formulation

The fourth possible source of variation between the experiments is the preparation and the composition of the applied formulation. To enhance the clinical application of the transdermal delivery system, it is important to reconsider the composition of the drug formulation that is applied on the skin. In ultrasonic imaging, clinically-approved ultrasound gel is used to enable good acoustic coupling between the skin and the transducer. Furthermore, a semisolid formulation has the clinical advantages of being easy to apply onto the skin and to prevent drug leakage away from the treatment area.

In Chapter 2, the therapeutic application mixture was composed for 50 wt.% of ready-to-use Anagel®, 25 wt.% NCs (final 5 mg/mL) and 25 wt.% therapeutic agent in solution. However, the Anagel® was removed from the formulation in Chapter 3 due to visual precipitation when mixing high concentrations of Sumatriptan with the Anagel® and NCs, making it a liquid suspension. Unfortunately, occasionally the formulation leaked out of the formulation holder upon coupling with the ultrasound setup. Also, after the ultrasound exposure, the remaining formulation in the holder had to be disposed of manually as careful as possible to prevent contamination to other parts of the mouse. In clinical settings, packaging the formulation into a patch can increase the ease of (self) administrating, which would make it possible to use this technology outside the laboratory.

When increasing the viscosity of the formulation to enhance the ease of topical application, it is essential to find a viscosity enhancement product (preferably aqueous

medium to allow good acoustic coupling) that does not contain surfactants (preventing deactivation of the NCs by dissolution of the gas pocket in the crevice), nor deactivates the therapeutic agents when mixed or stored over time.

Currently, the therapeutic agent is homogeneously mixed through the formulation. By using a patch design, high concentrations of therapeutic agent could be placed at the patch-skin interface. As a result, the concentration gradient between the formulation and the skin would be increased, potentially leading to higher delivered dosage by cavitation-enhanced transport. In addition, pre-fabricating the formulation in a package or patch form can reduce the batch-to-batch variation between experiments, and furthermore can enhance the storage, shelf-life, transport and stability of the drug in the formulation.

5.2.5 Cavitation optimisation

The fifth source of variability in the research has been the variable levels of cavitation activity detected using the same exposure pressures. A simple solution to this issue could be to set the exposure on the level of cavitation detected rather than the pressure applied. However, more work is needed to identify exactly what level of cavitation is required and how this changes with the therapeutic agent applied and the source of the skin being treated.

5.2.6 Therapeutic agent

The sixth and probably the most influenceable parameter is the type of therapeutic agent used for transdermal delivery. Without any intervention, molecules larger than 500 Da or strongly hydrophilic cannot cross the SC. Even though low- and high-molecular-weight molecules have shown to be successfully delivered into the skin by ultrasound-mediated delivery, sonophoresis seems to work better for hydrophilic drugs. Morimoto et al. have shown that the transdermal transport of hydrophilic molecules (up to 40 kDa) was enhanced *in vitro* in hairless rats after insonation to 41 kHz (120 mW/cm^2 for 5 min). In contrast, lipophilic rhodamine B dye (443 Da) was not able to transport into the skin. In another study by Ueda et al., nine drug molecules with different octanol/water partition coefficients showed that the flux of hydrophilic drugs across harvested hairless rat skin was enhanced by about sevenfold after insonation at 150 kHz and 2.0 W/cm^2 [295]. In great contrast, no enhanced effect was observed in the flux of lipophilic molecules. However, there is still a lack of understanding of the different delivery profiles between hydrophilic and lipophilic molecules, and what the correlation is between the type of therapeutic agent and the insonation parameters used (frequency, cavitation activity, duration, etc.).

In addition, the stability of the therapeutic agent in the formulation, upon insonation, and in the tissue strongly determines the efficiency of the therapy. This is of particular importance when using naked nucleic acid molecules as therapeutic agents. DNA loss is a fundamental problem for any gene therapy or genic immunization studies, since the loss of naked DNA plasmid by translates into the loss of transfection and finally therapeutic outcome.

To enhance the stability of the dbDNA™ construct, entrapment of the DNA into nano-carriers are currently widely investigated. Different potential nanomaterial and shapes are intensively studied for gene delivery that can protect the DNA as well as enhance the transfection efficiency into the targeted cells. A detailed overview of promising nano-carriers is described by Riley et al. [296].

Furthermore, it was found in Chapter 4 that the highest dose delivery of dbDNA™ construct was found after ID injection, but only a transfection efficiency of 0.1%. On the other hand, inertial cavitation delivered up to 0.01% of the applied dose from which 34.2% of the delivered dose was still detected 24 hours post-treatment and potentially successfully transfected into the cells. By combining both technologies it would be possible to use the high dose delivery efficiency of ID injection together with the high transfection efficiency of ultrasound-mediated cavitation. To prevent the technology from becoming too invasive, microneedles can also be used to deposit localised genetic material into the skin in combination with ultrasound to enhance the transfection efficiency.

5.2.7 Clinical relevance and development

Ultrasound for enhancing drug delivery transdermally is growing in clinical interest. The potential of using NCs that can induce sustained inertial cavitation over a prolonged period of time, generated a novel research field to enhance transdermal drug delivery with a needle-free device. Cavitation-enhanced delivery has shown to be of high clinical relevance in regard to the delivery of a small therapeutic agent. Further work is required to determine the pharmacokinetics of this technology, and downsizing the therapeutic setup will enhance the potential to use this technology at home or in the clinic. A cost-effective device could be feasible for patients needing regular repeating dosing.

However, since minor skin bruising was observed in the hypodermis after 10-minutes cavitation treatment, regular use may need particular protocols.

In the field of gene therapy, cavitation-enhanced transfection has shown for the first time to induce an immune response with a dbDNA™ construct. Although the achieved induced antibody response was not sufficient to protect the mice against a potentially lethal flu, for further clinical application of cavitation-enhanced vaccination it is essential to enhance the dose delivery by using a synergistic gene delivery system, and to protect the dbDNA™ from fast clearance/degradation from the inoculation site.

Last, but not least, this thesis also identified several parameters that may hinder transdermal delivery, which can underpin future investigations to further evaluate the potential of this technology.

References

1. Choices, N., *Vaccination schedule-Vaccinations-NHS Choices.* 2014.
2. Prausnitz, M.R., S. Mitragotri, and R. Langer, *Current status and future potential of transdermal drug delivery.* Nat Rev Drug Discov, 2004. **3**(2): p. 115-24.
3. Singh, R., S. Singh, and J.W. Lillard, Jr., *Past, present, and future technologies for oral delivery of therapeutic proteins.* J Pharm Sci, 2008. **97**(7): p. 2497-523.
4. Olsson, B., et al., *Pulmonary Drug Metabolism, Clearance, and Absorption.* Controlled Pulmonary Drug Delivery, 2011: p. 21-50.
5. Morales, J.O., et al., *Challenges and Future Prospects for the Delivery of Biologics: Oral Mucosal, Pulmonary, and Transdermal Routes.* AAPS J, 2017. **19**(3): p. 652-668.
6. Park, D., et al., *Sonophoresis in transdermal drug deliverys.* Ultrasonics, 2014. **54**(1): p. 56-65.
7. Bragulla, H.H. and D.G. Homberger, *Structure and functions of keratin proteins in simple, stratified, keratinized and cornified epithelia.* J Anat, 2009. **214**(4): p. 516-59.
8. Elias, P.M., *Epidermal Barrier Function - Intercellular Lamellar Lipid Structures, Origin, Composition and Metabolism.* Journal of Controlled Release, 1991. **15**(3): p. 199-208.
9. Bos, J.D. and M.M. Meinardi, *The 500 Dalton rule for the skin penetration of chemical compounds and drugs.* Exp Dermatol, 2000. **9**(3): p. 165-9.
10. Marieb, E.N., *Essentials of human anatomy & physiology*. 9th ed. 2009, San Francisco, CA: Pearson/Benjamin Cummings. xxiv, 632 p.
11. Williams, S., *Advanced Glycation End Products (AGEs)—It's aging you quicker!*, in *Metrin Skincare*. 2016, Metrin Skincare.
12. Sandby-Moller, J., T. Poulsen, and H.C. Wulf, *Epidermal thickness at different body sites: Relationship to age, gender, pigmentation, blood content, skin type and smoking habits.* Acta Dermato-Venereologica, 2003. **83**(6): p. 410-413.
13. Laurent, A., et al., *Echographic measurement of skin thickness in adults by high frequency ultrasound to assess the appropriate microneedle length for intradermal delivery of vaccines.* Vaccine, 2007. **25**(34): p. 6423-6430.
14. Albanna, M.Z. and J.H. Holmes, *Skin tissue engineering and regenerative medicine*. 2016, London, UK ; San Diego, CA, USA: Elsevier/AP, Academic Press is an imprint of Elsevier. xxii, 443 pages.
15. Chen, Z., et al., *Overcoming or circumventing the stratum corneum barrier for efficient transcutaneous immunization.* Drug Discov Today, 2018. **23**(1): p. 181-186.
16. Menon, G.K., *New insights into skin structure: scratching the surface.* Advanced Drug Delivery Reviews, 2002. **54**: p. S3-S17.
17. Lorand, L. and R.M. Graham, *Transglutaminases: crosslinking enzymes with pleiotropic functions.* Nat Rev Mol Cell Biol, 2003. **4**(2): p. 140-56.
18. Candi, E., R. Schmidt, and G. Melino, *The cornified envelope: A model of cell death in the skin.* Nature Reviews Molecular Cell Biology, 2005. **6**(4): p. 328-340.
19. Nemes, Z. and P.M. Steinert, *Bricks and mortar of the epidermal barrier.* Exp Mol Med, 1999. **31**(1): p. 5-19.
20. Wertz, P.W., et al., *Composition and morphology of epidermal cyst lipids.* Journal of investigative dermatology, 1987. **89**(4): p. 419-425.
21. Benson, H.A.E. and A.C. Watkinson, *Transdermal and topical drug delivery : principles and practice*. 2012, Hoboken, N.J.: Wiley. xv, 446 p.
22. Larouche, D., et al., *[Regenerative medicine: stem cells, cellular and matricial interactions in the reconstruction of skin and cornea by tissue engineering]*. Pathol Biol (Paris), 2009. **57**(4): p. 299-308.
23. Bal, S.M., et al., *Advances in transcutaneous vaccine delivery: Do all ways lead to Rome?* Journal of Controlled Release, 2010. **148**(3): p. 266-282.
24. Combadiere, B. and C. Liard, *Transcutaneous and intradermal vaccination.* Hum Vaccin, 2011. **7**(8): p. 811-27.
25. Banchereau, J. and R.M. Steinman, *Dendritic cells and the control of immunity.* Nature, 1998. **392**(6673): p. 245-52.
26. Heath, W.R. and F.R. Carbone, *The skin-resident and migratory immune system in steady state and memory: innate lymphocytes, dendritic cells and T cells.* Nat Immunol, 2013. **14**(10): p. 978-85.
27. Kelsoe, G., *Studies of the humoral immune response.* Immunol Res, 2000. **22**(2-3): p. 199-210.

28. Scheuplein, R.J. and I.H. Blank, *Permeability of the skin.* Physiol Rev, 1971. **51**(4): p. 702-47.
29. Scheuplein, R.J., *Mechanism of percutaneous absorption. II. Transient diffusion and the relative importance of various routes of skin penetration.* J Invest Dermatol, 1967. **48**(1): p. 79-88.
30. Scheuplein, R.J., *Analysis of permeability data for the case of parallel diffusion pathways.* Biophys J, 1966. **6**(1): p. 1-17.
31. Scheuplein, R.J., *Properties of the skin as a membrane.* Adv Biol Skin, 1972. **12**: p. 125-52.
32. Arora, A., M.R. Prausnitz, and S. Mitragotri, *Micro-scale devices for transdermal drug delivery.* Int J Pharm, 2008. **364**(2): p. 227-36.
33. Pathan, I.B. and C.M. Setty, *Chemical Penetration Enhancers for Transdermal Drug Delivery Systems.* Tropical Journal of Pharmaceutical Research, 2009. **8**(2): p. 173-179.
34. Herman, A. and A.P. Herman, *Essential oils and their constituents as skin penetration enhancer for transdermal drug delivery: a review.* J Pharm Pharmacol, 2015. **67**(4): p. 473-85.
35. Trommer, H. and R.H. Neubert, *Overcoming the stratum corneum: the modulation of skin penetration. A review.* Skin Pharmacol Physiol, 2006. **19**(2): p. 106-21.
36. Gratieri, T., et al., *Next generation intra- and transdermal therapeutic systems: Using non- and minimally-invasive technologies to increase drug delivery into and across the skin.* European Journal of Pharmaceutical Sciences, 2013. **50**(5): p. 609-622.
37. Priya, B., T. Rashmi, and M. Bozena, *Transdermal iontophoresis.* 2006.
38. Zempsky, W.T., et al., *Evaluation of a low-dose lidocaine iontophoresis system for topical anesthesia in adults and children: a randomized, controlled trial.* Clin Ther, 2004. **26**(7): p. 1110-9.
39. Raiman, J., et al., *Delivery and stability of LHRH and Nafarelin in human skin: the effect of constant/pulsed iontophoresis.* Eur J Pharm Sci, 2004. **21**(2-3): p. 371-7.
40. Paudel, K.S., et al., *Challenges and opportunities in dermal/transdermal delivery.* Ther Deliv, 2010. **1**(1): p. 109-31.
41. Dhote, V., et al., *Iontophoresis: a potential emergence of a transdermal drug delivery system.* Sci Pharm, 2012. **80**(1): p. 1-28.
42. Ita, K., *Transdermal iontophoretic drug delivery: advances and challenges.* J Drug Target, 2016. **24**(5): p. 386-91.
43. Cross, S. and M. Roberts, *Physical enhancement of transdermal drug application: is delivery technology keeping up with pharmaceutical development?* Current drug delivery, 2004. **1**(1): p. 81-92.
44. Yarmush, M.L., et al., *Electroporation-based technologies for medicine: principles, applications, and challenges.* Annu Rev Biomed Eng, 2014. **16**: p. 295-320.
45. Gehl, J., et al., *Updated standard operating procedures for electrochemotherapy of cutaneous tumours and skin metastases.* Acta Oncol, 2018: p. 1-9.
46. Low, L., et al., *DNA vaccination with electroporation induces increased antibody responses in patients with prostate cancer.* Hum Gene Ther, 2009. **20**(11): p. 1269-78.
47. Todorova, B., et al., *Electroporation as a vaccine delivery system and a natural adjuvant to intradermal administration of plasmid DNA in macaques.* Scientific Reports, 2017. **7**.
48. Fisher, P.D., et al., *Adipose tissue: a new target for electroporation-enhanced DNA vaccines.* Gene Therapy, 2017. **24**(12): p. 757-767.
49. Ginsberg, A.A., et al., *Improvement of DNA Vaccines by Electroporation.* Gene Vaccines, 2012: p. 145-162.
50. Ake, J.A., et al., *Safety and Immunogenicity of PENNVAX-G DNA Prime Administered by Biojector 2000 or CELLECTRA Electroporation Device With Modified Vaccinia Ankara-CMDR Boost.* J Infect Dis, 2017. **216**(9): p. 1080-1090.
51. Amante, D.H., et al., *Skin Transfection Patterns and Expression Kinetics of Electroporation-Enhanced Plasmid Delivery Using the CELLECTRA-3P, a Portable Next-Generation Dermal Electroporation Device.* Hum Gene Ther Methods, 2015. **26**(4): p. 134-46.
52. Potter, H. and R. Heller, *Transfection by Electroporation.* Curr Protoc Mol Biol, 2018. **121**: p. 9 3 1-9 3 13.
53. Blagus, T., et al., *In vivo real-time monitoring system of electroporation mediated control of transdermal and topical drug delivery.* Journal of controlled release, 2013. **172**(3): p. 862-871.
54. Kang, T.H., et al., *Enhancement of protein vaccine potency by in vivo electroporation mediated intramuscular injection.* Vaccine, 2011. **29**(5): p. 1082-1089.
55. Donnelly, R.F. and T.R.R. Singh, *Novel delivery systems for transdermal and intradermal drug delivery*. 2015: John Wiley & Sons.
56. Murthy, S.N., *Magnetophoresis: an approach to enhance transdermal drug diffusion.* Pharmazie, 1999. **54**(5): p. 377-9.

57. Murthy, S.N., S.M. Sammeta, and C. Bowers, *Magnetophoresis for enhancing transdermal drug delivery: Mechanistic studies and patch design.* J Control Release, 2010. **148**(2): p. 197-203.
58. Benson, H.A., et al., *Enhanced skin permeation and hydration by magnetic field array: preliminary in-vitro and in-vivo assessment.* J Pharm Pharmacol, 2010. **62**(6): p. 696-701.
59. Schramm, J. and S. Mitragotri, *Transdermal drug delivery by jet injectors: Energetics of jet formation and penetration.* Pharmaceutical Research, 2002. **19**(11): p. 1673-1679.
60. Mitragotri, S., *Current status and future prospects of needle-free liquid jet injectors.* Nat Rev Drug Discov, 2006. **5**(7): p. 543-8.
61. Baxter, J. and S. Mitragotri, *Jet-induced skin puncture and its impact on needle-free jet injections: Experimental studies and a predictive model.* Journal of Controlled Release, 2005. **106**(3): p. 361-373.
62. Benson, H.A. and S. Namjoshi, *Proteins and peptides: strategies for delivery to and across the skin.* J Pharm Sci, 2008. **97**(9): p. 3591-610.
63. Burkoth, T.L., et al., *Transdermal and transmucosal powdered drug delivery.* Crit Rev Ther Drug Carrier Syst, 1999. **16**(4): p. 331-84.
64. Weissmueller, N.T., et al., *Alternative vaccine administration by powder injection: Needle-free dermal delivery of the glycoconjugate meningococcal group Y vaccine.* PLoS One, 2017. **12**(8): p. e0183427.
65. Cao, Y., et al., *Sustained epidermal powder drug delivery via skin microchannels.* J Control Release, 2017. **249**: p. 94-102.
66. Dean, H.J., D. Fuller, and J.E. Osorio, *Powder and particle-mediated approaches for delivery of DNA and protein vaccines into the epidermis.* Comparative Immunology Microbiology and Infectious Diseases, 2003. **26**(5-6): p. 373-388.
67. Dean, H.J. and D. Chen, *Epidermal powder immunization against influenza.* Vaccine, 2004. **23**(5): p. 681-6.
68. Drape, R.J., et al., *Epidermal DNA vaccine for influenza is immunogenic in humans.* Vaccine, 2006. **24**(21): p. 4475-4481.
69. Jones, S., et al., *DNA vaccination protects against an influenza challenge in a double-blind randomised placebo-controlled phase 1b clinical trial.* Vaccine, 2009. **27**(18): p. 2506-12.
70. Bremseth, D.L. and F. Pass, *Delivery of insulin by jet injection: recent observations.* Diabetes Technol Ther, 2001. **3**(2): p. 225-32.
71. McAllister, L., et al., *Needle-free jet injection for administration of influenza vaccine: a randomised non-inferiority trial.* Lancet, 2014. **384**(9944): p. 674-81.
72. Grohskopf, L.A., et al., *Prevention and Control of Seasonal Influenza with Vaccines.* MMWR Recomm Rep, 2016. **65**(5): p. 1-54.
73. Prausnitz, M.R. and R. Langer, *Transdermal drug delivery.* Nature Biotechnology, 2008. **26**(11): p. 1261-1268.
74. Bachhav, Y.G., et al., *Effect of controlled laser microporation on drug transport kinetics into and across the skin.* J Control Release, 2010. **146**(1): p. 31-6.
75. Bachhav, Y.G., A. Heinrich, and Y.N. Kalia, *Controlled intra- and transdermal protein delivery using a minimally invasive Erbium:YAG fractional laser ablation technology.* European Journal of Pharmaceutics and Biopharmaceutics, 2013. **84**(2): p. 355-364.
76. Scheiblhofer, S., et al., *Skin vaccination via fractional infrared laser ablation - Optimization of laser-parameters and adjuvantation.* Vaccine, 2017. **35**(14): p. 1802-1809.
77. Birchall, J., et al., *Cutaneous gene expression of plasmid DNA in excised human skin following delivery via microchannels created by radio frequency ablation.* Int J Pharm, 2006. **312**(1-2): p. 15-23.
78. Levin, G., et al., *Combined micro-channel generation and iontophoresis for transdermal delivery of pharmaceutical agents*. 2009, Google Patents.
79. Levin, G., et al., *Transdermal delivery of human growth hormone through RF-microchannels.* Pharm Res, 2005. **22**(4): p. 550-5.
80. Prausnitz, M.R., *Microneedles for transdermal drug delivery.* Adv Drug Deliv Rev, 2004. **56**(5): p. 581-7.
81. van der Maaden, K., W. Jiskoot, and J. Bouwstra, *Microneedle technologies for (trans)dermal drug and vaccine delivery.* Journal of Controlled Release, 2012. **161**(2): p. 645-655.
82. Kim, Y.C., J.H. Park, and M.R. Prausnitz, *Microneedles for drug and vaccine delivery.* Adv Drug Deliv Rev, 2012. **64**(14): p. 1547-68.
83. Larraneta, E., et al., *Microneedle arrays as transdermal and intradermal drug delivery systems: Materials science, manufacture and commercial development.* Materials Science & Engineering R-Reports, 2016. **104**: p. 1-32.

84. Bhatnagar, S., K. Dave, and V.V.K. Venuganti, *Microneedles in the clinic.* J Control Release, 2017. **260**: p. 164-182.
85. Daddona, P.E., et al., *Parathyroid hormone (1-34)-coated microneedle patch system: clinical pharmacokinetics and pharmacodynamics for treatment of osteoporosis.* Pharm Res, 2011. **28**(1): p. 159-65.
86. Palylyk-Colwell, E. and C. Ford, *A Transdermal Glucagon Patch for Severe Hypoglycemia*, in *CADTH Issues in Emerging Health Technologies*. 2016: Ottawa (ON). p. 1-7.
87. ClinicalTrials.gov. *A Study to Evaluate the Long-Term Safety of M207 in the Acute Treatment of Migraine (ADAM), ClinicalTrials.gov Identifier: NCT03282227*. Available from: https://clinicaltrials.gov/ct2/show/NCT03282227 (accessed May 18, 2018).
88. Prausnitz, M.R., *Engineering Microneedle Patches for Vaccination and Drug Delivery to Skin.* Annu Rev Chem Biomol Eng, 2017. **8**: p. 177-200.
89. Hirobe, S., et al., *Clinical study and stability assessment of a novel transcutaneous influenza vaccination using a dissolving microneedle patch.* Biomaterials, 2015. **57**: p. 50-8.
90. Rouphael, N.G., et al., *The safety, immunogenicity, and acceptability of inactivated influenza vaccine delivered by microneedle patch (TIV-MNP 2015): a randomised, partly blinded, placebo-controlled, phase 1 trial.* Lancet, 2017. **390**(10095): p. 649-658.
91. Gill, H.S., et al., *Effect of microneedle design on pain in human volunteers.* Clin J Pain, 2008. **24**(7): p. 585-94.
92. Goss, S., et al., *Dependence of the ultrasonic properties of biological tissue on constituent proteins.* The Journal of the Acoustical Society of America, 1980. **67**(3): p. 1041-1044.
93. Ahuja, A.S., *Ultrasonic attenuation in soft tissues: reasons for large magnitude and linear frequency dependence.* Ultrason Imaging, 1980. **2**(4): p. 391-6.
94. Leighton, T.G., *What is ultrasound?* Progress in Biophysics & Molecular Biology, 2007. **93**(1-3): p. 3-83.
95. Hamilton, M.F. and D.T. Blackstock, *Nonlinear acoustics*. 1998, San Diego, CA: Academic Press. xviii, 455 p.
96. Ziskin, M.C., *Fundamental Physics of Ultrasound and Its Propagation in Tissue.* Radiographics, 1993. **13**(3): p. 705-709.
97. Merino, G., et al., *Frequency and thermal effects on the enhancement of transdermal transport by sonophoresis.* J Control Release, 2003. **88**(1): p. 85-94.
98. Meidan, V.M., A.D. Walmsley, and W.J. Irwin, *Phonophoresis - Is It a Reality.* International Journal of Pharmaceutics, 1995. **118**(2): p. 129-149.
99. Tang, H., et al., *An investigation of the role of cavitation in low-frequency ultrasound-mediated transdermal drug transport.* Pharmaceutical Research, 2002. **19**(8): p. 1160-1169.
100. Tezel, A., A. Sens, and S. Mitragotri, *Investigations of the role of cavitation in low-frequency sonophoresis using acoustic spectroscopy.* Journal of Pharmaceutical Sciences, 2002. **91**(2): p. 444-453.
101. Nyborg, W.L.M., *Acoustic streaming*, in *Physical acoustics*. 1965, Elsevier. p. 265-331.
102. Leighton, T., A. Walton, and M. Pickworth, *Primary bjerknes forces.* European Journal of Physics, 1990. **11**(1): p. 47.
103. Hill, C.R., J.C. Bamber, and G.R. ter Haar, *Physical principles of medical ultrasonics*. 2004, ASA.
104. Coussios, C.C. and R.A. Roy, *Applications of acoustics and cavitation to noninvasive therapy and drug delivery.* Annual Review of Fluid Mechanics, 2008. **40**: p. 395-420.
105. Leighton, T., *The acoustic bubble*. 2012: Academic press.
106. Flynn, H.G., *Physics of Acoustic Cavitation.* Journal of the Acoustical Society of America, 1959. **31**(11): p. 1582-1582.
107. Stride, E., *Physical Principles of Microbubbles for Ultrasound Imaging and Therapy.* Translational Neurosonology, 2015. **36**: p. 11-22.
108. Elder, S. and W. Nyborg, *Acoustic streaming resulting from a resonant bubble.* The Journal of the Acoustical Society of America, 1956. **28**(1): p. 155-155.
109. Mitragotri, S., D. Blankschtein, and R. Langer, *Transdermal drug delivery using low-frequency sonophoresis.* Pharm Res, 1996. **13**(3): p. 411-20.
110. Marmottant, P. and S. Hilgenfeldt, *Controlled vesicle deformation and lysis by single oscillating bubbles.* Nature, 2003. **423**(6936): p. 153-6.
111. Tachibana, K. and S. Tachibana, *Use of ultrasound to enhance the local anesthetic effect of topically applied aqueous lidocaine.* Anesthesiology, 1993. **78**(6): p. 1091-6.
112. Suslick, K.S. and L.A. Crum, *Sonochemistry and sonoluminescence*. 1998: Wiley-Interscience: New York.

113. Pecha, R. and B. Gompf, *Microimplosions: cavitation collapse and shock wave emission on a nanosecond time scale.* Phys Rev Lett, 2000. **84**(6): p. 1328-30.
114. Fong, S.W., et al., *Numerical analysis of a gas bubble near bio-materials in an ultrasound field.* Ultrasound Med Biol, 2006. **32**(6): p. 925-42.
115. Polat, B.E., et al., *Ultrasound-mediated transdermal drug delivery: Mechanisms, scope, and emerging trends.* Journal of Controlled Release, 2011. **152**(3): p. 330-348.
116. Tang, H., D. Blankschtein, and R. Langer, *Effects of low-frequency ultrasound on the transdermal permeation of mannitol: comparative studies with in vivo and in vitro skin.* J Pharm Sci, 2002. **91**(8): p. 1776-94.
117. Tezel, A., et al., *Frequency dependence of sonophoresis.* Pharm Res, 2001. **18**(12): p. 1694-700.
118. Polat, B.E., et al., *Transport pathways and enhancement mechanisms within localized and non-localized transport regions in skin treated with low-frequency sonophoresis and sodium lauryl sulfate.* Journal of pharmaceutical sciences, 2011. **100**(2): p. 512-529.
119. Kushner, J.t., D. Blankschtein, and R. Langer, *Experimental demonstration of the existence of highly permeable localized transport regions in low-frequency sonophoresis.* J Pharm Sci, 2004. **93**(11): p. 2733-45.
120. Kushner, J.t., D. Blankschtein, and R. Langer, *Heterogeneity in skin treated with low-frequency ultrasound.* J Pharm Sci, 2008. **97**(10): p. 4119-28.
121. Webb, I.R., S.J. Payne, and C.C. Coussios, *The effect of temperature and viscoelasticity on cavitation dynamics during ultrasonic ablation.* J Acoust Soc Am, 2011. **130**(5): p. 3458-66.
122. Gyongy, M. and C.C. Coussios, *Passive cavitation mapping for localization and tracking of bubble dynamics.* J Acoust Soc Am, 2010. **128**(4): p. EL175-80.
123. Coussios, C.C., J.R.T. Collin, and A.P. Muckle, *Non-invasive monitoring and control of inertial cavitation dynamics during HIFU exposure in vitro.* 6th International Symposium on Therapeutic Ultrasound, 2007. **911**: p. 164-170.
124. Gyongy, M. and C.C. Coussios, *Passive Spatial Mapping of Inertial Cavitation During HIFU Exposure.* Ieee Transactions on Biomedical Engineering, 2010. **57**(1): p. 48-56.
125. Arvanitis, C.D., et al., *Cavitation-Enhanced Extravasation for Drug Delivery.* Ultrasound in Medicine and Biology, 2011. **37**(11): p. 1838-1852.
126. Mitragotri, S., D. Blankschtein, and R. Langer, *Ultrasound-mediated transdermal protein delivery.* Science, 1995. **269**(5225): p. 850-3.
127. Mitragotri, S., D. Blankschtein, and R. Langer, *Transdermal drug delivery using low-frequency sonophoresis.* Pharmaceutical research, 1996. **13**(3): p. 411-420.
128. Paliwal, S., G.K. Menon, and S. Mitragotri, *Low-frequency sonophoresis: ultrastructural basis for stratum corneum permeability assessed using quantum dots.* J Invest Dermatol, 2006. **126**(5): p. 1095-101.
129. Schoellhammer, C.M., D. Blankschtein, and R. Langer, *Skin permeabilization for transdermal drug delivery: recent advances and future prospects.* Expert Opinion on Drug Delivery, 2014. **11**(3): p. 393-407.
130. Tang, H., et al., *An investigation of the role of cavitation in low-frequency ultrasound-mediated transdermal drug transport.* Pharm Res, 2002. **19**(8): p. 1160-9.
131. Kost, J., et al., *Transdermal monitoring of glucose and other analytes using ultrasound.* Nat Med, 2000. **6**(3): p. 347-50.
132. Mitragotri, S., et al., *Transdermal extraction of analytes using low-frequency ultrasound.* Pharmaceutical Research, 2000. **17**(4): p. 466-470.
133. Lavon, I. and J. Kost, *Ultrasound and transdermal drug delivery.* Drug Discov Today, 2004. **9**(15): p. 670-6.
134. Farinha, A., et al., *Skin impedance reduction for electrophysiology measurements using ultrasonic skin permeation: initial report and comparison to current methods.* Biomedical instrumentation & technology, 2006. **40**(1): p. 72-77.
135. Kim, D.K., S.W. Choi, and Y.H. Kwak, *The effect of SonoPrep(R) on EMLA(R) cream application for pain relief prior to intravenous cannulation.* Eur J Pediatr, 2012. **171**(6): p. 985-8.
136. Dragicevic, N. and H.I. Maibach, *Percutaneous Penetration Enhancers Physical Methods in Penetration Enhancement*. 2017: Springer.
137. Inc., T.S. *The U-Strip – Ultrasonic Transdermal Drug Delivery*. Available from: http://www.transdermalspecialties.com/products.html (accessed April 16, 2018).
138. Mitragotri, S., et al., *Synergistic effect of low-frequency ultrasound and sodium lauryl sulfate on transdermal transport.* J Pharm Sci, 2000. **89**(7): p. 892-900.

139. Nayak, A., et al., *Lidocaine carboxymethylcellulose with gelatine co-polymer hydrogel delivery by combined microneedle and ultrasound.* Drug Deliv, 2016. **23**(2): p. 658-69.
140. Chen, B.T., J.S. Wei, and C. Iliescu, *Sonophoretic enhanced microneedles array (SEMA)-Improving the efficiency of transdermal drug delivery.* Sensors and Actuators B-Chemical, 2010. **145**(1): p. 54-60.
141. Han, T. and D.B. Das, *Permeability Enhancement for Transdermal Delivery of Large Molecule Using Low-Frequency Sonophoresis Combined with Microneedles.* Journal of Pharmaceutical Sciences, 2013. **102**(10): p. 3614-3622.
142. Kost, J., et al., *Synergistic effect of electric field and ultrasound on transdermal transport.* Pharmaceutical Research, 1996. **13**(4): p. 633-638.
143. Zorec, B., et al., *Ultrasound and electric pulses for transdermal drug delivery enhancement: Ex vivo assessment of methods with in vivo oriented experimental protocols.* Int J Pharm, 2015. **490**(1-2): p. 65-73.
144. Le, L., J. Kost, and S. Mitragotri, *Combined effect of low-frequency ultrasound and iontophoresis: applications for transdermal heparin delivery.* Pharm Res, 2000. **17**(9): p. 1151-4.
145. Fang, J.Y., et al., *Transdermal iontophoresis of sodium nonivamide acetate. V. Combined effect of physical enhancement methods.* Int J Pharm, 2002. **235**(1-2): p. 95-105.
146. Watanabe, S., et al., *Enhanced transdermal drug penetration by the simultaneous application of iontophoresis and sonophoresis.* Journal of Drug Delivery Science and Technology, 2009. **19**(3): p. 185-189.
147. Hikima, T., et al., *Mechanisms of synergistic skin penetration by sonophoresis and iontophoresis.* Biol Pharm Bull, 2009. **32**(5): p. 905-9.
148. Spierings, E.L., J.A. Brevard, and N.P. Katz, *Two-minute skin anesthesia through ultrasound pretreatment and iontophoretic delivery of a topical anesthetic: a feasibility study.* Pain Med, 2008. **9**(1): p. 55-9.
149. Bhatnagar, S., H. Schiffter, and C.C. Coussios, *Exploitation of acoustic cavitation-induced microstreaming to enhance molecular transport.* J Pharm Sci, 2014. **103**(6): p. 1903-12.
150. Feiszthuber, H., et al., *Cavitation-enhanced delivery of insulin in agar and porcine models of human skin.* Phys Med Biol, 2015. **60**(6): p. 2421-2434.
151. Bhatnagar, S., *Cavitation-Enhanced Transdermal Vaccine Delivery By Ultrasound*, in *Department of Engineering Science*. 2014, University of Oxford: Oxford.
152. Kwan, J.J., et al., *Ultrasound-Propelled Nanocups for Drug Delivery.* Small, 2015. **11**(39): p. 5305-14.
153. Myers, R., et al., *Polymeric Cups for Cavitation-mediated Delivery of Oncolytic Vaccinia Virus.* Mol Ther, 2016. **24**(9): p. 1627-33.
154. Myers, R., et al., *Ultrasound-mediated cavitation does not decrease the activity of small molecule, antibody or viral-based medicines.* Int J Nanomedicine, 2018. **13**: p. 337-349.
155. Godin, B. and E. Touitou, *Transdermal skin delivery: predictions for humans from in vivo, ex vivo and animal models.* Adv Drug Deliv Rev, 2007. **59**(11): p. 1152-61.
156. Jung, E.C. and H.I. Maibach, *Animal models for percutaneous absorption.* J Appl Toxicol, 2015. **35**(1): p. 1-10.
157. Danilenko, D.M., G.D.L. Phillips, and D. Diaz, *In Vitro Skin Models and Their Predictability in Defining Normal and Disease Biology, Pharmacology, and Toxicity.* Toxicologic pathology, 2016. **44**(4): p. 555-563.
158. Cantrell Jr, J.H., R.E. Goans, and R.L. Roswell, *Acoustic impedance variations at burn–nonburn interfaces in porcine skin.* The Journal of the Acoustical Society of America, 1978. **64**(3): p. 731-735.
159. Roberts, M.E. and K.R. Mueller, *Comparisons of in vitro nitroglycerin (TNG) flux across yucatan pig, hairless mouse, and human skins.* Pharm Res, 1990. **7**(6): p. 673-6.
160. Bronaugh, R.L., R.F. Stewart, and E.R. Congdon, *Methods for in vitro percutaneous absorption studies. II. Animal models for human skin.* Toxicol Appl Pharmacol, 1982. **62**(3): p. 481-8.
161. Kwan, J.J., et al., *Ultrasound-Propelled Nanocups for Drug Delivery.* Small, 2015.
162. Kwan, J.J., et al., *Ultrasound-induced inertial cavitation from gas-stabilizing nanoparticles.* Phys Rev E Stat Nonlin Soft Matter Phys, 2015. **92**(2-1): p. 023019.
163. Anagel Ultrasound Gel; product code: UGEl 250/UGEL 5000 [Online]; Ana Wiz Ltd: Surrey, U., 2004, http://www.ultrasound-gel.co.uk/gel-shop/technical-specifications.html (accessed October 13, 2015).
164. Weiner, G.J., *Building better monoclonal antibody-based therapeutics.* Nat Rev Cancer, 2015. **15**(6): p. 361-70.

165. van Blokland, A.C., Bhatnagar, S., Carlisle, R., Coussios, C.C., *Mediating and monitoring transdermal drug delivery using cavitation-enhanced ultrasound*, in *BioEngenuity: Improving Human Health Keynotes*. 10 November 2016: Oxford, United Kingdom.
166. van Blokland, A.C., Bhatnagar, S., Feddern, L., Carlisle, R., Coussios, C.C., *Mediating and monitoring transdermal drug delivery using cavitation-enhanced ultrasound*, in *MeiBioEng16*. 5 September 2016: Keble College, Oxford, United Kingdom.
167. Gershbein, L.L., *Percutaneous toxicity of thioglycolate mixtures in rabbits.* J Pharm Sci, 1979. **68**(10): p. 1230-5.
168. Ghosh, S. and D. Blankschtein, *The role of sodium dodecyl sulfate (SDS) micelles in inducing skin barrier perturbation in the presence of glycerol.* J Cosmet Sci, 2007. **58**(2): p. 109-33.
169. Yanase, K. and I. Hatta, *Disruption of human stratum corneum lipid structure by sodium dodecyl sulphate.* Int J Cosmet Sci, 2018. **40**(1): p. 44-49.
170. Welss, T., D.A. Basketter, and K.R. Schroder, *In vitro skin irritation: facts and future. State of the art review of mechanisms and models.* Toxicol In Vitro, 2004. **18**(3): p. 231-43.
171. ThermoFisher Scientific. *Fluorescence SpectraViewer*. [cited 2018 March 24]; Available from: https://www.thermofisher.com/nl/en/home/life-science/cell-analysis/labeling-chemistry/fluorescence-spectraviewer.html.
172. Bhatnagar, S., et al., *Exploitation of sub-micron cavitation nuclei to enhance ultrasound-mediated transdermal transport and penetration of vaccines.* J Control Release, 2016. **238**: p. 22-30.
173. IMITREX® tablet [package insert]. GlaxoSmithKline LLC, P., PA, USA. Available from: https://www.gsksource.com/pharma/content/dam/GlaxoSmithKline/US/en/Prescribing_Information/Imitrex_Tablets/pdf/IMITREX-TABLETS-PI-PIL.PDF (accessed April 17, 2017).
174. Lambert, G.A., *Preclinical neuropharmacology of naratriptan.* Cns Drug Reviews, 2005. **11**(3): p. 289-316.
175. Organization, W.H. *Online Q&A: How common are headaches?* 2014; Available from: http://www.who.int/features/qa/25/en/ (accessed May 28, 2017).
176. Organization, W.H., *Headache disorders.* 2016.
177. Pierce, M., et al., *Zelrix: a novel transdermal formulation of sumatriptan.* Headache, 2009. **49**(6): p. 817-25.
178. Olesen, I.J., *The headaches*. 3rd edition ed. 2006, Philadelphia, Pa: Lippincott Williams & Wilkins.
179. Jhee, S.S., et al., *Pharmacokinetics and pharmacodynamics of the triptan antimigraine agents: a comparative review.* Clin Pharmacokinet, 2001. **40**(3): p. 189-205.
180. Adelman, J.U. and R.D. Adelman, *Current options for the prevention and treatment of migraine.* Clinical Therapeutics, 2001. **23**(6): p. 772-788.
181. Burstein, R., B. Collins, and M. Jakubowski, *Defeating migraine pain with triptans: a race against the development of cutaneous allodynia.* Ann Neurol, 2004. **55**(1): p. 19-26.
182. Dahlof, C., *Sumatriptan nasal spray in the acute treatment of migraine: a review of clinical studies.* Cephalalgia, 1999. **19**(9): p. 769-78.
183. Tepper, S.J., et al., *Sumatriptan suppositories for the acute treatment of migraine. S2B351 Study Group.* Int J Clin Pract, 1998. **52**(1): p. 31-5.
184. Tayel, S.A., et al., *Sumatriptan succinate sublingual fast dissolving thin films: formulation and in vitro/in vivo evaluation.* Pharm Dev Technol, 2015: p. 1-10.
185. Shivanand, K., et al., *In vivo bioavailability studies of sumatriptan succinate buccal tablets.* Daru, 2011. **19**(3): p. 224-30.
186. Telo, I., et al., *In-vitro characterization of buccal iontophoresis: the case of sumatriptan succinate.* International Journal of Pharmaceutics, 2016. **506**(1-2): p. 420-428.
187. Reed, M.L., et al., *Persistent Frequent Nausea Is Associated With Progression to Chronic Migraine: AMPP Study Results.* Headache, 2015. **55**(1): p. 76-87.
188. IMITREX® injection [package insert]. GlaxoSmithKline LLC, P., PA, USA. Available from: https://www.gsksource.com/pharma/content/dam/GlaxoSmithKline/US/en/Prescribing_Information/Imitrex_Injection/pdf/IMITREX-INJECTION-PI-PPI.PDF (accessed April 17, 2017).
189. Wu, D., et al., *Improvement of Transdermal Delivery of Sumatriptan Succinate Using a Novel Self-dissolving Microneedle Array Fabricated from Sodium Hyaluronate in Rats.* Biological & Pharmaceutical Bulletin, 2015. **38**(3): p. 365-373.
190. Wu, D., et al., *Permeation of sumatriptan succinate across human skin using multiple types of self-dissolving microneedle arrays fabricated from sodium hyaluronate.* Journal of Drug Targeting, 2016. **24**(8): p. 752-758.

191. Zecuity® [package insert]. NuPath Inc., W., MA, USA; January 2013. Available from: http://www.zecuity.com/pdf/ZECUITY_PI.pdf (accessed April 27, 2016).
192. FDA. *FDA Drug Safety Communication: FDA evaluating the risk of burns and scars with Zecuity (sumatriptan) migraine patch*. 2-6-2016; Available from: https://www.fda.gov/Drugs/DrugSafety/ucm504588.htm (accessed June 16, 2016).
193. Vikelis, M., K.C. Spingos, and A.M. Rapoport, *The iontophoretic transdermal system formulation of sumatriptan as a new option in the acute treatment of migraine: a perspective.* Therapeutic Advances in Neurological Disorders, 2015. **8**(4): p. 160-165.
194. Vikelis, M., D.D. Mitsikostas, and A.M. Rapoport, *Sumatriptan transdermal iontophoretic patch (NP101-Zelrix (TM)): review of pharmacology, clinical efficacy, and safety in the acute treatment of migraine.* Neuropsychiatric Disease and Treatment, 2012. **8**: p. 429-434.
195. Goldstein, J., et al., *A Sumatriptan Iontophoretic Transdermal System for the Acute Treatment of Migraine.* Headache, 2012. **52**(9): p. 1402-1410.
196. Smith, T.R., et al., *Twelve-Month Tolerability and Efficacy Study of NP101, the Sumatriptan Iontophoretic Transdermal System.* Headache, 2012. **52**(4): p. 612-624.
197. Schulz, M., et al., *Therapeutic and toxic blood concentrations of nearly 1,000 drugs and other xenobiotics.* Crit Care, 2012. **16**(4): p. R136.
198. Nair, A.B. and S. Jacob, *A simple practice guide for dose conversion between animals and human.* Journal of basic and clinical pharmacy, 2016. **7**(2): p. 27.
199. Cosson, V.F., et al., *Mixed effect modeling of sumatriptan pharmacokinetics during drug development .1. Interspecies allometric scaling.* Journal of Pharmacokinetics and Biopharmaceutics, 1997. **25**(2): p. 149-167.
200. Tezel, A. and S. Mitragotri, *Interactions of inertial cavitation bubbles with stratum corneum lipid bilayers during low-frequency sonophoresis.* Biophysical Journal, 2003. **85**(6): p. 3502-3512.
201. Mitragotri, S. and J. Kost, *Low-frequency sonophoresis: a noninvasive method of drug delivery and diagnostics.* Biotechnol Prog, 2000. **16**(3): p. 488-92.
202. Mitragotri, S., D. Blankschtein, and R. Langer, *Ultrasound-Mediated Transdermal Protein Delivery.* Science, 1995. **269**(5225): p. 850-853.
203. Mitragotri, S. and J. Kost, *Transdermal delivery of heparin and low-molecular weight heparin using low-frequency ultrasound.* Pharmaceutical Research, 2001. **18**(8): p. 1151-1156.
204. Park, D., et al., *Transdermal drug delivery aided by an ultrasound contrast agent: an in vitro experimental study.* Open Biomed Eng J, 2010. **4**: p. 56-62.
205. Park, D., et al., *Sonophoresis Using Ultrasound Contrast Agents for Transdermal Drug Delivery: An in Vivo Experimental Study.* Ultrasound in Medicine and Biology, 2012. **38**(4): p. 642-650.
206. Gyongy, M. and C.C. Coussios, *Passive cavitation mapping for localization and tracking of bubble dynamics.* Journal of the Acoustical Society of America, 2010. **128**(4): p. E175-E180.
207. Commons, W., V.d.o.l.m.b.a. white).svg, Editor. 2013, Gwilz.
208. Wan, M., Y. Feng, and G. ter Haar, *Cavitation in biomedicine*. 2015: Springer.
209. Vikelis, M., D.D. Mitsikostas, and A.M. Rapoport, *Sumatriptan transdermal iontophoretic patch (NP101-Zelrix): review of pharmacology, clinical efficacy, and safety in the acute treatment of migraine.* Neuropsychiatr Dis Treat, 2012. **8**: p. 429-34.
210. Mecklenburg, L., et al., *The nude mouse skin phenotype: the role of Foxn1 in hair follicle development and cycling.* Exp Mol Pathol, 2001. **71**(2): p. 171-8.
211. Snyder, L.R., J.J. Kirkland, and J.W. Dolan, *Introduction to modern liquid chromatography*. 2011: John Wiley & Sons.
212. Harvey, D., *Modern analytical chemistry*. Vol. 381. 2000: McGraw-Hill New York.
213. Ilyichev, V.I., V.L. Koretz, and N.P. Melnikov, *Spectral Characteristics of Acoustic Cavitation.* Ultrasonics, 1989. **27**(6): p. 357-361.
214. Gurtner, G.C., et al., *Wound repair and regeneration.* Nature, 2008. **453**(7193): p. 314-21.
215. Lee, J.N., et al., *The effects of depilatory agents as penetration enhancers on human stratum corneum structures.* Journal of Investigative Dermatology, 2008. **128**(9): p. 2240-2247.
216. Ravichandran, S., L.J. Mortensen, and L.A. DeLouise, *Quantification of human skin barrier function and susceptibility to quantum dot skin penetration.* Nanotoxicology, 2011. **5**(4): p. 675-86.
217. Kushida, K., et al., *Application of calcium thioglycolate to improve transdermal delivery of theophylline in rats.* Chem Pharm Bull (Tokyo), 1984. **32**(1): p. 268-74.
218. Obaidi, M., et al., *Improved Pharmacokinetics of Sumatriptan With Breath Powered Nasal Delivery of Sumatriptan Powder.* Headache, 2013. **53**(8): p. 1323-1333.

219. Sheshala, R., N. Khan, and Y. Darwis, *Validated high performance liquid chromatography (HPLC) method for the determination of sumatriptan in rabbit plasma: Application to pharmacokinetic study.* African Journal of Pharmacy and Pharmacology, 2012. **6**(2): p. 98-107.
220. Duquesnoy, C., et al., *Comparative clinical pharmacokinetics of single doses of sumatriptan following subcutaneous, oral, rectal and intranasal administration.* Eur J Pharm Sci, 1998. **6**(2): p. 99-104.
221. Pereira, T.A., D.N. Ramos, and R.F. Lopez, *Hydrogel increases localized transport regions and skin permeability during low frequency ultrasound treatment.* Sci Rep, 2017. **7**: p. 44236.
222. Tezel, A., et al., *Synergistic effect of low-frequency ultrasound and surfactants on skin permeability.* J Pharm Sci, 2002. **91**(1): p. 91-100.
223. Kushner , J., D. Blankschtein, and R. Langer, *Experimental demonstration of the existence of highly permeable localize transport regions in low-frequency sonophoresis.* Journal of Pharmaceutical Sciences, 2004. **93**(11): p. 2733-2745.
224. Ueda, H., et al., *Acoustic Cavitation as an Enhancing Mechanism of Low-Frequency Sonophoresis for Transdermal Drug Delivery.* Biological & Pharmaceutical Bulletin, 2009. **32**(5): p. 916-920.
225. Bian, S., et al., *A multimodal instrument for real-time in situ study of ultrasound and cavitation mediated drug delivery.* Rev Sci Instrum, 2017. **88**(3): p. 034302.
226. Riedel, S., *Edward Jenner and the history of smallpox and vaccination.* Proc (Bayl Univ Med Cent), 2005. **18**(1): p. 21-5.
227. Ada, G., *Overview of vaccines and vaccination.* Mol Biotechnol, 2005. **29**(3): p. 255-72.
228. Kendirgi, F., et al., *Novel linear DNA vaccines induce protective immune responses against lethal infection with influenza virus type A/H5N1.* Hum Vaccin, 2008. **4**(6): p. 410-9.
229. Ulmer, J.B., U. Valley, and R. Rappuoli, *Vaccine manufacturing: challenges and solutions.* Nat Biotechnol, 2006. **24**(11): p. 1377-83.
230. Plotkin, S.A., *Vaccines, vaccination, and vaccinology.* J Infect Dis, 2003. **187**(9): p. 1349-59.
231. Baxter, D., *Active and passive immunity, vaccine types, excipients and licensing.* Occup Med (Lond), 2007. **57**(8): p. 552-6.
232. Plotkin, S.A., *Correlates of protection induced by vaccination.* Clin Vaccine Immunol, 2010. **17**(7): p. 1055-65.
233. Carrat, F. and A. Flahault, *Influenza vaccine: the challenge of antigenic drift.* Vaccine, 2007. **25**(39-40): p. 6852-62.
234. Zambon, M.C., *Epidemiology and pathogenesis of influenza.* J Antimicrob Chemother, 1999. **44 Suppl B**: p. 3-9.
235. Taubenberger, J.K. and D.M. Morens, *1918 Influenza: the mother of all pandemics.* Emerg Infect Dis, 2006. **12**(1): p. 15-22.
236. Treanor, J., *Influenza vaccine--outmaneuvering antigenic shift and drift.* N Engl J Med, 2004. **350**(3): p. 218-20.
237. Moscona, A., *Neuraminidase inhibitors for influenza.* N Engl J Med, 2005. **353**(13): p. 1363-73.
238. Tong, S., et al., *New world bats harbor diverse influenza A viruses.* PLoS Pathog, 2013. **9**(10): p. e1003657.
239. Kilbourne, E.D., *Influenza pandemics of the 20th century.* Emerg Infect Dis, 2006. **12**(1): p. 9-14.
240. Falconer, M., *The National Influenza Immunisation Programme 2017/18*, P.H. England, Editor. 2017: London, United Kingdom.
241. Gerdil, C., *The annual production cycle for influenza vaccine.* Vaccine, 2003. **21**(16): p. 1776-9.
242. Lin, Y., et al., *The characteristics and antigenic properties of recently emerged subclade 3C.3a and 3C.2a human influenza A(H3N2) viruses passaged in MDCK cells.* Influenza Other Respir Viruses, 2017. **11**(3): p. 263-274.
243. Audsley, J.M. and G.A. Tannock, *Cell-based influenza vaccines: progress to date.* Drugs, 2008. **68**(11): p. 1483-91.
244. Moro, P.L., et al., *Surveillance of adverse events after the first trivalent inactivated influenza vaccine produced in mammalian cell culture (Flucelvax((R))) reported to the Vaccine Adverse Event Reporting System (VAERS), United States, 2013-2015.* Vaccine, 2015. **33**(48): p. 6684-8.
245. Manini, I., et al., *Egg-Independent Influenza Vaccines and Vaccine Candidates.* Vaccines (Basel), 2017. **5**(3).
246. Cox, M.M. and J.R. Hollister, *FluBlok, a next generation influenza vaccine manufactured in insect cells.* Biologicals, 2009. **37**(3): p. 182-9.
247. Kutzler, M.A. and D.B. Weiner, *DNA vaccines: ready for prime time?* Nat Rev Genet, 2008. **9**(10): p. 776-88.

248. Crank, M.C., et al., *Phase 1 study of pandemic H1 DNA vaccine in healthy adults.* PLoS One, 2015. **10**(4): p. e0123969.
249. Xenopoulos, A. and P. Pattnaik, *Production and purification of plasmid DNA vaccines: is there scope for further innovation?* Expert Review of Vaccines, 2014. **13**(12): p. 1537-1551.
250. Williams, J.A., A.E. Carnes, and C.P. Hodgson, *Plasmid DNA vaccine vector design: Impact on efficacy, safety and upstream production.* Biotechnology Advances, 2009. **27**(4): p. 353-370.
251. Mairhofer, J., et al., *A novel antibiotic free plasmid selection system: advances in safe and efficient DNA therapy.* Biotechnol J, 2008. **3**(1): p. 83-9.
252. Poulet, H., et al., *Development and registration of recombinant veterinary vaccines. The example of the canarypox vector platform.* Vaccine, 2007. **25**(30): p. 5606-12.
253. Bergman, P.J., et al., *Development of a xenogeneic DNA vaccine program for canine malignant melanoma at the Animal Medical Center.* Vaccine, 2006. **24**(21): p. 4582-5.
254. Ferraro, B., et al., *Clinical applications of DNA vaccines: current progress.* Clin Infect Dis, 2011. **53**(3): p. 296-302.
255. Walters, A.A., et al., *Comparative analysis of enzymatically produced novel linear DNA constructs with plasmids for use as DNA vaccines.* Gene Ther, 2014. **21**(7): p. 645-52.
256. Scott, V.L., et al., *Novel synthetic plasmid and Doggybone (TM) DNA vaccines induce neutralizing antibodies and provide protection from lethal influenza challenge in mice.* Human Vaccines & Immunotherapeutics, 2015. **11**(8): p. 1972-1982.
257. Rice, J., C.H. Ottensmeier, and F.K. Stevenson, *DNA vaccines: precision tools for activating effective immunity against cancer.* Nat Rev Cancer, 2008. **8**(2): p. 108-20.
258. Iurescia, S., D. Fioretti, and M. Rinaldi, *Strategies for improving DNA vaccine performance.* Methods Mol Biol, 2014. **1143**: p. 21-31.
259. Hasson, S.S.A.A., J.K.Z. Al-Busaidi, and T.A. Sallam, *The past, current and future trends in DNA vaccine immunisations.* Asian Pacific Journal of Tropical Biomedicine, 2015. **5**(5): p. 344-353.
260. Zaric, M., et al., *Microneedle-mediated delivery of viral vectored vaccines.* Expert Opin Drug Deliv, 2017. **14**(10): p. 1177-1187.
261. Billich, A., *Technology evaluation: FluMist, University of Michigan.* Curr Opin Mol Ther, 2000. **2**(3): p. 340-4.
262. Grohskopf, L.A., et al., *Prevention and Control of Seasonal Influenza With Vaccines: Recommendations of the Advisory Committee on Immunization Practices-United States, 2017-18 Influenza Season.* Am J Transplant, 2017. **17**(11): p. 2970-2982.
263. Pedro, G.S., et al., *Ultrasound-mediated gene delivery of naked plasmid DNA in skeletal muscles: A case for bolus injections.* Journal of Controlled Release, 2014. **195**: p. 130-137.
264. Ramamoorth, M. and A. Narvekar, *Non viral vectors in gene therapy- an overview.* J Clin Diagn Res, 2015. **9**(1): p. GE01-6.
265. Liang, H.D., J. Tang, and M. Halliwell, *Sonoporation, drug delivery, and gene therapy.* Proc Inst Mech Eng H, 2010. **224**(2): p. 343-61.
266. Barry, M.E., et al., *Role of endogenous endonucleases and tissue site in transfection and CpG-mediated immune activation after naked DNA injection.* Hum Gene Ther, 1999. **10**(15): p. 2461-80.
267. Fechheimer, M., et al., *Transfection of Mammalian-Cells with Plasmid DNA by Scrape Loading and Sonication Loading.* Proceedings of the National Academy of Sciences of the United States of America, 1987. **84**(23): p. 8463-8467.
268. Tata, D.B., F. Dunn, and D.J. Tindall, *Selective clinical ultrasound signals mediate differential gene transfer and expression in two human prostate cancer cell lines: LnCap and PC-3.* Biochemical and Biophysical Research Communications, 1997. **234**(1): p. 64-67.
269. Kim, H.J., et al., *Ultrasound-mediated transfection of mammalian cells.* Hum Gene Ther, 1996. **7**(11): p. 1339-46.
270. Greenleaf, W.J., et al., *Artificial cavitation nuclei significantly enhance acoustically induced cell transfection.* Ultrasound in Medicine and Biology, 1998. **24**(4): p. 587-595.
271. Bao, S.P., B.D. Thrall, and D.L. Miller, *Transfection of a reporter plasmid into cultured cells by sonoporation in vitro.* Ultrasound in Medicine and Biology, 1997. **23**(6): p. 953-959.
272. Anwer, K., et al., *Ultrasound enhancement of cationic lipid-mediated gene transfer to primary tumors following systemic administration.* Gene Therapy, 2000. **7**(21): p. 1833-1839.
273. Taniyama, Y., et al., *Local delivery of plasmid DNA into rat carotid artery using ultrasound.* Circulation, 2002. **105**(10): p. 1233-1239.
274. Bekeredjian, R., et al., *Ultrasound-targeted microbubble destruction can repeatedly direct highly specific plasmid expression to the heart.* Circulation, 2003. **108**(8): p. 1022-1026.

275. Koike, H., et al., *An efficient gene transfer method mediated by ultrasound and microbubbles into the kidney.* Journal of Gene Medicine, 2005. **7**(1): p. 108-116.
276. Taniyama, Y., et al., *Development of safe and efficient novel nonviral gene transfer using ultrasound: enhancement of transfection efficiency of naked plasmid DNA in skeletal muscle.* Gene Therapy, 2002. **9**(6): p. 372-380.
277. Lu, Q.L., et al., *Microbubble ultrasound improves the efficiency of gene transduction in skeletal muscle in vivo with reduced tissue damage.* Gene Therapy, 2003. **10**(5): p. 396-405.
278. Kodama, T., et al., *Evaluation of Transfection Efficiency in Skeletal Muscle Using Nano/Microbubbles and Ultrasound.* Ultrasound in Medicine and Biology, 2010. **36**(7): p. 1196-1205.
279. Luo, D. and W.M. Saltzman, *Enhancement of transfection by physical concentration of DNA at the cell surface.* Nature Biotechnology, 2000. **18**(8): p. 893-895.
280. Li, T.L., et al., *Gene transfer with echo-enhanced contrast agents: Comparison between Albunex, Optison, and Levovist in mice - Initial results.* Radiology, 2003. **229**(2): p. 423-428.
281. Wang, X.H., et al., *Gene transfer with microbubble ultrasound and plasmid DNA into skeletal muscle of mice: Comparison between commercially available microbubble contrast agents.* Radiology, 2005. **237**(1): p. 224-229.
282. Danialou, G., et al., *Ultrasound increases plasmid-mediated gene transfer to dystrophic muscles without collateral damage.* Mol Ther, 2002. **6**(5): p. 687-93.
283. Miller, D.L. and C. Dou, *Induction of apoptosis in sonoporation and ultrasonic gene transfer.* Ultrasound Med Biol, 2009. **35**(1): p. 144-54.
284. Tezel, A., et al., *Low-frequency ultrasound as a transcutaneous immunization adjuvant.* Vaccine, 2005. **23**(29): p. 3800-3807.
285. Dahlan, A., et al., *Transcutaneous immunisation assisted by low-frequency ultrasound.* International Journal of Pharmaceutics, 2009. **368**(1-2): p. 123-128.
286. Tezel, A., et al., *Topical delivery of anti-sense oligonucleotides using low-frequency sonophoresis.* Pharmaceutical Research, 2004. **21**(12): p. 2219-2225.
287. Van den Berg, J. and J. Haanen, *Gene therapy with naked DNA: Potential steps towards deregulation*. Division of Immunology, The Netherlands Cancer Institute, CGM/2010-06, 2010. .
288. Manthorpe, M., et al., *Gene-Therapy by Intramuscular Injection of Plasmid DNA - Studies on Firefly Luciferase Gene-Expression in Mice.* Human Gene Therapy, 1993. **4**(4): p. 419-431.
289. Arranz, A. and J. Ripoll, *Advances in optical imaging for pharmacological studies.* Front Pharmacol, 2015. **6**: p. 189.
290. Trombetta, C.M., et al., *Overview of Serological Techniques for Influenza Vaccine Evaluation: Past, Present and Future.* Vaccines (Basel), 2014. **2**(4): p. 707-34.
291. Organization, W.H., *Manual for the laboratory diagnosis and virological surveillance of influenza.* 2011.
292. Wang, B., et al., *Single radial haemolysis compared to haemagglutinin inhibition and microneutralization as a correlate of protection against influenza A H3N2 in children and adolescents.* Influenza Other Respir Viruses, 2017. **11**(3): p. 283-288.
293. Hobson, D., et al., *The role of serum haemagglutination-inhibiting antibody in protection against challenge infection with influenza A2 and B viruses.* J Hyg (Lond), 1972. **70**(4): p. 767-77.
294. Ng, S., et al., *Estimation of the Association Between Antibody Titers and Protection Against Confirmed Influenza Virus Infection in Children.* Journal of Infectious Diseases, 2013. **208**(8): p. 1320-1324.
295. Ueda, H., K. Sugibayashi, and Y. Morimoto, *Skin penetration-enhancing effect of drugs by phonophoresis.* Journal of Controlled Release, 1995. **37**(3): p. 291-297.
296. Riley, M.K. and W. Vermerris, *Recent Advances in Nanomaterials for Gene Delivery-A Review.* Nanomaterials, 2017. **7**(5).